Precision measurement of the $\beta - \bar{\nu}_e$ angular correlation coefficient *a* in free neutron decay
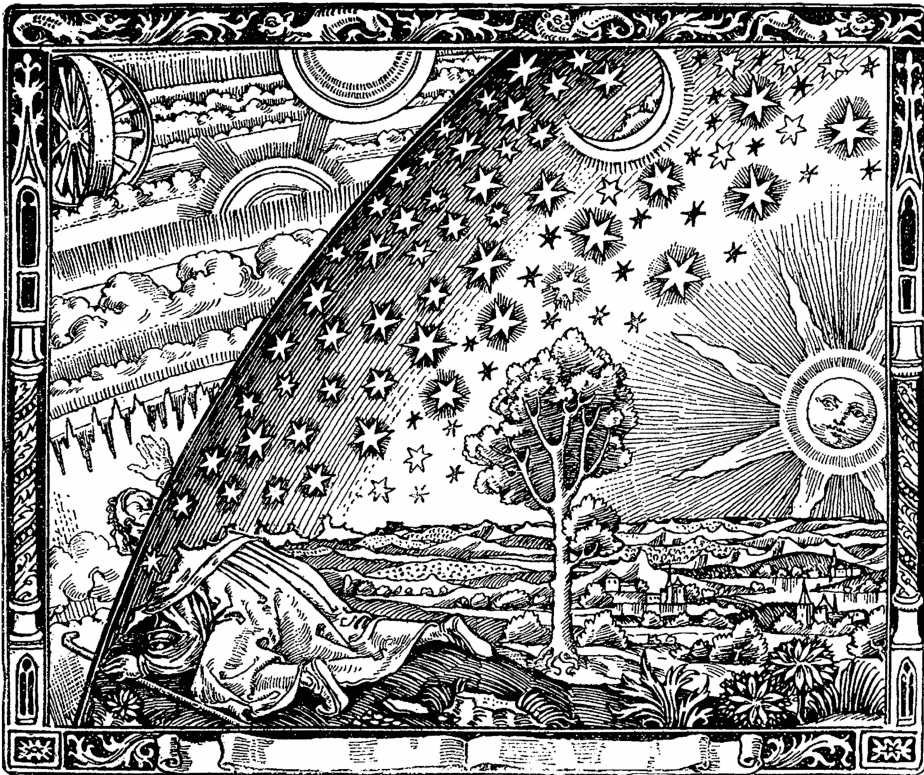
Ph.D. Thesis
of

Alexander Georg Wunderle

Faculty of Physics, Mathematics and Computer Science
at the Johannes Gutenberg-Universität
in Mainz

Datum der mündlichen Prüfung:
10.02.2017

"Non est ad astra mollis e terris via"
Seneca

Source: [Fla88]

Abstract

To investigate and test the Standard Model of particle physics (SM) at the low energy frontier, free neutron decay is an ideal lab. It is unencumbered by nuclear structure effects and the matrix elements are well known. In free neutron decay the ratio of the weak coupling constants $\lambda = g_A/g_V$ can be measured via several observables. One of these observables is the $\beta - \bar{\nu}_e$ angular correlation coefficient a, which is measured by the aSPECT experiment. In 2013 aSPECT had a successful beam-time, with the goal to improve the almost 40 year old precision of $\delta a/a \approx 4\,\%$ to about $1\,\%$.

Part of this thesis was the preparation of the beam-time 2013, including overcoming the main systematics of past beam-times: a saturation of the DAQ and discharges from residual gas. The saturation could be overcome by inventing a DAQ with logarithmic amplification, the discharges have been solved by reducing the field emission of electrodes and improved vacuum. The other part of this thesis was the analysis of the data taken 2013. For the data analysis a a new data structure The*ia* has been written, combining the data from the different sub-systems at one place allowing a detailed analysis of systematics event-by-event. Using The*ia* the pulse-height of each event could be corrected for noise peaks and double peaks via a spline interpolation. This interpolation has also been used to determine the pile-up rate and correct for it. In 2013 several individual experimental configurations with different systematics have been measured. The stability of the count rate during these configurations has been investigated and proven to fluctuate statistically only. Furthermore, for each configuration the background from residual gas has been determined. Additionally, first corrections of the experimentally enhanced effects have been determined and implemented into a global fit function, together with corrections for the pile-up and the background. Fitting the measured proton spectra with this function results in an a-value with a relative uncertainty of

$$\frac{\delta a}{a} = 0.82\,\%.$$

This result is already very precise, but not yet accurate, as some systematics still have to be included for a final analysis. Furthermore, the uncertainty of the fit and therefore a is currently limited by the fit quality of $\chi^2_{red} = 2.28$, meaning the fit function does not yet describe the measured data fully. Implementing the missing systematics will improve the fit quality and hence improve the resulting a in terms of accuracy and potentially also in terms of precision.

In conclusion it can be said, that the beam-time 2013 was successful. A significant improvement of the uncertainty of a by a factor of 4 has already been achieved, although the analysis is not completed yet. For the final analysis a precision of $\delta a/a \leq 1\,\%$ is expected.

Contents

List of Figures

List of Tables

Hors d'œuvre

«In 1932, [James] Chadwick made a fundamental discovery in the domain of nuclear science: he proved the existence of neutrons - elementary particles devoid of any electrical charge. In contrast with the helium nuclei (alpha rays) which are charged, and therefore repelled by the considerable electrical forces present in the nuclei of heavy atoms, this new tool in atomic disintegration need not overcome any electric barrier and is capable of penetrating and splitting the nuclei of even the heaviest elements. Chadwick in this way prepared the way towards the fission of uranium 235 and towards the creation of the atomic bomb. For this epoch-making discovery he was awarded the Hughes Medal of the Royal Society in 1932, and subsequently the Nobel Prize for Physics in 1935.»

Nobel Lectures[Nob65]

Since the discovery of the neutron by Chadwick [Cha32] the knowledge of its properties and interactions has been expanded considerably. Today, the neutron and its interactions are described within the Standard Model of particle physics (SM). The SM was developed in the 1950s and 1960s and has been successful without parallel since then. It unifies three of the four fundamental interactions, knows twelve fundamental fermions and 13 (Gauge) bosons and can explain a lot of questions of fundamental physics [PRSZ06]. Unfortunately, the SM does not include gravity and can not explain observations like Dark Mater or Dark Energy [BHS05, BAB+12]. Furthermore, it needs many input parameters, which can not be determined ab initio and have to be determined empirically. One of these parameters is the ratio of the weak coupling constants for the axial-vector and vector interaction $\lambda = g_A/g_V$. These interactions play a role in several reactions of particle physics, some examples are given in fig. 0.1. Hence, a precise knowledge of λ is of great importance for a wide field of fundamental particle physics.

The most prominent and longest known reaction described by λ is the β-decay. A Feynman graph of a β-decay for low and high momentum transfer Q is shown in fig. 1.1. In the SM the β-decay is described by the decay of a d quark to an u quark by exchange of a W^- boson, which then decays into an electron e^- and an electron-antineutrino $\bar{\nu}_e$. The most simplistic "core" undergoing β-decay, is the neutron itself. John M. Robson discovered in 1951 [Rob51], that free neutrons decay into a proton p, an electron e^- and an electron-antineutrino $\bar{\nu}_e$

$$n \xrightarrow{\beta} p + e^- + \bar{\nu}_e + 782.3 \, \text{keV}.$$
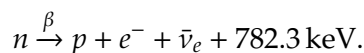
This neutron decay is mediated in the SM by axial-vector and vector couplings, so its a mixture between a Gamow-Teller (axial) and Fermi (vector) transition. The ratio λ of these
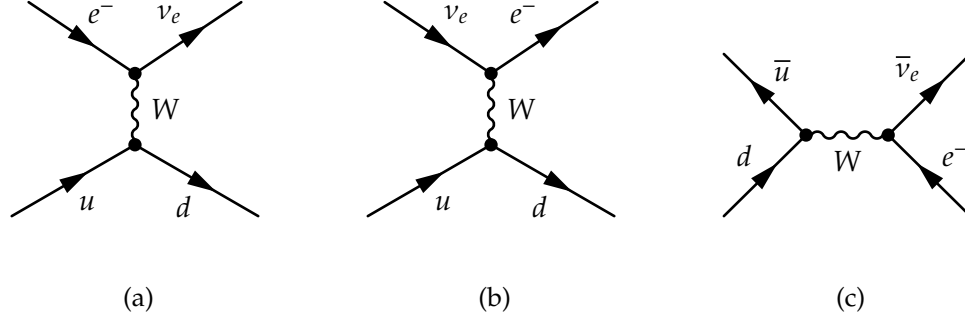
Figure 0.1.: Feynman graph with similar vertices as the β-decay. The time arrow is pointing
from left to right.
(a) neutron star formation,
(b) neutrino scattering,
(c) W production

couplings can be determined in free neutron decay by measuring the decay rate, which is proportional to various correlaction coefficients [Jac75]

$$\frac{dW}{dE_e d\Omega_e d\Omega_{\bar{\nu}_e}} \propto \left\{ 1 + a \frac{\vec{p}_e \vec{p}_{\bar{\nu}_e}}{E_e E_{\bar{\nu}_e}} + b \frac{m_e}{E_e} + \vec{\sigma}_n \left(A \frac{\vec{p}_e}{E_e} + \dots \right) + \dots \right\}.$$

Here, $\vec{p}$ is the momentum of the particle, m its mass and E its energy. $\vec{\sigma}_n$ is the polarisation of the neutron. The correlation coefficients shown here are the $\beta - \bar{\nu}_e$ angular correlation a, the Fierz interference term b and the β asymmetry A. This β asymmetry is basically the quantaty measured in the Wu experiment, discovering first Parity violation [WAH$^+$57]. Some of these correlation coefficients are depicted in fig. 1.2. The aSPECT experiment aims to measure the $\beta - \bar{\nu}_e$ angular correlation a. This correlation is linked in the SM to λ by

$$a = \frac{1 - |\lambda|^2}{1 + 3|\lambda|^2}.$$

Together with the lifetime of the neutron

$$\tau_n^{-1} = G_F^2 V_{ud}^2 \left(1 + 3|\lambda|^2 \right)$$

a can be used to test the unitarity of the Cabibbo-Kobayashi-Maskawa (CKM) matrix [HT15]. V_{ud} is the first matrix element of the CKM matrix and G_F the Fermi coupling constant.

Furthermore, within the SM λ is the same for the different reactions, hence deviations in λ would hint to physics beyond the SM. For example additional interactions like scalar, pseudo-scalar or tensor [SBNC06]. In fig. 0.2 two graphs for the current constraints from neutron β-decay on physics beyond the SM are depicted. These two graphs show, that precision experiments with neutrons are higly competitive with the Large Hadron Collider (LHC) in the search for new physics beyond the SM. A precision in the %-region corresponds to an energy scale of about 300 GeV, whereas a precision in the ‰-region corresponds to about 2 TeV [CRM13].

For precise measurements of λ in β-decay the neutron is an ideal lab. It is unencumbered by nuclear structure effects and the matrix elements are well known. Further, λ can be
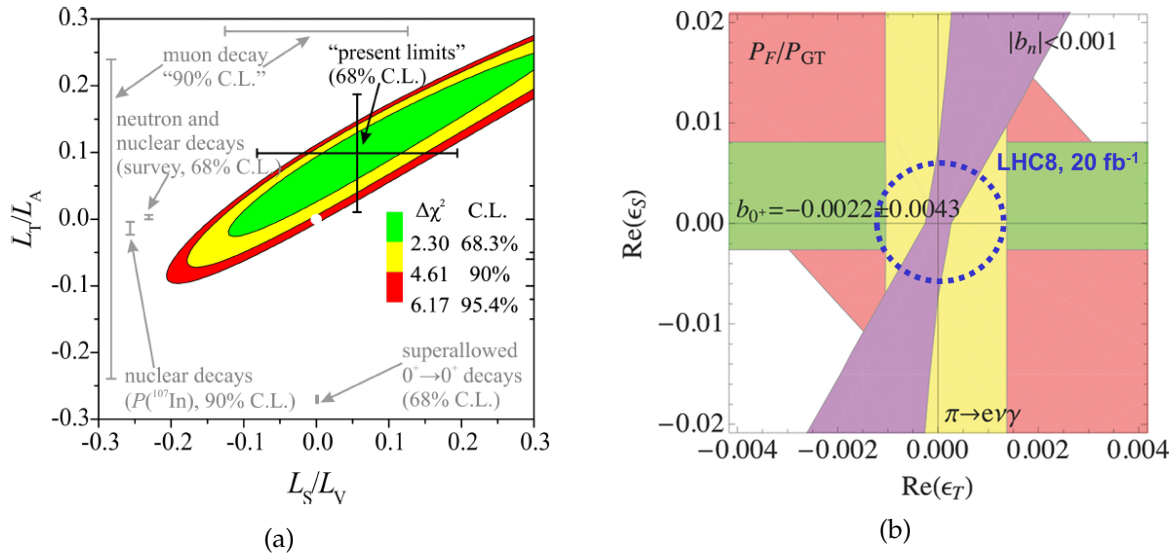
Figure 0.2.: Constraints on scalar and tensor couplings.

(a) Current limit from neutron decay (a, A and B only), taken from [Kon11]. The SM values are shown as white spot in the origin. Analogous limits from other decay, like muon decay are indicated, as well.

(b) 90 % CL. limits from from super-allowed nuclear decays (green), radiative pion decay (yellow) and measurements of the ratio inline image(red), along with the expected bound from future measurements of the Fierz term b in neutron decay (purple). Further, the limit form the LHC for $\sqrt{s}$ = 8 TeV is shown. Adapted from [NCGA13].

determined from several observables in free neutron decay, so the system is overdetermined and redundant. This redundancy allows to check experimentally for systematic effects and therefore improve the knowledge on λ. Further, this redundancy permits uniquely sensitive checks of model validities and limits [Dub91, DS11, SBNC06]. Currently, the ratio of the weak coupling constants is known to $\lambda = -1.2723(23)$ from free neutron decay only [O+14]. This value is an average of several different measurements, calculated by the Particle Data Group (PDG). The most precise determination of λ is currently achieved by measurements of the β asymmetry A [MMD+13, MPB+13]. These measurements determined λ to a precision of less than $\delta\lambda/\lambda \leq 0.15$ %. For the $\beta - \bar{\nu}_e$ correlation coefficient a on the other hand, only a precision of about $\delta\lambda/\lambda = 15$ % is reached. So there is a lot of room for improvement there, to make the consistency check using a method with totally different systematics for a determination of λ from a. Past measurements of a reached a precision of $\delta a/a \approx 4$ % [SDW78, BDvdG+02, Kom16]. The goal of the aSPECT experiment and this thesis is to improve this 40 year old precision to about $\delta a/a \approx 1$ %, corresponding to $\delta\lambda/\lambda \approx 3$ %.

1. Theoretical Background

In this chapter a short introduction into the theoretical background of the β-decay of the free neutron is given. First, a historical introduction to Fermis and the V-A theory is given, as well as the current description in the Standard Model of particle physics (SM). Also observables in free neutron decay from which the ratio of the weak coupling constants can be derived are explained, with focus on the $\beta - \bar{\nu}_e$ angular correlation. Last an overview of past and competing experiments measuring the $\beta - \bar{\nu}_e$ angular correlation in free neutron decay is given.

1.1. The β-decay of the Free Neutron

Free neutrons, meaning not bound in a nucleus, decay via β-decay into a proton p, an electron e^- and an electron-antineutrino $\bar{\nu}_e$

$$n \xrightarrow{\beta} p + e^- + \bar{\nu}_e + 782.3 \, \text{keV}. \tag{1.1}$$

β-decay is described by the Weak Interaction and is classified within the SM into two decay modes. If angular momentum is transferred to the electron (lepton), the decay mode is called forbidden, if no angular momentum is transferred allowed. This terminology already shows, that forbidden modes are strongly suppressed, but can be realised in nature. The probability of forbidden decays is proportional to the square of $|\vec{p}|R/\hbar$, where $|\vec{p}|$ is the momentum and R the nuclear radius. With momenta in the order of MeV/c and a radius of about 1 fm for the free neutron, the probability for forbidden decays is in the order of 10^{-3} to 10^{-4} [PRSZ06]. Hence, the decay of the free neutron can be considered as a pure allowed decay.

The spin of the electron $\vec{\sigma}_e = 1/2$ and of the antineutrino $\vec{\sigma}_{\bar{\nu}_e} = 1/2$ can couple to a total spin $\vec{S}$ of 0 or 1. Transitions, where the spins couple to a singlet state $\vec{S} = 0$ are called Fermi decay, transitions to the triplet state $\vec{S} = 1$ Gamow-Teller decays. Correspondingly, the spin

$\vec{J}$ of the proton changes as

$$\begin{aligned} \Delta J &= 0 & \text{Fermi decays} && (1.2) \\ \Delta J &= 0,1 & \text{Gamow-Teller decays.} && (1.3) \end{aligned}$$
$$(\text{but not } 0 \rightarrow 0)$$

1.1.1. Fermi's Theory

The first theoretical description of the Weak Interaction was done by Enrico Fermi [Fer]. His phenomenological description of the β-decay was in analogy to the Electro-Magnetic Interaction. In fig. 1.1a a Feynman graph of a X-ray emission from an excited electron in an atom is shown. In fig. 1.1b the analogy of a β-decay in Fermi's theory is given. The coupling of the Electro-Magnetic Interaction of the photon and electron is given by the Hamiltonian

$$\mathcal{H} = e j_\mu^{em} A^\mu, \tag{1.4}$$

with the electron charge e, the 4-vector potential of the electromagnetic field A^μ and the electro-magnetic current density $j_\mu^{em} = \overline{\Psi}_e \gamma_\mu \Psi_e$. Here, $\Psi_e, \overline{\Psi}_e$ is the electron spinor function and the corresponding adjoint function, respectively. $\gamma_\mu = (\gamma^0, \gamma^1, \gamma^2, \gamma^3)$ are the γ-matrices[1]. Assuming a point like interaction, Fermi replaced the 4-vector potential by a leptonic current, the electro-magnetic by a hadronic current and the charge by a coupling constant G_F

$$\begin{aligned} A^\mu &\rightarrow J_\mu^{lep} = \overline{\Psi}_e \gamma_\mu \Psi_{\bar{\nu}_e}, & (1.5) \\ j_\mu^{em} &\rightarrow J_\mu^{had} = \overline{\Psi}_p \gamma_\mu \Psi_n, & (1.6) \\ e &\rightarrow \frac{G_F}{\sqrt{2}}. & (1.7) \end{aligned}$$

This coupling constant G_F is called Fermi coupling constant and can be determined with high accuracy from muon decay $\left(G_F/(\hbar c)^3 = 1.166\,378\,7(6) \times 10^{-5} \,\text{GeV}^{-2} \right)$ [TBC$^+$13]. With these replacements the Hamiltonian eq. (1.4) can be rewritten as

$$\mathcal{H} = \frac{G_F}{\sqrt{2}} J_\mu^\dagger J^\mu + h.c., \tag{1.8}$$

where $h.c.$ is the hermitian conjugate and J_μ the sum of the hadronic and leptonic current

$$J_\mu = J_\mu^{had} + J_\mu^{lep}. \tag{1.9}$$

Originally parity was conserved within Fermi's theory, till in 1956 Lee and Yang [LY56] postulated the possibility of parity violation in β-decay. Parity violation was shortly after confirmed by Wu *et al.* [WAH$^+$57] in the β-decay of ^{60}Co. Wu *et al.* discovered, that polarised ^{60}Co atoms emit the electron in opposite direction to their spin, which has been confirmed by other experiments and elements as well. Hence, Fermi's theory of the nuclear β-decay had to be expanded.

---

[1] $\gamma^0 = \begin{pmatrix} i & 0 \\ 0 & i \end{pmatrix}, \vec{\gamma} = \begin{pmatrix} 0 & \vec{\sigma} \\ -\vec{\sigma} & 0 \end{pmatrix}, \gamma^5 = i\gamma^0\gamma^1\gamma^2\gamma^3$, with the Pauli matrices $\vec{\sigma}$

Table 1.1.: Current-current interactions constructed by Gamow and Teller [GT36].

operator	name	number of matrices
$\overline{\Psi}\Psi$	scalar (S)	1
$\overline{\Psi}\gamma_\mu\Psi$	vector (V)	4
$\overline{\Psi}\gamma_\mu\gamma^\nu\Psi$	tensor (T)	6
$\overline{\Psi}\gamma_5\Psi$	pseudo-scalar (P)	1
$\overline{\Psi}\gamma_5\gamma_\mu\Psi$	axial-vector (A)	4

1.1.2. V-A Theory

Fermi's theory has been expanded by Gamow and Teller 1936 [GT36]. They constructed a more general form of the Hamiltonian including all interaction terms, which are invariant under Lorentz-, parity- and time-reversal transformations. Gamow and Teller constructed 16 linear independent 4×4 matrices from the γ-matrices, see table 1.1. With these operators the Hamiltonian can be written in its most general form [GJL95]

$$\mathcal{H} = \frac{G_W}{\sqrt{2}} \sum_i \left\{ L_i \left(\overline{\Psi}_p \Gamma_i \Psi_n \right) \cdot \left(\overline{\Psi}_e \Gamma_i (1 - \gamma_5) \Psi_{\bar{\nu}_e} \right) + R_i \left(\overline{\Psi}_p \Gamma_i \Psi_n \right) \cdot \left(\overline{\Psi}_e \Gamma_i (1 + \gamma_5) \Psi_{\bar{\nu}_e} \right) \right\} + h.c.. \tag{1.10}$$

G_W is a general weak coupling constant, $i \in [S, V, T, P, A]$ and Γ_i the corresponding operator to the interaction, given in table 1.1

$$\Gamma_S = 1, \quad \Gamma_V = \gamma_\mu, \quad \Gamma_T = -i \frac{[\gamma_\mu, \gamma_\nu]}{2\sqrt{2}}, \quad \Gamma_P = \gamma_5, \quad \Gamma_A = -i\gamma_\mu\gamma_5. \tag{1.11}$$

The Hamiltonian eq. (1.10) is constructed, so that the first part if the sum corresponds to left-handed[2] and the second to right-handed currents. The corresponding coupling constants L_i for left-handed and R_i for right-handed currents have to be determined experimentally. $(1 - \gamma_5)\Psi_{\bar{\nu}_e}/2$ and $(1 + \gamma_5)\Psi_{\bar{\nu}_e}/2$ are the left-handed and right-handed projections of the antineutrino wave functions, respectively. If the coupling constants $L_i \neq R_i$, than the Hamiltonian violates parity, if the coupling constants have a complex phase, time-reversal invariance is violated. Fermi transitions ($\Delta J = 0$) are mediated by scalar and vector couplings, Gamow-Teller transitions on the other hand are mediated by axial-vector and tensor couplings.

Experimentally observed is a maximal parity violation in the Weak Interaction. This means, only left-handed components of vector and axial-vector couplings contribute to β-decay. Hence, eq. (1.10) can be simplified to the Hamiltonian of the V-A theory

$$\mathcal{H} = \frac{G_W}{\sqrt{2}} \sum_{i=V,A} L_i \left(\overline{\Psi}_p \Gamma_i \Psi_n \right) \cdot \left(\overline{\Psi}_e \Gamma_i (1 - \gamma_5) \Psi_{\bar{\nu}_e} \right) + h.c. \tag{1.12}$$

$$= g_V \left(\overline{\Psi}_p \gamma_\mu (1 + \lambda\gamma_5) \Psi_n \right) \cdot \left(\overline{\Psi}_e \gamma_\mu (1 - \gamma_5) \Psi_{\bar{\nu}_e} \right) + h.c.. \tag{1.13}$$

---

[2]Left-handed particles have a helicity of $h = \frac{\vec{s}\vec{p}}{|\vec{s}||\vec{p}|} = 1$, right-handed have $h = -1$.

(a)   (b)   (c)
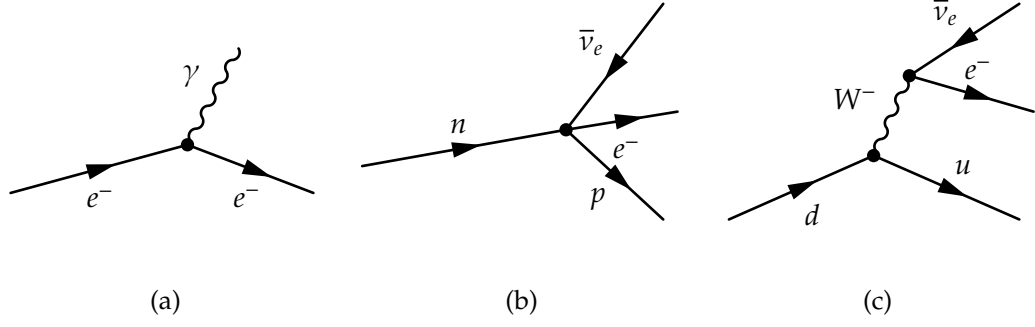
Figure 1.1.: Feynman graphs of the β-decay, the time arrow points from left to right.
(a) Simple picture of an electron emitting a photon in an excited atom.
(b) Point-like interaction as in the V-A or Fermi theory.
(c) Exchange of a W-boson as in the Standard Model of particle physics.

Here, g_V and g_A are the vector and axial-vector coupling constants and λ their ratio

$$g_V = \frac{G_W}{\sqrt{2}} L_V, \quad g_A = \frac{G_W}{\sqrt{2}} L_A, \quad \lambda = \frac{g_A}{g_V}. \tag{1.14}$$

1.1.3. The Standard Model of Particle Physics

The Hamiltonian of the V-A theory eq. (1.13) describes parity violation in β-decay, but it still assumes point-like interaction, see fig. 1.1b. However, neutrons and protons are not elementary particles, they are composed of quarks. This, among other discoveries lead to the fundamentals of the SM by Salam, Glashow and Weinberg in the 1960s [Sal69, Gla61, Wei67]. The SM keeps the idea of leptonic and hadronic currents, as in the V-A theory, but the interaction is not point-like any more. In the SM a $W^\pm$ boson is exchanged between the leptonic and hadronic currents. In general the Weak Interaction is described by the exchange of a $W^\pm$ or Z^0 boson, see fig. 1.1c. These exchange bosons $W^\pm$, Z^0 are very heavy and rest mass $M_{W,Z}$ is far greater than their energy, hence due to the Heisenberg uncertainty relation $\tau \leq \hbar/M_{W,Z}$, they exist only for short times. With a mass of $M_W = 80.385(15)\,\text{GeV}/c^2$ and $M_Z = 91.1876(21)\,\text{GeV}/c^2$ [O$^+$14] and c as speed of light, as maximum speed, the interaction has a range of only $2.5 \times 10^{-18}\,\text{m}$. Hence, in the low energy limit (low momentum transfer $Q \ll M_{W,Z}$) the β-decay in the SM is also a point-like interaction. For free neutron decay, with $Q \approx 780\,\text{keV}$, this is the case. As already mentioned, in the SM neutrons and protons are not elementary particles, they are composed of up (u) and down (d) quarks and β-decay converts a down quark of the neutron (udd) into an up quark (uud), a.k.a. a proton.

The six known quarks of the SM are grouped into three generations, depending on their mass and charge, see table 1.2. In general most transitions occur within a generation, but due to the Weak Interaction transition between generations are possible. Nevertheless, the eigenstates of the Weak Interaction are not the same, as the mass eigenstates of the quarks. The transition between the weak and mass eigenstates can be described by a rotation matrix with sine and cosine of the Cabibbo angle θ_C [Cab63]

$$\begin{pmatrix} |d'\rangle \\ |s'\rangle \end{pmatrix} = \begin{pmatrix} \cos\theta_C & \sin\theta_C \\ -\sin\theta_C & \cos\theta_C \end{pmatrix} \begin{pmatrix} |d\rangle \\ |s\rangle \end{pmatrix}. \tag{1.15}$$

Table 1.2.: The six known quarks in the SM, grouped depending on their mass and charge. The mass increases from upper left to lower right. The top row has a charge of $+2/3$, the lower row of $-1/3$.

quark generations			charge
u	c	t	$+\frac{2}{3}$
d	s	b	$-\frac{1}{3}$

Here, $|d'\rangle$, $|s'\rangle$ are the eigenstates of the Weak Interaction and $|d\rangle$, $|s\rangle$ the ones of the mass, which coincide with the eigenstates of the Strong and Electro-Magnetic interactions. With the discovery of the third generation of quarks, this matrix has been extended to the well known CKM matrix

$$\begin{pmatrix} |d'\rangle \\ |s'\rangle \\ |b'\rangle \end{pmatrix} = \begin{pmatrix} V_{ud} & V_{us} & V_{ub} \\ V_{cd} & V_{cs} & V_{cb} \\ V_{td} & V_{ts} & V_{tb} \end{pmatrix} \begin{pmatrix} |d\rangle \\ |s\rangle \\ |b\rangle \end{pmatrix}. \tag{1.16}$$

In the CKM matrix the square of the single matrix element $\left|V_{qq'}\right|^2$ is the probability of a transition from $|q\rangle$ to $|q'\rangle$. To account for that in β-decay, the coupling constants are multiplied with an additional factor $|V_{ud}|$

$$G_V = g_V \cdot |V_{ud}|, \qquad G_A = g_A \cdot |V_{ud}|. \tag{1.17}$$

The SM has three generations of quarks. Since the CKM matrix has to be unitary, this means, that each row has to be equal to one, e.g.

$$|V_{ud}|^2 + |V_{us}|^2 + |V_{ub}|^2 \overset{!}{=} 1. \tag{1.18}$$

Any deviation from one would hint to another generation of quarks and therefore to physics beyond the SM. The currently known values matrix elements $\left|V_{ij}\right|$ of the CKM matrix are given by [O$^+$14]

$$\left|V_{ij}\right| = \begin{pmatrix} 0.97425(22) & 0.2253(8) & 0.00413(49) \\ 0.225(8) & 0.986(16) & 0.00411(13) \\ 0.0084(6) & 0.00400(27) & 1.021(32) \end{pmatrix}. \tag{1.19}$$

So far, this matrix unitary [HT15]. For more information about the SM the reader is referred to any good particle physics book, e.g. [PRSZ06].

1.2. Observables in Free Neutron Decay

In the previous section, the theoretical description of β-decay itself has been described. In this section the decay probability will be discussed, as well as observables in β-decay. The overall decay probability W can be calculated by Fermi's golden rule [OF50]

$$W = \frac{2\pi}{\hbar} \left|\mathcal{M}_{fi}\right|^2 \rho_e'(E_e). \tag{1.20}$$

Here, ρ_e' is the phase space density of the final states and $\mathcal{M}_{fi}$ the transition matrix element. Using the Hamiltonian eq.(1.13) the decay probability can be expressed as function of
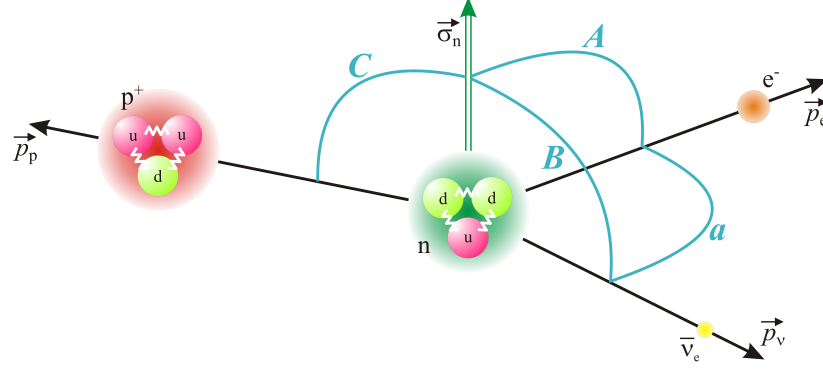
Figure 1.2.: Sketch of some observables in free neutron decay. Shown is a neutron n with its spin $\vec{\sigma}_n$ and its decay products, proton p, electron e^- and electron-antineutrino $\bar{\nu}_e$, as well as some observables between their momenta.

The aSPECT experiment measures the correlation coefficient between the electron momentum $\vec{p}_e$ and the momentum of the electron-antineutrino $\vec{p}_{\bar{\nu}_e}$, also known as a or the $\beta - \bar{\nu}_e$ angular correlations coefficient.

the coupling constants. This calculation has been performed by Jackson *et. al.* [JTW57] for β-decay in 1957. The distribution of electron and electron-antineutrino (E_e and $E_{\bar{\nu}_e}$, respectively) and their momenta ($\vec{p}_e, \vec{p}_{\bar{\nu}_e}$) has been calculated to

$$\frac{dW}{dE_e d\Omega_e d\Omega_{\bar{\nu}_e}} = \frac{G_F^2 |V_{ud}|}{(2\pi)^4 \hbar} \rho_e'(E_e)\, \xi \left\{ 1 + a\frac{\vec{p}_e \vec{p}_{\bar{\nu}_e}}{E_e E_{\bar{\nu}_e}} + b\frac{m_e}{E_e} + \vec{\sigma}_n \left(A\frac{\vec{p}_e}{E_e} + B\frac{\vec{p}_{\bar{\nu}_e}}{E_{\bar{\nu}_e}} + D\frac{\vec{p}_e \times \vec{p}_{\bar{\nu}_e}}{E_e E_{\bar{\nu}_e}} \right) + \ldots \right\}. \tag{1.21}$$

a, A, b, B, D are the correlation coefficients of the different correlations, a graphical representation of these correlations is given in fig. 1.2. Further, in neutron decay ξ is the sum of the squares of the coupling constants [GJL95]

$$\xi = \left(|L_S|^2 + |L_V|^2 + |R_S|^2 + |R_V|^2 \right) + 3 \left(|L_A|^2 + |L_T|^2 + |R_A|^2 + |R_T|^2 \right). \tag{1.22}$$

Here, the factor of 3 for the second half indicates the triplet state of the Gamow-Teller decay by the axial-vector and tensor couplings, whereas the singlet state of a Fermi decay is mediated by the scalar and vector couplings. Within the SM ξ simplifies to

$$\xi = |L_V|^2 + 3|L_A|^2, \tag{1.23}$$

or with the commonly known coupling constants from the Weak Interaction eq. (1.14)

$$\xi = \frac{|g_V|^2 + 3|g_A|^2}{G_F^2 |V_{ud}|}. \tag{1.24}$$

The correlation coefficients a, b, A, B, D can be expressed as a function of the coupling constants L_i, R_i. In the SM a, A, B, D depend only on the ratio of the weak coupling constants λ, whereas $b = 0$. By measuring one of these observables, one can determine $|\lambda|$. Measuring several of these observables allows cross-checks on the result, as the system is redundant

and overdetermined. For an experimentalist this allows to cross-check for the different systematics of the different experimental measurements. An example for determing λ is given by the PDG[O$^+$14] in fig. 2.21. With the currently known value $\lambda = -1.2723(23)$ the sensitivities of the single observables can be derived

$$\frac{\delta a}{\delta \lambda} \approx 0.298, \qquad \frac{\delta A}{\delta \lambda} \approx 0.374, \qquad \frac{\delta B}{\delta \lambda} \approx 0.076. \tag{1.25}$$

The *a*SPECT experiments discussed in this thesis measures the angular correlation coefficient *a*, also known as the $\beta - \bar{\nu}_e$ angular correlation. In general *a* can be expressed as

$$a = \frac{1}{\xi} \left(|L_V|^2 - |L_S|^2 + |L_T|^2 - |L_A|^2 + |R_V|^2 - |R_S|^2 + |R_T|^2 - |R_A|^2 \right), \tag{1.26}$$

which simplifies within the SM to

$$a = \frac{1 - |\lambda|^2}{1 + 3|\lambda|^2}. \tag{1.27}$$

Currently *a* is known to $a = -0.103(4)$ [O$^+$14]. This non-zero value of *a* does not violate parity, as it does not contradict $L_i = R_i$, nor does it violate time-reversal invariance, cf. eq. (1.26).

As can be seen from eq. (1.26) a measurement of *a* can be used to search for scalar and tensor type interactions, not only for vector and axial-vector types. Nevertheless, within this work the analysis will be constraint to the SM only, i.e. eq. (1.27). This limits *a* to values between $a = -1/3$ (pure Gamow-Teller decay, $g_V = 0$) and $a = +1$ (pure Fermi decay, $g_A = 0$).

For more information of the β-decay of the neutron, the observables of it and its interactions, as well as limits from the neutron decay on the SM the reader is referred to [Abe08, Dub91, DS11, SBNC06]

1.2.1. Deriving *a* from the Proton Recoil Spectrum

Measuring *a* experimentally is not an easy task. As the electron-antineutrino $\bar{\nu}_e$ can not be detected with reasonable experimental efforts for this kind of experiment, one has to measure *a* indirectly. This can be achieved by measuring precisely the shape of the recoil spectrum of the decay proton. The link between the proton recoil energy and the angle between the electron *e* and electron-antineutrino $\bar{\nu}_e$ can be seen by looking at the two extreme cases, see fig. 1.3. If the electron *e* and the electron-antineutrino $\bar{\nu}_e$ are emitted in the same direction (small angle $\theta_{e\bar{\nu}_e}$ between electron and electron-antineutrino), the proton *p* gains more kinetic energy E_p, which corresponds to more positive values of *a*. In case the electron and the electron-antineutrino are emitted in opposite direction (large $\theta_{e\bar{\nu}_e}$), the proton gains less kinetic energy, hence more negative *a*.

$$\theta_{e\bar{\nu}_e} \downarrow \quad \Rightarrow \quad E_p \uparrow \quad \Rightarrow \quad a \uparrow$$
$$\theta_{e\bar{\nu}_e} \uparrow \quad \Rightarrow \quad E_p \downarrow \quad \Rightarrow \quad a \downarrow$$

Therefore, different emission angles $\theta_{e\bar{\nu}_e}$, or in other words different values of *a*, change the shape of the proton recoil spectrum. This change on the spectral shape is illustrated in
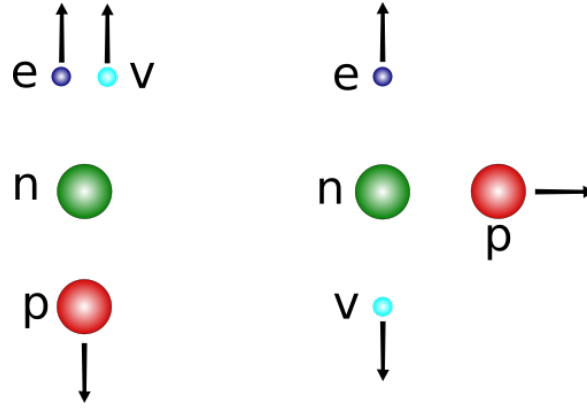
Figure 1.3.: Illustration of the impact of the angle $\theta_{e\bar{\nu}_e}$ between electron e and electron-antineutrino $\bar{\nu}_e$ on the recoil of the proton p. Shown are the two extreme cases for the emission of the electron e and the $\bar{\nu}_e$. If the two particles are emitted in the same direction, small $\theta_{e\bar{\nu}_e}$ (left) the proton gains more kinetic energy E_p. If the electron and the electron-antineutrino are emitted in opposite direction, large $\theta_{e\bar{\nu}_e}$ (right), the proton gains less kinetic energy, due to the large differences in masses and classical energy and momentum conservation.

fig. 1.4. Shown are two simulated differential and the integral spectrum for two different values of a. In blue (solid line) is drawn the spectrum for the currently known value of $a = -0.103$ from the PDG, [O$^+$14], and for a hypothetical on of $a = +0.3$ in red (dashed line). Clearly the shift to higher energies in the spectral shape for the hypothetical value of a can be seen.

In *a*SPECT a is determined by a fit of the theoretical proton recoil spectrum to the measured data. So not only a precise measurement of the spectrum is needed, but also an even more precise theoretical description has to be known, to derive a from the measured data. In the following paragraph a description of the precise proton recoil spectrum is given, as well as a short introduction how it is calculated. For the complete calculation, including the tabulated values of the various corrections, see [Glü93].

Calculation of the Proton Recoil Spectrum

For most purposes the spectrum calculated by Nachtmann in 1968 [Nac68] is sufficient, as it already includes relative corrections

$$\omega_{Nachtmann}(T_0) \propto g_1(T_0) + a \cdot g_2(T_0). \tag{1.28}$$

The functions g_1 and g_2 have been calculated by [DBvdG$^+$00]. This formula shows nicely the linear dependence of the spectrum on a. Unfortunately, eq. (1.28) does not include any radiative or Coulomb corrections, which are needed to determine a on the 1 % level. Therefore, Glück included higher order Coulomb corrections and radiative corrections in 1993 [Glü93], allowing to determine λ with a precision of about 0.1 % or a with about 0.03 %. This precision is sufficient, to determine a and especially the systematics of the experiment on a sub-percent level. For the explanation of the calculation the original notation of [Glü93] is kept for easier comparison. Here, $1, 2, i, f$ refer to the electron-anineutrino, the electron, the neutron, the proton and the speed of light is set to one, $c = 1$.
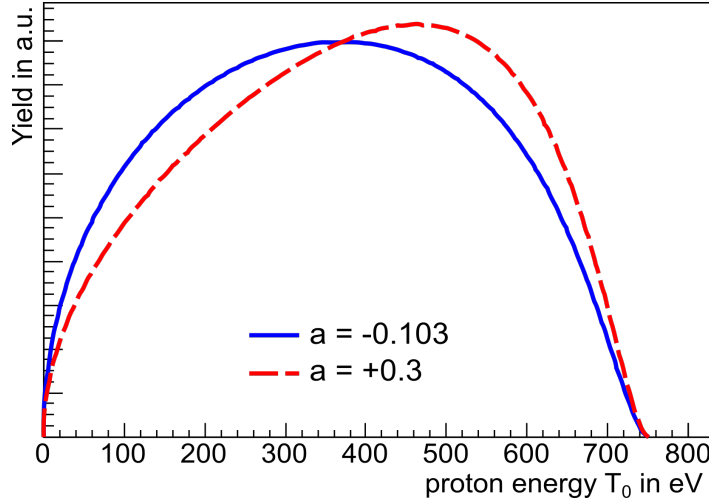
Figure 1.4.: Calculated proton recoil spectra for different values of a. To calculate these spectra eq. (1.29) has been used. In blue (solid line) is drawn the spectrum for the currently known value of $a = -0.103$ from [O$^+$14]. In red (dashed line) is a spectrum drawn for a hypothetical value of $a = +0.3$.

Glück calculated the differential proton recoil spectrum to

$$\omega_{0C\alpha}(E_f) = \tilde{\omega}_{0C}(E_f)[1 + 0.01 r_C(y)][1 + 0.01 r_\rho + 0.01 r_p(y)]. \tag{1.29}$$

This proton recoil spectrum includes:

- the differential proton spectrum $\tilde{\omega}_{0C}(E_f)$, including relativistic corrections and a first approximation of Coulomb corrections,

- higher order Coulomb corrections $r_C(y)$,

- radiative, model-independent order-α corrections

  - energy independent $r_\rho = 1.505$,

  - energy dependent $r_p(y)$.

The exact calculation of $\tilde{\omega}_{0C}(E_f)$ is integrating over a Dalitz distribution $W_0(E_2, E_f)$ from the minimal electron energy $E_{2min}(E_f)$ to the maximal $E_{2max}(E_f)$ for a given proton energy E_f, eq. (3.11) in [Glü93]. For *a*SPECT $\omega_{0C\alpha}$ is fitted to measured data. For each fit iteration $\omega_{0C\alpha}$ has to be recalculated with a new set of parameters, hence a fast calculation of $\omega_{0C\alpha}$ is needed, otherwise the fit gets far to time consuming. Therefore, an approximation of the exact integral is used, which is given also by Glück. This approximation can be calculated orders of magnitude faster, than the exact solution. Hence, it allows to fit a dataset within about 30 min, instead of several hours. On the other side it is still more than sufficient for a 1 % measurement of a, with a deviation of only 10^{-4} from the exact calculation [Sch17]. This approximation is given by

$$\tilde{\omega}_{0C}(E_f) \approx m_i \frac{G_V^2}{4\pi^3} \left[\Omega(E_{2max}(E_f)) - \Omega(E_{2min}(E_f)) \right], \tag{1.30}$$

with

$$
\begin{aligned}
\Omega(E_2) \;=\; & (1 + \lambda^2)\left[E_{2m}E_2^2(1 + \pi\alpha\beta) - \frac{2}{3}E_2^3 + \frac{1}{2}\pi\alpha E_{2m}m_2^2 \ln\frac{1+\beta}{1-\beta} - 2\pi\alpha\beta E_2\left(m_2^2 + \frac{1}{3}\beta^3 E_2^2\right)\right] \\
& -(1 - \lambda^2)m_f(E_{fm} - E_f)E_2(1 + \pi\alpha\beta). \qquad\qquad (1.31)
\end{aligned}
$$

Here, α is the fine-structure constant, E_f, E_2 are the proton, electron energy, respectively and m_f, m_2 their rest masses. Further is

$$
\beta = \frac{\sqrt{E_2^2 - m_2^2}}{E_2}, \qquad E_{2m} = \Delta - \frac{\Delta^2 - m_2^2}{2m_i}, \qquad E_{fm} = m_f + \frac{\Delta^2 - m_2^2}{2m_i}, \qquad (1.32)
$$

with $\Delta = m_i - m_f$, the total energy of the decay, E_{2m}, E_{2f} the endpoint energy of the electron, proton, respectively.

The Coulomb corrections take the dependence of the proton recoil on the proton energy into account and are calculated by a Fermi function $F_C(E_2, E_f) = F((Z = 1), E_2)Q(Z = 1, E_2)$, with F the normal Fermi function and Q the Fermi function including relativistic recoil corrections. F_C can be approximated for electron energies $E_2 - m_2 > 5\,\text{keV}$ to

$$
\hat{F}_C(E_2, E_f) \approx 1 + \underbrace{\frac{\alpha\pi}{\beta_r}}_{\text{1st order}} + \underbrace{\alpha^2\left[\frac{11}{4} - \gamma_E - \ln(2\beta_r E_2 R) + \frac{\pi^2}{3\beta_r^2}\right]}_{r_C(y)}, \qquad (1.33)
$$

with

$$
\beta_r = \left|\beta - (1 - \beta^2)v_f c_f\right|, \quad v_f = \frac{|\vec{p}_f|}{E_f}, \quad c_f = \frac{\vec{p}_2\vec{p}_f}{|\vec{p}_2||\vec{p}_f|}, \quad R \approx 1\,\text{fm}, \quad \gamma_E \approx 0.5772. \qquad (1.34)
$$

The first order of Coulomb corrections is already included in eq. (1.30), the higher orders $r_C(y)$ are given in table III of [Glü93]. y is here the relative proton energy $y \equiv (E_f - m_f)/(E_{fm} - m_f)$. The radiative corrections $r_p(y)$ are given in table IV of [Glü93]. To calculate a continuous proton spectrum, the tabulated values of the higher-order Coulomb corrections $r_C(y)$ and the radiative corrections $r_p(y)$ have been interpolated with a spline function.

Having now a continuous and precise description of the proton recoil spectrum, one can replace the parameter λ in eq. (1.31) by $\lambda = \sqrt{(1 - a)/(3a + 1)}$ from eq. (1.27). Substituting this relation into eq.(1.31) leads to a new $\tilde{\Omega}(E_2, a)$ with a as an additional parameter. $\tilde{\Omega}(E_2, a)$ can then be used to calculate an a-dependent proton recoil spectrum $\tilde{\omega}_{0C\alpha}(E_f, a)$, cf. eq. (1.30). An example of the proton spectrum for two different values of a is shown in fig. 1.4. With the a-dependent proton recoil spectrum $\tilde{\omega}_{0C\alpha}(E_f, a)$ one can fit experimentally measured spectra with a as a free fit parameter. In this way a can be determined from the shape of experimental spectra by a fit. For more details on the fit procedure of aSPECT, see section 2.3.

1.3. Previous and Competing Measurements of a

In this section, a short overview of past and current measurements of a from free neutron decay is given. As shown previously, λ can be determined from several observables in

(a)

(b)
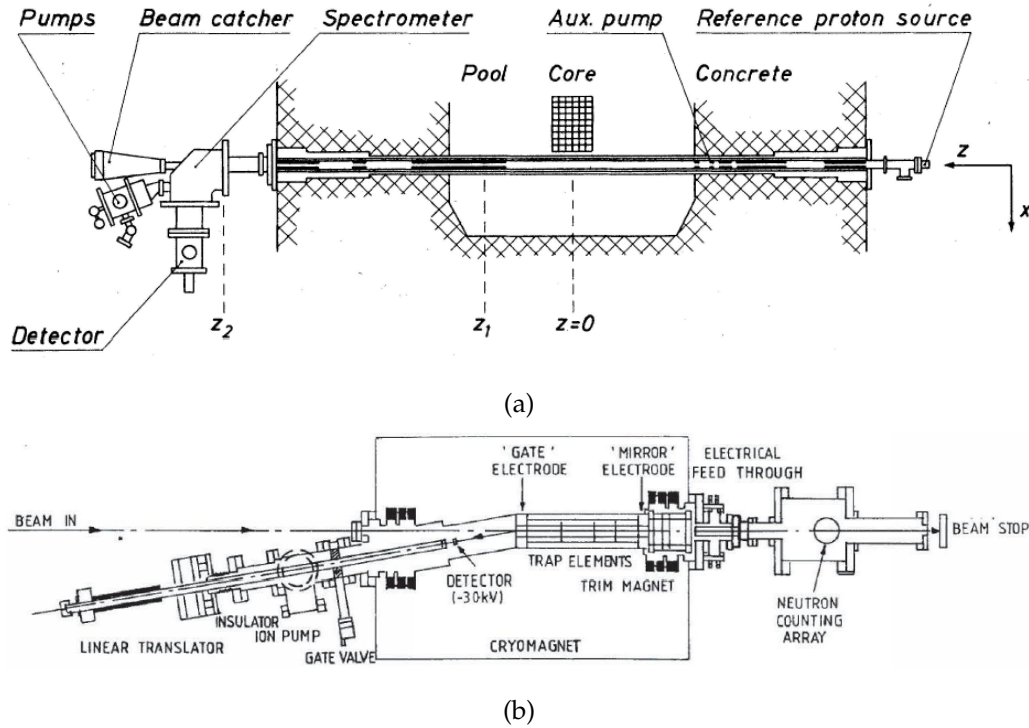
Figure 1.5.: Schematic set-up of previous *a* measurements.
(a) Stratowa *et.al.* [SDW78]
(b) Bryne *et.al.* [BDvdG$^+$02]

free neutron decay. Currently, λ is known to $-1.2723(23)$. The PDG calculates this value from several measurements, most of them measured the β-asymmetry A, one the proton asymmetry C and one the neutrino asymmetry B. Reason for this is, asymmetry measurements can be performed with few systematics and therefore high precision. For example, the latest measurement of PERKEO [MMD$^+$13], which measures A, has an uncertainty of less than 0.15 % in λ, whereas the latest measurement of *a* by Bryne [BDvdG$^+$02] results in an uncertainty of about $\delta\lambda/\lambda \approx 15\,\%$. So there is a lot of room for improvement for an *a* measurement.

Previous Experiments

There are several past experiments, which measured *a* in free neutron decay. Here, only the latest two by Stratowa *et.al.* [SDW78] and Bryne *et.al.* [BDvdG$^+$02] will be presented.

Stratowa *et.al.* performed the first precision measurement of *a* in free neutron decay. They measured the shape of the proton recoil spectrum and determined from that *a*. A schematic of their experimental set-up is given in fig. 1.5a. The decay volume was in-pile near the core of the reactor. A through going tube was used, with no direct view to the reactor or moderator to reduce the background level. The protons from the decay were analysed in a spherical electrostatic spectrometer, which accepted only protons with a momentum parallel to the tube. Stratowa *et.al.* achieved a result of $a = -0.1017(51)$, which corresponds to an uncertainty of $\delta a/a \approx 5\,\%$. This uncertainty was dominated by systematics, like calibration of the proton detector. Nevertheless, their result hasn't been surpassed for three decades.

$p_e \uparrow\uparrow p_\nu \quad p_e \uparrow\downarrow p_\nu$

(a)

(b)
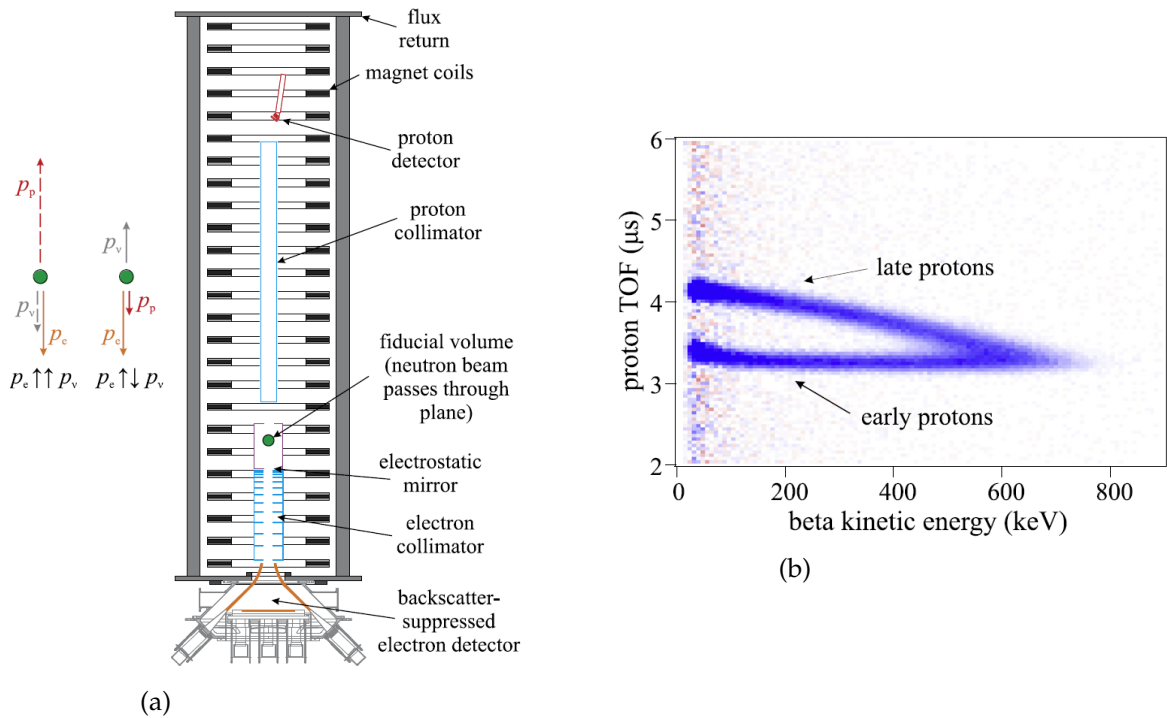
Figure 1.6.: The aCORN experiment
(a) schematic of the experimental set-up
(b) simulated data, TOF versus electron energy
Details, see text. Pictures taken from [BBPP14].

In 2002 Bryne *et.al.* were able to improve slightly the result of Stratowa. Bryne *et.al.* also determined *a* from the shape of the proton recoil spectrum. Here, a cold neutron beam passed through a Penning-like trap. The decay protons then were guided from a high magnetic field region to a low one. This caused a momentum transfer from transversal to longitudinal one, similar to *a*SPECT, see section 2.1.2. The energy of the protons has then been measured by a superimposed electric field, resulting in $a = -0.1054(55)$. This is a similar precision (5 %) as Stratowa. The uncertainty of Bryne is mainly dominated by incomplete energy transfer from transverse to longitudinal motion and violation of the adiabatic conditions.

Competing Experiments

Currently, there are two experiments competing with *a*SPECT to improve the results of Stratowa and Bryne. One is the aCORN experiment, the other one the Nab experiment.

The aCORN experiment [WFT+05, WBC+09] uses a different approach to determine *a*. Protons and electrons from the decay are measured in coincidence. The experimental set-up is shown in fig. 1.6a. aCORN measures the electron energy, as well as the Time Of Flight (TOF) between electron and proton. In this way, the events will be sorted into to groups. In the first group N_I are protons emitted towards the proton detector, in the second group N_{II} are protons emitted in the opposite direction. Therefore, protons in the second group will have a longer flight path, due to the necessary reflection. Hence, they

are detected later at the proton detector, see fig. 1.6b. This method relies on the constructed asymmetry of the experiment, leading directly to *a* by

$$a(E_e) = \frac{1}{v_e} K(E_e) \frac{N_I - N_{II}}{N_I + N_{II}}, \tag{1.35}$$

with $K(E_e)$ as instrumental constant, which has to be calculated. In general, the method of aCORN is more sensitive to *a*, than measuring the shape of the proton recoil spectrum, but it lacks of statistics, as only a fraction of the neutron decays in the decay volume of aCORN contributes to the signal. The aCORN collaboration took data in 2013 at NG6 beamline in the NCNR (NIST Center for Neutron Research). The analysis is almost finished with a preliminary result of $a = -0.1079(40)$. This includes a statistical uncertainty of $\delta a_{stat}/a = 2.80\%$ and a systematic uncertainty of $\delta a_{sys}/a = 2.41\%$ [BBPP14, Kom16]. The collaboration claims their statistical and systematic uncertainty to be independent, therefore they add up the two uncertainties quadratically resulting in an total uncertainty of $\delta a/a = 3.67\%$. From 2015 to 2016 aCORN has taken data at a more intense beamline at the NCNR collection ten times more data than in the previous run. Together with improved systematics aCORN hopes to achieve a precision of $\delta a/a < 2\%$ with this data.

The Nab experiment [PAA+09, AAl+] uses a similar detection principle as aCORN. Electrons and protons from the decay are detected in coincidence, a schematic of Nab is shown in fig. 1.7a. Nab measures the electron energy and the time t_p between electron and proton. Further, Nab uses the linear dependence between the proton momentum p_p^2 and the cosine of the angle between electron and electron-antineutrino $\cos \theta_{e\bar{v}_e}$

$$p_p^2 = p_e^2 + 2p_e p_{\bar{v}_e} \cos \theta_{e\bar{v}_e} + p_{\bar{v}_e}^2. \tag{1.36}$$

As the momentum of the electron-antineutrino $p_{\bar{v}_e}$ depends almost only on the kinetic energy of the electron E_e or (p_e), this relation reduces to a linear one between p_p^2 and $\cos \theta_{e\bar{v}_e}$ for a given p_e. p_p^2 and $\cos \theta_{e\bar{v}_e}$ are then mapped for all given p_e^2, see fig. 1.7b. *a* is determined from the slopes of the $1/t_p^2$ distributions for different E_e. The Nab experiment is currently under construction. The magnet system is supposed to be delivered in summer 2016. After the setting up and testing the system, the Nab collaboration hopes to achieve a final systematic uncertainty of $\delta a_{sys}/a = 0.1\%$ [BBPP14].
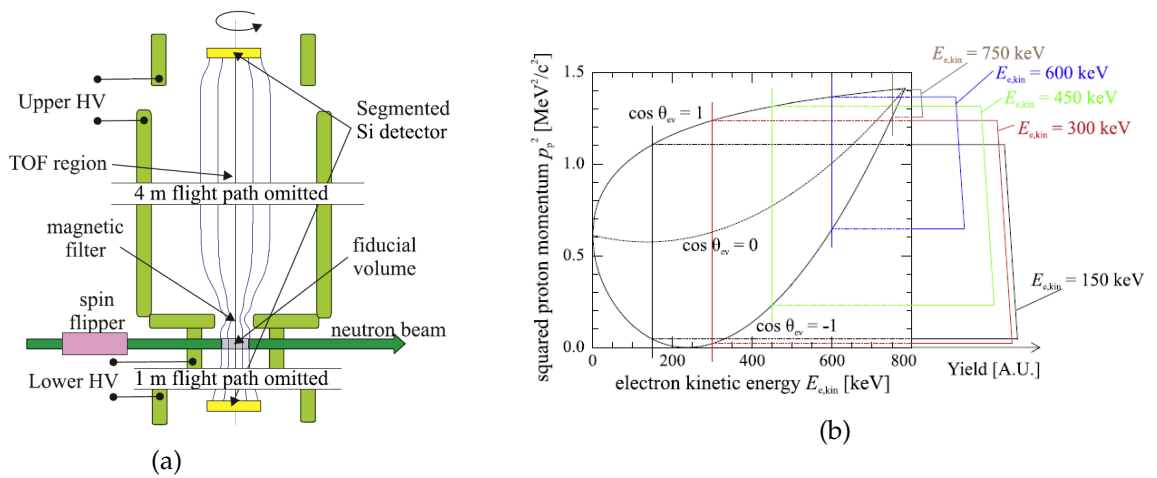
Figure 1.7.: The Nab experiment
        (a) schematic of the experimental set-up
        (b) measurement principle
        For details, see text. Pictures taken from [BBPP14].

2. The *a*SPECT Experiment

In this chapter an overview of the experimental set-up of *a*SPECT is given. In section 1.2.1 has been explained, how *a* can be determined from the spectral shape of the proton recoil spectrum. The aim of *a*SPECT is to measure the spectral shape of the proton recoil spectrum with high precision to improve the uncertainty of *a* from currently $\delta a/a \approx 4\,\%$ [O$^+$14] to about $\delta a/a \approx 1\,\%$. To do so, the proton recoil spectrum is measured with a spectrometer of Magnetic Adiabatic Collimation with Electrostatic filter (MAC-E filter) type, see section 2.1.2. Further, the systematics and experimental effects of the experiment and their influence on the shape of the proton recoil spectrum and therefore *a* are explained in section 2.2. Solutions to minimize these effects are explained in this section as well. Furthermore, in section 2.3 a description is given how the systematic effects are included in the fit function, as well as how the uncertainty of the fit is determined. Finally, in section 2.3.2 the concept of an ideogram is explained.

2.1. Principle of Measurement

2.1.1. The Institute Laue-Lagevin

The Institut Laue-Langevin (ILL) is an international research facility situated in Grenoble (France). It hosts a nuclear research reactor producing neutrons for several kinds of experiments, mostly material sciences, but also for fundamental research. The *a*SPECT experiment was hosted in 2013 at the PF1b experimental zone, which provides a cold neutron flux with a mean wave length of 4.0 Å to 4.5 Å. With 1.8×10^{10} neutrons/cm^2/ sec [ILL], PF1b currently is the strongest neutron source for unpolarized neutrons in the world and therefore ideally suited to host the *a*SPECT experiment. In this thesis the focus will be on the 2013 beam-time and the improvements leading to it.

2.1.2. Experimental Set-Up

*a*SPECT uses the measurement principle of a MAC-E filter. The technique of a MAC-E filter was first proposed by [KR83, PBB$^+$92] and is used widely in electron spectroscopy [HH76, BPT80] and to determine the neutrino mass [WDB$^+$99]. Here will be only explained the
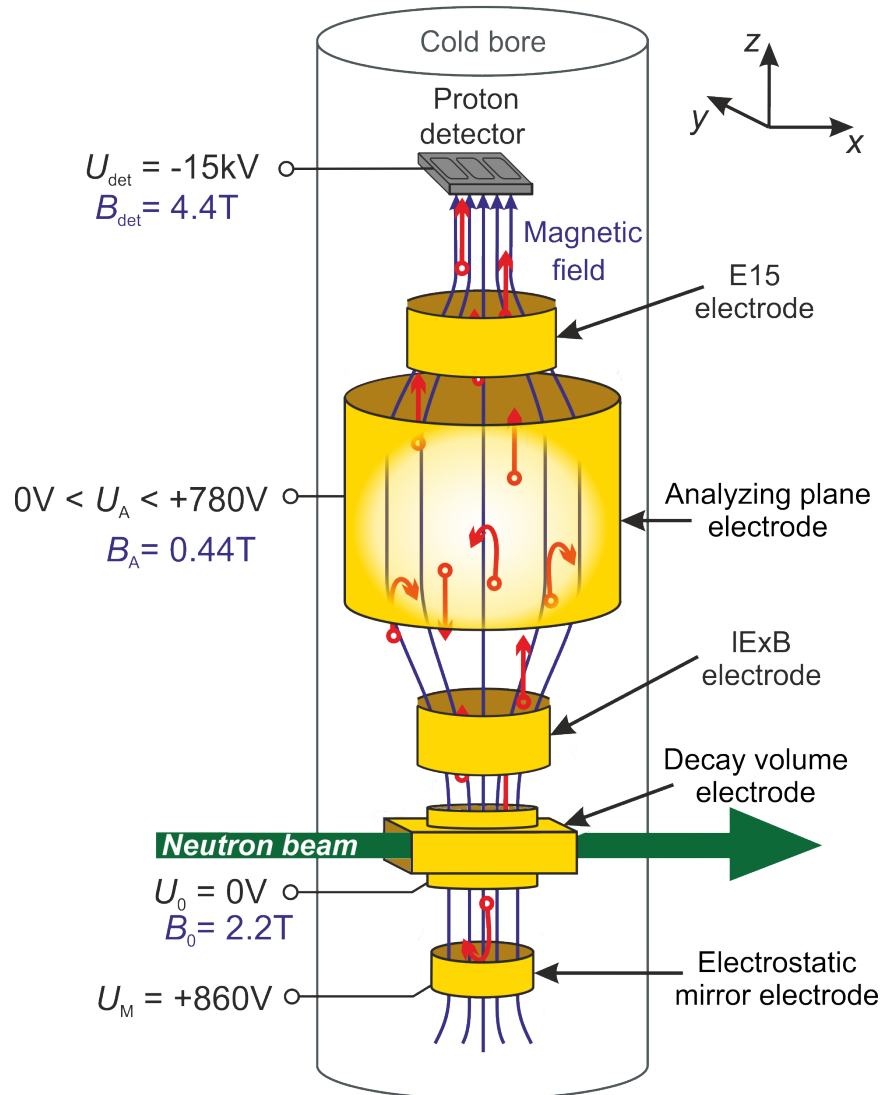
Figure 2.1.: Schematic of the aSPECT-experiment. Neutrons are guided through the spectrometer, protons from neutron decays in the Decay Volume (DV) are guided adiabatically by the magnetic field towards the detector. Protons with momentum in negative z-direction are reflected by an electrostatic mirror, providing a 4π acceptance. By adiabatically decreasing the magnetic field towards the Analysing Plane (AP) region the protons can be energy-selected with an electrostatic retardation potential. After the AP the protons are accelerated by a high electric field of $-15\,\text{kV}$ and focused by a high magnetic field onto the detector.

general principle of MAC-E filters, for details the reader is referred to [PBB+92]. In fig. 2.1 a schematic of *a*SPECT is drawn. The whole system is operated under Ultra-High Vacuum (UHV) conditions, meaning pressures in the order of $O(10^{-10}\,\text{mbar})$. An unpolarized cold neutron beam is guided through the spectrometer. For details of the guiding and collimation in *a*SPECT, see [Bor10]. These neutrons decay along the whole guide. If a neutron decays inside the so-called Decay Volume (DV), the protons (and electrons) are confined radially by the Lorentz force

$$\vec{F} = q\left(\vec{v} \times \vec{B}\right) + q\vec{E}, \tag{2.1}$$

due to the B-field of *a*SPECT. Here, q and $\vec{v}$ are the charge and the velocity of the particle and $\vec{B}$, $\vec{E}$ the magnetic, electric field, respectively. In case of *a*SPECT the electric potential and field in the DV are $\Phi_0 \equiv 0$, $E_0 \equiv 0$ by definition and the magnetic one $B_0 \approx 2.2\,\text{T}$. The motion of the proton motion has to fulfil the adiabatic approximation [Jac75, GBB+05]

$$\frac{\partial E}{E} \ll 1 \qquad \text{and} \qquad \frac{\partial B}{B} \ll 1. \tag{2.2}$$

For adiabatic motion the flux $\Phi_{mag} = B\pi r^2$ enclosed by the cyclotron motion of proton is a constant of motion. The magnetic moment μ of the current loop of the proton is then

$$\mu = I \cdot A = (q \cdot v_\perp)\left(\pi r^2\right) = \frac{q\omega r^2}{2}, \tag{2.3}$$

whereas $\omega = \frac{qB}{\gamma m}$ is the gyration frequency of the proton, q the charge of the proton, r the cyclotron radius of it and $v_\perp$ its velocity perpendicular to the magnetic field. In neutron decay, the energy transfer to the proton is low, so the proton has only low kinetic energies and can be treated non-relativistic. With the definition of ω one can rewrite eq. (2.3) to

$$\mu = \frac{p_\perp^2}{2mB} = const. \tag{2.4}$$

If the magnetic field B is adiabatically reduced, the perpendicular momentum $\vec{p}_\perp$ will reduce according to eq. (2.4), as the mass of the proton m and the magnetic moment are both constant. Further, the overall momentum $\vec{p}$ of the proton is a constant, hence by adiabatically reducing the strength of the magnetic field, perpendicular momentum $\vec{p}_\perp$ is converted to parallel momentum $\vec{p}_\parallel$. This effect is called inverse magnetic mirror effect and illustrated in fig. 2.2. Using the inverse magnetic mirror effect a MAC-E filter converts transversal momentum $p_\perp$ or kinetic energy $T_\perp$ of a particle to longitudinal one $p_\parallel, T_\parallel$. The region with the lowest magnetic field is called Analysing Plane (AP). In this region the momentum transfer is maximal and in the ideal case 100 %, so all momenta are aligned parallel to the magnetic field. By applying a electrostatic potential in this AP, particles can be energy selected, as this potential acts as a barrier or retardation for the particles. Any particle with charge q and a kinetic energy $T_0 > qU_{ret}$ will pass the retardation potential U_{ret}. Any particle with a lower energy $T_0 \le qU_{ret}$ will be reflected by the retardation potential. This is how a MAC-E filter in principle works. First, the momentum of the particles is converted to longitudinal one, second by applying a retardation potential an energy selection can be achieved. A variation of U_{ret} results in an integral spectrum.

In case of *a*SPECT the protons are focused onto a detector after passing the AP by a high magnetic field of $B_{det} = 4.4\,\text{T}$. This strong magnetic field causes a back conversion
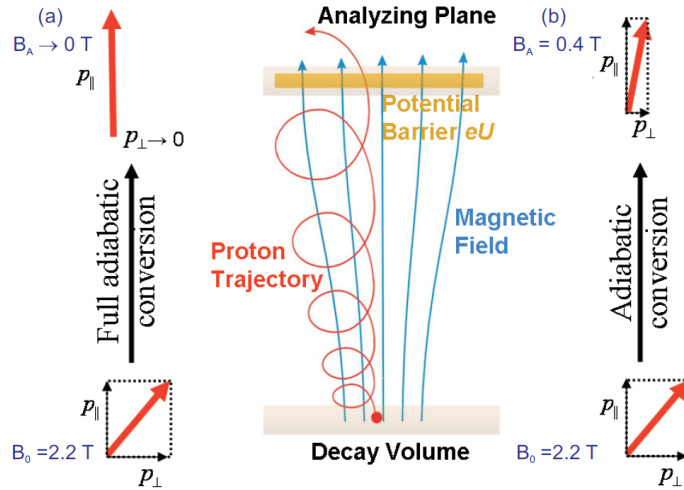
Figure 2.2.: Principle of a MAC-E filter. Shown is the conversion of perpendicular momentum (relative to the magnetic field lines) to longitudinal one for (a) an ideal and (b) for the real aSPECTexperiment. In case of aSPECT the conversion is only about 80 % of the momentum corresponding to an energy resolution of 20 %. The final energy selection is done by an electrostatic potential barrier qU applied in, the Analysing Plane (AP) region. Graph taken from [Bor10]

of momentum (eq. (2.4)) and would cause a reflection of protons with a low initial parallel momentum $\vec{p}_\parallel$. To overcome this magnetic mirror effect and to be able to detect the protons with a semiconductor detector, the protons are accelerated by $-15\,\mathrm{kV}$. For details of the proton detection see section 2.2.4 and [Sim10]. To achieve a 4π acceptance an electrostatic mirror below the DV is installed, reflecting protons adiabatically towards the AP.

2.2. Systematic and Experimental Effects

In the previous section the principle of an ideal MAC-E filter has been explained. Unfortunately, the world is not ideal and experiments are disturbed by systematic effects. In this section an overview of the main known systematic effects of aSPECT is given, as well as their influence on a. Further, experimental improvements since 2008 to reduce these effects and the possibilities to determine their influence on the proton recoil spectrum are explained. For more details of aSPECT the reader is referred to [ZBvdG+00] and [GBB+05] with a first description of the mayor systematic effects. Information about the beam-time 2006 and the experimental set-up of it, can be found in [Hor11]. For details of the beam-time 2008 the reader is referred to [KGB+09] and [SGB+09], as well as to [Sim10, Bor10, Gua11, Kon11]. Information about the beam-time 2011 can be found in [Mai14]. In these Ph.D. theses information of the experimental set-up can be found, which has not been changed for 2013, like details on the superconducting magnet system and the electrode system generating the magnetic field and electric potentials for aSPECT, respectively.

2.2.1. Transmission Function

In section 2.1.2 an ideal MAC-E filter has been explained. Ideal in this case means a 100 % conversion of momenta, so no remaining perpendicular momentum $\vec{p}_\perp$. Equation (2.4)

shows, that a complete conversation could only be achieved by reducing the magnetic field at the place of the retardation to zero or increase the field at the place of the decay to infinity. Experimentally both is obviously not possible. Reducing the magnetic field at the place of retardation to very low values increases the experimental efforts to achieve a homogeneous field, e.g. the KATRIN experiment with a low magnetic field of about 3 G has to compensate already the earth magnetic field. Additionally, decreasing the B field increases the gyration radii of the particles, hence to detected the complete flux tube from the DV the diameter of the experiment has to increase, e.g. the main spectrometer of KATRIN has an diameter of about 10 m [AAB+04]. Increasing the field in the DV on the other hand is technically limited, fields in the order of 20 T with a bore tube diameter of $O(10\,\mathrm{cm})$ are hard to achieve [KIT, Mag]. Hence, a compromise between desired momentum conversion and experimental effort has to be found. For *a*SPECT the low magnetic field in the AP is $B_{ret} \approx 0.44\,\mathrm{T}$. With the magnetic field $B_0 \approx 2.2\,\mathrm{T}$ in the DV, this gives a magnetic field ratio r_B of

$$r_B = \frac{B_{ret}}{B_0} = 0.202\,887(5). \tag{2.5}$$

A magnetic field ratio of about 0.2 means the initial perpendicular energy $T_{0\perp}$ is converted to 80 % into parallel energy $T_{\parallel}^{AP}$ in the AP. Hence, the transmission of the particle depends now on its initial energy T_0 and the fraction of transversal energy $T_{0\perp}$. Or in other words, the initial energy and the emission angle θ_0. To determine, if a particle can overcome the retardation voltage U_{ret} one can consider three different cases: If the initial energy is $T_0 \leq T_{tr}^{min} = qU_{ret}$ the particle can not overcome the retardation voltage. If the initial energy is $T_0 \geq T_{tr}^{max}$ the particle will overcome the retardation voltage. T_{tr}^{max} is the maximal transmission energy, so the energy a particle emitted with $\theta_0 = 90\,°$ must have, to overcome the retardation voltage. For a $r_B \approx 0.2$ this is 20 % more than T_{tr}^{min}. For all energies between $T_{tr}^{min} < T_0 < T_{tr}^{max}$ the transmission depends on the initial energy and angle. For *a*SPECT this Transmission Function F_{tr} has been calculated by [GBB+05] to

$$F_{tr} = \begin{cases} 0 & \text{if } T_0 \leq T_{tr}^{min} \\ 1 - \sqrt{1 - \frac{B_0}{B_{ret}}\left(1 - \frac{qU_{ret}}{T_0}\right)} & \text{if } T_{tr}^{min} < T_0 < T_{tr}^{max} \\ 1 & \text{if } T_0 \geq T_{tr}^{max} \end{cases} . \tag{2.6}$$

As can be seen the Transmission Function of *a*SPECT is a function of the magnetic field ratio r_B and the retardation voltage U_{ret}. In the limit of $r_B \to 0$ eq. (2.6) becomes a step function, as expected for an ideal MAC-E filter. In fig. 2.3a the Transmission Function of *a*SPECT is drawn for $r_B = 0.203$, $U_{ret} = 400\,\mathrm{V}$ and $U_{ret} = 50\,\mathrm{V}$. Further, the differential spectrum for $a = -0.103$ and a hypothetical value of $a = +0.3$ is drawn. Convoluting the differential spectrum with the Transmission Function results in the integral spectrum *a*SPECT measures, see fig. 2.3b. From this graph can already be seen, due to the convolution of the Transmission Function F_{tr} with the differential spectrum, any uncertainty in F_{tr} corresponds directly to an uncertainty in a. Slight deviations in r_B and/or U_{ret} would cause a difference in the slope of F_{tr}. These differences in the slope would cause a difference in the shape of the integral proton spectrum and lead to a wrong value of a. In case of *a*SPECT an uncertainty of the magnetic field ratio of $\delta r_B/r_B = 10^{-4}$ corresponds to an uncertainty in a of $\delta a/a = 0.1\,\%$ [GBB+05]. An uncertainty of the retardation voltage of $\delta U_{ret} = 10\,\mathrm{mV}$ corresponds also to an uncertainty of $\delta a/a = 0.1\,\%$ [GBB+05]. In the next two paragraphs an overview of the current knowledge of these two uncertainties and the way to determine them is given.
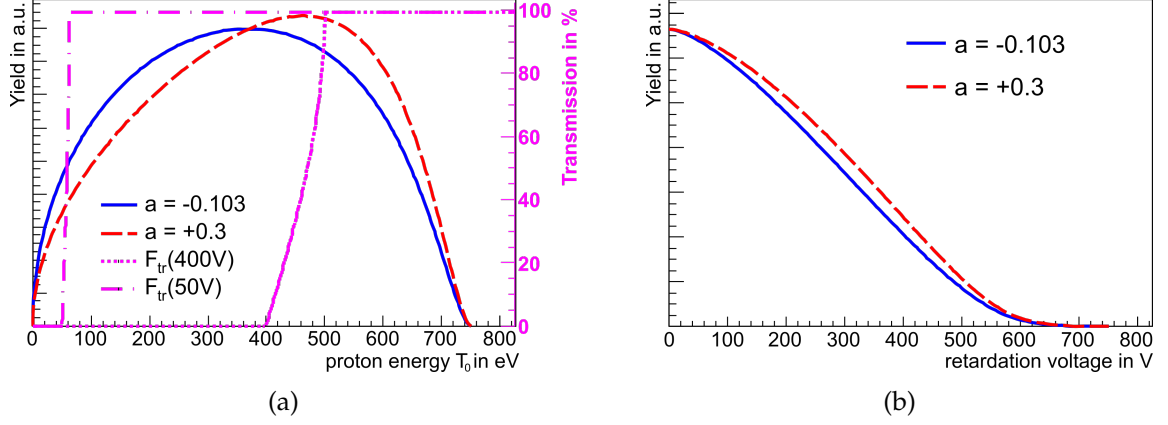
Figure 2.3.: Simulated proton recoil spectra for different values of a. Shown is a differential spectrum (a) and an integral one (b) for two different values of a. In blue (solid line) is drawn the spectrum for the currently known value of $a = -0.103$ from [O$^+$14]. In red (dashed line) is a spectrum drawn for a hypothetical value of $a = +0.3$. In pink (dotted line) the Transmission-Function F_{tr} of aSPECT for $U_{ret} = 400\,\text{V}$ and $U_{ret} = 50\,\text{V}$ is drawn.

Magnetic Field Ratio r_B

The magnetic field ratio r_B has to be know with a precision of $\delta r_B / r_B = 10^{-4}$ [GBB$^+$05]. This includes the spatial homogeneity of the B field in the DV and AP, as well as the temporal stability. Further, the ratio has to be stable on the same level by changing the experimental conditions, e.g. ramping the magnet, open/closing vacuum shutters, inserting the detector electrode.

The B-field profile (fig. 2.4a) and the homogeneity of the B field in DV and AP has been measured using a hall probe (MPT-141 by Group3 Technologies) [Gua11]. Unfortunately, the precision of the hall probe is under lab conditions at PF1b in the order of $O(10^{-3})$. Therefore, a Nuclear Magnetic Resonance (NMR) system has been devised to measured the field with high precision in the DV- and AP-regions, see [Gua11, Sch17]. This system has been used to determine the homogeneity and stability of the magnetic field after the beam-time 2013. Further, influences due to ramping the magnet, vacuum shutters, detector electrode, etc. have been investigated. The analysis of the measurement is not finalized yet, but the field ratio has been already determined to $r_B = 0.202887$ with an uncertainty of $\delta r_B / r_B < 5 \cdot 10^{-5}$ [Sch17]. This uncertainty includes uncertainties of the measurement method, external influences, stability and homogeneity. This low uncertainty of r_B corresponds to an uncertainty of $\delta a / a < 0.05\,\%$, which is more than low enough for the aim of a $1\,\%$ measurement.

Retardation Voltage U_{ret}

The retardation voltage is defined as the difference between the electric potential Φ_0 a decay proton experiences in the DV and the retardation potential Φ_{ret} it experiences in the AP

$$U_{ret} = \Phi_{ret} - \Phi_0. \tag{2.7}$$

(a)

(b)
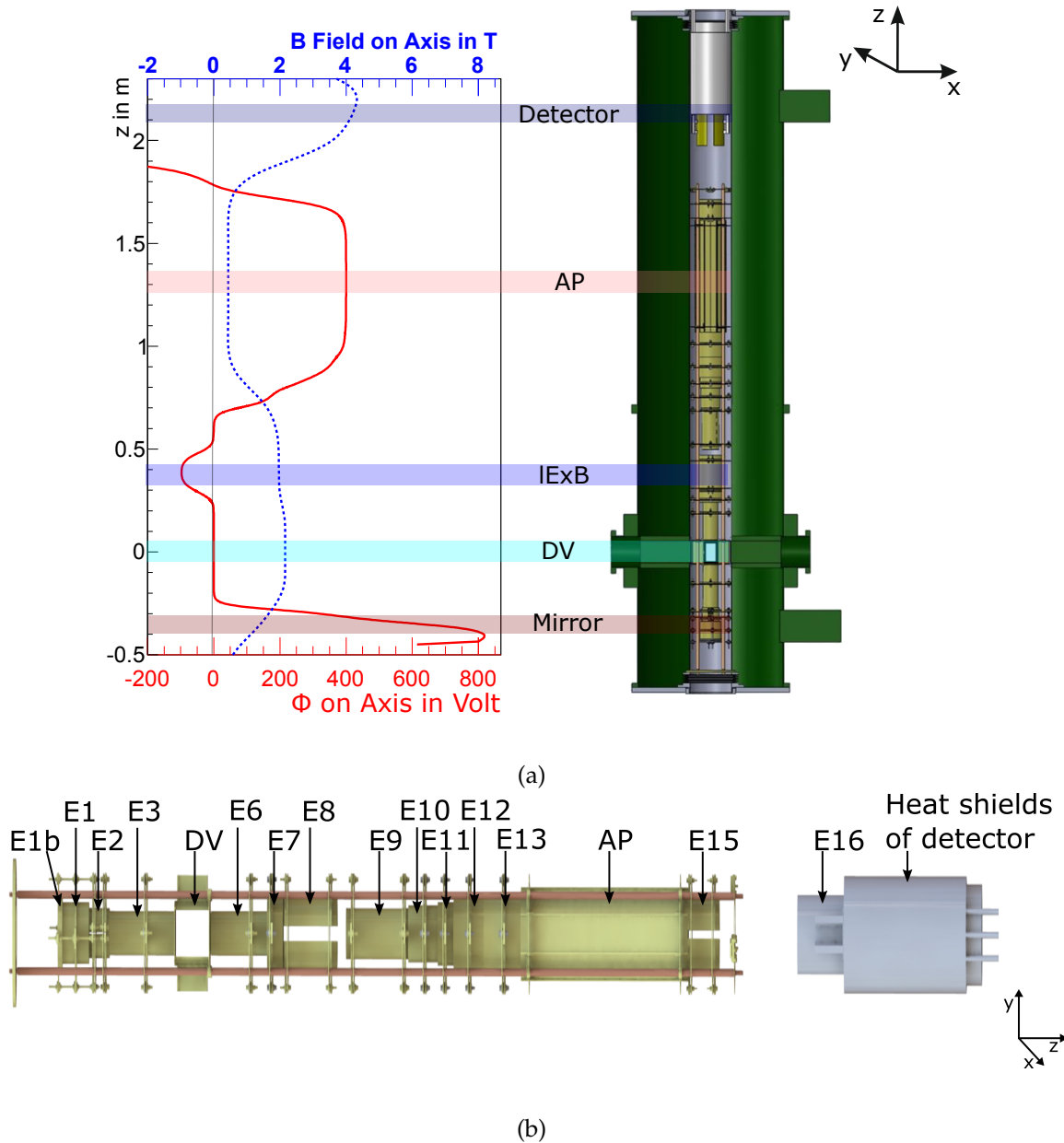
Figure 2.4.: Magnetic field, electric potential and CAD sketch of *a*SPECT.
(a) On the right is shown a cut through of the magnet system with the electrode system inside. The magnetic field and electric potential generated by these systems are shown on the left. In red (solid line) the electric potential for $U_{ret} = 400\,\text{V}$ is drawn, in blue (dashed line) the magnetic field for 70 A in the magnet system. Highlighted are the interesting regions of the potential and B-field, as well as the electrodes generating them.
(b) Zoom into the electrode system, including the naming scheme of the electrodes. The interesting regions of the electric potential are the E1b, E1 and E2 electrode (Mirror) generating a positive potential to reflect adiabatically the protons upwards. The DV electrode (DV) defining the 0 V potential for the protons from the decays. The E8 electrode (lExB), generating an ExB drift to empty the trap between Mirror and AP. The AP electrode generating the retarding potential and finally the detector electrode accelerating the protons by $-15\,\text{kV}$ to be detected by the SDD detector. The standard voltages used during the beam-time 2013 can be found in table 2.1. Please be aware, the drawing has been stretched in radial direction for better visualisation.
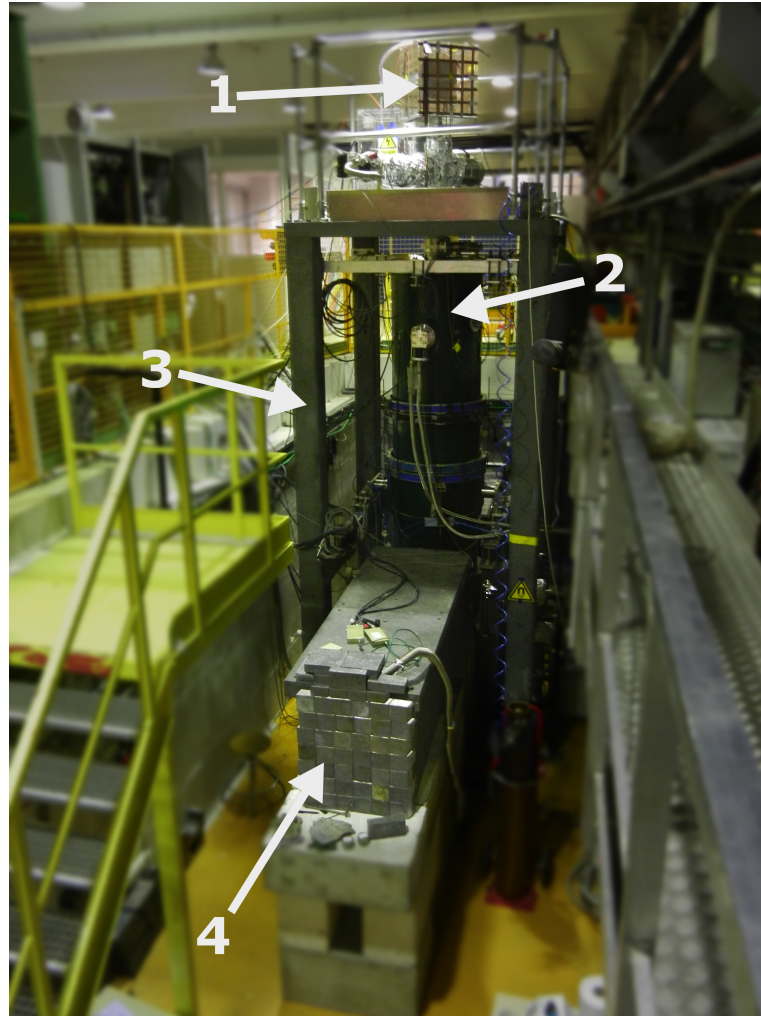
Figure 2.5.: Technical realisation of aSPECT. Shown is a picture of the actual aSPECT-experiment at the PF1b beam place at the ILL. From top to bottom is shown the detector electronics in a Faraday cage (1), the supra-conducting magnet system (2) inside the magnetic shielding (3), which reduced the stray field from the magnet. Also shown is the beam dump (4) of the neutron beam line.

Table 2.1.: Standard settings of the electrode system.

electrode	voltage in V	comment
detector	-15 000	proton acceleration
E16 A/B	-1750 / -2250	ExB drift shifting the proton projection on the detector in y-direction
E15 R/L	$0.9851(1) \times$ AP	variable, for details, see fig. 2.14
AP	0 - 780	actual retardation voltage, variable
E13	$0.9910(1) \times$ AP	⎫
E12	$0.8923(1) \times$ AP	⎬ adiabatic momentum transfer to AP, variable
E11	$0.6839(1) \times$ AP	
E10	$0.4353(1) \times$ AP	⎭
E9	0	
E8 R/L	-200/-1	ExB drift to empty trap between mirror and AP
E7	0	
E6	0	
DV	0	defines zero start potential Φ_0 of protons
E3	0	
E2	380	⎫
E1	800	⎬ electro-static mirror for 4π acceptance
E1b	860	⎭

The retardation voltage has to be known in the order of $O(10\,\text{mV})$, to achieve an uncertainty in a of $O(0.1\,\%)$. The correlation between the uncertainty of U_{ret} and a is given by [GBB$^+$05]

$$\frac{\delta a}{a} = 0.01\% \frac{\delta U_{ret}}{\text{mV}}. \tag{2.8}$$

The retardation voltage is applied by a precision power supply (FUG HCN 0,8M-800) and monitored by a precision Digital Multimeter (DMM) (Agilent 3458A). This multimeter is able to measure at a precision of $\delta_{DMM} < 13\,\text{mV}$ under lab conditions, see appendix D. This corresponds to an uncertainty of $\delta a/a < 0.13\,\%$. Unfortunately, the applied voltage is modified by several effects, influencing the spatial distribution of the potential in both DV and AP, as well as its temporal stability. These effects are

- field leakage into the DV and AP electrodes

- surface contact potential fluctuations of the electrodes themselves

- RF noise on the electrodes

and will be explained in detail in the next paragraphs.

Field Leakage

The electric potential inside an electrode, which is not completely closed, is influenced by field leakage. In case of *a*SPECT the interesting electrodes are the DV and AP electrode, as they define the retardation voltage eq. (2.7). In fig. 2.6 a photograph of these electrodes is shown. In general the size of the openings of the electrodes are kept as small as possible to minimise the field leakage into the electrode. Minimising the openings is limited by

practical reasons like proton and neutron flux size, which have still to pass the AP, DV respectively. Further technical reasons, like the necessary pumping cross-section limits this possibility. In the following the origins and amount of field leakage for the DV and AP electrodes are explained.

For the AP electrode shown in fig. 2.6 the field leakage originates mainly from the difference of the voltage U_{ret} applied to the electrode and the surrounding bore tube of the magnet, which is on ground potential. To minimise the leakage through the openings on top/bottom, the electrode has been made very long. Additionally electrodes on a similar voltage as the AP electrode have been installed above and below it, see table 2.1. This shields the actual AP from its surrounding and reduces the inhomogeneity in the AP to < 2 mV [Kon11]. How sensitive *a*SPECT is to field leakage can be seen by electric field simulations done by [Kah15]. Here, a retardation voltage of 400 V has been simulated, resulting in an offset in the order of $O(100\,\text{mV})$. This field leakage corresponds to an uncertainty of $\delta a/a \approx 1\,\%$, if not taken into account. For the final analysis, this field leakage will be determined by simulations, resulting in a correction in the order of 1 %.

For the DV electrode the situation is a bit more complicated. The DV electrode and the surrounding bore tube are both on ground potential, therefore no potential should leak into the DV. Unfortunately, there are two effects changing the potential in the DV electrode. One effect is a potential charging of the internal collimation, due to charged decay products of the neutron beam, for technical details of the collimation see [Bor10]. Insulators hit by these decay particles can charge up, which would lead to a field leakage into the DV, for details see [Kon11]. To avoid any charge up, the internal collimation has been rebuild from boron nitride, which has been enriched with titanium to make it conductive (ESK DiMet Type 4). A picture of the internal collimation, can be seen in fig. 2.7. This avoids any potential charging of the collimation. The actual beam shaping is done with lithium fluoride apertures placed inside the collimation. These apertures have been sputtered with a layer of titanium to make them conductive as well. Hence, a charge up and therefore field leakage from it, is avoided. The other effect changing the potential inside the DV is due to the work function differences of gold (DV), stainless steel (bore tube) and boron nitride (collimation). Stainless steel has a work function in the order of 4.4 eV, whereas gold has a work function of about 5.3 eV [Hay12]. Please be aware, that the actual difference between the gold of the DV electrode and the bore tube of the magnet will be measured by [Sch17], as the work function strongly depends on the stainless steel used and the crystallographic orientation of the gold. Nevertheless, from these numbers a lower potential outside of the DV electrode than inside of it is expected. Although it is a small difference it is enough to shift the potential inside the central position of the DV electrode in the order of $O(-30\,\text{mV})$, see fig. 2.7 (b). If this shift in the starting potential would not be taken into account, it would cause an additional uncertainty in *a* of $\delta a/a = 0.3\,\%$. To investigate the field leakage experimentally the complete electrode system of *a*SPECT has been set to different potentials relative to the ground potential of the bore tube. In fig. 2.8 a) is shown a scan for different voltages of the electrode system, data from the 20130704/ScanDV measurement. The whole electrode system was set to voltages from $-10\,\text{V}$ to $10\,\text{V}$ with respect to the bore tube. This corresponds to a change of the potential inside of the DV in the order of $O(\pm300\,\text{mV})$, respectively. The AP was set to 50 V and the electrostatic mirror was set to 0 V, so reflected protons can not intervene with the measurement. In fig. 2.8 b) the simulated electric potential along the z-axis in the DV is drawn. The electric potential shows a clear potential well directly inside
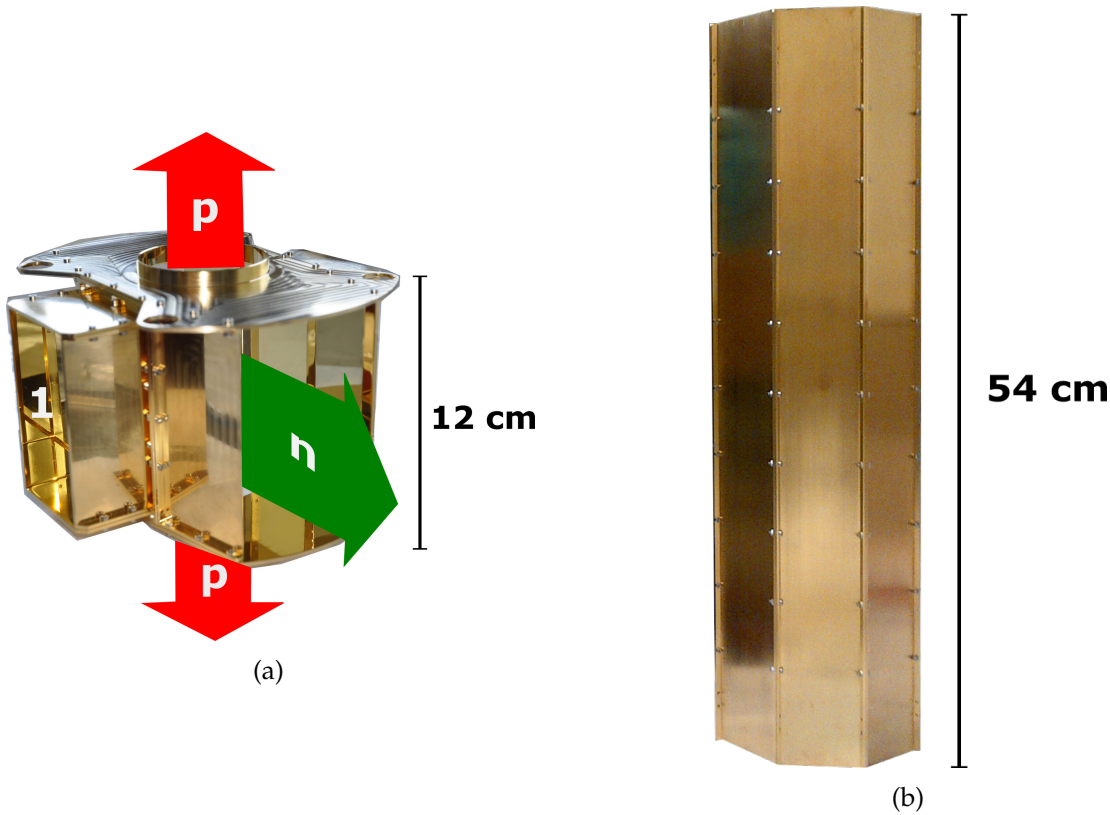
Figure 2.6.: Photographs of the DV (a) and AP (b) electrodes used in the 2013 beam-time. Both electrodes are made of OFHC (CW 009A) copper, electroplated with a gold layer (1 μm) and a silver layer (10 μm) in between as barrier. The electrodes are made of separate plates, which are screwed together. This has the advantage, that the complete inner surface of both electrodes is flat and can be scanned with a Kelvin Probe.

(a) The neutrons (n) are flying though the DV electrode. Protons (p) from decays inside the DV are radially confined by the magnetic field and leave the DV electrodes in z-direction though openings on top and bottom. Additionally, two side ports (1) are integrated to increase the pumping cross section and allow access to the DV. This access also allows to measure the neutron beam profile directly in the DV, see section 2.2.2, or to introduce radioactive sources for test measurements.

(b) The AP electrode is made of 8 similar plates, forming an octagonal of 54 cm length with a diameter of 14 cm. The length of this electrode allows to produce a very homogeneous retardation potential for the protons.

(a)

(b)
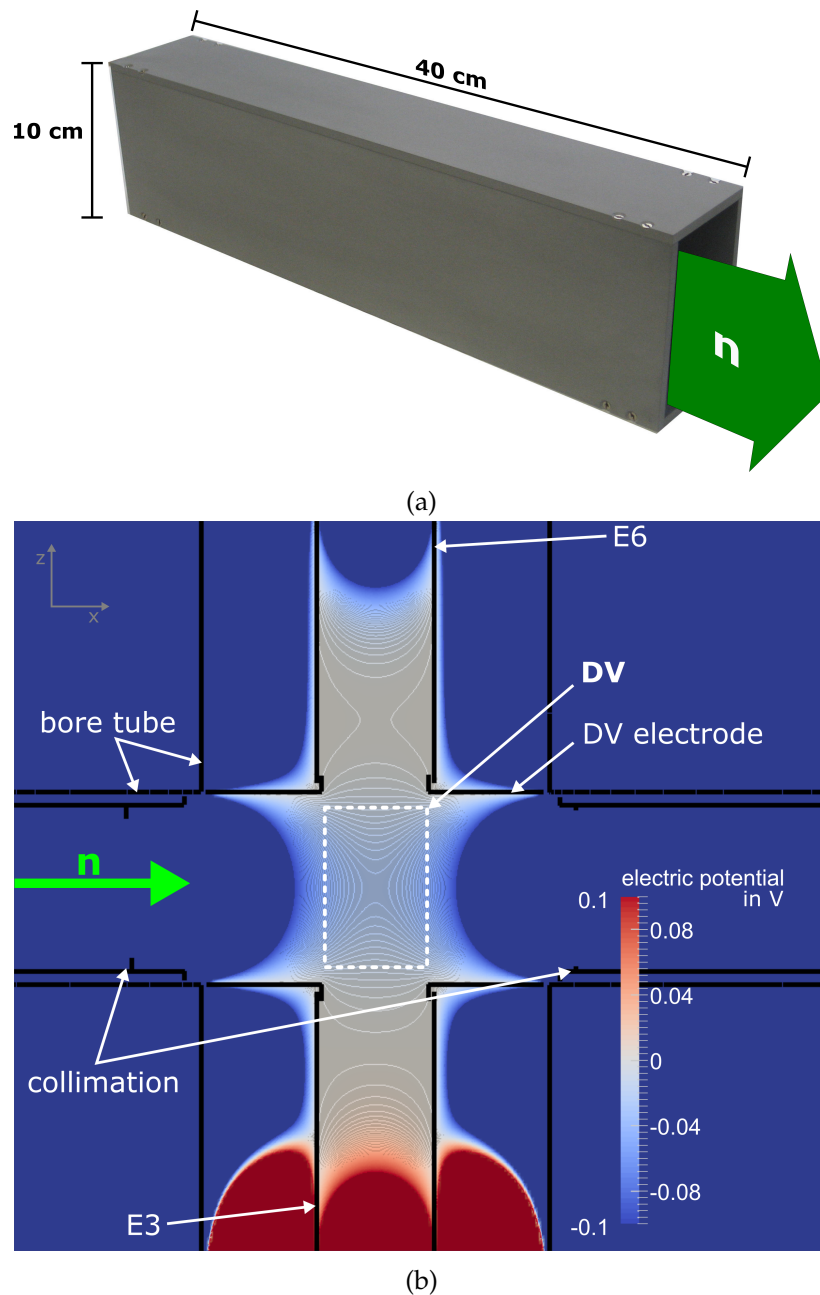
Figure 2.7.: Internal collimation and field leakage in *a*SPECT
  (a) Internal collimation of *a*SPECT made of boron nitride, enriched with titanium
  to make it conductive. The actual beam shaping is done with lithium fluoride
  apertures inside the collimation (not shown on the photograph).
  (b) Simulation of the field leakage into the DV, due to work function differences
  between gold (DV) and stainless steel (bore tube), boron nirtide (collimation).
  The potential of gold has been set by definition to 0 V, the one of stainless steel
  to −1 V, the one of boron nitride to −1 V. Already these small differences reduce
  the electric potential in the middle of the DV by 30 mV and therefore has to be
  taken into account.

(a)

(b)
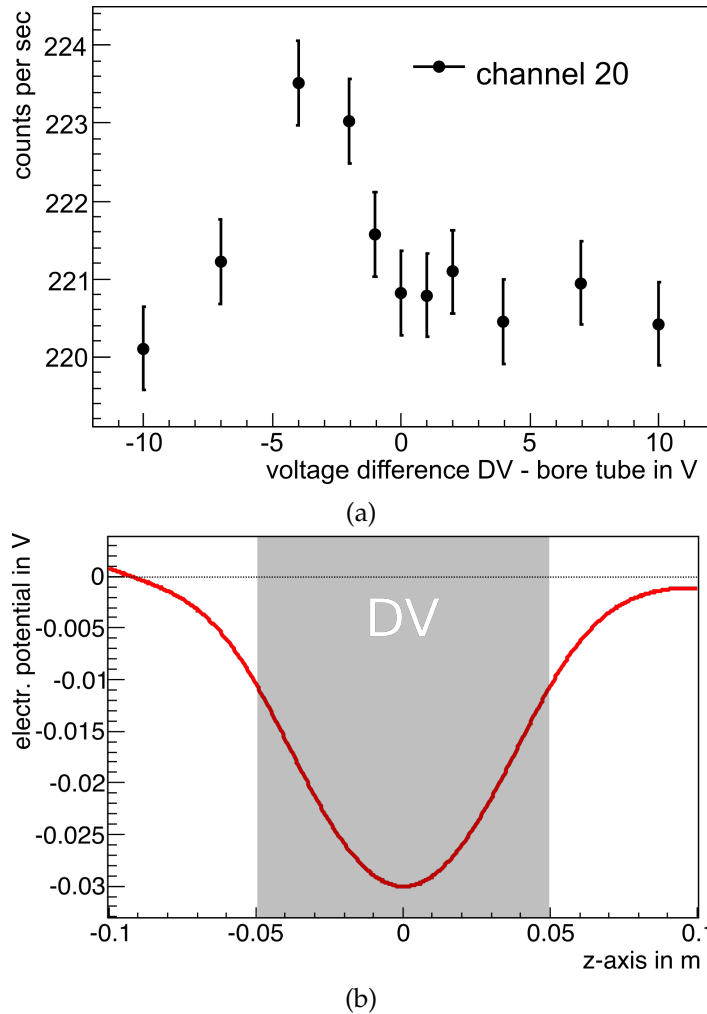
Figure 2.8.: Countrates for different ground potentials of the electrode system and simulated electric potential in the DV

(a) Shown is the countrate for different ground potentials of the electrode system with respect to the surrounding bore tube and an retardation voltage of 50 V. A background measurement with 780 V retardation voltage has already been subtracted. The electrostatic mirror was set to 0 V for this measurement, so reflected protons would not intervene with the measurement. The data show an increase for the voltages −1 V and −3 V, due to the elimination of a potential well shown in b). Data taken measurement 20130704/ScanDV, errorbars are statistical errors only.

In (b) is shown the simulated electric potential, cf. fig. 2.7 b) along the z-axis in the DV. The potential well in the DV is caused by the field leakage from to bore tube and the collimation In this well protons with very low kin. energy and/or angles close to 90° are trapped. Setting the electrode system to more positive values increases the well, which does not have a significant influence on the measured countrates. On the other hand, negative values in the range of −1 V to −3 V for the electrode system equalises the potential difference between the electrode system and the bore tube, hence the potential well vanishes and an increase of the countrate is observed. Setting the electrode system to even more negative values (<-5 V) will turn the potential well into a potential barrier for protons emitted at places with $z < 0$. Hence, protons with low kin. energy and/or angles close to 90° will be reflected by this barrier. This can be seen as slight decrease in the countrate in a).

the DV, caused by field leakage, cf fig. 2.7 b). In this potential well protons with low kin. energy and/or angles close to 90° are trapped and therefore not detected. Changing the voltage of the electrode system, relative to the bore tube, changes the field leakage into the DV and therefore this potential well. This change of the well can than be seen as countrate change on the detector. Setting the electrode system to voltages >0 V increases this potential well, which does not significantly decrease the countrate any further. Setting the electrode system to voltages in the range of −1 V to −3 V equalises the potential well. In this range lies also the expected work function differences between gold (DV) and stainless steel (bore tube). Hence, the trap for the proton is gone and an increase in the countrate is observed. Setting the electrode system to even more negative values >−5 V on the other hand, will turn the potential well into a barrier. Therefore, protons emitted below $z < 0$ and with low kin. energy and/or angles close to 90° can not overcome this barrier and will be reflected. This leads then to a decrease in countrate, which is also observed experimentally. Hence, the field leakage into the DV can be measured experimentally, by measuring the countrate for different voltages of the electrode system. To correct for the effect, the exact work function difference between gold and stainless steel will be measured, this difference will then be implemented into a particle tracking simulation to determine the exact distribution of the electric potential in the DV and their influence on a and its uncertainty [Sch17].

Another possibility to investigate the effect of trapped protons in the DV is to apply an E-field in the DV that accelerates protons towards the detector. To generate such a field, the E3 electrode below the DV has been set to 4 V and the E6 electrode above to −4 V. This does not change the mean potential in the DV, but generates an electric field in the order of $O(6\,\mathrm{Vm}^{-1})$ along the z-axis. This field pulls out any protons from traps generated by the field leakage. Such a configuration is shown in fig. 2.9 and has been measured during the beam-time 2013, see config 7 in fig. 3.16. As can be seen the shift in a between config 7 and the "standard" measurement (config 1) is small and within their uncertainties. Hence, proton traps in the DV are not a major problem for *a*SPECT, if the electro-static mirror is turned on, cf. section 3.3.2. But keep in mind, the field leakage can still generate a general offset in the retardation voltage U_{ret}, influencing all measurements. This general offset will also be slightly retardation voltage dependent, as the field leakage in the AP depends on the difference between the applied voltage and the bore tube. Therefore, a detailed particle tracking simulation, including the neutron density distribution in the DV, as well as the distribution of the electrostatic potential, influenced by the field leakage and the surface contact potential (see next paragraph), has to determine the exact effect on a.

Surface Contact Potential

As shown in the previous paragraph the work function difference of the bore tube and the DV electrode causes a field leakage into the DV and therefore modifies the electrostatic potential inside the electrode. This effect is also present in weaker form inside the electrode itself and can therefore change the real retardation voltage seen by the protons. Any offset and fluctuation of the retardation voltage, due to work function differences of the gold itself can therefore significantly influence the value and uncertainty of a.

As already mentioned, *a*SPECT uses OFHC (CW 009A) copper electrodes, which are covered by a gold layer of about 1 μm, with a layer of 10 μm silver as barrier in between. Due to the crystallographic structure of the upper gold layer the work function can fluctuate between about 5.0 eV to 5.5 eV [Hay12, Val09]. This maximal 500 meV difference of the
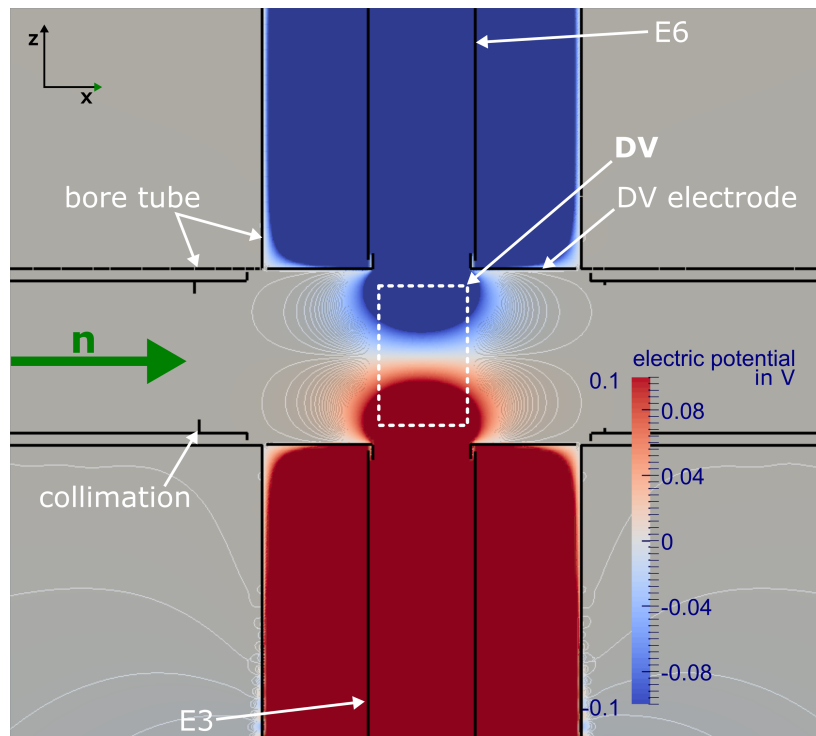
(a)
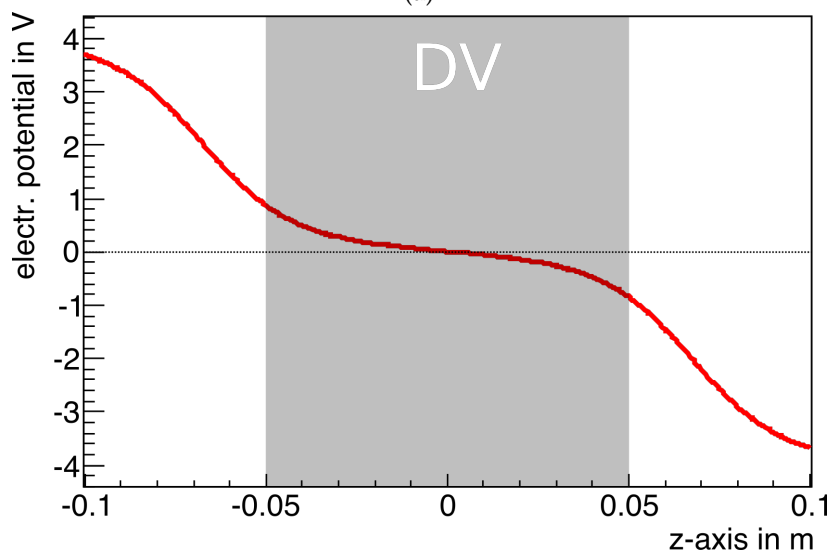
(b)

Figure 2.9.: Simulation of the electric potential in the DV with voltages of $4\,\text{V}$ and $-4\,\text{V}$ applied to the E3 and E6 electrode, respectively. This does not change the mean potential inside the DV, but generates a field accelerating protons towards the detector and therefore empties potential proton traps inside the DV. In (a) is drawn a cut through the DV region, visualising the field leakage into the DV by applying a voltage to E3 and E6. In (b) is shown the electric potential along the z-axis in the DV, accelerating the protons towards the detector (pos. z-values).

potential inside the DV and AP electrodes would cause in worst case an uncertainty in *a* of $\delta a/a \approx 5\%$, if not corrected. Clearly far to much for a desired precision of 1 % for the beam-time 2013. Furthermore, the given values are literature values for a clean, pure gold surface, which never has been exposed to air. Any surface exposed to air will immediately be covered by several layers of water and potentially dust, which modifies the potentials seen by particles in the electrode and especially change the fluctuations of the potential over the complete surface of the material. Hence, the actual potential and its fluctuation seen by the particles is of interest, the so called surface contact potential.

The mentioned 500 meV would be the worst case scenario, for different kinds of crystal orientation over one electrode surface and/or between different electrodes. For *a*SPECT all electrodes are electroplated by the same method and at the same time. Afterwards they are cleaned and stored in the same way to minimise differences between them. These differences can be measured using a Kelvin Probe. Please keep in mind, for *a*SPECT only the difference between the surface contact potential of the electrodes of the DV and AP is of interest, as these two electrodes define the retardation voltage seen by the protons. Hence, the absolute value of the work function/surface contact potential has not to be known, only the difference and fluctuation of it. For details of the work principle of a Kelvin Probe and the details of the work function measurement, the reader is referred to [Sch12, Kon11, Kah15, Sch17]. In this thesis only the general effects of fluctuations of the surface contact potential will be given. Fluctuations of the surface contact potential cause a spatial inhomogeneity of the potential inside the electrode, similar to the effect of field leakage. This spatial inhomogeneity causes a position dependent potential inside of the electrodes. Therefore, depending on the position of the decay the proton experiences a slightly different start potential and also a slightly different retardation potential in the AP. This could even cause a to early retardation of the proton, before their momentum has been converted maximally. On the other hand inhomogeneities in the DV itself can cause trapping of low energetic protons or ExB drifts inside the electrode.

To determine the inhomogeneities in the potential of the DV and AP, their electrodes have been measured in detail at ambient air uaing a Kelvin Probe. An exemplary scan of one of the electrode surfaces is shown in fig. 2.10 a). Clearly, three different regions of work function over the sample surface can be seen. These differences are in the range of 100 meV to 200 meV and caused by the tree different crystal orientations of gold, for details see [Sch12, Kah15]. As these measurements have been performed after the beam-time 2013, the long-term stability of the electrodes has been investigated as well. To do so, one part of the AP electrode has been measured several times. This reference sample AP83, like every other electrode, has been stored since the beam-time 2013 in a commercial freezer at about $-35\,°C$ to slow down the diffusion of gold into silver and copper. In fig. 2.10 b) the surface contact potential of AP83 over two month is shown. The AP83 sample shows a surface contact potential of 96(35) meV over this time period. This uncertainty of 35 mV therefore defines the reproducibility of these measurements. These measurements have been done in 2015, to cross check, how the measurements from 2015 are linked to the situation in 2013, new test samples have been produced. These test samples were made exactly the same way, as the *a*SPECT electrodes. These test samples show with in the reproducibility the same surface contact potential as the *a*SPECT electrodes. Hence, the difference and/or fluctuation measured in 2015 can safely be extrapolated to the situation in 2013. For a complete overview of the surface contact potential measurements and their results, see
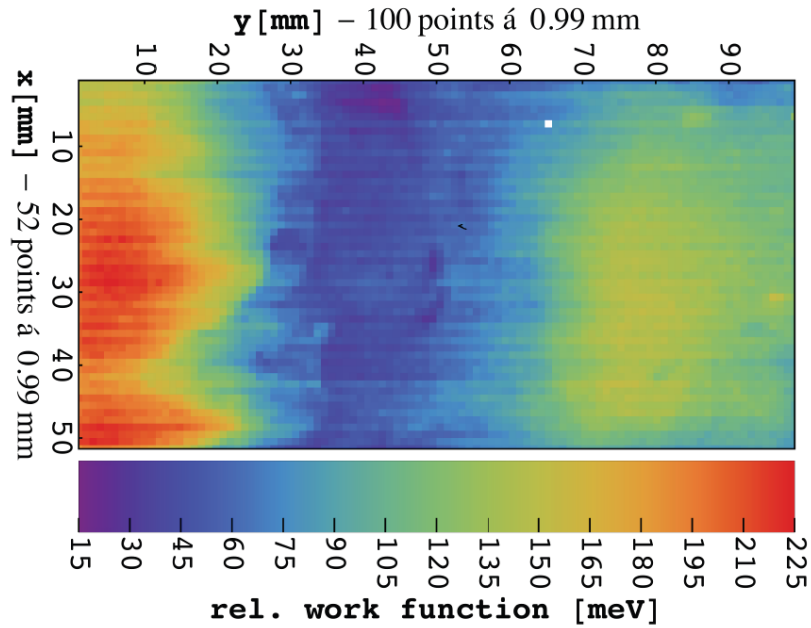
(a)
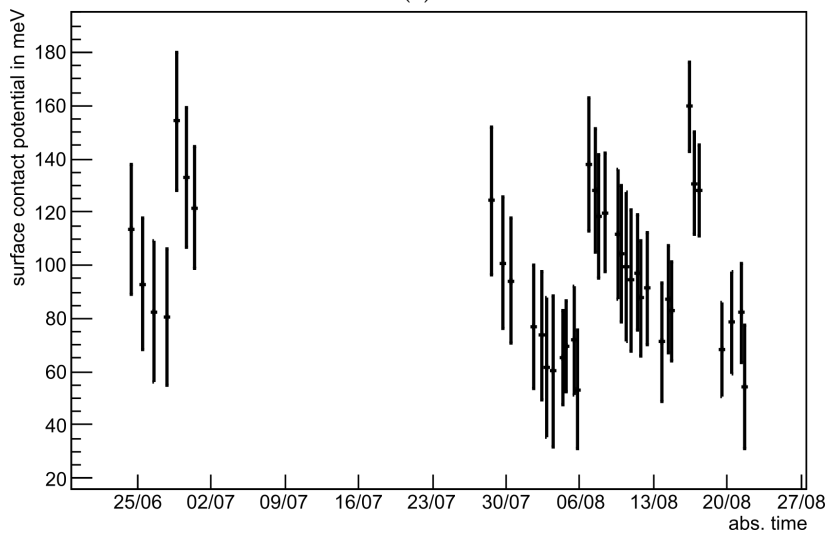
(b)

Figure 2.10.: Measurement of the surface contact potential. Shown is in (a) an example of a Kelvin Probe measurement of the surface contact potential, taken from [Sch12]. Clearly three different regions with different work function can be seen, presumably due to the crystal orientation of the gold. These fluctuations of the surface work function/surface contact potential causes a variation of the retardation voltage and a corresponding uncertainty. This uncertainty of the retardation voltage corresponds directly to one in *a* and therefore has to be minimised as far as possible.

In (b) is drawn the surface contact potential of a reference sample AP83 measured several times over two months in 2015. This measurement defines the reproducibility of the Kelvin Probe measurements and is used to determine the long-term stability.

[Sch17].

Further, to investigate the difference in the surface contact potential, due to desorption of water layers in vacuum, samples of the *a*SPECT electrodes have been scanned with a High Vacuum (HV) Kelvin Probe. Additionally, as the *a*SPECT electrodes are cooled by the cold bore tube of the magnet, tests with a cooled sample have been performed, to investigate the effect of freeze out on the surfaces [Bic15]. The measurements with the HV Kelvin Probe and the one at air showed, that the desorption of water layers in vacuum, as well as freeze out on the surfaces change the absolute value of the surface contact potential, but neither the difference between two electrodes, nor the fluctuation on them. The same is true for the temperature dependency of the work function of materials. There is a small change of the work function, due to the temperature change in the order of $O(-3\times10^{-5}\text{eVK}^{-1})$ [KWZ79]. All these effects change the absolute value of the surface contact potential. But as in *a*SPECT all electrodes are made of copper, electro-plated with silver and gold, and they are all in the same environment, all electrode surfaces are effected in the same way. Hence, their absolute value of surface contact potential will change, but the difference between them will stay the same. Therefore, any difference measured at ambient air, will be the same as in cold condition under vacuum.

All electrode parts of the DV and AP electrode have been measured therefore with a Kelvin Probe at air. So far the measured difference between these two electrodes is in average 5(20) mV. Please keep in mind, this is just a mean value between these electrode. The fluctuations within one electrode are in the range of 25 mV to 55 mV. So the retardation voltage seen by the protons varies, depending on the position of the decay and the place of retardation. To determine the actual retardation voltage and its uncertainty seen by the protons, the measured fluctuations are implemented in a particle tracking software [FGT$^+$], as well as the measured neutron beam profile. Including also the field leakage, this allows to simulate the inhomogeneity of the potential seen by the protons and determine the shift and uncertainty on *a*, due to fluctuations of the retardation voltage. For details of these measurement see [Kon11, Sch12, Kah15, Sch17] and for the simulations, see [Sch17].

RF Noise on Electrodes

So far only spatial inhomogeneities have been discussed, but also temporal fluctuations of the applied retardation voltage are possible. These fluctuations can occur from instabilities of the power supply, or from RF noise. This RF noise can be picked up by cables or the elctrodes themselves. The instabilities or temporal drifts of the power supply (FUG HCN 0,8M-800) are measured with the precision DMM (Agilent 3458A), which is calibrated at least annually. For an analysis of the stability of the power supply and the DMM, see [Pay11]. Furthermore, the RF noise between the DV and AP electrode has been determined with an oscilloscope (Agilent DSO5054A) to $\delta U_{ret} < 200$ mVpp at about 1.8 mHz. This noise has been reduced by shorting the electrode supply cables with a 0.1 μF capacity. This capacitor acts as a short cut for AC noise on the electrodes, but does not influence the DC voltage applied to the electrode. Using this method the noise could be reduced to $\delta U_{ret} < 40$ mVpp at about 1.8 MHz. This causes an additional uncertainty in *a* in worst case of $\delta a/a \approx 0.4\%$, cf eq. (2.8). For this analysis, the RF noise has been taken into account as additional uncertainty for the retardation voltage, see eq. (3.14).

2.2.2. Edge Effect

The protons from decays in the DV are guided by the magnetic field towards the detector, see fig. 2.1. In aSPECT a Silicon Drift Detector (SDD) with three active pads is used. Each of these pads has an active area of $1 \times 1\,cm^2$, see fig. 2.17. Unfortunately, this sensitive area is not big enough to cover the whole proton flux coming from the DV. Hence, not all protons from the decay can be detected. On the one hand, this causes a loss of statistics, but due to the strong neutron flux at PF1b a statistical sensitivity of about 1.8 % per pad and day can be reached. On the other hand this introduces an incomplete, energy dependent projection of the proton flux onto the detector the so called edge effect.

Protons with a non zero radial momentum $\vec{p}_\perp \neq 0$, gyrate around the magnetic field lines. Due to this gyration, a proton will hit the detector not at the position of the magnetic field line, but in a distance of the gyration radius r from there. For protons on field lines towards the center of the detector, this gyration is unimportant, as they will hit the detector anyway. But for protons on field lines close to the detector edges, the gyration causes a $\vec{p}_\perp$ dependent smearing of the projection of the protons on the detector. Protons, which should be detected might not be and vice versa, see fig. 2.11. Shown are two neutron beam profiles, one with a constant neutron intensity and a realistic one. In both cases the gain or loss of protons occurs, but in case of a beam profile with constant intensity the amount of protons lost and gained equals. This is not the case for non-uniform beam profiles. There a netto gain or loss of protons occurs, depending on the shape of the profile. As the gyration radius depends on the transversal energy ($T_\perp$) and therefore the recoil energy T_0, this gain/loss will change the shape of the measured proton spectrum and therefore lead to a wrong value of a. The edge effect shifts a in the order of a few percent $\Delta a/a \approx O(1\,\%)$ [Kon11]. The edge effect can be corrected by particle tracking simulations to an uncertainty of $\delta a/a \approx O(0.1\,\%)$. For these simulations detailed information of the position of the detector and the neutron beam profile, hence the density distribution of neutrons in the DV is needed. The uncertainty of the detector position and the neutron beam profile therefore limit the uncertainty of the edge effect. The neutron beam profile is determined by activating copper foils in the neutron flux before the DV, inside of it and after it. There ^{64}Cu and ^{65}Cu is activated by neutrons from the beam with a half-life of $\tau_{1/2} \approx 12.7\,h$ and $\tau_{1/2} \approx 5.1\,min$, respectively. The activity is determined by exposing the activated Cu foil to a X-ray detecting imaging plate about an hour after the activation, so only ^{64}Cu is still active. This imaging plate is then scanned by an ordinary PC scanner. Details on the principle of measuring the neutron beam profile can be found in [Bor10, Vir13]. To measure the profile inside the DV electrode the set-up of 2008 has been changed so a manipulator can be introduced inside the DV holding the copper plate. Information on the neutron beam profile of the beam-time 2013 and the new manipulator can be found in [Vir13]. To determine the position of the detector a thin copper wire is activated in the neutron beam. This wire is then moved with neutron beam off along the y-axis. By detecting the emitted electrons from the activated copper, the exact magnetic projection of the DV in y-direction onto the detector can be determined. The projection in x-direction is done by turning the manipulator and therefore reducing its projection in x-direction. With this method the projection area could be determined in y- and x- direction with an error of $\pm 2.5\,mm$. Details of this measurement and the position of the detector relative to the DV can be found in [Vir13].

The position of the detector and the measured neutron beam profile (fig. 3.18) are then used as input into a particle tracking program, to determine the shift of the proton recoil
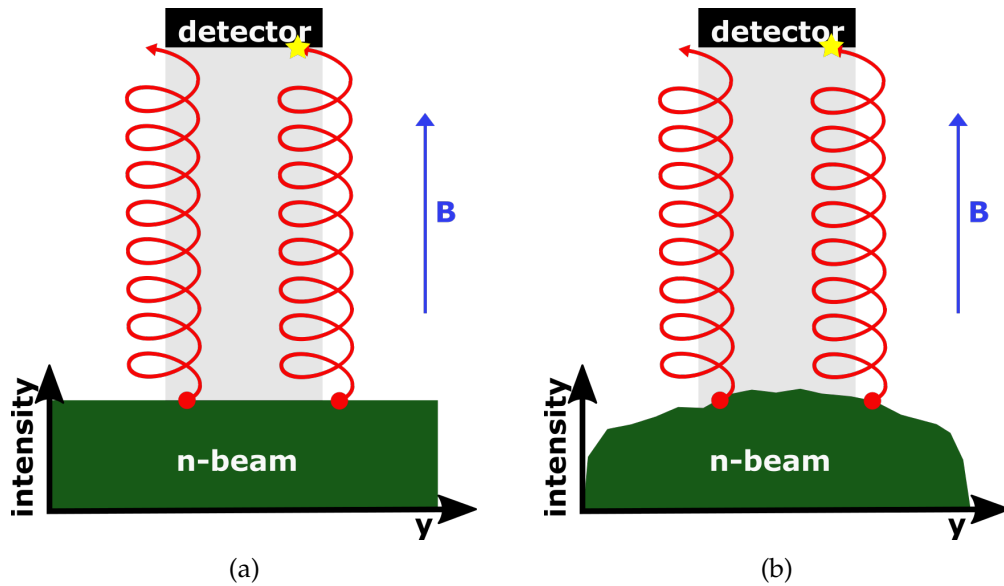
Figure 2.11.: Sketch of the edge effect. Shown are two different neutron beam profiles, in (a) the ideal case with a constant neutron beam intensity, in (b) the realistic case with a non-constant neutron intensity. In grey is drawn the projection of the detector onto the neutron beam. Exemplary are shown two protons close to the edges of the projected area. The left spiral (both sketches) shows a proton emitted inside, the right spiral a proton emitted outside the projection area. Due to their gyration, the left proton is not detected, although it should have been, the right one hits the detector, although emitted outside the projection area. In case (a) this happens with equal probability and there is no nett effect. In case (b) this probability is not equal, hence there is a netto gain/loss of protons. This netto gain/loss depends on the gyration radius r, i.e. the recoil energy and therefore will change the shape of the proton recoil spectrum. For details on this effect, as well as methods to determine and correct it, see text. For the actually measured neutron beam intensity distribution and their correction, see section 3.3.2

spectrum. To increase the edge effect experimentally and therefore the precision of its determination, two different beam profiles have been used during the beam-time 2013. Also different settings of the ExB drift electrodes have been used, as they shift the proton beam and therefore the projection onto the detector. Additionally, the ExB drifts break the radial symmetry of the spectrometer and therefore, introduces a dependency on the azimuthal angle φ of the edge effect. For all these settings and effects of aSPECT a simulation is needed to determine the edge effect for each setting and correct for it. As this is a very complicated simulation, a first hand estimate for the edge effect and its correction has been applied to the 2013 data, for details of this analysis, see section 3.3.1.

2.2.3. Background

For any precision experiment, background is a problem. In case of aSPECT there are two categories of background, constant and retardation voltage dependent one. As mentioned a will be determined by the shape of the proton recoil spectrum. Therefore, any constant background is no harm to the experiment, as it does not influence the shape of the spectrum, but only produces a constant offset to the spectrum. Constant means not time and retardation voltage dependent. On the other hand, any background that is retardation voltage dependent will strongly influence the shape of the recoil spectrum. To determine the strength of this influence, the theoretical spectrum (eq. (1.29)) for a given a has been calculated plus an additional retardation voltage dependent background. The calculated spectrum including background can than be fitted resulting in a different value a' to determine the influence of the background on a. In this way, the dependency of the background on a can be determined. In case of aSPECT an uncertainty of the retardation voltage dependent background of $0.01\,\mathrm{s}^{-1}$ corresponds to an uncertainty of $\delta a/a = 0.1\,\%$ [Kon11]. Although a constant background is not the problem for aSPECT it has to be kept as low as possible and determined as good as possible, as any uncertainty of a constant background could also mean a retardation voltage dependence of the same amount hidden in there. Any time dependence could also mimic a retardation voltage dependency, since runs with different retardation voltages are performed sequentially, see fig. 2.16. In the next paragraphs sources for constant and non-constant background are explained, as well as the methods to reduce the background from these sources. Finally, the methods to measure the remaining background during the beam-time are described.

Constant Background

There are two types of sources for constant background in aSPECT. Sources which are completely independent of aSPECT, like neutron guides close by, surrounding experiments in the experimental hall, or simply the adjacent reactor. These sources produce essentially high energetic γs and can not be controlled by aSPECT. It can be determined by measuring the background during a reactor cycle and after a cycle, when the reactor is shut down and all adjacent experiments are off. It has been determined to $3.56(31) \times 10^{-2}\,\mathrm{s}^{-1}$ with reactor on and $0.94(16) \times 10^{-2}\,\mathrm{s}^{-1}$ with reactor off [Mai14]. Compared to a countrate of about $450\,\mathrm{s}^{-1}$ at a retardation voltage of $50\,\mathrm{V}$, these background rates are low enough for a $1\,\%$ measurement.

The other type of sources for constant background are related to aSPECT. These sources are

- electronic noise,

- γs from neutron capture,

- electrons from neutron decays,

- electrons from backscattering,

- small, self-sustaining discharges from Penning-like traps.

The electronic noise has been reduced by a sufficiently high trigger threshold. Additionally, the detector electronics is cooled by dry air to reduce the temperature and therefore the noise. Although there is a slight temperature dependence of the noise [Sim10, Mai14], it depends not on the retardation voltage and therefore it does not intervene with a measurement of a. Further, in aSPECT the separation between electronic noise and proton signal is very good, hence the noise can be cut-off in a pulse-height spectrum without loosing to much of the proton signal, see fig. 2.12. All this leads to a proton signal practically free of electronic noise. High energetic electrons are cut off from the proton signal similar to the electronic noise. The remaining low energetic electrons, with energies similar to the the proton energy after the acceleration (< 15.75 keV), can not be cut off and are a source of constant background in the order of $O(6\,\mathrm{s}^{-1})$ underlying the proton peak. Unfortunately, there is no way to eliminate this background experimentally. The same is true for γs from neutron capture in the guide and especially the beam dump behind aSPECT, see fig. 2.5. Of course both are shielded by about 10 cm of lead, but apart from that, this background can not be reduced any more. Another source of background are electrons, which are backscattered from the bottom plate of the bore tube or electrodes [Kon11]. Finally, slow burning, Penning-like traps are a source of background, cf. [Hor11, Bor10, Mai14]. The mechanism how these traps produce background is explained in the next paragraph, as well as techniques to reduce background from them. Such traps can occur in several places of the spectrometer, like the AP electrode, the electrostatic mirror or at one of the ExB electrodes. The background from these traps can be retardation voltage dependent, but does not necessarily have to. Obviously, the trap in the AP electrode is retardation voltage dependent, traps at other places depend mostly on the setting of the electrode, so can be different for different configurations of aSPECT. These traps will have only an indirect dependency on the retardation voltage, as the background from these traps can be blocked by the retardation voltage. These traps and how their influence can be reduced is explained in the next paragraph.

Non-Constant Background

The main source for non-constant or retardation voltage dependent background are Penning-like traps in the spectrometer. This is a known phenomena for such experiments [BVB$^+$10, BCK$^+$11]. A Penning-like trap confines charged particles radially with a magnetic field and in z-direction with an electrostatic potential. Having a closer lokk to fig. 2.4a on will see, that in principle aSPECT itself is one huge Penning-like trap. In these traps, ionised residual gas gets trapped, which is created by field emission from negative electrodes. In case of aSPECT the most negative electrode is the detector electrode at $U_{det} = -15$ kV, creating initial electrons, e.g. by field emission due to surface roughness, or impact of protons/ionised residual gas. These electrons are accelerated towards the positive potential of the AP electrode and a small fraction of them ($O(10^{-6})$) ionises residual gas. Secondary electrons from these ionisations are also accelerated by the AP potential, but will get trapped inside the potential well of the AP electrode. Depending on the place of their creation they gain enough energy to ionise also residual gas, and so on. Positive ions from secondary
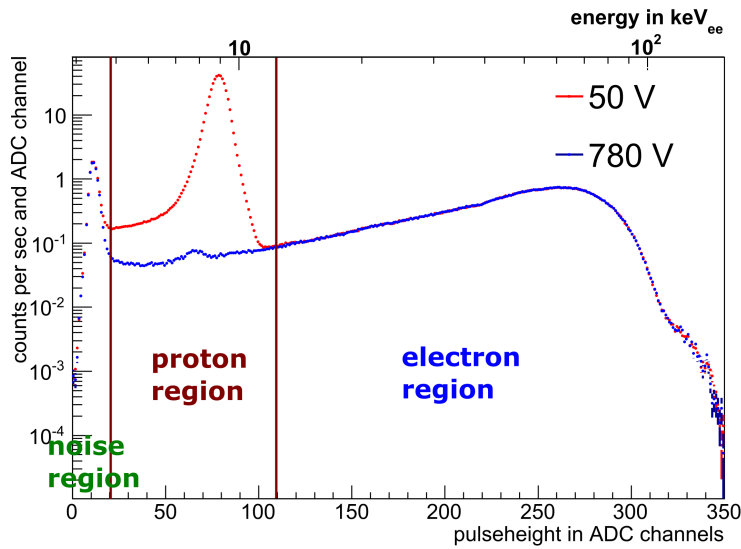
(a)
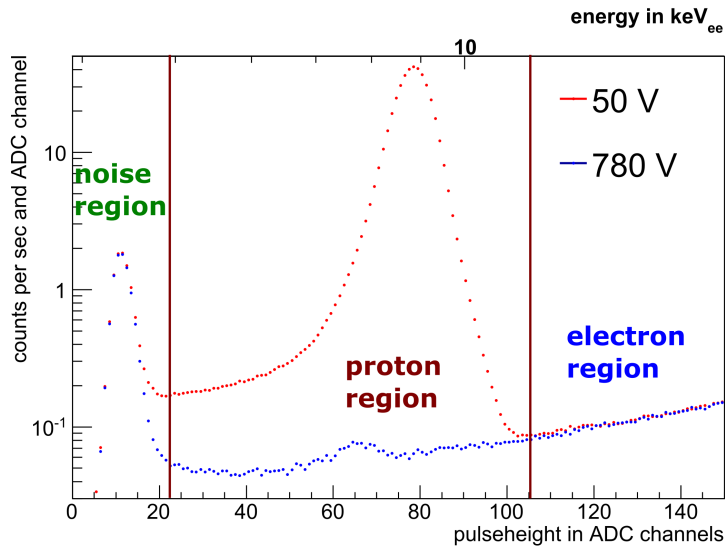
(b)

Figure 2.12.: Pulseheight spectrum from measurement config 1 (table C.1) ch20, with a retardation voltage of 50 V and 780 V. The error bars shown are statistical only and smaller than the size of the markers. Shown is the countrate per sec vs. ADC channel, for the whole spectrum (a) and a zoom at lower energies (b). Three different regions can be identified. For low energies < ca. 25 ADC channels electronic noise. Between 25 and 110 ADC channels the the region of interest, the so called proton region. Please keep in mind a retardation voltage of 780 V blocks all protons, so the remaining signal if background only. At higher energies > 110 ADC channels is the so called electron region. The proton countrate for one retardation voltage is determined by integration over the events in the proton region. This is done for all retardation voltages used, leading to the final measured proton spectrum, cf. table 2.2. For more details, see text.

ionisations are accelerated towards the detector electrode. If they hit the detector, they will cause background events with an energy similar to the one of protons from the decay. If the positive ions hit the detector electrode, they will create also electrons in addition to the already present field emission. These processes can lead to an amplification of the background countrate until a high voltage breakdown happens or loss mechanisms lead to an equilibrium, in which the discharge continues to burn at a more or less constant level [Pen77, TFK78]. The biggest trap of this kind in *a*SPECT is created by the AP electrode, cf. fig. 2.4. It causes a trap of about 1 m length and 0.14 m diameter in which residual gas can be ionised. Its depth is variable from 0 V to 780 V, depending on the voltage applied to the AP electrode. This retardation voltage dependent depth then causes the retardation voltage dependence of the background. Furthermore, these processes can occur also in other parts of the spectrometer in less strength, as any potential difference can cause field emission, e.g. between the bore tube and the electro-static mirror. Any ions from these traps will be blocked also by the retardation voltage in the AP. This introduces an additional retardation voltage dependency of an otherwise constant background.

Background from Penning-like traps has always been a problem for *a*SPECT [Hor11, Bor10, Pau11]. These traps can not only produce background, but in the worst case self-sustaining discharges, strong enough to destroy the detector of *a*SPECT. Therefore, these traps are not only a problem for a successful measurement, but can also be a serious danger to the experiment itself. This happened the last time during a beam-time in 2011, where strong discharges due to penning-like traps occurred and made a successful measurement impossible. In fig. 2.13 two examples of the countrate evolution in 2011 are shown. In a) is drawn the countrate for the different retardation voltages of one measurement block, cf. fig. 2.16, in b) is shown the countrate with U_{ret} = 400 V measured during different measurement blocks. In 2011 the measurement cycle was different, than in 2013, cf fig. 2.15. 2011 the neutron shutter has been opened ($t \sim 18$ s) before the retardation voltage has been ramped up ($t \sim 30$ s). Opening the neutron shutter causes a strong increase in countrate, where the ramping of the retardation voltage causes a decrease of countrate, depending on the voltage setting it blocks more or less of the protons - up to a complete blocking at 780 V. The retardation voltage is then ramped down at $t \sim 70$ s and the shutter closed at $t \sim 105$ s. Infig. 2.13 a) the drop of the countrate, due to the ramping of the retardation voltage can be seen, the amount of decrease naturally depends on the strength of the retardation voltage. On the other hand an increase of countrate, due to background from Penning-like traps can be seen, when the retardation voltage is on (40 s $\lesssim t \lesssim 70$ s). Unfortunately, this increase from background was not very predictable and somehow erratic. The background from the traps did depend in the retardation voltage, higher voltages showed in general higher background levels, but not necessarily. In fig. 2.13 a) one sees, that e.g. the measurement at 200 V shows a stronger increase, than the 400 V measurement. The strongest increase in this measurement block occurred at 600 V and not at the expected 780 V. Even worse, the increase for one given retardation voltage was not always the same, when measured several times. In fig. 2.13 b) the countrate evolution for a retardation voltage of 400 V measured several times is shown. The increase of countrate when the retardation voltage was up (40 s $\lesssim t \lesssim 70$ s), was sometimes relatively low (4th block down), or sometimes very strong (3th block up). This meant, that these individual measurements could not be combined to increase the statistical sensitivity. They would have had to be corrected individually with a relatively large uncertainty of the correction. To large to reach the a statistical uncertainty
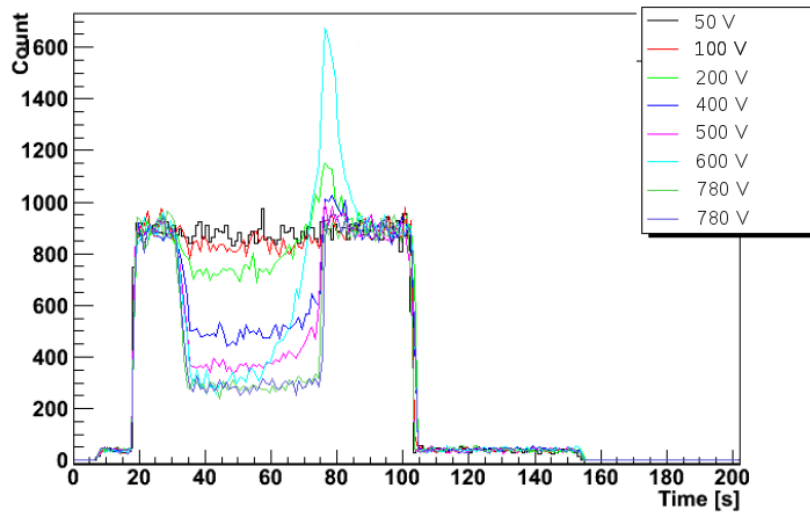
(a)
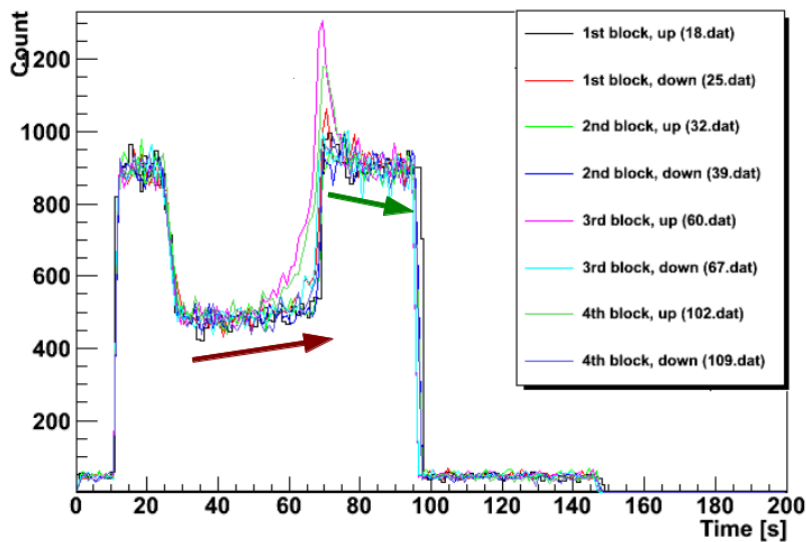
(b)

Figure 2.13.: Background situation in 2011. Shown are two graphs from the beam-time in 2011, visualising the background problematic from Penning-like discharges. Here the neutron shutter was opened at $t \sim 18\,s$, causing a strong increase of the countrate. At $t \sim 30\,s$ the retardation voltage was ramped up, causing a decrease of countrate. The retardation voltage was ramped down at $t \sim 70\,s$ and the shutter closed at $t \sim 105\,s$.

(a) Shown is one measurement block with different retardation voltages. After the drop of countrate due to the ramp up of the retardation voltage an increase of the countrate, due to background from Penning-like traps is observed. This increase is in general for higher retardation voltages stronger, but not necessarily. The highest background was observed during this measurement block for 600 V and 200 V.

(b) Shown is the countrate for $U_{ret} = 400V$ during several measurement blocks. For all measurements an increase, due to background is observed. Unfortunately, this increase differs for the individual measurements, making a common correction impossible.

low enough for a 1 % measurement. Therefore, the focus after 2011 was on getting rid of these discharges from Penning-like traps. For more details of the beam-time 2011 and the problems that occurred in there, the reader is referred to [Pau11]. The problematic of these discharges could be solved during offline tests in 2012, where the system has been improved and tested without a neutron beam. For details on these offline tests, see [Mil12, Mai14] Within this work only the improvements of the system to overcome these discharges from Penning-like traps are described.

Experimental Ways to Reduce the Background

Background from Penning-like traps can be reduced by either reducing the amount of residual gas, which decreases the probability of ionisation. Or by reducing the field emission, initially causing the ionisation of residual gas. Or by reducing the number of ionised particles stored in a trap, e.g. by applying an ExB drift in or close to the trap. All three methods have been used in the past for *a*SPECT and will be described in more detail. Reducing the amount of residual gas means improving the vacuum, which is on first sight an easy task, but gets worse with the details. First, the outgasing of all parts in the vacuum system has been reduced by either improved cleaning procedures or new materials. The electrodes have been cleaned in a warm ultrasonic bath in three steps, first with an industrial soap (Henkel P3-almeco 36), then in 2-Propanol (a.k.a. Isopropanol) and last in distilled water. All other parts small enough, like screws, vacuum feed-throughs, etc. have been cleaned the same way. All other parts to big to fit in the bath have been thoroughly wiped with 2-Propanol and distilled water using clean-room-wipes. Additionally the MACOR parts have been replaced by PEEK, as it is less fragile with similar outgasing rates. The boron glass of the internal collimation, see [Bor10], has been replaced by plates made of titanium diboride and boron nitride (ESK DiMet Type 4) cleaned with acetone and distilled water. Second, the pumping power of the vacuum pumps has been increased by cascading the Turbo Molecular Pump (TMP), an additional external getter pump (SAES Getters C 500-MK5 ST707), an additional TMP at the detector and new internal getter pumps (SAES Getters CapaciTorr D400-2) have been installed. For details of the vacuum system and pumping procedure see [Bor10]. Further, the field emissions in *a*SPECT have been reduced. To do so, the detector electrode has been mechanically polished and electro-polished afterwards, to reduce the surface roughness and therefore the field emission from it. The other electrodes have been smoothed by polishing all rough edges and recoated, as the old gold coating already diffused into the copper.

As a third possibility to reduce background from Penning-like traps the electrode E15, located directly above the AP electrode, has been divided to act as an additional ExB drift electrode. In fig. 2.14 this 'new' electrode is shown. It introduces an additional ExB drift field close to the particle trap in the AP region. To do so, one side of the electrode has been set to a voltage of 68 % of the AP voltage. Lowering the voltage on one side of the E15 has an significant influence on the field leakage into the AP. It lowers the actual AP, meaning the plane of the highest electric potential, by 3.3 cm [Hor15]. This means the magnetic AP has to be lower as well, using the external correction coils [Gua11], but is in general no problem. But on the other hand, the additional ExB drift has an significant effect on the background. The retardation voltage dependence of the background has been reduced from $0.5\,s^{-1}$ to $0.15\,s^{-1}$ [Mai14].
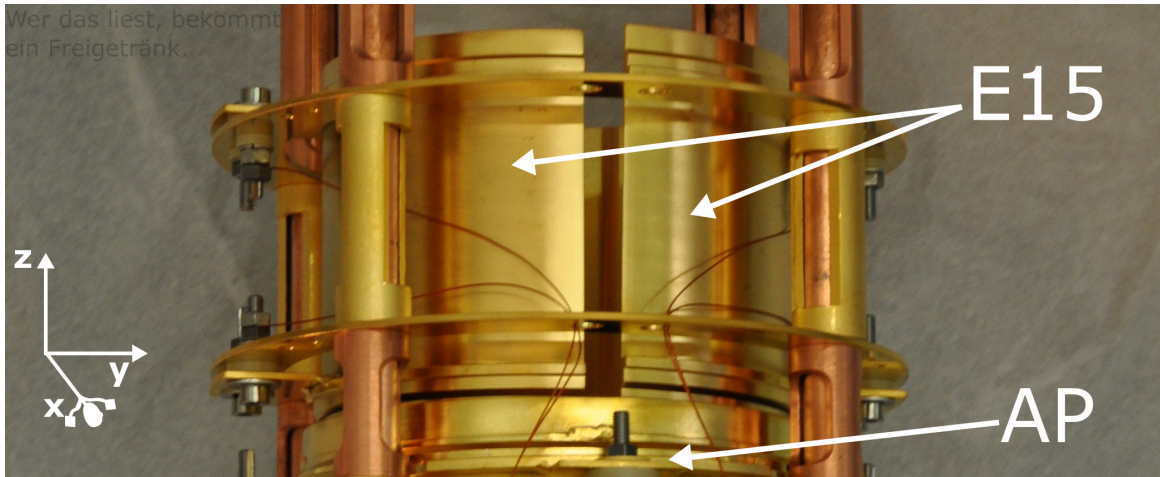
Figure 2.14.: E15 as dipole electrode, used as additional ExB drift electrode to reduce the retardation voltage dependent background of the Penning-like trap in the AP. For details, see text.

Techniques to Determine the Remaining Background

Despite all efforts to reduce the background, there will always be some background in the proton signal. In this paragraph techniques to determine this remaining background are given. In fig. 2.15 a schematic of the composition of the signal of aSPECT is drawn. Shown is the countrate vs. the time for a measurement cycle of aSPECT. Such a cycle is done for a given retardation voltage and then restarted for another setting of the retardation voltage. The cycle starts with the activation of the DAQ at t_0, at $t_{APon} \approx 20\,\text{s}$ the AP electrode is ramped to the retardation voltage used for this cycle, at $t_{open} \approx 40\,\text{s}$ the neutron shutter is opened for 50 s to 200 s, until it is closed at t_{close}. 30 s after closing the shutter the AP electrode is ramped to 0 V at $t_{AP,off}$. The cycle is finished about 50 s later by stopping the DAQ. The retardation voltages used during the beam-time 2013 are tabulated in table 2.2 together with typical countrates. The individual cycles for one retardation voltage are then combined to measurement blocks, where each retardation voltage is used at least once. The sequence of the the single cycles is interchanged to avoid any systematic effects on the background by the sequence itself. A typical example of such measurement blocks is shown in fig. 2.16. Drawn are four measurement blocks, the first two blocks are in ascending (descending) order of the retardation voltage, the last two ones are in interchanging order of the retardation voltage.

The general background level is determined with the 780 V measurements. This voltage is above the endpoint of the proton recoil spectrum and therefore only background is detected. The main component of this background in the proton region are low energetic electrons from the decay, labelled constant background in fig. 2.15. But there is also a significant amount of ions from residual gas [Bor10, Mai14], labelled non-constant background in fig. 2.15. This non-constant background increases with time until a steady state is reached. Unfortunately, this increase can be only seen at 780 V, for lower voltages the increase is to small in relation to the proton signal [Mai14]. Fortunately, the retardation voltage dependent background can be determined indirectly. After closing the neutron shutter the countrate is higher than before opening the neutron shutter. This higher countrate is due to the particle
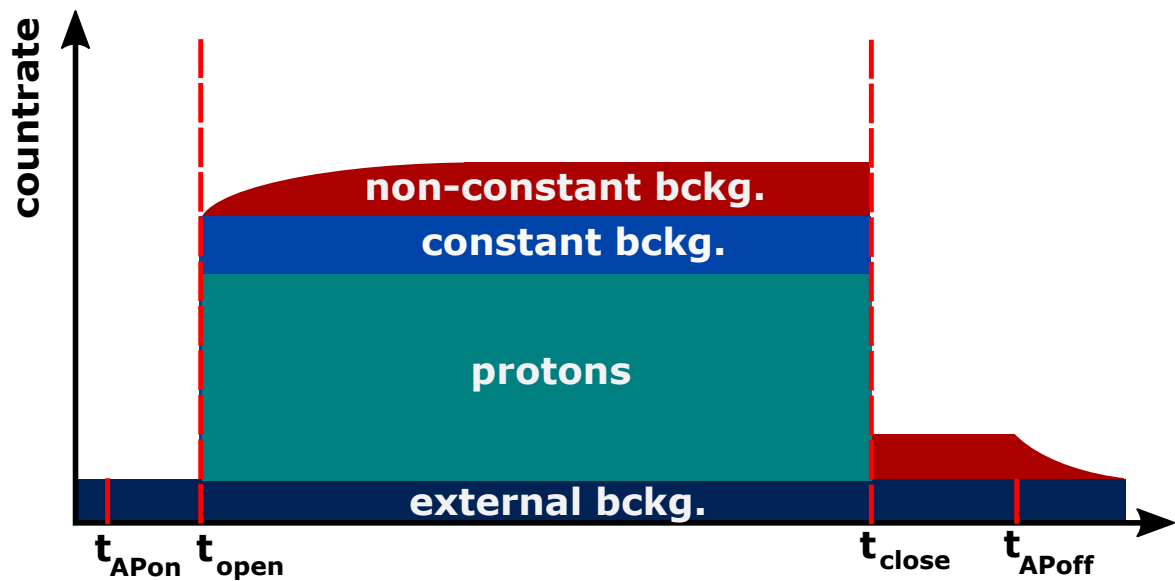
Figure 2.15.: Single DAQ cycle of aSPECT. Shown is the countrate versus the time for a measurement cycle of aSPECT for one given retardation voltage. The cycle starts with the activation of the DAQ at t_0, at $t_{APon} \approx 20\,$s the AP electrode is ramped to the retardation voltage used during this cycle, at $t_{open} \approx 40\,$s the neutron shutter is opened for 50 s to 200 s, until it is closed at t_{close}. About 30 s later the AP electrode is ramped to 0 V at $t_{AP,off}$. The cycle is finished about 50 s later by stopping the DAQ and then repeated for another retardation voltage.

Table 2.2.: Retardation voltages used during the beam-time 2013 including the countrates at the specific voltage. Data for channel 20 from the measurements config 1, see table 3.1.

AP voltage in V	countrate in s^{-1}
50	448.72(21)
100	418.42(17)
250	291.55(14)
350	196.36(12)
400	149.33(10)
450	105.37(08)
500	66.51(06)
550	35.93(04)
600	17.68(02)
780	8.01(12)
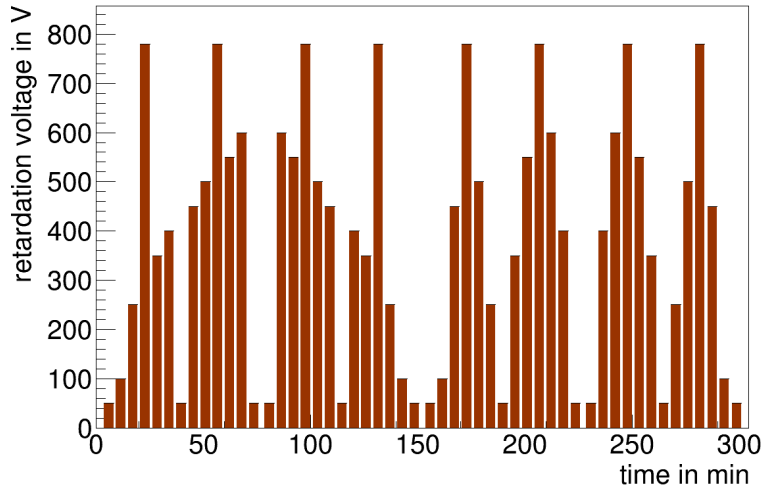
Figure 2.16.: Typical sequence of retardation voltages used during the beam-time 2013. Shown are four measurement blocks from the measurement 20130628. The first two blocks are in ascending (descending) order of the retardation voltage, the last two ones are in interchanging order of the retardation voltage. Interchanging the retardation voltage has been done, to avoid any systematic increase (decrease) of the background level, depending on the sequence of retardation voltages and hence creating a retardation voltage dependent background.

trap in the AP electrode. This can be seen by the decrease in countrate while ramping down the AP electrode to 0 V (t_{APoff}). An investigation of the background in 2013, including several models for the retardation voltage dependency, has been done by [Mai14] and also been performed in section 3.2.2. An investigation of the background with the neutron shutter open has been done by [Sti15] with focus on identifying background by the shape of the detector pulse. In general the pulse-shape of a particle hitting a silicon detector is dependent on its specific charge. That a particle identification is possible has been shown by various experiments, eg. [PBH+94]. Unfortunately, with the current DAQ system of *a*SPECT, it is not possible to determine background by its pulse-shape. The shape of a single pulse is mainly determined by the pulse shaper of the DAQ, therefore now differences in the pulse-shape for different particles can be seen. An additional, 'new' DAQ system has been tested during the beam-time 2013 [Vir13], which saves the unshaped signal from the detector. This new DAQ might be able to distinguish between pulse shapes of protons and heavier ions, but further investigations are needed, to prove that.

2.2.4. Detector and Electronic Effects

In this section a short description of the detector and the DAQ used in *a*SPECT is given, as well as systematic effects from it. *a*SPECT uses a Silicon Drift Detector (SDD) (pnSensor UM-141101) to detect the protons from the decay, see fig. 2.17. This semi-conductor detector has three active areas, each of 1 cm^2 and a thin dead-layer $O(< 100\,\text{nm})$. This thin deadlayer allows a low acceleration voltage for the protons of only $U_{det} = -15\,\text{kV}$ to overcome the
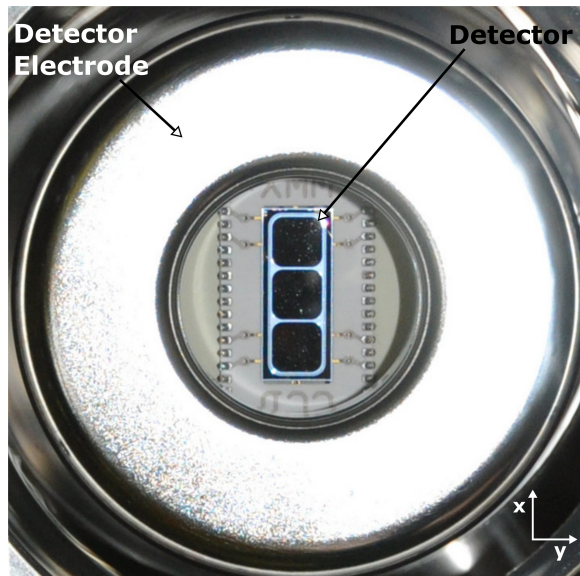
Figure 2.17.: Photograph of the *a*SPECT detector housed inside the detector electrode. *a*SPECT uses a Silicon Drift Detector (SDD) with three pads. The detector electrode is set to $-15\,\text{kV}$ to accelerate the protons, so they can overcome the deadlayer of the detector. For details, see text

dead-layer and be detected. The signal from the detector is first amplified by a preamplifier, then shaped by a pulse shaper[1] and finally digitised by a sampling Analog-to-Digital-Converter (ADC) [MGK$^+$06]. The digitized pulses are stored on a PC for further analysis. The original system used in the beam-time 2008 was designed to achieve a high separation of the proton signal from electronic noise. Unfortunately, the used amplifications in the preamplifier and shaper were too high, causing a saturation of the devices and therefore a signal cut-off. This saturation was the mayor uncertainty of 2008, as it introduced an uncertainty of $\delta a/a \approx 20\,\%$ [Kon11]. A detailed description of the DAQ, the saturation and its effect on the data analysis can be found in [Sim10, SGB$^+$09]; within this thesis only a short description of it is given to understand the problematic and its solution for the beam-time 2011 and later ones.

In fig. 2.18 a schematic of the signal is shown in the different stages of the DAQ. The first stage is the detector itself (top). Shown are two exemplary signals, in both cases the first signal increase is due to an electron, the second, due to a proton. In a) the electron has a very high energy, in b) the electron energy is lower. These signals are amplified by the preamplifier (middle). In red (solid line) is shown the signal for the 2008 set-up. The ideal signal without saturation is drawn as dotted line. Due to a saturation of the electronics, high energetic signals were cut off in 2008. In a) the energy of the electron is so high, that the proton would not be detected at all, due to the saturation. In b) a part of the proton signal gets cut off, as it sits already on the slope of the electron signal. This first saturation of the preamplifier could be solved by reducing the amplification of the preamplifier by a factor of 2, blue (dash dotted) line. In the next step the signal from the preamplifier gets shaped by the shaper. In the shaper also a saturation could appear, cutting off high

---

[1]At *a*SPECT the term shaper is used for a spectroscopy amplifier.
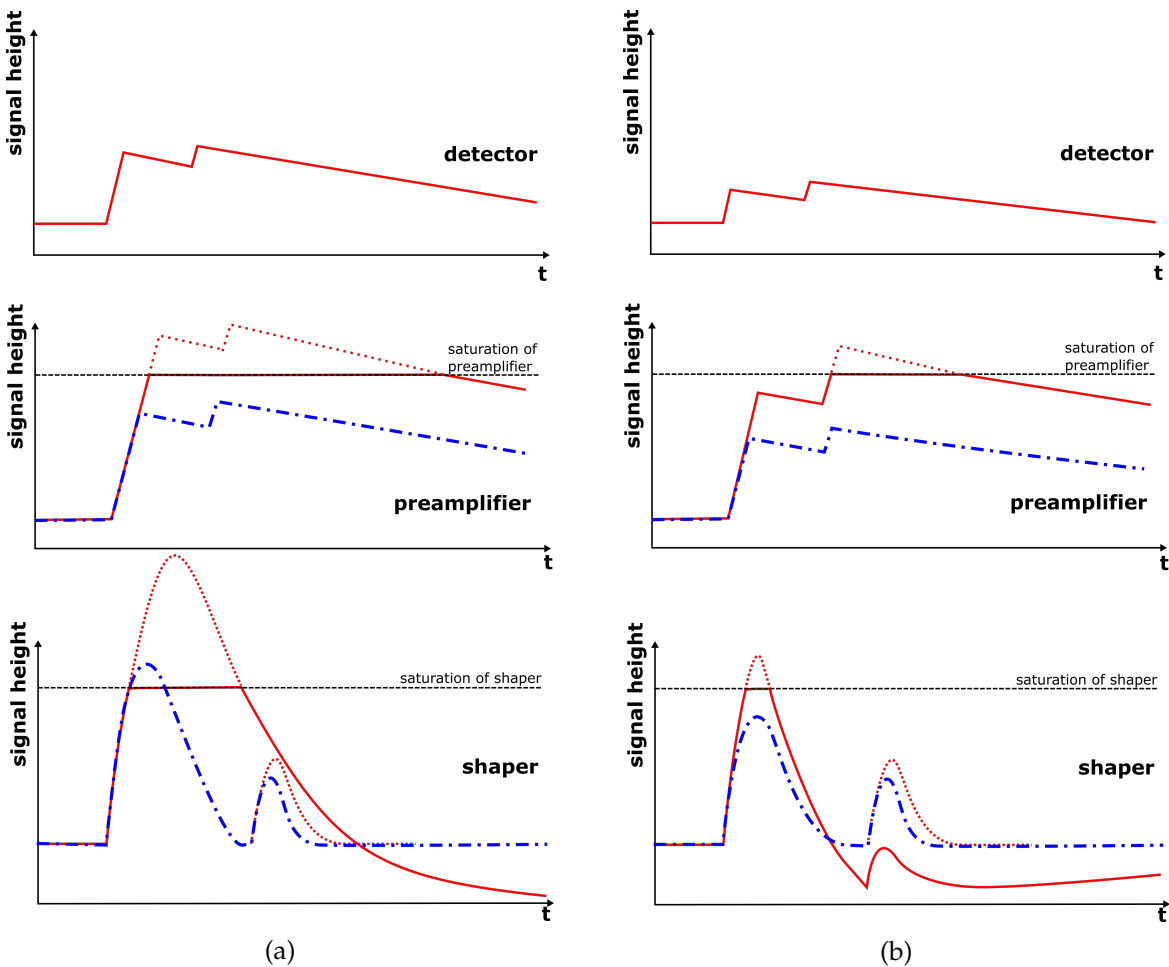
Figure 2.18.: Signal processing of the *a*SPECT DAQ system from detector, to preamplifier and shaper[1]. In red (solid) line is drawn the signal with saturation, as occurred in 2008, also the ideal case is drawn in red (dotted) line. The new system with reduced amplification in the preamplifier and logarithmic amplification in the shaper is drawn in blue (dash dotted) line.

In (a) is shown a high energetic electron followed by a proton. The signal of the proton is lost completely, due to saturation in the preamplifier. In (b) is drawn the signal of an electron with lower energy followed by a proton. Here the proton is detected, but with a reduced pulse-height. These two effects caused a systematic effect for *a*SPECT in 2008 in the order of $\delta a/a \approx 20\,\%$. This uncertainty is due to the fact, that high energetic protons arrive faster (in shorter times) to the correlated electron. This means high energetic protons were lost more likely, than low energetic ones introducing an energy dependent effect.

energetic signals (first peak). In a) the pulse-height of the electron would be reduced, the proton would not be detected. In b) the electron pulse-height would also be reduced and the proton would be detected. But the signal after high energetic particles went into an undershoot, causing any particle detected on this undershoot to have a reduced pulse-height. So in b) the proton would be detected, but with reduced pulse-height. For *a*SPECT these two effects caused a problem, as the probability for high energetic protons to arrive faster (within shorter times to the correlated electron from the same decay) at the detector is higher, than for low energetic protons. Hence, high energetic protons have more likely a reduced pulse-height or are lost at all, resulting in an energy depending effect in the order of $\delta a / \approx 20\%$. This effect due to the saturation of the DAQ was solved by reducing the amplification of the shaper and very elegantly by changing the linear amplification of the shaper to a logarithmic one. The logarithmic amplification enhances low energetic signals still enough, to have a good separation between electronic noise and proton signal. But high energetic signals, like electrons, are only slightly more amplified, to avoid any saturation. The signal for this logarithmic shaper is drawn in blue (dash dotted) line. These signals or pulses are then digitised by the ADC and their pulse-heights can then be drawn in a pulse-height spectrum fig. 2.12. Here the countrate per second and ADC channel is drawn. Shown is an exemplary pulse-height spectrum of the central detector pad for a retardation voltage of 50 V. Three regions can be identified, electronic noise from 0 to ca. 25 ADC channels, the proton region from ca. 25 to ca. 110 ADC channels and the electron region with pulse-heights above ca. 110 ADC channels. The proton countrate is determined by integrating over all events detected in the proton region. This integration is done for all retardation voltages used, providing a countrate for each retardation voltage (table 2.2), resulting in an integral spectrum fig. 3.8. As one can see the exact definition of the proton region, meaning the integration limits, have an influence on the proton count-rate. A strong shift in *a* of $\Delta a/a = 9.6\%$ for changing the lower integration limit in 2008 was a first hint at the saturation problem. In 2013 this shift could be lowered to $\Delta a/a \lesssim 0.8\%$ for both, the upper and lower integration limit. For details, of the limits used in 2013 and their uncertainty on *a*, see section 3.2.

The DAQ system has been tested in detail after the beam-time 2013 by [Ros15]. Roß used an electronic pulser, which is able to produce pulses similar to the ones from the SDD. This pulser emulates correlated events, by producing pulse-pairs with a variable pulse-height and time delay between the pulses. This allows to test the DAQ with high energetic, electron-like pulses followed by low energetic, proton-like pulse with a variable time delay between 2 µs to 20 µs. The typical time-delay between and electron and an proton from one decay is $O(6\,\mu s)$. No saturation or loss of events has been observed in the DAQ used 2013. Further, a ^{133}Ba source has been used to calibrate the system in terms of energy, see fig. 2.19. Unfortunately, for these calibration a different ADC_{test} had to be used, so the calibration curve

$$chADC_{test}^{20} = -708.5(10) + 1108.7(3) \cdot \ln\left(\frac{E}{keV}\right) \tag{2.9}$$

had to be converted to calibrate the one $ADC_{beam-time}$ from 2013. This has been done by using a ^{133}Ba spectrum taken during the beam-time [Mai14]. A fit through the 17.5 keV, 31.5 keV and 80.89 keV peaks has been used to interpolate between the ADC_{test}t and $ADC_{beam-time}$. The conversion is given by

$$chADC_{beam-time}^{20} = 8.54(11) \cdot 10^{-2} - 66.3(34) \cdot chADC_{test}^{20}. \tag{2.10}$$

With this calibration the ADC channels in fig. 2.12 have been converted to energy (upper x-axis). This calculation has been done for all three channels of *a*SPECT, see appendix A. For more details on the measurements with the pulser and the energy calibration, the reader is referred to [Ros15].

Further, a second DAQ system has been tested during the beam-time 2013. This new DAQ digitises the signal from the preamplifier directly and performs a software shaping of the signal. This software shaping provides more flexibility in the shaping and obviously avoids any saturation problematic in the shaper. Further, it opens the possibility to investigate single pulses in more detail, for a possible background identification. For more details on this new DAQ the reader is referred to [Vir13].

With the saturation problematic solved, only minor systematic effects from the detector and DAQ have to be considered. One of these effects is the number of backscattered protons in the detector and the energy loss of protons in the dead layer of the detector, see section 3.3.4. The dead layer can be determined using the energy calibration. From fig. 2.12 one can determine the position of the proton peak at around 8.8 keV, knowing the protons are accelerated by $U_{det} = -15$ kV, this corresponds to an average proton energy of 15.4 keV at the detector. Hence, the protons lose roughly 6.6 keV in the dead layer. With this energy loss the dead layer can be calculated to $s_{deadlayer} = 90(10)$ nm with a pstar simulation [pst]. Another systematic is the dead time of the whole DAQ system. During the beam-time 2013 an event window of 4 µs has been used, plus an additional 0.2 µs due to the nature of the trigger of the ADC [Sim10]. This gives a total dead time of $T_{dead} = 4.2$ µs. With this "non-extendable" dead time [Leo94] the measured count rate in the proton region C_{meas} is corrected using the following formula

$$C_{corr} = \frac{C_{meas}}{1 - C_{total} \cdot T_{dead}},$$
(2.11)

where C_{total} is the total count rate detected.

2.2.5. Adiabatic Motion of Protons

Calculations by [GBB$^+$05] showed that the adiabatic conditions eq. (2.2) are fulfilled sufficiently by *a*SPECT. But there is always room for improvement, calculations by [Kon11] showed a further possibility to improve the adiabticity by separating the E1 electrode into two parts E1 and E1b, see section 2.2.1. Actually, it was already made of a cylindric electrode, combined with a copper wire grid at the bottom. This grid has been separated from the cylinder, so it could be set to a slightly higher potential, see table 2.1. This slightly higher potential causes a more adiabatic reflection of protons in the electrostatic-mirror. As already discussed in section 2.2.1 RF noise of $O(100$ mV$)$ has been observed on the electrodes of *a*SPECT. This fluctuation of the potential in the electrostatic mirror and the AP electrode could in principle cause a 'heat-up' of the protons trapped between these two potentials. This means, protons with an energy slightly below the retardation potential could gain some energy during their reflection in the electrostatic mirror and then pass the AP. The exact influence of this potential 'heating' has to be determined by a particle tracking simulation.

2.2.6. Doppler Effect

As already mentioned in section 2.1.1 *a*SPECT is installed at a cold neutron beam. Cold neutrons have an average kinetic energy of about $T_n \approx 5$ meV corresponding to a velocity
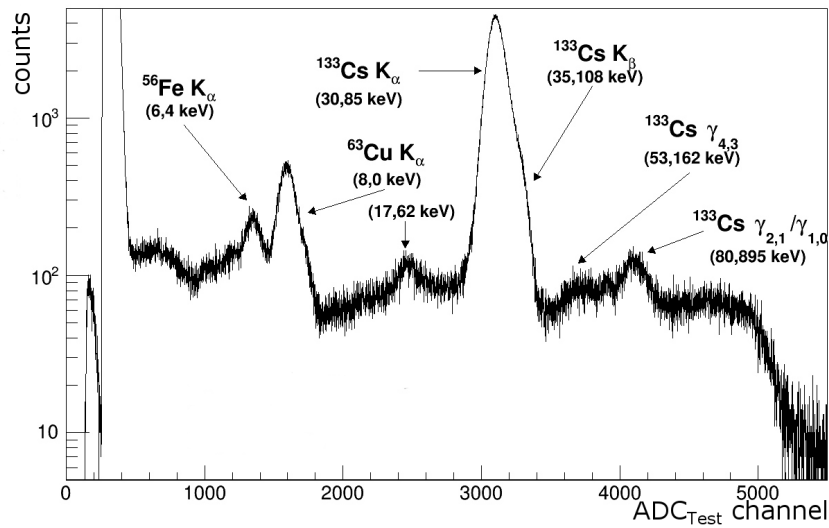
(a)
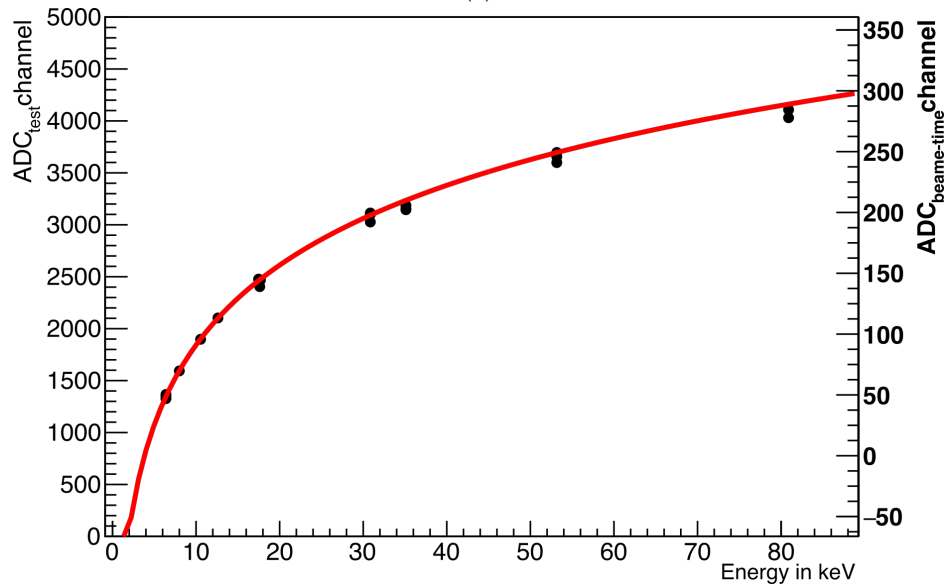
(b)

Figure 2.19.: ^{133}Ba spectrum and amplification curve of the *a*SPECT DAQ. In (a) is shown the ^{133}Ba spectrum taken with the test DAQ after the beam-time 2013 using a logarithmic amplification. This spectrum has been used to determine the amplification curve shown in (b). A similar spectrum taken with the DAQ used during the beam-time has been used to calculate the conversion from test DAQ and the one used during the beam-time. For details, see text. Pictures adapted from [Ros15].

$v_n \approx 1\,\mathrm{km s^{-1}}$. This motion of the neutrons relative to the lab system causes an energy shift of the observed energy, due to the Doppler effect. A proton with an energy $T_{CMS} = 400\,\mathrm{eV}$ in its Center of Mass System (CMS) would be shifted by $\delta T_{CMS} = 2\sqrt{T_n T_{CMS}} \approx 2.8\,\mathrm{eV}$, due to the Doppler effect. Compared to the required accuracy of $O(10\,\mathrm{meV})$ of the retardation voltage, this effect would be enormous and require a very precise measurement of the neutron velocity profile. Nevertheless, aSPECT uses an electro-static mirror electrode and has therefore a full 4π acceptance of the decay protons. Due to the 4π acceptance the Doppler shift cancel mostly out. The remaining effect of a Doppler shift due to neutron motion has been calculated for aSPECT to be $\delta T_{CMS}/T_{CMS} < 10^{-4}$ at $T_{CMS} = 500\,\mathrm{eV}$ [GBB$^+$05]. This Doppler broadening can be interpreted as uncertainty of the retardation voltage and therefore be translated into an uncertainty of the retardation voltage of $\delta_{Doppler} = 0.1\,\mathrm{mV}$.

2.3. Determination of *a* and its Uncertainty

In this section a general overview of the procedure to fit the proton recoil spectrum is given and how a is determined from this fit. Further, it is explained how the uncertainty of a is calculated using this fit. For details of the fit function and the uncertainty of a, due to the systematics covered within this work, see section 3.1.3.

2.3.1. The Fit Function and its Uncertainty

In section 2.2.4 has been described, how a pulse-height spectrum is measured for one retardation voltage. Integration over the proton region leads to one point in the integral proton recoil spectrum, cf. fig. 2.12. Repeating this for all voltages leads then to the complete integral proton spectrum, see table 2.2 and fig. 3.8. To determine a from this measured spectrum the theoretical spectrum is fitted to it. Therefore, the theoretical spectrum $\omega_{0C\alpha}(T_0)$ eq. (1.29) is convoluted with the Transmission Function $F_{tr}(T_0, U_{ret})$ of aSPECT eq. (2.6). The resulting fit function $f_{fit}(U_{ret})$ is then fitted to the measured spectrum with a as a free fit parameter. In this way, the shape of the measured spectrum determines the value of a, see fig. 2.3. The systematic effects of aSPECT like background or edge effect, can be included in the fit function as functional term $f_{sys}(U_{ret})$

$$f_{fit}(U_{ret}) = \{\omega_{0C\alpha}(T_0) * F_{tr}(T_0, U_{ret})\} + f_{sys1}(U_{ret}) + f_{sys2}(U_{ret}) + \ldots \tag{2.12}$$

Including all systematic effects directly into the fit function, instead of correcting the a value after the fit, has two major advantages. First, any correlation between systematic effects is directly given by the correlation matrix of the fit parameters. Second, the uncertainty δ_a of a can directly be determined using a χ^2 surface. In principle the measured spectrum could be corrected first by the systematic effects and then fitted by the theoretical integral spectrum spectrum $\omega_{0C\alpha}(T_0) * F_{tr}(T_0, U_{ret})$. This would lead to the same value of a, but to a wrong uncertainty δ_a of a, if one does not take great care. The reason for this is simple and explained at the example of the background in aSPECT. The background is measured at 780 V retardation voltage. One could now correct the proton spectrum of the background by subtracting the 780 V measurement from all other measured retardation voltages. But this would correlate all measurements/points in the proton spectrum and their uncertainties to this single measurement. As the fit function assumes uncorrelated data points, the correlated uncertainty of a from the fit would be wrong. Further, simply subtracting the 780 V measurement assumes a constant background for all voltages, i.e. no retardation

voltage dependency. This is in general not the case, so subtracting 780 V would over correct the measurements at lower voltages, assuming an increasing background for higher retardation voltages. Therefore, including the systematics directly into the fit function has the great advantage that this procedure will lead to the correct uncertainty δa.

For details which systematics are included in the fit function, as well as the the correlation of the fit parameters, see section 3.1.3. In the following the principle of a χ^2 fit and the determination of its uncertainty will be explained. The fitting routine varies the set of fit parameters $\boldsymbol{\theta}$ of the fit function f_{fit}, so that

$$\chi^2(\boldsymbol{\theta}) = \sum_{i=1}^{N} \frac{\left(y_i(x_i) - f_{fit}(x_i, \boldsymbol{\theta})\right)^2}{\delta_i} \tag{2.13}$$

is minimised, relative to given data points y_i with uncertainties of δ_i. The quality of the fit, meaning how good f_{fit} describes the measured data, is described the reduced χ^2_{red}

$$\chi^2_{red}(\boldsymbol{\theta}) = \frac{\chi^2(\boldsymbol{\theta})}{ndf}, \tag{2.14}$$

with ndf the number of degrees of freedom. If $\chi^2_{red} \simeq 1$ the fit function and the measured data agree perfectly, meaning the measured data fluctuate only statistically around the fit function. For $\chi^2_{red} \gg 1$ the measured data is not well described by the fit function and a different function should be used/searched for. In the case of *a*SPECT this would mean that there are unknown systematics in the data changing the shape of the spectrum.

The set of parameters $\hat{\boldsymbol{\theta}}$ for which χ^2 is minimal, are called estimate of the parameters of the fit function. The uncertainty of the single, estimated parameters $\hat{\theta}_i$ are determined by a so called χ^2 surface. To calculate a χ^2 surface, one particular parameter $\hat{\theta}_i$ is varied by $\Delta\theta_i$. For this new value $\hat{\theta}_i + \Delta\theta_i$ all other parameters are minimised again. The variation $\Delta\theta_i$ is increased, till

$$\chi^2(\boldsymbol{\theta}) = \chi^2(\hat{\boldsymbol{\theta}}) + \Delta\chi^2. \tag{2.15}$$

The shift $\Delta\chi^2$ is normally $\Delta\chi^2 = 1$, only if the probability is below 5 % it is rescaled to $\Delta\chi^2 = \sqrt{\chi^2_{red}}$. This probability is calculated by $1 - D_{ndf}\left(\chi^2_0\right)$ (eq. (2.24)). By varying all N parameters in this way, a N dimensional surface is gained. This surface is a N-dimensional ellipsoid for least square fits. If this surface deviates from an ellipsoid, the approach of fitting with a least square method (eq. (2.13)) is not valid and a maximum likelihood method has to be used [O+14], with a likelihood fit adapted to the specific problem. To check, how much the real χ^2 surface deviates from a perfect ellipsoid, a perfect ellipsoid $\chi^2_{ellipsoid}$ is fitted to the real χ^2_{real} surface. Then the mean squared error

$$\epsilon = \frac{1}{N} \sum_i^{N} (\chi^2_{real} - \chi^2_{ellipsoid})^2 \tag{2.16}$$

is calculated. A low $\epsilon < 0.0001$ corresponds to a good agreement between real and perfect χ^2 surface [Sch15]. In case of *a*SPECT a least square fit is valid and no likelihood has to be found, see section 3.3.3, paragraph "Validity of the Fit".
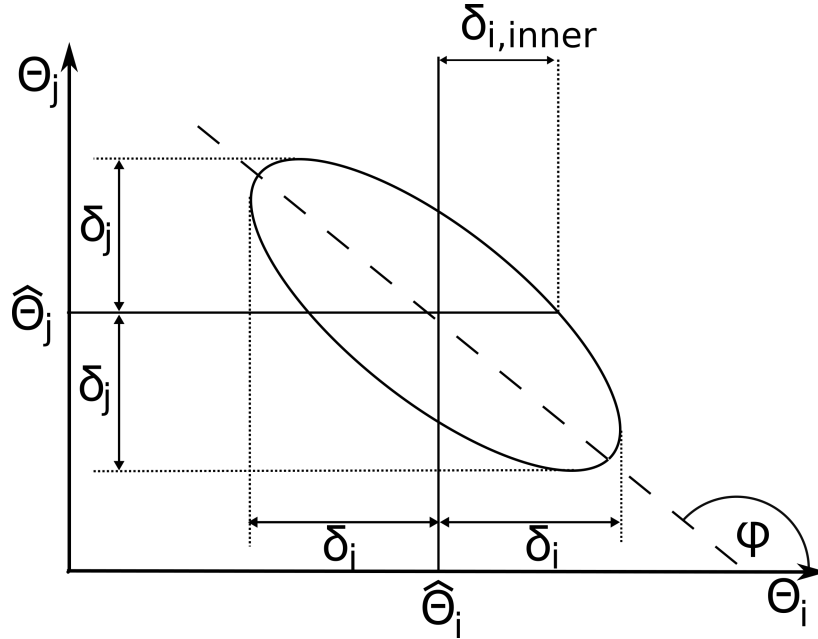
Figure 2.20.: Two-dimensional χ^2 surface for the parameters θ_i, θ_j. The projection of the surface onto the parameter axis corresponds to the correlated error δ_i of the parameter, whereas the cut with fixed parameter corresponds to the uncorrelated error $\delta_{i,inner}$. The correlation between the parameters can be calculated by eq. (2.17). In this example the correlation is negative. For more details how this surface is gained, see text.

For a valid χ^2 minimisation, this surface should be an ellipsoid, as shown here. To cross check, how well the real χ^2 surface is described by an ellipsoid, the mean square error ϵ, eq. (2.16), is calculated. A low ϵ shows a low deviation from an perfect ellipsoid.

In fig. 2.20 a 2-dimensional example of a χ^2 surface is shown. From this surface the individual uncertainties δ_i of the parameters $\hat{\theta}_i$ are determined via the projection of the surface onto the parameter axis θ_i. The uncertainties δ_i are the correlated uncertainties of the parameters, whereas the uncorrelated uncertainty $\delta_{i,inner}$ is the cut of the χ^2 surface for the estimated value of $\hat{\theta}_i$. This uncorrelated uncertainty corresponds to the statistical uncertainty of the measurement. For completely uncorrelated parameters $\hat{\theta}$, the two uncertainties are the same, leading to a non-tilted elliptical χ^2 surface. The correlation coefficient ρ_{ij} between the parameters $\theta_{i,j}$ can be calculated from the major axis of the ellipse by

$$\tan 2\varphi = \frac{2\rho_{ij}\delta_i\delta_j}{\delta_j^2 - \delta_i^2}. \tag{2.17}$$

The correlation coefficient is a dimensionless number with values between +1 and -1. For independent parameters the correlation is zero. Unfortunately, the converse statement is not necessarily true. Parameters depending on each other can have a zero correlation. For examples of this and further information of calculation of uncertainty and statistics, the reader is referred to [Jam06, O+14]. For details, which parameters/systematics have been
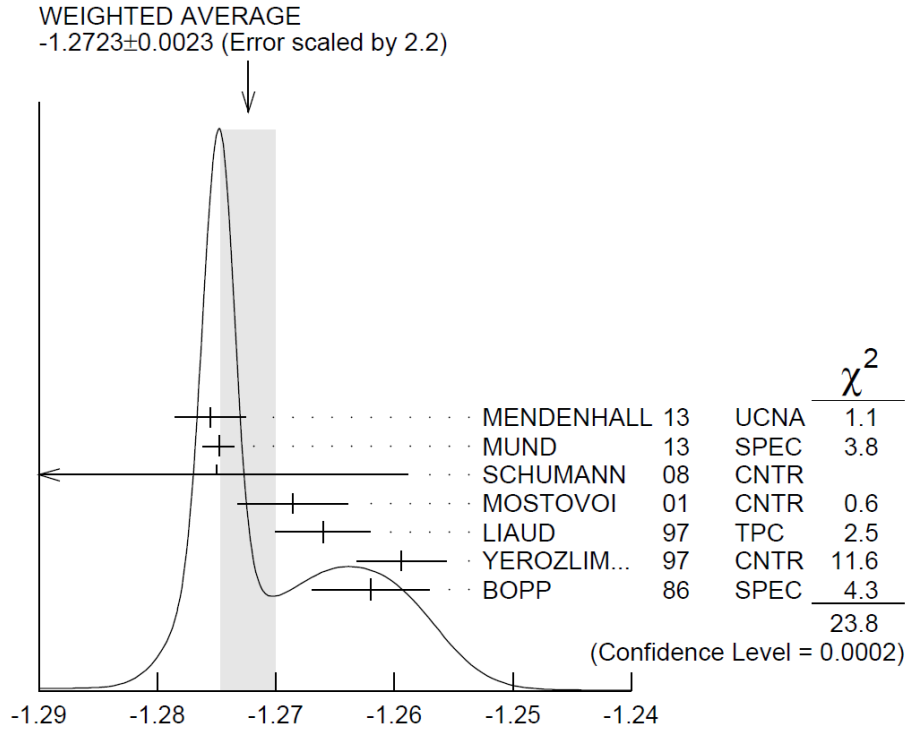
Figure 2.21.: Ideogram of the ratio of the weak coupling constants $\lambda \equiv \frac{g_A}{g_V}$ determined from observables in free neutron decay, taken from [O$^+$14]. On the x-axis is drawn λ, whereas on the y-axis the relative weight $\left(w_i = \frac{1}{\delta_i}\right)$ of the single measurements to the weighted average is drawn. This weighting is visualised by the sum of i Gauß functions, with $\sigma_i^{\text{Gauß}} \equiv \delta_i$ and the area of the Gauß function proportional to the inverse of the uncertainty of the measurement $1/\delta_i$. For details of the calculation of the mean and its uncertainty, see text.

included in the fit function in this work and the correlation between them, the reader is referred to section 3.1.3.

2.3.2. Ideogram

During the beam-time 2013 aSPECT has measured a in different/individual configurations with different experimental settings. This has been done to investigate different systematic effects of the experiment in detail. A way to visualise the results of the individual measurements a_i with δ_i is a so-called ideogram. An ideogram for the 2013 data, without correction of the experimentally enhanced effects shown in fig. 3.16. To understand such an ideogram its the principle will be explained in this section. In an ideogram the a_i are drawn on the x-axis with their uncertainties δ_i. To visualise the individual contribution of the a_i to the weighted mean, for each a_i is a Gauß function calculated. The mean of this Gauß function is a_i and $\sigma_i^{\text{Gauß}} = \delta_i$, whereas the area under the Gauß function is proportional to the inverse of the uncertainty $1/\delta_i$. These individual Gauß functions are then add up, allowing to see the individual weights of the measurements and potentially identify systematic shift of the individual measurements a_i. In fig. 2.21 an example of an ideogram is shown for the ratio of

the weak coupling constants λ (eq. (1.14)). The ideogram allows to easily see the distribution between the latest, most precise measurement from Mendenhall and Mund, as well as the older less precise ones. As these are independent measurements of different experiments the weighted mean can be calculated by

$$\mu_w \equiv \frac{1}{w} \sum_{i=1}^{N} w_i a_i, \tag{2.18}$$

where w_i is the inverse of the individual uncertainties

$$w_i = 1/\delta_i^2 \tag{2.19}$$

and overall weight

$$w = \sum_i w_i. \tag{2.20}$$

To calculate the uncertainty of this mean value the χ^2_{red} eq. (2.14) of the N measurements is calculated, with $ndf = N - 1$, the expectation value for Gaussian distributed data. Three cases are considered then, if the reduced χ^2_{red} is less or equal to 1, if it is larger than 1, but not much, or if it is much larger than 1. If it is smaller or equal to 1, the weighted mean and the uncertainty are calculated as given in eq. (2.18) and eq. (2.23). If χ^2_{red} is much larger than 1, the PDG either chooses to calculate no mean, or if they do calculate one, they make an educated guess on the uncertainty and quote the problems with the data. In the third case, if χ^2_{red} is slightly larger than 1, the uncertainties δ_i are scaled by a factor

$$S = \sqrt{\chi^2_{red}}. \tag{2.21}$$

The reason for this is quite simple, the large χ^2 is due to an underestimation of at least one δ_i. Not knowing which one, all of them are scaled by S, so that $\chi^2 = N - 1$. If the δ_i are widely varying, the PDG uses only values with a low δ_i. Their cut off for δ_i is arbitrarily chosen to

$$\delta_i \leq 3\sqrt{N} \cdot \delta_{\mu_w}, \tag{2.22}$$

with δ_{μ_w} the unscaled uncertainty

$$\delta_{\mu_w} = \frac{1}{\sqrt{w}}. \tag{2.23}$$

The reason for this is, that low precision values contribute only slightly to the mean value and its uncertainty, but on the other hand can have significant influence on the χ^2.

Unfortunately, this procedure can not be applied to the individual measurements done by the same experiment. As already said, calculating the weighted mean μ_w and its uncertainty δ_{μ_w} is only valid for independent measurements. This is clearly not the case for several measurements of one experiment. This can be easily seen in the limit of infinite measurements $N \to \infty$. Here, the overall weight eq. (2.20) would become infinite, hence the uncertainty of the weighted mean eq. (2.23) would become zero. But a zero-uncertainty can not be the case for one experiment, as the systematic uncertainties intrinsic to all measurements of the experiment can not decrease with the number of measurements. E.g. the uncertainty of the Transmission-Function of aSPECT is limited by the uncertainty of r_B and

U_{ret}, cf. section 2.2.1. These uncertainties are determined separately and are always a part of the uncertainty of a measurement with aSPECT, no matter how often one repeats the measurement. Therefore, in the final analysis the individual measurements of aSPECT will be fitted together in one multi-dimensional fit including all systematics and uncertainties at once, see eq. (2.12). In this way, the uncertainty of a is determined taking the systematics correctly into account. For details of this multi-dimensional fit, see section 3.1.3.

In both cases, dependent, or independent measurements a confidence level is given in the ideogram. The confidence level is calculated by the Cumulative Distribution Function (CDF) of the χ^2 distribution

$$D_{ndf}\left(\chi_0^2\right) = \int_{\chi_0^2}^{\infty} \frac{t^{\frac{ndf}{2}-1} \cdot e^{-\frac{t}{2}}}{\Gamma(ndf/2) \cdot 2^{\frac{ndf}{2}}} dt. \tag{2.24}$$

Here, ndf is the number of degrees of freedom and $\Gamma(x) = (x-1)!$, a gamma function. The CDF $D_{ndf}\left(\chi_0^2\right)$ evaluates at χ_0^2 is the probability, that a random distributed χ^2 will take a value $\chi^2 \geq \chi_0^2$. Or in other words, the probability measuring a value with higher χ^2, assuming normal/Gaussian distributed values. Probabilities below 0.05 are in general considered not to be in agreement with random distributed data, for probabilities below 0.01 the disagreement is considered to be highly significant.

For more information on confidence levels, calculation/propagation of uncertainty and statistical analysis, the reader is referred to any good statistics book, e.g. [Jam06], [Bra99]. For a full description of the data treatment of the PDG, see [O+14].

3. Analysis of the 2013 Beam-Time Data

In this chapter the analysis of the experimental data of the beam-time 2013 from the detector signal to a final *a* value is described, see section 3.1. Within this thesis a new data structure has been been invented, simplifying the data handling and able to handle huge amounts of data. This new data structure allows to determine the correct pulse-height of an event, section 3.1.1, as well as to estimate the amount of pile-up events, section 3.1.2. Further, the retardation voltage dependent background has been investigated and quantified, section 3.2.2. Finally, a comparison of the individual runs of *a*SPECT to test different systematics has been performed, see section 3.3. This includes a comparison without any correction of the experimentally enhanced systematics, section 3.3.1, as well as the implementation of first hand corrections of these systematics, section 3.3.2. Their influence and the current limit on the uncertainty of *a* are discussed in section 3.3.3. In section 3.3.4 are given the systematic effects not yet investigated, including the way to determine them. Finally, in section 3.4 some comments and suggestions for a future measurement/experiment are discussed.

3.1. Data Treatment

In fig. 2.18 an exemplary signal path from the detector to the shaper is shown. This signal is then digitized by an ADC. In the following, this system is called shaped DAQ (sDAQ). During the beam-time 2013 an additional DAQ system has been used, which digitizes the signal of the preamplifier and applies a software shaping, details see [Vir13]. In this thesis, this system without a hardware shaping is called unshaped DAQ (uDAQ). Both systems provide raw data files with a separate file for each DAQ cycle, cf. fig. 2.15. These raw files are stored on a PC in a folder named after the day, the measurement started, eg. 20130628 for the 28th of June in 2013. If several measurements have been started during one day, the files for each measurement are stored within a sub-folder named after the purpose of the measurement, eg. ContMeas for continuous measurement to gain statistics. The raw files are converted into a new, Root Object-Oriented Technology (ROOT) [BR97] based data structure, called "THE Investigation of *a*" (Thei*a*). This data structure has been written within this thesis, to be able to handle billion of single events one by

one within a reasonable time. The first conversion from raw to The*ia* file is similar to the systems used before, see [Hor11, Pet07, Sim10] for the sDAQ and [Vir13] for the uDAQ. These "Raw-Events" contain only informations about the event itself, like detector channel, timestamp, event type and pulse shape for each event separately. Informations about the spectrometer settings, like retardation voltage, magnetic field, etc. are not included yet. These settings of the spectrometer are controlled by the so-called slow control, consisting of several Laboratory Virtual Instrumentation Engineering Workbench (LabVIEW) programs [lab]. For details of this slow control system, see [Sim10]. Each of these slow control programs provides an ASCII file containing information about the condition of a sub-system. So all the information, about the Set and Actual values for the electrode voltages, the pressure, the condition of the neutron shutter etc. is stored in separate places. On the one hand such a system is very flexible, as each sub-system can be changed individually without influencing the other systems, on the other hand it makes an analysis of the gained data extremely complicated. To overcome this shortness The*ia* uses these various log-files, determines the time difference between the various PC systems the data is stored on and provides each single event with information about the spectrometer settings. These events including slow control data are called "Low-Level events" containing information like Set and Actual value for the retardation voltage, same for the other electrodes, pressure, Set and Actual value of the current in the magnet system, neutron shutter status and so on. Low-Level events are for both systems the same, meaning, analyses using Low-Level events do not have to know, which system has been used. The user can make usage of it, as all information stored in Raw-Events, are also stored in Low-Level events. Further, first basic analysis steps are already included in Low-Level events, like the determination of the baseline and the pulse-height. In section 3.1.1 this pulse height determination and its short comings are explained, as well as an improved method to determine the pulse-height using a spline interpolation. This spline interpolation is used further used for the determination of pile-up events, section 3.1.2. Events, which have been fitted with a spline and a corrected pulse-height are then called "High-Level Analysis" (HLA) events. These HLA events are used to create a pulse-height spectrum for each retardation voltage, including the dead time correction eq. (2.11). By integrating over the proton region of the pulse-height spectrum, see fig. 2.12, the integral proton spectrum is gained, see fig. 3.8. The integral proton spectrum is then fitted with the fit function f_{fit} eq. (2.12) to determine a from it. The systematic effects included in f_{fit} within this thesis are given in section 3.1.3.

3.1.1. Determination of the Correct Pulse-Height

In fig. 3.2 a histogram of a typical pulse for a proton-like event from the sDAQ is shown. The event has been digitized by the ADC with a time resolution of 50 ns per bin. The baseline of the event is defined as the average of the first 15 time bins (0.75 µs), here shown as red line. The pulse-height is defined as the difference between the maximum of the histogram and the baseline. The maximum of the histogram is determined by the ROOT function `TH1->GetBinContent(GetMaximumBin())`, which returns the maximum of the given histogram `TH1`. The pulse-height is shown as green (dashed) line in fig. 3.2. Also shown are the two trigger windows w1 and w2. An event is triggered of the difference in pulse-height between the two trigger windows is bigger than 6-8 ADC channels (depending on the channel and run setting) for three consecutive time bins. For a detailed description of the trigger algorithm, see [Sim10].
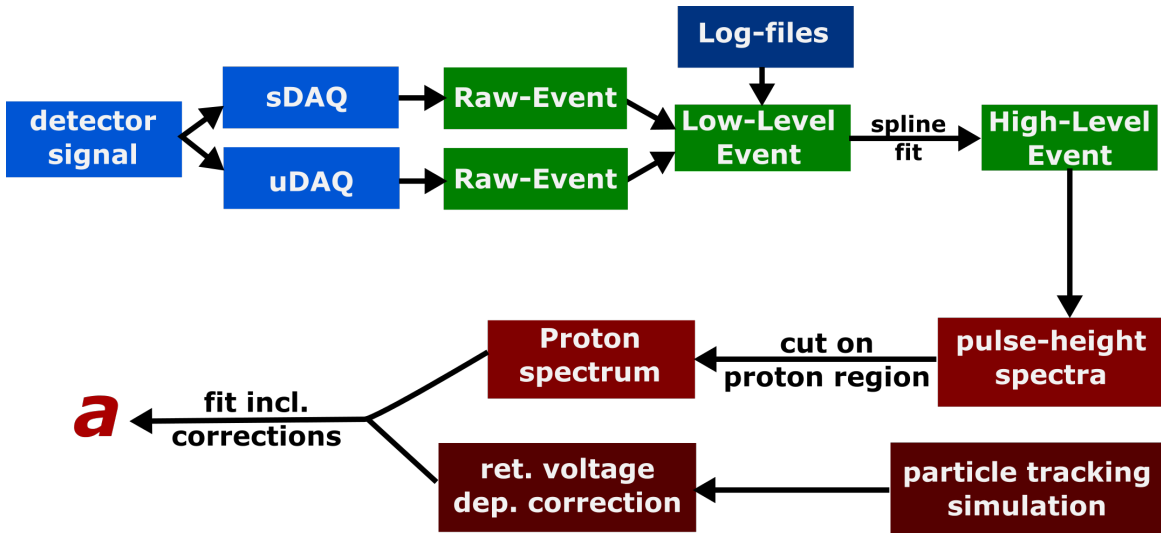
Figure 3.1.: Schematic of the *a*SPECT signal processing. In blue are shown the raw data, as from the DAQ, or the slow control log files. In green the new, ROOT based data structure Thei*a*. In red are shown the analysing steps using the data structure, as well as the particle tracking simulations used to determine the influence of systematic effect. The results of these two processes are then combined in a single fit to the proton spectrum, which results in a value for *a* and its uncertainty.
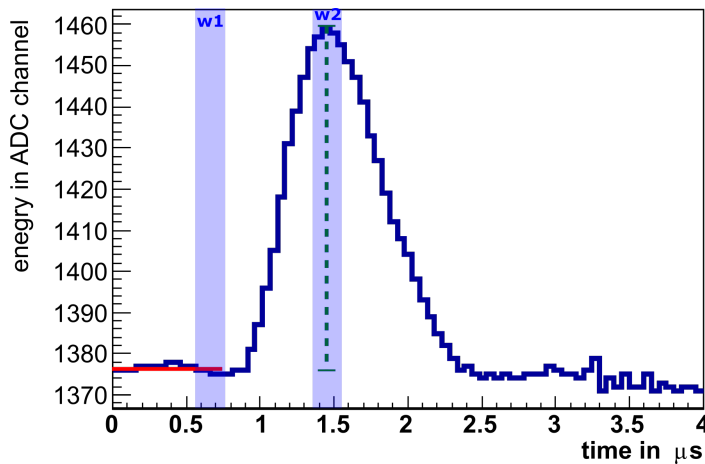
Figure 3.2.: Typical proton-like event, from run 20130628/ContMeas, file 1, event number 56334, channel 21. The baseline of the event is defined as the average of the first 15 time bins (0.75 µs), here shown as red line. The pulse-height of the event is defined as the difference between the maximum of the histogram and the baseline, here shown as green, dashed line. With a pulse-height of 82.6 ADCchannels this event lies perfectly in the proton region, cf. fig. 2.12. Also shown are the two trigger windows w1 and w2, a difference of 6-8 ADC channels pulse-height (depending on the channel and run settings) between them triggers an event.

This method of determining the pulse-height is simple and fast. But it has the major disadvantage, the maximum of the histogram might not be the maximum of the pulse been triggered on. Examples for such a misinterpretation are shown in fig. 3.3. Shown is a spiky noise event (3.3a), a high energetic electron-like event in the same event window as a proton-like event, on which has been triggered on (3.3b). Further, a proton-like event, shortly after a noise event, on which have been triggered (3.3c), and a pile-up event of two proton-like events (3.3d). With the simple determination of the pulse-height, the pulse-height of all these events would have been overestimated. Hence, they would have been wrongly sorted in the pulse-height spectrum, leading to a wrong proton rate in the proton region and therefore also in the recoil spectrum. In the following an algorithm to determine the correct pulse-height on which has been triggered is explained.

First, to get rid of the spikes on some events, the event is smoothed, using the build in smoothing of ROOT `TH1->Smooth()`. This smoothing acts as a software low-pass filter. It reduces the fluctuation of the signal, but does not change the overall shape of it. After smoothing a curve sketching is performed, to identify the pulse on which has been triggered. This curve sketching is done via a spline interpolation of the event. The spline interpolation fits the event with a polynomial between each point (in our case each bin of the histogram) under the condition, that at each point the function and its derivative are continuous. To fulfil these conditions, a polynomial of at least third order has to be fitted between the points. For this analysis a `TSpline3` from ROOT has been used. Using a spline interpolation for fitting the pulse shapes from *a*SPECT has two reasons. First, due to the logarithmic amplification of the shaper, the exact analytical function of pulse shape is not known. Second, a spline interpolation is much faster than a normal fit of a function. Therefore, saving a significant amount of computation time in the order of days to weeks for one run only[1]. Having a spline interpolation f_{spline} and therefore a functional description of the pulse shape of the event, a simple curve sketching can be done. The curve sketching identifies pulses in the event window via a change of the sign in the derivative of the spline f'_{spline}. Starting at the time $t_0 = 18$ time bins ($\hat{=} 0.9\,\mu s$), the algorithm searches for a negative derivative for three adjacent time bins to identify the position t_1 of the first peak, see eq. 3.1. Please be aware, the algorithm uses the time in bins, not μs. Having identified the first peak, the algorithm continues to search for a second one. Therefore, a second increase of the signal, or in other words a positive derivative is looked for, see eq. 3.2. t_2 is then the position of the dip between the two peaks. The position of the second peak t_3 is then identified by the same condition, as the first one, a falling signal a.k.a. a negative derivative of the spline eq. 3.3.

$$f'_{spline}(t_1) \wedge f'_{spline}(t_1 + 1) \wedge f'_{spline}(t_1 + 2) \overset{!}{<} 0 \qquad \text{for the first peak} \tag{3.1}$$

$$f'_{spline}(t_2) \wedge f'_{spline}(t_2 + 1) \wedge f'_{spline}(t_2 + 2) \overset{!}{>} 0 \qquad \text{for the dip between the peaks} \tag{3.2}$$

$$f'_{spline}(t_3) \wedge f'_{spline}(t_3 + 1) \wedge f'_{spline}(t_3 + 2) \overset{!}{<} 0 \qquad \text{for the second peak} \tag{3.3}$$

$$\text{with} \quad t_1 \;<\; t_2 < t_3$$

Actually, $t_{1,2,3}$ are the positions of the first bin, where the change of the sign occurs. Hence, the position of the peak (dip) is $t_{peak(dip)} = t_i - 1$, $i = 1, 2, 3$. Taking three adjacent points to
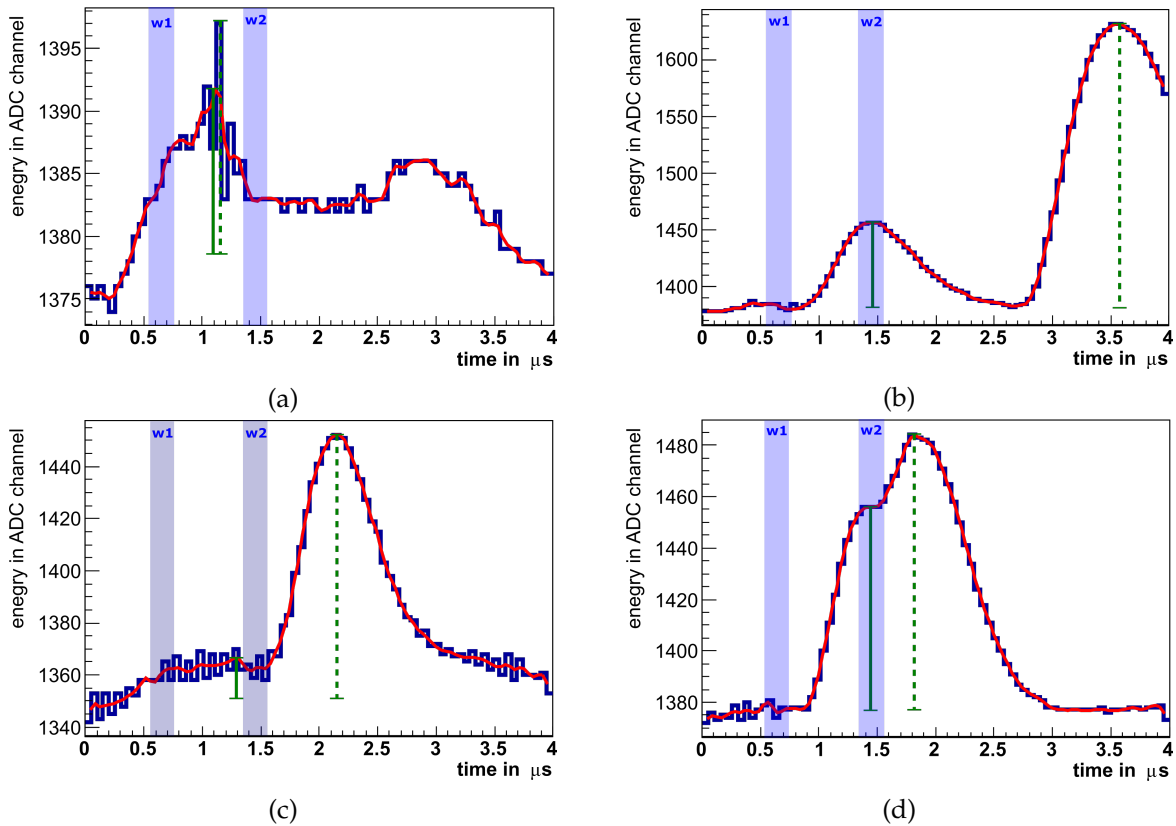
Figure 3.3.: Examples of corrected pulse-height events. Shown are four example events for the correction of the pulse-height via a spline interpolation. The pulse shape of the events is drawn in blue. The trigger windows w1 and w2 are also indicated. In red, smooth line is shown the spline interpolation of the event. In green, dashed line is drawn the original pulse-height, in green, solid line the corrected pulse-height. All events are from run 20130628/ContMeas, file 1 a,b,c and file 2 d. The first example (a) is a spiky noise event (ev. no. 13482, channel 20), (b) a high energetic electron-like event in the same event window as an proton-like event, on which has been triggered, (ev. no.26347, channel 20) . Further, a proton-like event (c), shortly after a noise event, on which have been triggered (ev. no. 91114, channel 20). Last, (d) a pile-up event of two proton-like events (ev. no. 350884, channel 20). For details of the spline interpolation and how these pulse-heights are corrected, see text.

fulfil the same condition ensures to find the peak and not a small fluctuation of the signal, still present after the smoothing. This algorithm is able to separate two peaks up to a time difference of $\Delta t \geq 0.4\,\mu\text{s}$ between the two peaks, see fig. 3.6. Peaks with a shorter time difference Δt can still be identified, if there is a distinguishable plateau between the two peaks, due to pile-up, see fig. 3.3d. To find the position of the plateau between the two peaks, the pulse is scanned backwards from $t_i = 80$ time bins ($\hat{=}\,4\,\mu\text{s}$) to $t_i = 18$ time bins ($\hat{=}\,0.9\,\mu\text{s}$). A plateau is defined by the following empirical condition

$$\left| f'_{spline}(t_i) - f'_{spline}(t_i - 0.5) \right| \overset{!}{<} 3 \quad \text{for three adjacent } t_i \tag{3.4}$$

$$\wedge \quad \left| f'_{spline}(t_i) \right| \overset{!}{<} 1 \quad \text{for three adjacent } t_i. \tag{3.5}$$

These conditions mean, the algorithm searches for the first position within the pulse with a flat, low increase of signal (eq. 3.5) and a low change of signal between consecutive bins (eq. 3.4). As position of the plateau is then taken $t_{plateau} = t_i + 1$. The corrected pulse-height ph_{spline} of the event is then the value of the spline at the position of the first peak(plateau)

$$ph_{spline} = f_{spline}(t_{peak(plateau)}). \tag{3.6}$$

Both, the position $t_{peak(plateau)}$ and the corresponding pulse-height are saved to "High-Level" events. This is the last step, done by the new data structure The*ia*, which can now be used to analyse the data.

First, the influence of the corrected pulse-height on the pulse-height spectrum is investigated. Therefore, all events with a difference $ph_{original} - ph_{spline} > 10$ ADC channels between the original pulse-height $ph_{original}$ and the corrected one ph_{spline} are searched for. This is a rather small fraction of events of about 0.38 %. These events are plotted in fig. 3.4a. Shown is the corrected pulse-height vs. the original one. All events are below a line $ph_{spline} = ph_{original} - 10$, which means the algorithm works well, it does not increase any pulse-height, but identifies to high ones. Further, two for *a*SPECT interesting regions can be seen, events with

$$ph_{orig} > 110 \quad \wedge \quad 30 < ph_{spline} < 110 \quad \text{(red, dotted square in fig. 3.4a)} \tag{3.7}$$

and events with

$$ph_{spline} < 30 \quad \wedge \quad 30 < ph_{orig} < 110 \quad \text{(green, solid square in fig. 3.4a).} \tag{3.8}$$

The first group, eq. 3.7, are originally electron-like events, that are corrected to proton-like events by the pulse-height correction. In fig. 3.4b the pulse-shapes of all these events is shown. To get such an graph, the baseline of each event is normalized to zero and then the single shapes are overlayed, where the color corresponds to the number of entries. These are events with a proton-like pulse-height in the region $1\,\mu\text{s}$ to $1.7\,\mu\text{s}$ followed by an electron-like pulse-height after about $1.7\,\mu\text{s}$. A single event of this kind is shown in fig. 3.3b. Hence, the spline interpolation corrects these events perfectly to the triggered proton-like event. This is important, as the dead time correction, cf. eq. (2.11), is only valid, if the event triggered on, is also the event considered in the analysis. The second group of events, eq. 3.8, are originally proton-like events, but are corrected to noise events. That this correction is valid, can be seen in fig. 3.4c. Here the main pulse starts to rise at around $1.5\,\mu\text{s}$, where as the trigger is at $1\,\mu\text{s}$. A closer look shows a slight increase of the pulse shape in the region

(a)

(b)

(c)
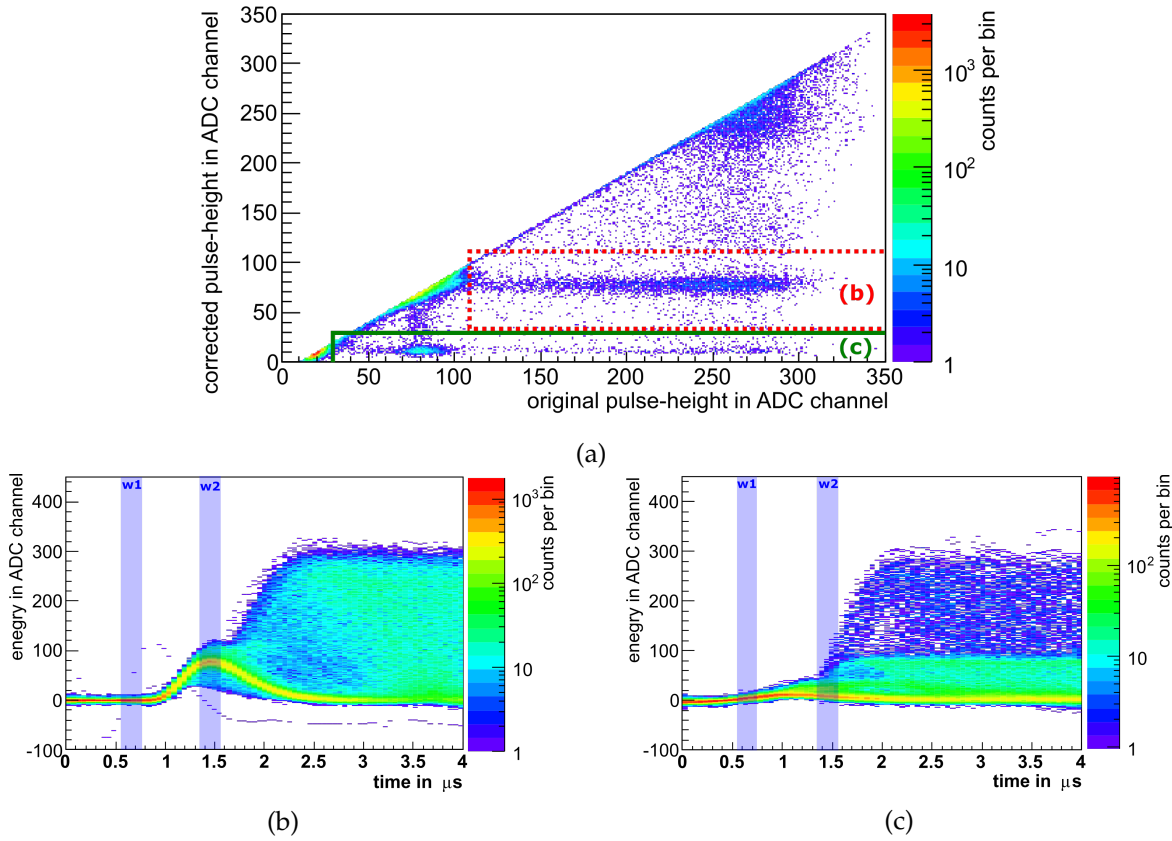
Figure 3.4.: Comparison of the corrected pulse-height vs. the original one. Shown are all events, where the corrected pulse-height differs at least 10 ADC channels from the original one. In (a) the corrected pulse-height from the spline interpolation is drawn vs. the original pulse-height. This corresponds to only 0.38 % of the complete data set, meaning most events of the data set are do not need to be corrected. From these corrected events, most are drawn along a line $ph_{spline} = ph_{original} - 10$, which means they differ not much more than 10 ADC channels from the original one. But there are two groups of events interesting for the determination of a, here marked as (b) and (c). The first group (b) are proton-like events, followed by an electron-like event. This is confirmed by a closer look at the pulse shape of these events, figure (b). The second group of events (c) are noise events, followed by an proton- or electron-like event, cf. figure (c). For details see text.
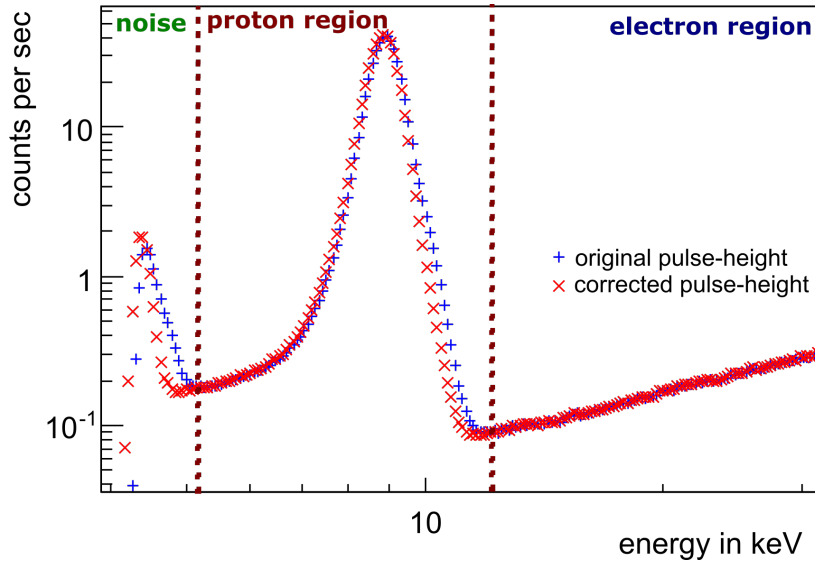
Figure 3.5.: Zoom on the proton region for two pulse-height spectra with and without corrected pulse-height of runs 20130628(29)(30)(0702) combined, channel 20. Statistical uncertainties are shown, but smaller than the marker size. The correction of the pulse-height with a spline interpolation reduces the electronic noise below ADC channel 25 and therefore improves the separation between noise and proton region. The correction also shifts the proton peak slightly to lower energies and reduces the right side of it. These are pile-up events, like fig. 3.3d. For more details and the shift in a due to the pulse-height correction, see text.

between $1\,\mu s$ to $1.5\,\mu s$. These are noise events like fig. 3.3c, which have been triggered, followed by a real event. So the spline interpolation corrects these events as well.

In fig. 3.5 a zoom into a pulse-height spectrum from run 20130628/ContMeas is shown for the original (blue crosses) and the corrected (red stars) pulse-height. The correction reduces significantly the electronic noise below ADC channel 25. This improves the separation between proton region and noise region and allows to make the cut on the proton region at lower energies. Therefore more low energetic protons can be included, without increasing the noise level. On the other hand, the correction of the pulse-height moves slightly the proton peak to lower energies, as the correction clears up pile-up events, like fig. 3.3d. This shift in the high energetic side of the proton peak has also be seen by [Sti15] and confirmed to be pile-up events. To investigate the influence of the pulse-height correction on a two proton spectra from the same dataset have been generated with and without the pulse-height correction and than fitted. The comparison of the a values from the spectra with and without pulse-height correction showed a shift in a by $\Delta a/a = -0.1\,\%$ for the corrected spectrum. This small shift is already significant, comparing to the desired precision of $\delta a/a \approx 1\,\%$. A shift to lower a values is expected, as two peaks in the event window are more likely for higher countrates (low retardation voltages), than for low countrates (high retardation voltages), cf. section 3.1.2. This means, for low retardation voltages more events are corrected from the electron region to the proton region, than for high retardation voltages. Hence, the countrate for low retardation voltages will increase more, than for higher ones, leading to a slightly more negative a. For a discussion of real pile-up events,

where the two peaks can not be distinguished any more and the correction of pulse-height fails, see the next section.

3.1.2. Pile-Up Events

In the previous section has been shown how a spline interpolation is used to determine the correct pulse-height of an event. This algorithm can also be used to determine the pulse-height of any second peak, that might occur within the event window of $4\,\mu s$. Further, using the spline interpolation the time $t_{1,3}$ (eqs. 3.1, 3.3) of the first and of the second peak can be determined and therefore the time difference between the two peaks $\Delta t = t_3 - t_1$. In fig. 3.3d an example of an event with two peaks is shown, where the time difference Δt is already so small, that the two peaks add up. Such events are called pile-up events. With a time difference of $\Delta t \approx 0.4\,\mu s$ this event is at the limit, what can be separated with the spline interpolation. Smaller time differences can not be separated any more, which means the pulse-height of the two peaks will add up and the pulse-height of the first peak can not be determined correctly. Such pile-up events have therefore a to high pulse-height and be interpreted wrongly as electron-like events in the pulse-height spectrum, cf. fig. 2.12. The simple solution to include these pile-up events would be to increase the upper integration limit of the proton region, so all events in the pulse-height spectrum are included. Unfortunately, increasing the integration limit also increases significantly the background level, which means statistical sensitivity would be lost. As this loss of statistical sensitivity would increase significantly the uncertainty of a, a correction for the loss of pile-up events, due to the upper integration limit has to be found. Such a correction can be determined using the spline interpolation to identify events with two peaks. In a first step all events with two clearly separated peaks and the first peak having a pulse-height in the proton region are identified. To this pulse-height of the first peak, the pulse-height of the second is added. If the sum of both pulse-heights is higher, than the upper integration limit, the event is selected. This selection ensures only events from the proton region are taken, where a pile-up would push the first peak out of the proton region. Pile-up events, which would be still within the proton region are not considered, as they are counted anyway. Using also the information of the time difference Δt between the two peaks, one can extrapolate this measured rate of double peak events to $\Delta t = 0$. This extrapolated rate corresponds to the missed pile-up rate, which needs to be corrected for. The complete procedure is explained in detail in the next paragraph in detail, as well as the correction for the integral proton spectrum gained from it.

In fig. 3.3b an example of a double peak event is shown. Here an electron-like event follows a proton-like event. Using the spline interpolation, the pulse-height of the first peak ph_1 and of the second peak ph_3 can be determined, as well as their time t_1, t_3, respectively. Having these information, the dataset of a run is scanned for events matching the following conditions:

$$ph_3 \;\geq\; 5.2\,\text{keV}_\text{ee}, \tag{3.9}$$
$$5.2\,\text{keV}_\text{ee} \;\leq\; ph_1 \leq 11.5\,\text{keV}_\text{ee}, \tag{3.10}$$
$$ph_\Sigma \;=\; ph_1 + ph_3 \geq 11.5\,\text{keV}_\text{ee}. \tag{3.11}$$

Eq. 3.9 means the dataset is scanned for events, with a second peak above noise level. Eq. 3.10 means, the dataset is scanned only for proton-like events in the first peak. $5.2\,\text{keV}_\text{ee}$ is
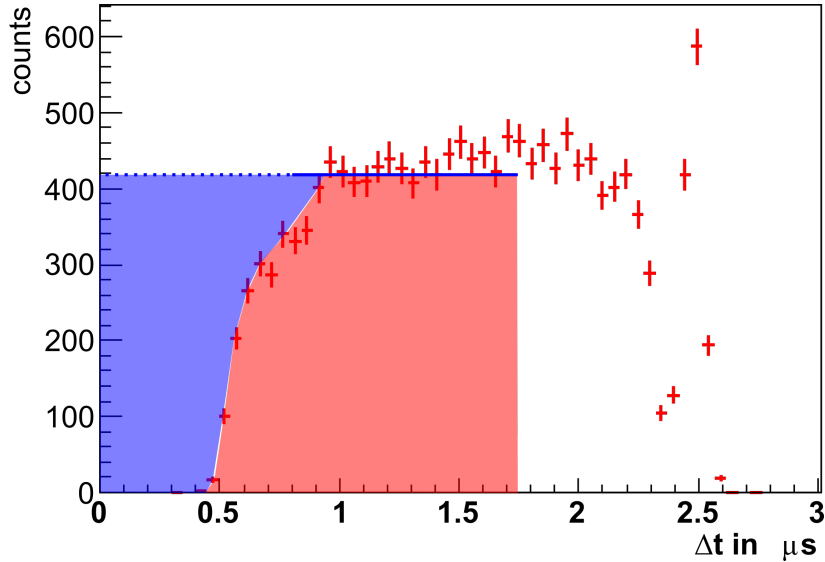
Figure 3.6.: Double peak events per Δt for pile-up correction. Drawn are in red markers the number of events with two peaks in the event window, data taken from config 1 with a retardation voltage of $50\,\text{V}$, channel 20. A constant rate of events is observed in the range of $0.8\,\mu\text{s}$ to $2.2\,\mu\text{s}$. This constant rate can be extrapolated to $\Delta t = 0$, allowing to determine the number of pile-up events, missed by the DAQ system. This number of missed events is drawn here as blue area, in red is drawn the number of events, where the first peak still can be separated from the second one. The number of events divided by the measurement time is then the rate of pile-up events used as correction, see fig. 3.7. For details, how the number of double peak events, the resulting extrapolating and therefore the pile-up rate is determined, please see text.

the lower integration limit and $11.5\,\text{keV}_{\text{ee}}$ the upper one. If an event matches these two first conditions, the pulse-height of the two peaks are added up to simulate a pile of the two peaks, eq. 3.11. If ph_Σ is higher, than the upper integration limit, the simulated pile-up of the two peaks would shift the first peak out of the proton region. This is exactly the effect of pile-up, just extrapolated with events, where the two peaks still can be distinguished. To get the number of real pile-up events not distinguishable by the DAQ, all events matching eqs. 3.9 to 3.11 are then sorted into a histogram, depending on the time difference Δt between the two peaks, see fig. 3.6. In red markers are shown the counts of events fulfilling eqs. 3.9 to 3.11, depending on the time Δt between the two peaks. A constant distribution of counts in the time region between $0.8\,\mu\text{s}$ to $2.2\,\mu\text{s}$. For time differences bigger than $2.2\,\mu\text{s}$ a decrease is observed, with an increase short before the end of the time window. This behaviour is due to the algorithm determining a peak using the spline interpolation. A peak is identified by a negative derivative of the spline, cf. section 3.1.1. In other words, if the second peak is to 'late', its decrease is not recorded any more, hence it can not be identified, causing the gap in fig. 3.6. On the other hand, the increase of events, with a second pulse at around $2.5\,\mu\text{s}$ is due to a bug in the spline interpolation, as it decreases at the end of the event window anyway, which is wrongly identified as second pulse. Nevertheless, this can be tolerated, as the pulse-height of the first pulse is still determined correctly and the number of counts

is only interesting for shorter time differences, where real pile-ups can occur. Starting at time differences $\Delta t < 0.8\,\mu s$ the number of counts decreases. At this point the separation of two pulses starts to fail and pulses with a time difference shorter than $\Delta t < 0.4\,\mu s$ can not be separated any more. So in the region from $0\,\mu s$ to $0.8\,\mu s$ pile-up occur. To understand this behaviour and how the number of pile-up events is determined, one has to do some theory on detector characteristics.

Random processes with a constant probability of occurrence per time unit, such as nuclear decay with a steady-state source, can be described by a Poisson random process. Using the Poisson distribution, one can derive the probability $I(t)dt$ of a next event taking place in the time interval dt after a delay of t

$$I(t)dt = re^{-rt}dt, \tag{3.12}$$

with r the count rate of the decay [Kno00]. *a*SPECT has an overall decay rate of maximal $r = 1800\,s^{-1}$ at $50\,V$ retardation voltage, the average time to the next event is given by

$$\bar{t} = \frac{2}{r} \approx 1.1\,ms. \tag{3.13}$$

This time is far longer, than the event window $dt = 4\,\mu s$ for *a*SPECT. Therefore, the exponential in eq. (3.12) can be approximated by a constant n_0 during the time dt, cf. fig. 3.6. This constant n_0 is determined using a fit in the region $0.8\,\mu s$ to $1.8\,\mu s$, which is then extrapolated to $\Delta t = 0\,\mu s$. This constant n_0 is the number of pile-up events expected per time bin of $50\,ns$. To get the full number of pile-up events $n_{pile-up}$ missed in the time region $0\,\mu s$ to $1.8\,\mu s$, one determines first the number of expected events n_{ex} and subtract form it the number of actually measured events n_{meas}. The number of expected events n_{ex} is the sum of the expectation value n_0 from $0\,\mu s$ to $1.8\,\mu s$ $n_{ex} = \sum_0^{1.8} n_0$. In fig. 3.6 this is marked as filled area, blue and red together. The number of measured events is determined in the same way, just summing up over the actually measured double peak events. n_{meas} is marked as red area in fig. 3.6. The number of pile-up events $n_{pile-up}$ is then the difference $n_{ex} - n_{meas}$ and marked as blue area. This is so far only the number of pile-up events occurred for this specific retardation voltage and run. To get the rate of pile-up $r_{pile-up}$, $n_{pile-up}$ is divided by the measuring time t_{meas}. The measuring time is the nett time of a run, when the shutter was open, see table 3.2. This is the same measuring time used to determine the rate of events in the general pulse-height spectrum, cf. fig. 2.12.

The rate of pile-up events $r_{pile-up}$ depends only on the time difference Δt the detector and DAQ system can resolve, as well as the countrate measured by the detector. Hence, the different detector channels, as well as the various configurations, used to investigate the different systematics of *a*SPECT (details, see section 3.3) can be combined to determine one single pile-up correction. To do so, the procedure to determine the rate of pile-up events $r_{pile-up}$ has been applied to each detector channel, configuration and retardation voltage separately. The pile-up rates determined from that are then drawn together into one graph, depending on the countrate measured in the proton region of the pulse-height spectrum. In fig. 3.7 this combined pile-up correction is shown. Drawn are as black markers the individual pile-up rates, depending on the measured countrate in the proton region. Unfortunately, only the data from config 1,3,7 could be used, as all other configurations had a to low statistics in double peak events, to make a good extrapolation to $\Delta t = 0$. Nevertheless, this data is more than sufficient for a common pile-up correction and also shows, that the
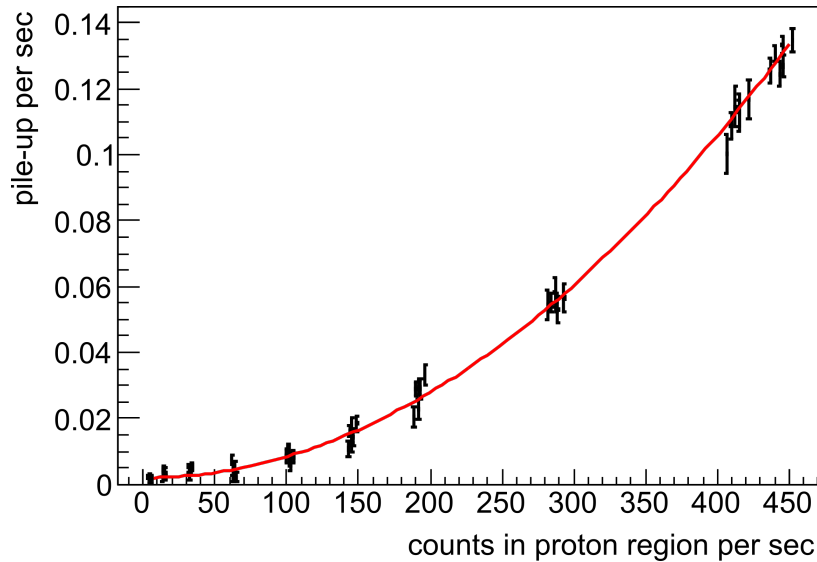
Figure 3.7.: Pile-up correction. Shown are the rate of missed pile-ups, depending on the
           countrate in the proton region. Data taken from config 1,3,7, channel 20 and
           21. As expected the rate of pile-up events decreases with decreasing countrate.
           In red is drawn an exponential fit (cf. eq. (3.12)) to the data, visualising the
           implemented correction in the fit function. For details, how this correction has
           been determined and implemented into the fit function, please see text.

pile-up rate is independent on the setting of aSPECT. As expected the pile-up rate decreases
for lower countrates, down to almost zero. It does not reach zero, as even for a retardation
voltage of 780 V a low countrate is measured in the proton region, although no protons can
reach the detector. This is due to electron-electron pile-up, still occurring at this low event
rate. In red is drawn an exponential fit to the data (cf. eq. (3.12)), which is then used as
pile-up correction in the fit function. How this correction is implemented, see section 3.1.3.

To investigate the effect of the pile-up correction on a the integral spectra of the different
configurations have been fitted, with and without pile-up correction. The pile-up correction
shifted the a value in the order of $O(-0.5\%)$. As already explained for the corrected pulse-
height a shift to lower a values is expected, as the countrate for a low retardation voltage (high
countrate) increases more, due to the pile-up correction, than the one for high retardation
voltages (low countrate). Hence, the spectrum is slightly shifted to lower proton energies,
leading to a slightly more negative value of a.

3.1.3. Fitting of Proton Recoil Spectra

Having determined the pulse-height spectrum, including corrections for the pulse-height
(section 3.1.1) and the dead time (eq. (2.11)), as well as an energy calibration (fig. 2.19), the
next step is determining the integral proton recoil spectrum by integrating over the proton
region from $5.2\,\text{keV}_\text{ee}$ to $11.5\,\text{keV}_\text{ee}$. This is done for each channel and retardation voltage
separately, leading to the final integral proton spectrum. In fig. 3.8 an example of an integral
spectrum is shown, a complete list of all spectra, for all configurations and channels can
be found in appendix B. For each data point of this proton recoil spectrum (red squares)
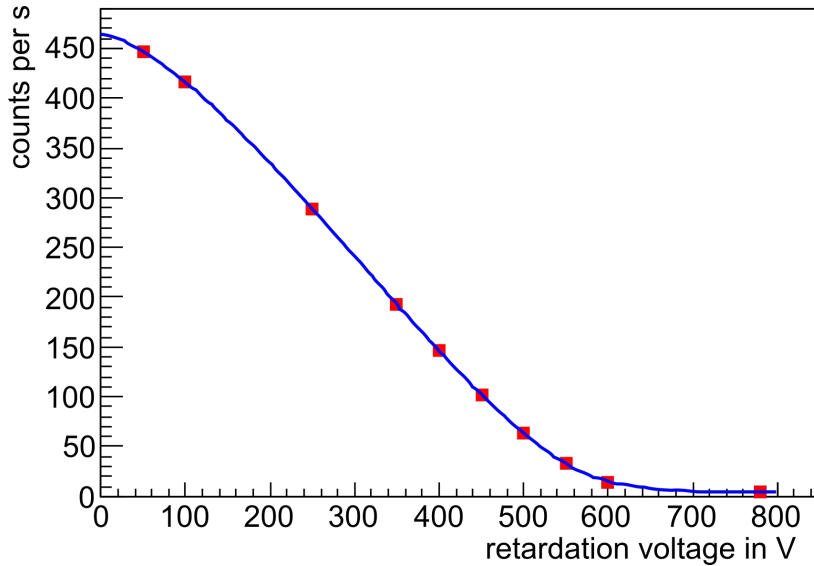
Figure 3.8.: Fit of integral proton spectrum for channel 20, config 1 (table 3.1). In red are drawn the data points, please keep in mind the error bars of the points are smaller then the marker size. As blue line is shown the fit of the proton spectrum, including a linear background description.

the uncertainties are determined separately. The uncertainty in y-direction is simply the statistical uncertainty, in x-direction its the uncertainty in the retardation voltage $\delta_{U_{ret}}$. This uncertainty of the retardation voltage is the Root-Mean-Square (RMS) of the fluctuation of the measured voltage by the Agilent 3458A DMM $\delta_{measured}$ and the systematic uncertainty of the DMM δ_{DMM}. How δ_{DMM} is calculated is explained in detail in appendix D. Further, an additional uncertainty for the Doppler effect $\delta_{Doppler}$, the RF noise δ_{RF}, the surface contact potential δ_{scp} and the field leakage $\delta_{leakage}$ is taken into account. These uncertainties are independent from each other and can be added up quadratically. The uncertainty on the retardation voltage for each point of the proton spectrum is then

$$\delta_{U_{ret}} = \sqrt{\delta^2_{measured} + \delta^2_{DMM} + \delta^2_{Doppler} + \delta^2_{RF} + \delta^2_{scp} + \delta^2_{leakage}}. \tag{3.14}$$

The uncertainty due to the Doppler effect is $\delta_{Doppler} = 0.1\,\text{mV}$ for each voltage, cf. section 2.2.6 and for the RF noise $\delta_{RF} = 40\,\text{mV}$, see section 2.2.1. Taking such a high uncertainty for the RF noise is certainly an upper limit, this uncertainty can be pushed further down with particle tracking simulations. The same is true for the fluctuation of the surface contact potential $\delta_{scp} = 30\,\text{mV}$ [Kah15] and the field leakage $\delta_{leakage} = 20\,\text{mV}$, cf. section 2.2.1. The analysis of the fluctuations of the surface contact potential and their effect on the retardation voltage, as well as the effect of field leakage will be completed by [Sch17]. Finally, taking all these uncertainties into account leads to uncertainties of $\delta_{U_{ret}} \approx 54\,\text{mV}$. Please be aware, that this uncertainty does not include any offset, due to field leakage and fluctuation of the surface contact potential. So far these offsets still have to be determined [Sch17] and have to be included in a final analysis.

Fitting Procedure

As explained in section 2.3 systematic effects of the experiment can be included directly in the fit function. In this thesis two final correction have been implemented in the fit function f_{fit}. These are a correction for the pile-up $f_{pile-up}$ (fig. 3.7) and a background correction f_{bckg}, resulting in

$$
\begin{aligned}
f_{fit}(U_{ret}, Int, a, r_B, pConst, pSlope, cBG, lBG) \; &= \; \overbrace{Int \cdot [\omega_{0C\alpha}(a, T_0) * F_{TR}(r_B, T_0, U_{ret})]}^{n_{proton}} \\
&- \; f_{pile-up}\left(n_{proton}, pConst, pSlope\right) \\
&+ \; f_{bckg}(U_{ret}, cBG, lBG). \quad (3.15)
\end{aligned}
$$

Here, the theoretical differential proton spectrum $\omega_{0C\alpha}$ (eq. (1.29)) is convoluted with the Transmission Function F_{TR} (eq. (2.6)) to calculate the theoretical countrate for a given value of a, a given retardation voltage U_{ret} and a given magnetic field ratio r_B. U_{ret} is the independent variable, whereas a and r_B a free fit parameters. This calculated countrate describes the shape of the integral spectrum, but not necessarily matches the measured countrate. Therefore, it has to be scaled by a factor Int to match the measured data, resulting in the calculated proton rate n_{proton}. The parameter Int is also a free fit parameter. The magnetic field ratio r_B (eq. (2.5)) has been implemented into the fit routine as extra dimension. Extra dimension means, the fit program will minimise the fit function f_{fit} to the measured proton countrates and simultaneously to a separate (extra dimension) data point with the coordinates and uncertainty of r_B. In this way the program determines the overall minimal χ^2 of the fit and therefore includes all uncertainties of the parameters directly into their correlated uncertainties, cf. section 2.3. In the same way the pile-up correction $f_{pile-up}$ is implemented. The dataset shown in fig. 3.7 is implemented as extra dimension. To this pile-up dataset an exponential with an offset is fitted the calculated proton rate, $f_{pile-up} = pConst + exp(pSlope \cdot n_{proton})$. $pConst$ and $pSlope$ are free fit parameters. As pile-up events are missed/not recorded events, this correction has to be subtracted from the calculated countrate. For details of the background correction f_{bckg}, see section 3.2.2. Details of thge first hand corrections for the experimentally enhanced systematics, can be found in section 3.3.2. For details on systematics effect, still to be investigated and implemented in the fit function, see section 3.3.4.

As actual fitting program has been used the DatFit package from [Sch15], which is a numerical fitting package implemented in Mathematica [Wol15]. It has been already proven its validity and flexibility in several experiments [SAB+00, HSH+01, ADF+08]. DatFit uses a χ^2 minimisation method, see section 2.3. For a correct determination of the correlated and uncorrelated uncertainties of the fit, the correlation between all free fit parameters have to be below at least 95 % [Sch15]. To achieve a low correlation, several steps have been implemented in the fit function. First, the fit function f_{fit} has been normalised to its area $\int dU_{ret} f_{fit}$. Second, several data channels have been fitted together as multi-dimensional fit. These steps lead to a sufficiently low correlation between the single fit parameters, see fig. 3.9.

As the area $\int dU_{ret} f_{fit}$ depends on a, it has to be recalculated for each step of the fit. This is very time consuming and not feasible. Therefore, the area has been calculated for the SM a from -0.3333 to 1 in 0.001 steps. These single values have then been interpolated by a
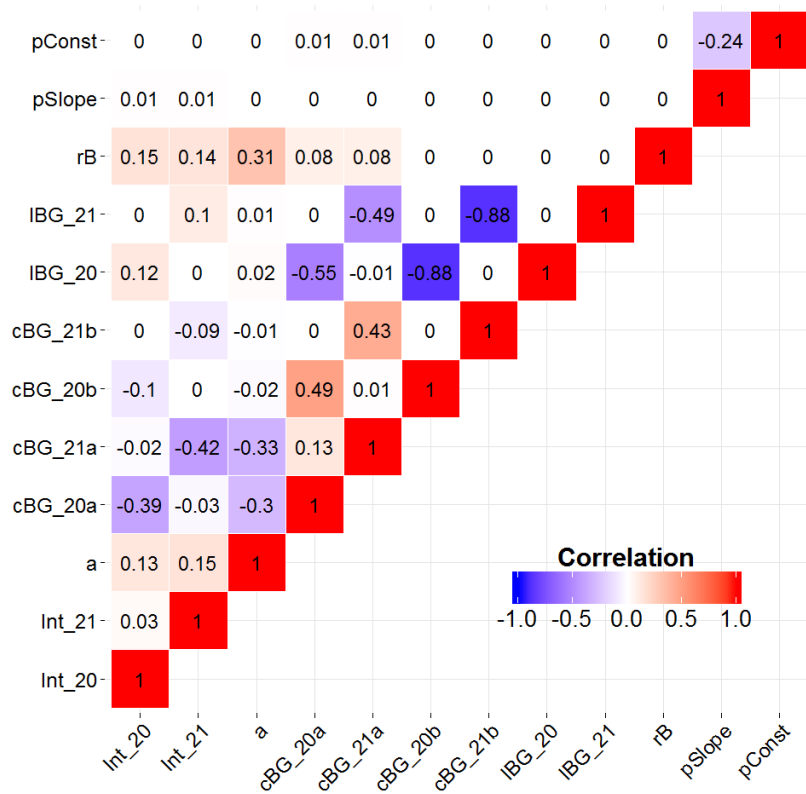
Figure 3.9.: Correlation matrix from fit of config 1. Shown is the correlation matrix of the fit parameter $Int, cBG, a, lBG, r_B, pSlope, pConst$ from the fit function f_{fit} of a fit to the config 1 data. Both channels $20, 21$ have been fitted in a multidimensional fit. A linear background model has been used for this fit, where cBG corresponds to the constant part of the background and lBG the slope of its retardation voltage dependency. Here, the highest correlation of -88% is observed between the slope lBG and the constant part of the background in the after shutter data $cBGb$. For details of the background see section 3.2.2. $pConst$ and $pSlope$ are the parameters of the pile-up correction. As this correction is only fitted to an extra dataset, there is basically no correlation of these two parameters, to the other ones.

The correlation between all fit parameters could be reduced sufficiently using a multidimensional fit for both channels, as well as normalising the fit function to its area. Having a low correlation is in the one hand important for the numerical minimisation of the fit to work well and to reduce the error between fit parameters. For details, see text.

(a)

(b)
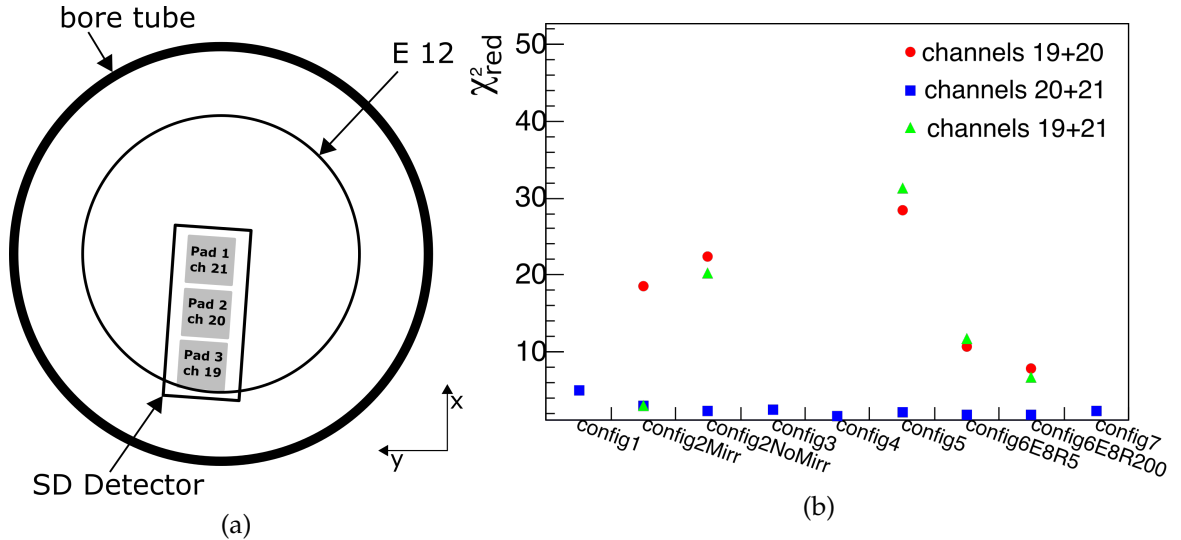
Figure 3.10.: The channel 19 anomaly.

In (a) is shown the view of the SDD into the *a*SPECT spectrometer. The flux tube seen by Pad3, reading channel 19, intersects with the E12 electrode, due to the positioning of the detector. This intersection causes proton scattering on the surface of E12, distorting the proton spectrum measured by channel 19. This distortion can not be reproduced by the fit function f_{fit}, leading to high χ^2_{red} values for fits including channel 19. For details, see text.

In (b) are shown the reduced χ^2_{red} values for the different channels of the detector, for all possible combinations of the three channels. Fits including channel 19 show a dramatically higher χ^2_{red} (if the χ^2_{red} value is not shown for a specific configuration, it is out of scope).

Hence, due to the intersection of the flux tube seen by channel 19, this channel has to be excluded from the analysis. The flux tube of channels 20 and 21 are not intersected by any electrode, so their measured proton spectrum is not distorted. Therefore only channel 20 and 21 are used for the analysis.

spline. A spline has the advantage being very precise and the fit program can simply look up the area of the spectrum from the spline for a given *a* value, instead of calculating it. The derivative of the fit function needed to include x-uncertainties is determined from a two dimensional spline, allowing to look up the derivative at each retardation voltage U_{ret} for every possible value of *a*. Using splines in both cases saves a lot of computation time, without loosing any precision. With these implementations, a fit of the proton spectrum can be done with in a reasonable time, e.g. a multi-dimensional fit of two channels takes about 0.5 h to 1 h, including all corrections mentioned above.

The Channel 19 Anomaly

As already mentioned the SDD *a*SPECT uses has three different pads, see fig. 2.17. Unfortunately, the detector electrode and therefore the detector can not be placed at a predefined position inside *a*SPECT. The electrode is mounted at a 1.5 m long tube, reaching inside *a*SPECT. The position of the detector in x-y-direction can only be slightly modified,

by tilting the tube. As the tube is only fixed at one single point, a vacuum feed through, the tilting leads to a rather uncontrolled positioning of the detector electrode. For details on the detector mechanics, see [Sim10]. In the beam-time 2013 the detector was positioned slightly off axis [Vir13]. This off axis position caused the flux tube seen by channel 19 to intersect with the E12 electrode, see fig. 3.10a. The E12 electrode is one of the electrodes below the actual AP electrode E14, see fig. 2.4. This intersection of the flux tube with the electrode changes the shape of the proton recoil spectrum significantly. In fig. 3.10b are shown the reduced χ^2 values from the fit of the proton recoil spectrum for all combinations of the three channels and all configurations investigated. Only the combination of channel 20 and channel 21 show reasonable χ^2_{red} values. Combinations with channel 19 have extremely high χ^2_{red}, partly higher than the scale shown in the figure.

Therefore, the proton recoil spectrum measured with channel 19 can not be described properly with the used fit function. The reason for that is that protons in the flux tube scatter on the surface of electrode E12. This scattering might be inelastic, changing the spectrum, or elastic changing the momentum in z-direction, shortly before the actual AP, hence protons which should overcome the AP, might not and vice versa. Further, some of the protons will be absorbed on the surface. All these effects change the shape of the measured proton spectrum significantly, even if only a small part of the flux tube scatters. Unfortunately, these effects are far to complex and not well enough understood, to be described properly in the fit function. Therefore, channel 19 has to be excluded from the further analysis of a. The flux tubes seen by channel 20 and 21 on the other and do not intersect any of electrode and are therefore free of these effects. Hence, channel 20 and 21 only are used for the analysis of a.

3.2. Investigation of Systematics

In the previous section has been described how the raw data is treated and analysed to gain pulse-height spectra for the retardation voltages and from there the integral proton recoil spectrum. To this integral spectrum a fit is minimised to determine a. In this section this procedure is applied to various measurements of the aSPECT experiment. These measurements differ in the experimental setting of aSPECT and are used to investigate the systematics of the experiment. In table 3.1 are shown the data sets investigated within this thesis. These data sets are the main measurements of the beam-time 2013 to investigate the systematics of aSPECT in detail.

In this thesis, the retardation voltage dependent background is investigated in detail, see section 3.2.2. Further, an ideogram of the measurements without any further corrections of systematics is given in fig. 3.16, including an upper limit on the uncertainty on a. Further, first hand corrections have been applied to check qualitatively if the experimentally enhanced systematics are understood and can be corrected for. For a final analysis, including corrections and uncertainties, see [Sch17]. In the following all a-values are normalised to a standard value, so these are close to 1. Reasons for that is, on the one hand the values for different settings are easy to compare. On the other hand, final corrections of the systematics can shift the overall value of a significantly. Hence, any a value stated here would be precise, but not accurate.

Table 3.1.: List of analysed data sets. The name constitutes of the date the measurement was done. In the table is also listed the purpose of the measurement, as well as the configuration of aSPECT for details of the settings, see appendix C.

data set	comment	configuration changes of the configuration
20130628/9/0,20130702	first statistic run	config1 (table C.1) standard
20130705/6/7	test of E- and B-fields in DV changes also background conditions	config2 (table C.2) el.-static mirror on/off
20130726/7/8/9	ExB drift at E15 (cf section 2.2.3) changes edge effect and background condition	config3 (table C.3) asymmetric E15
20130730/1	reduced beam profile and ExB drift at E15 enhances edge effect	config4 (table C.4) ExB drift at E15, red. beam
20130801/3	reduced beam profile enhances edge effect	config5 (table C.5) ExB drift at E15, red. beam
20130804	red. beam profile, switching of lExB test influence of lExB on edge effect	config6 (table C.6) inverted lExB (E8),red. beam
20130805/6/7	el. field gradient in DV (fig. 2.9) protons traps in DV	config7 (table C.7) voltage on E3–E6
20130719/20/21/22	change to uDAQ test of DAQ electronics	config8 (table C.8) uDAQ

(a)   (b)
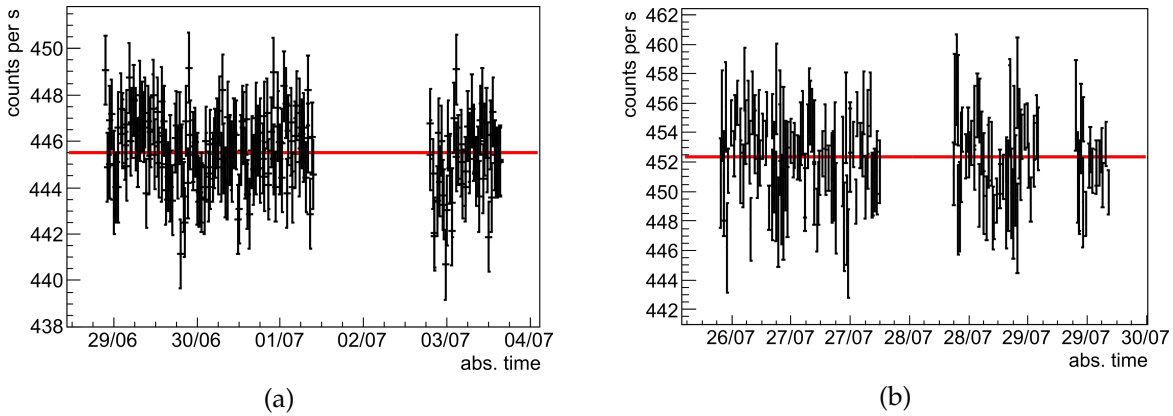
Figure 3.11.: Stability of countrate. Shown are all 50 V DAQ cycles, cf. fig. 2.15, performed during config 1 and 3. On the y-axis is drawn the countrate of the individual cycles and on the x-axis the absolute time in day/month of the measurement. The large gaps are due to an interruption of the measurement for systematic tests, or a break down of the measurement computer. To check, if these data fluctuate statistically only ($\chi^2_{red} \approx 1$) a constant has been fitted to the data (red line). For config 1 (a) this constant has a $\chi^2_{red} = 1.03$ and for config 3 (b) $\chi^2_{red} = 1.1$. Both values are compatible with $\chi^2_{red} \approx 1$, hence do not need any additional correction for a systematic, e.g. the reactor power.

3.2.1. Stability of Countrate

Before starting to investigate the different systematics of *a*SPECT, the stability of the countrate within each configuration has been checked. This is a cross check to the stability of the neutron beam/reactor and also a search for unknown systematics of *a*SPECT. Any fluctuation of the reactor power will lead to an fluctuation of the neutron intensity in the neutron guide of *a*SPECT. This fluctuation of the neutron intensity directly corresponds to a fluctuation of the measured proton rate. As for the analysis all single DAQ cycles for the same retardation voltage of one configuration are added up, a non statistical fluctuation of the neutron beam/countrate can introduce a new systematic shifting *a* and would have to be corrected for. In fig. 3.11 the countrates for a retardation voltage of 50 V from config 1 and 3 are shown. On the y-axis is drawn the measured countrate per single DAQ cycle and on the x-axis the absolute time. The large gaps between measurements are either due to systematics test of the system, not devoted to the configuration, or simply to a crash of the computer of the DAQ. The 50 V measurements have been chosen, due to their high proton to background ratio and 50 V has been measured four times more often, than any other retardation voltage, cf. fig. 2.16. Hence, it has the highest statistics and is most sensitive to non-statistical fluctuations. To check, if the measured countrate is consistent with a purely statistical fluctuation, a constant has been fitted to the measurement, red line in fig. 3.11. If the reduced χ^2_{red} is compatible with 1, the data fluctuates around this constant statistically [Jam06], if $\chi^2_{red} \gg 1$ the fluctuation is non statistical and the data would have to be corrected for the additional systematic fluctuation/drift. In case of *a*SPECT the reduced $\chi^2_{red} = 1.03$ for config 1 and $\chi^2_{red} = 1.1$ for config 3. Both values are compatible with $\chi^2_{red} \approx 1$, so the data fluctuate only statistical and need no further correction.
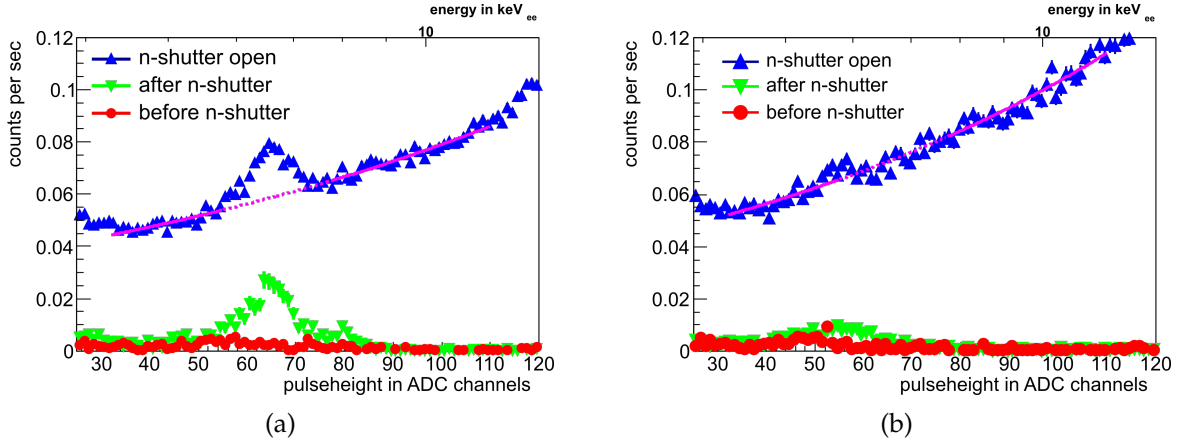
Figure 3.12.: Background from ionised residual gas. Shown are the countrates for a retardation voltage of 780 V before the neutron shutter has been opened (red circles), during it was open (blue triangles) and after it has been closed (green triangles) for config 1 (a) and 3 (b). The countrate for shutter open is in general higher, due to the electron background from the neutron beam. Please keep in mind, the 780 V measurement is above the endpoint of the proton spectrum, so no protons are detected here. For config 1 a clear peak from 55 ADC channels to 75 ADC channels can be observed. This peak is due to ionised residual gas, generated in a Penning-like trap in the AP electrode. This peak corresponds to the retardation voltage dependent background, as shown in fig. 3.13. It vanishes for config 3, due to in proved vacuum conditions.

3.2.2. Retardation Voltage Dependent Background

In section 2.2.3 has been explained that any retardation voltage dependent background strongly influences the measurement of a. Such a background will change the shape of the proton spectrum and lead to a wrong value of a. Therefore, the retardation voltage dependent background has to be known with high precision for each configuration. In this section the method is described, how to determine the retardation voltage dependent background. This includes an investigation of a proper background description, as well as the implementation of it in the fit function.

In fig. 2.15 is shown a schematic of the countrate during one measurement cycle of aSPECT. The dependency of the background on the retardation voltage is determined by measuring the countrate after the neutron shutter has been closed (t_{close}) and before the AP electrode is ramped to 0 V (t_{APoff}). This time is defined as after shutter time $\Delta t_{after} = t_{APoff} - t_{t_{close}}$. To avoid any disturbing effects on the countrate from closing the shutter or ramping the AP, a safety buffer of 1 s has been used after closing the shutter and before ramping the AP electrode. The countrate in the proton region (5.2 keV$_{ee}$ to 11.5 keV$_{ee}$) during Δt_{after} is determined for all retardation voltages seperately. But before investigating this retardation voltage dependent background, a cross check of the method to determine the background after closing the neutron shutter has to be done. To do so, the countrate in the proton region with neutron shutter open $\Delta t_{open} = t_{close} - t_{open}$ is compared to the countrate directly before opening $\Delta t_{before} = t_{open} - t_{APon}$ and after closing the shutter, respectively. This comparison is shown in fig. 3.12 for channel 20 in config 1 and 3 of the 780 V measurement. In blue triangles
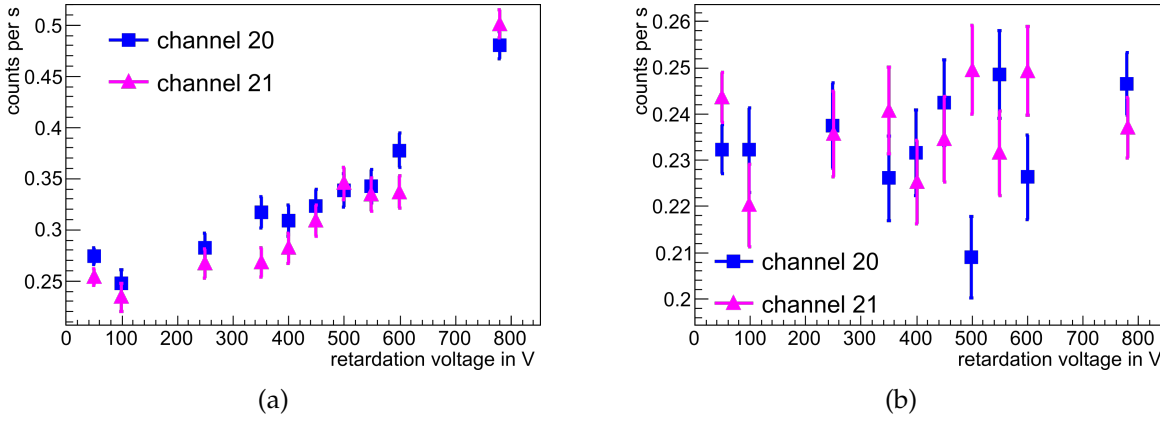
Figure 3.13.: Retardation voltage dependent background. Shown is the countrate after clos-
ing the neutron shutter in dependence of the applied retardation voltage for
config 1 (a) and 3 (b). A clear increase of the countrate for config 1 can be
seen, due to the Penning-like trap in the AP electrode. This increase is gone for
config 3, due to an improved vacuum. To this retardation voltage dependency
several descriptions have been fitted, eqs. 3.16 to 3.19. As shown in fig. 3.14, a
linear dependence describes all configurations best. For details, see text.

are shown the countrates for shutter open, this countrates are in general higher than for
before shutter (red circles) and after shutter (green triangles), due to the electron background
from the neutron beam. This background is obviously not present, if the neutron shutter
is closed. The shutter open and after shutter data in config 1 (fig. 3.12a) show a clear peak
around 55 ADC channels to 75 ADC channels, which is not present in the before shutter data
and completely vanished for config 3 (fig. 3.12b). This peak is due to ionised residual gas
created in the Penning-like trap of the AP electrode, cf. section 2.2.3. This peak is gone for the
before shutter data, simply due to the fact, that the AP has been ramped down between two
retardation voltages, see fig. 2.16. The retardation voltage has been ramped down, to reduce
this background from ionised residual gas and to make sure the level of background for each
retardation voltage is the same and not influenced by the voltage set before. To determine
the amount of background from this peak, the after shutter data haven been integrated
from 55 ADC channels to 75 ADC channels, giving a countrate of $cps_{after} = 0.248(12)\,\text{s}^{-1}$ of
ionised residual gas. For the shutter open data an exponential fit has been applied in
the range 35 ADC channels to 55 ADC channels and 75 ADC channels to 110 ADC channels
to determine the electron background. This electron background is then interpolated in
the range of the peak (55 ADC channels to 75 ADC channels). This interpolation for the
electron background has then been subtracted from the integral from 55 ADC channels
to 75 ADC channels of the shutter open data, to get a countrate of background from the
peak of ionised residual gas of $cps_{open} = 0.274(14)\,\text{s}^{-1}$. These two countrates cps_{after} and
cps_{open} are the same within their uncertainties. Therefore, the method to determine the
retardation voltage background by measuring the countrates after the neutron shutter has
been closed is justified and is a very useful tool to determine the background contribution
of retardation voltages below 780 V. Hence, in this way the retardation voltage dependency
of the background can be determined.

As already mentioned, this peak of ionised residual gas vanishes for config 3 and all

configurations measured later on during the beam-time. Reason for that is a significantly improved vacuum. Config 1 has been taken end of June 2013, config 3 end of July, cf. 3.1. Due to the longer pumping time of the system, the vacuum improved from configuration to configuration. The difference between config 1,2 and the others is then due to the two weeks of beam pause, where the system has been pumping, but no measurement were possible. Unfortunately, the pressure dependency can not be proven, as the pressure in aSPECT is measured several meters away from the AP, through a thin stainless steel tube. The pressure there is in the range of $1.9 \cdot 10^{-9}$mbar to $2.7 \cdot 10^{-9}$mbar with fluctuations within one configuration of $1 \cdot 10^{-10}$mbar. But most likely this pressure is dominated by out-gassing of the tube, not showing a realistic vacuum level inside the AP. A offline beam-time in 2012 showed a pressure level of 10^{-10}mbar in aSPECT. The newly introduced new ExB drift electrode E15 showed previously a clear reduction of the background level, see [Mai14]. Unfortunately, this clear influence on the background could not be seen for measurements during the beam-time 2013, most likely, as the vacuum level has been already improved significantly, when the ExB drift at the E15 was used.

Having determined, that the after shutter data correspond to background from ionised residual gas, a proper description of the retardation voltage dependency can be searched for. In fig. 3.13 the countrate measured after the neutron shutter has been closed is shown. For config 1 (a) a clear dependence of the background to the retardation voltage can be seen, which is gone for config 3 (b). This vanishing dependence is due to the vanishing background peak shown in fig. 3.12. To find the best mathematical description of this background dependency four functional dependencies have been investigated, a constant one $f_{bckg,constant}$ assuming no retardation voltage dependency at all. A description with linear $f_{bckg,linear}$, one with quadratic $f_{bckg,quadratic}$ and one with exponential $f_{bckg,exponential}$ increasing background.

$$f_{bckg,constant}(U_{ret}) \quad = \quad cBG \tag{3.16}$$

$$f_{bckg,linear}(U_{ret}) \quad = \quad cBG + lBG \cdot U_{ret} \tag{3.17}$$

$$f_{bckg,quadratic}(U_{ret}) \quad = \quad cBG + qBG \cdot U_{ret}^2 \tag{3.18}$$

$$f_{bckg,exponential}(U_{ret}) \quad = \quad cBG + e^{eBG1 + eBG2 \cdot U_{ret}} \tag{3.19}$$

These descriptions have been fitted to the countrates measured after closing the neutron shutter. An example is shown in fig. 3.15 for channel 20 and a linear background model. To investigate how well the measured background is described by the different descriptions (eqs. 3.16 to 3.19), the reduced χ^2_{red} of the fits have been compared. In fig. 3.14 the reduced χ^2_{red} for the different descriptions for config 1 and config 3 are shown. For config 1 (3.14a) clear differences between the background descriptions can be seen, whereas in config 3 (3.14b) the difference between the descriptions is marginal. This means in config 1 there is a clear retardation voltage dependence, which is best described by the quadratic description $f_{bckg,quadratic}$. On the other hand a constant background description $f_{bckg,constant}$ would be sufficient for config 3. Applying this investigation to all configurations shows, that the differences between a linear, quadratic and exponential description is low. Therefore, a linear description is used as standard for the retardation voltage dependent background, as it is the most simple description, describing the retardation voltage dependent background very well.

To correct for the retardation voltage background the functional dependency $f_{bckg,linear}$
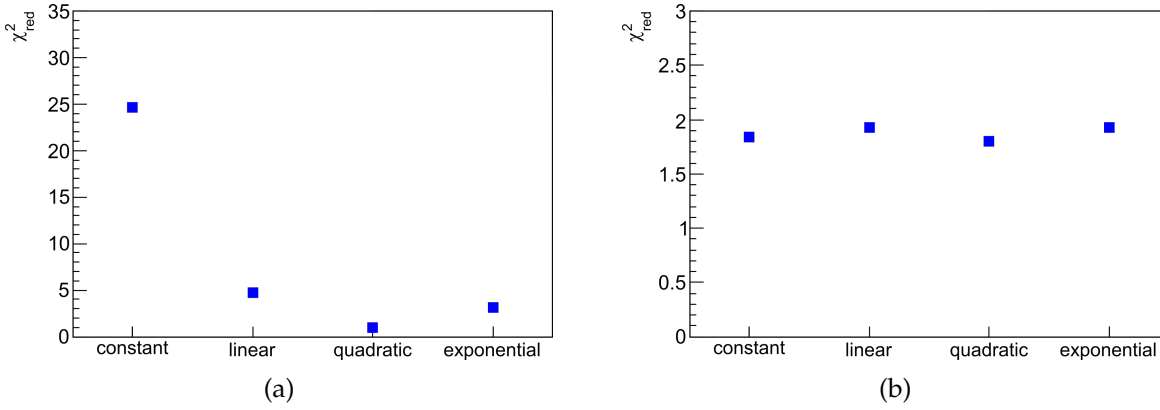
Figure 3.14.: Reduced χ^2_{red} for different background descriptions. Shown are the reduced χ^2_{red} for fits of different background descriptions (eq. (3.16) to (3.19)) to the after close data shown in fig. 3.13. For config 1 (a) clear differences in the different background descriptions can be seen, where a constant one describes the background worst and a quadratic one best. For config 3 (b) the differences between the descriptions are marginal, due to far better vacuum conditions. From this investigation the linear description of the retardation voltage background $f_{bckd,linear}$ has been chosen as correction for the background, as it describes all configurations well. For details of the background investigation, see text.

has been implemented in the fit function, as shown in section 3.1.3. This has been done for each configuration and also channel 20 and 21 separately. The after shutter data have been included to the data-set as extra dimension. To this extra dimension eq. 3.16 is fitted. Please be aware, that two constant backgrounds had to be implemented in this fit. *cBGa* for the constant background level in the measured proton spectrum and *cBGb* for the constant level of the after shutter data. Only the slope of the retardation voltage dependency *lBG* is fitted to both simultaneously. Reason for that is, although the retardation voltage dependency from ionised residual gas is the same, the constant background level with and without neutron beam, obviously is not, cf. fig. 3.12. To cross check, if the fit function uses the right correction for the background $f_{bckg,linear}$ a comparison between the global fit f_{fit} and a local one has been done. In the global fit the proton spectrum and the background have been fitted simoultaneusly. In the local fit eq. 3.16 has been fitted directly to the after shutter data. This comparison is shown in fig. 3.15 for config 1 and 3. Clearly, the uncertainty of the local fit is smaller in both cases, due to the fact, that the global fit takes the uncertainty of the measured proton spectrum into account. Hence, the parameters of $f_{bckg,linear}$ in the global fit are correlated to the other parameters of f_{fit}, cf. fig. 3.9. Please be aware, the high correlation of -88% occurs between cBGb and lBG, so the parameters fitted to the after shutter data only. This is is common for every linear fit. Nevertheless, for both configurations, the determined background correction coincides with in their uncertainties with the local determination of the background correction. So the global fit f_{fit} corrects the measured proton spectrum for the measured retardation voltage dependent background very well and as expected. As already explained the correction of the background is determined for each configuration and channel separately. This correction for the retardation voltage dependency is in the order of $\Delta a/a \approx 0.2\%$ to 0.6%, depending on the channel and configuration.

(a)   (b)
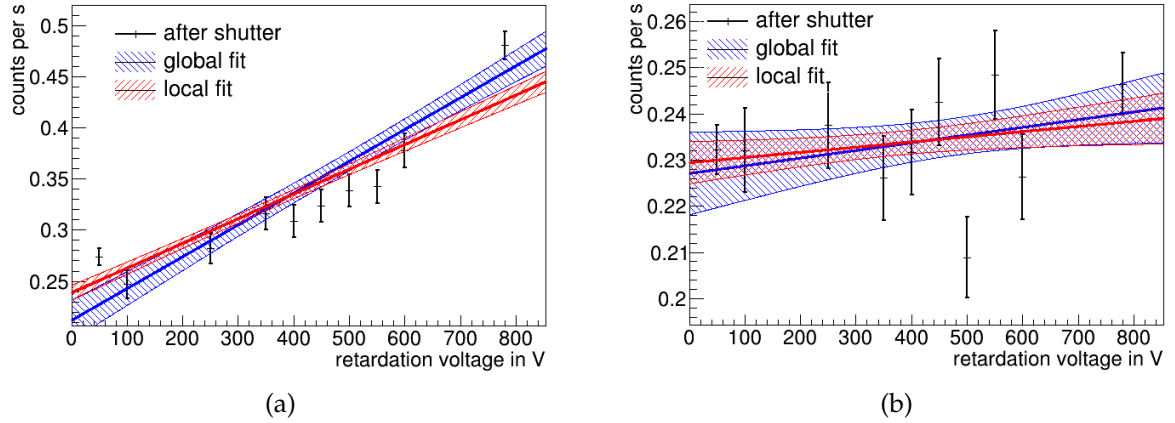
Figure 3.15.: Fit of the retardation voltage dependent background. Shown is the retardation voltage dependent background, as in fig. 3.13 for channel 20 only. To this data the background description $f_{bckd,linear}$ has been fitted, once as single (local) fit, just to the after shutter data, and once as global fit f_{fit} (section 3.1.3) to the after shutter and the measured proton spectrum simultaneously. This has been done, to cross check the background correction of $f_{bckd,linear}$ in f_{fit}. For both configurations 1 (a) and 3 (b) the local and global fit coincide within their uncertainties. Therefore can be concluded, the background correction works well and as expected.

3.3. Comparison of Configurations

In the previous sections has been explained, how the raw data has been treated to achieve the pulse-height spectra for the different retardation voltages and how from these pulse-height spectra the integral proton recoil spectrum is gained, section 3.1. Further, common systematics to all configurations, as pile-up (section 3.1.2), stability of the countrate (section 3.2.1) and retardation voltage dependent background (section 3.2.2) have been investigated. These common systematics have been included in the fit function (section 3.1.3) and with this fit function the various configurations of aSPECT have been fitted, see section 3.3.1. The different configurations of aSPECT are still subject to various systematics, like edge effect. In section 3.3.2 first hand corrections of these experimentally enhanced systematic effects are determined and implemented into the fit function. An ideogram including these first hand corrections is shown in section 3.3.3, as well as a discussion of the fit quality and the resulting current limits of the uncertainty of a. Finally, in section 3.3.4 the systematics, not yet included are explained, as well as a way to determine them.

> **Disclaimer**
> The uncertainty of a is determined in a multi-dimensional fit, see section 2.3. The correction of the different systematics are included directly into the fit function itself, see section 3.1.3. The great advantage of such a multi-dimensional fit is, that the corrections and their uncertainty are directly determined by the fit. Therefore, the systematics and their uncertainties are included correctly into the uncertainty of a. On the other hand, a multi-dimensional fit with the systematic corrections directly in the fit function, does not provide a classical error budget. Hence, the uncertainty on a can not be split up into a statistical and systematic uncertainty.

3.3.1. Comparison without Correction of the Experimentally Enhanced Systematics

In this section, the configurations stated in table 3.1 are investigated. For the configurations 1 to 7 the pulse-height, pile-up and background correction are included, as explained in section 3.1.1, section 3.1.2 and section 3.2.2, respectively. Config 8 uses a different DAQ system (uDAQ), without a hardware shaper, see section 3.1. This uDAQ has been tested the first time in 2013 and digitizes directly the unshaped pulses from the preamplifier. The shaping is done by software afterwards. This procedure is completely different from the DAQ used for config 1-7 and would required an in-detail analysis of the uDAQ to correct the systematics of config 8 on the same level, as for the others. Due to time reasons, this could not be done. Therefore, config 8 has been fitted without these corrections and a constant background description only. It is shown here as cross check to the normally used sDAQ only, to assure no saturation effect is present, as seen in 2008 section 2.2.4.

In fig. 3.16 an ideogram of the *a* values of the individual configurations is shown. Here config 1 has been arbitrarily chosen as standard to normalize to. Reason for this is to somehow blind the values of *a*, as they are still subject to systematic shifts. The configurations can be divided into three different groups. The first group are "standard" values, where the systematics have not been enhanced dramatically. These configurations are configs 1, 2 MirrON, 3, 7 and 8. In these configurations the experimental settings, like ExB drifts, position of the magnetic AP, etc. have been changed to investigated these second order effects. That these effects have only a minor influence on the *a* values investigated here can be seen, as all values of this group are the same, within their uncertainties. But still have to be taken into account in the final analysis, to achieve a precise and accurate value. The second group of values are configs 4, 5 and 6, where the neutron beam profile has been reduced to enhance the edge effect. In fig. 3.18 the measurement of the two beam profiles used during the beam-time 2013 is shown, as well as the section of the profiles, which is projected onto detector pad 2 (channel 20). The values for configurations with a reduced beam profile are shifted to more negative *a* values, which is expected from the fig. 3.18. Having a strong slope in the n-beam at the edge of the detector area at about -9 mm causes a strong loss of high energetic protons, cf. section 2.2.2. A loss of high energetic protons will shift the proton recoil spectrum in average to lower energies, hence result in a more negative value of *a*. A first qualitative estimate of this shift can be found in section 3.3.2. The third group of values is actually just one, config2 MirrOFF. Here, the electro-static mirror has been set to 0 V, so only protons emitted to the upper hemisphere of *a*SPECT are analysed and detected. Normally, one would expect the same value for *a*, than with the mirror on. *a* does not depend on the emission direction of the proton, so there should not be a difference between MirrOn and MirrOFF. But for practical reasons a slight magnetic field gradient is applied in the DV, causing a magnetic mirror effect in the DV itself. This effect is dependent on the emission angle of the proton and therefore causes an energy dependence in *a*SPECT. For more details on that and an estimate of it, see section 3.3.2.

The uncertainties in fig. 3.16 are still dominated by statistics. Only for configuration 1 and 2 the uncertainty of the background description, see section 3.2.2, increases the uncertainty of *a* significantly. All other correction, like pile-up, do not significantly contribute to the uncertainty of *a*. In fact, they improve the uncertainty on *a*, due to the better description of the measured proton spectrum. For a detailed explanation, how the corrections influence
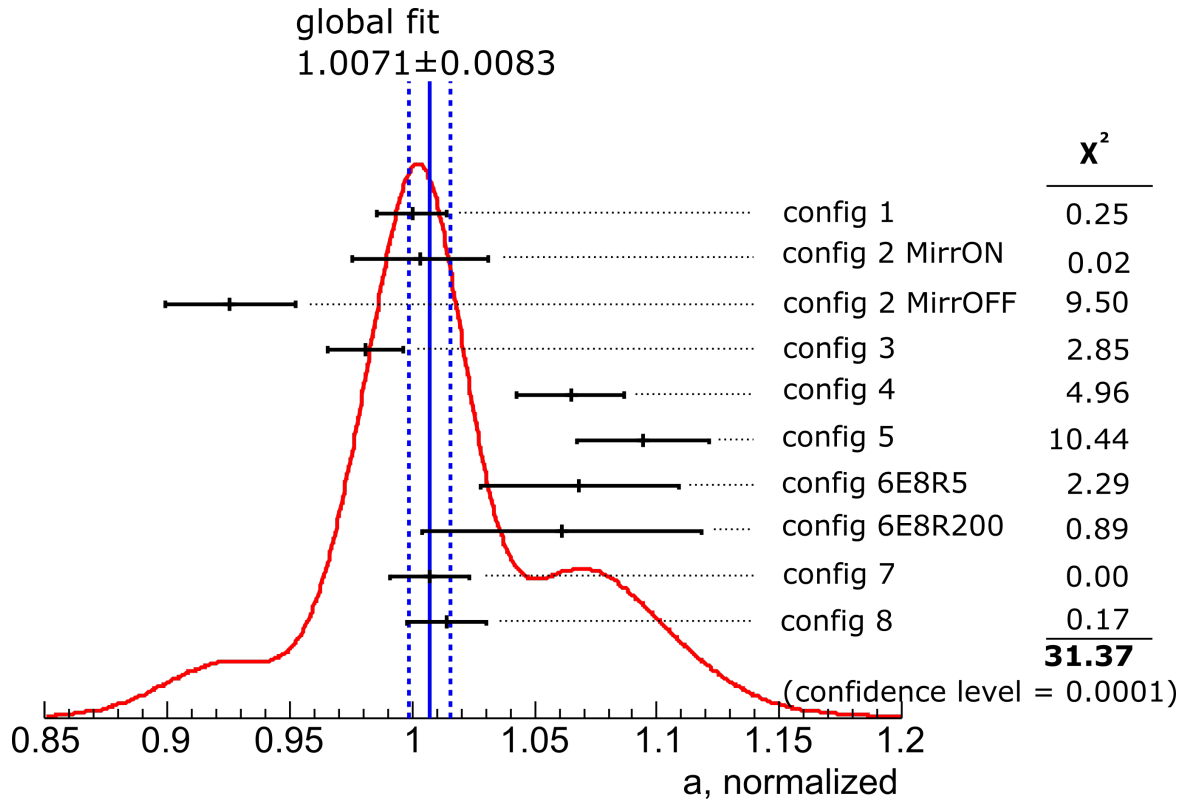
Figure 3.16.: Ideogram of a for different configurations without corrections of experimentally enhanced effects. All values have been normalized to the value of config 1 to blind the value of a, as it is still subject to systematic shifts. Config 8 uses a different DAQ system, which would have needed an in-detail investigation, therefore no pulse-height, pile-up and background correction could be applied to it. Hence, it is shown here only as cross check to the normal DAQ. Each of other configurations has been corrected for the pulse-height, pile-up and background. The fluctuation of the a values of the different configurations are due to experimentally enhanced systematics of aSPECT. E.g. during config 2 the electro-static mirror has been turned off and on again to be sensitive to E- and B-field gradients in the DV. For config 4 to 6 a reduced neutron beam profile has been used, to enhance the edge effect. Enhancing these systematics allows a more precise determination of them, see section 3.3.2. In blue, vertical lines are drawn the a values and uncertainty of a global, multi-dimensional fit to configuration 1 to 7. This fit converges successfully and has already a good precision of $\delta_a/a \approx 0.82\%$. But the low confidence level of only 0.0001 shows, that this value highly disagrees with Gaussian distributed data and needs to be corrected for the experimentally enhanced systematics. For a more detailed explanation, see text.

Table 3.2.: Pure measuring time of the individual configuration. The time stated here is the pure measuring time of the individual configurations with neutron shutter open $\Delta t_{open} = t_{close} - t_{open}$, cf. fig. 2.15.

configuration	time in h
1	45.7
2 MirrON	7.2
2 MirrOFF	16.2
3	23.5
4	10.3
5	7.4
6E8R5	2.9
6E8R200	1.5
7	20.3
8	11.3
Σ	146.3

the uncertainty of a see section 3.3.3. To get a feeling, how much statistics is needed, to achieve this precision level, the pure measurement times are given in table 3.2. Pure means here, only the time, when the neutron shutter was open $\Delta t_{open} = t_{close} - t_{open}$ is counted, cf. fig. 2.15.

To determine an overall value of a a global fit to the configs 1-7 has been done. In this global fit again the possibility of multi-dimensions have been used. Here, the channels 20 and 21 for each configuration has been fitted separately, with its own background correction. The pile-up, and magnetic field ratio r_B are fitted each as one common correction. The pulse-height correction is included as well. This leads to a fit function, cf. section 3.1.3,

$$
\begin{aligned}
f_{fit,global}(U_{ret}, \textbf{\textit{Int}}, a, r_B, pConst, pSlope, \textbf{\textit{cBG}}, \textbf{\textit{lBG}}) = {} & \overbrace{\textbf{\textit{Int}} \cdot [\omega_{0C\alpha}(a, U_{ret}) * F_{TR}(r_B, U_{ret})]}^{n_{proton}} \\
& - f_{pile-up}\left(n_{proton}, pConst, pSlope\right) \\
& + f_{bckg}(U_{ret}, \textbf{\textit{cBG}}, \textbf{\textit{lBG}}), \quad\quad (3.20)
\end{aligned}
$$

where $\textbf{\textit{Int}}, \textbf{\textit{cBG}}, \textbf{\textit{lBG}}$ are 18 dimensional vectors to account for the 2 channels of the 9 configurations. As one sees, a is still just a one dimensional parameter, meaning the global fit will search for the a value with a minimal χ^2 for all configurations together. The global fit converges, despite the still significant fluctuations of a, leading to an a value of

$$
a^{global}_{w/o\ corrections} = 1.0071(83). \quad\quad (3.21)
$$

Also drawn as blue lines in fig. 3.16. This corresponds to a relative uncertainty of 0.82 %. To check, if the χ^2 minimisation of the fit is still valid and therefore the conversion of the fit is valid, a closer look at the χ^2 surface is done, cf. fig. 2.20. In fig. 3.17 a cut through the χ^2 surface is shown. For details, how a χ^2 surface is calculated, see section 2.3. For a valid χ^2 minimisation a parabola is expected [Jam06], which is the case for the global fit of the
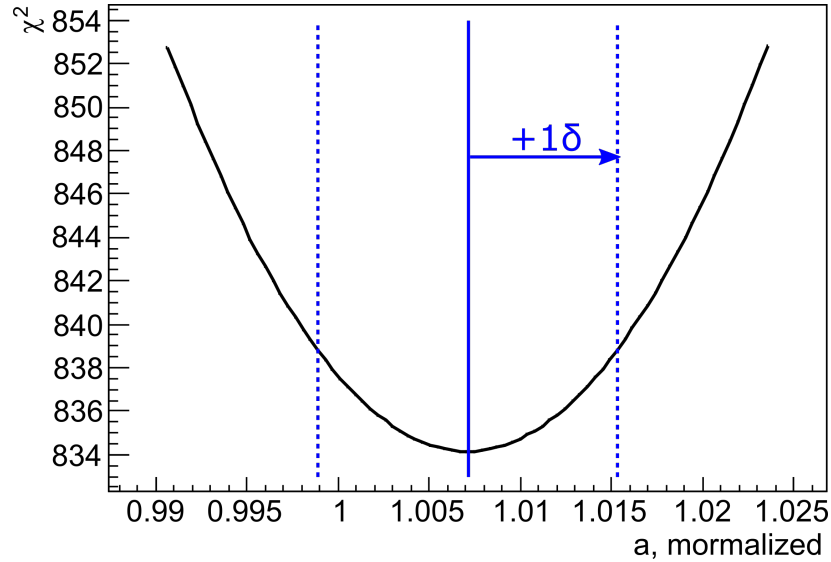
Figure 3.17.: Cut through the χ^2 surface of the global fit (eq. 3.20) without corrections. For a valid χ^2 minimisation a parabola is expected for the cut through and a low deviation ϵ (eq. (2.16)) from the ellipsoid. As can be seen from this graph χ^2 follows a parabola and the deviation from the N-dimensional ellipsoid is very low $\epsilon = 3 \times 10^{-10}$. Hence, even without corrections a valid global fit with a low uncertainty can be performed. For details, how a χ^2 surface is calculated, see section 2.3.

Also shown are the correlated uncertainties in a (blue, dashed lines). These uncertainties are gained from the projection of the ellipsoid onto the a-parameter axis, cf. fig. 2.20.

uncorrected aSPECT data. This can also be seen at the low deviation $\epsilon = 3 \times 10^{-10}$ of the real χ^2 surface from a perfect ellipsoid, cf. section 2.3.

So even without correction of the experimentally enhanced systematics a valid global fit can be performed. The relative uncertainty of 0.82 % of this global fit is already very low. But a closer look to fig. 3.16 shows a very low confidence level of 0.0001. This mean, it is extremely unlikely that the observed fluctuation is due to a pure statistically one. Furthermore, keep in mind, all configurations in fig. 3.16 are still subject to common systematic effects, like edge effect. So the value gained in this first investigation might already be precise, but not necessarily accurate. So to gain a precise and accurate value, with a good confidence level, the common systematics have to be corrected. In the next section the experimentally enhanced systematics of aSPECT will be investigated and first hand corrections to the fit function applied, leading to a lower fluctuation of a and therefore an improved value of a.

3.3.2. First Hand Corrections of the Experimentally Enhanced Systematics

In the previous section the individual configurations used during the beam-time 2013 have been fitted without any correction for the edge effect or electro-static mirror off. These two systematics have been experimentally enhanced, e.g. a reduced neutron beam profile
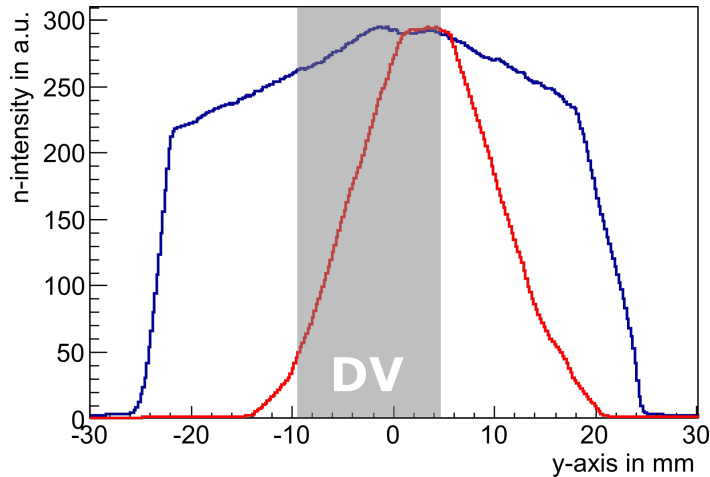
Figure 3.18.: Neutron beam profiles used during the beam-time 2013. In blue is drawn the normal/wide profile used for config 1,2,3,7,8, and in red the reduced one, used for config 4,5,6. Using two different beam profiles allows to determine the edge effect with higher precision, as the effect is strongly enhanced for the reduced beam profile. Also drawn is the region of the DV, which is projected onto the detector.

has been used for the configurations 4, 5, 6. In the next two sections corrections for the edge effect and B-, E-fields in the DV (mirror off) are determined and implemented into to the fit function. These corrections are first estimates only, to check if the systematic effects are understood accordingly and not meant to be a final analysis. Short comings of these first hand corrections, as well as a way to solve these short comings are discussed in section 3.3.4.

3.3.2.1. Edge Effect

All measurements of aSPECT are biased by the edge effect, see section 2.2.2. In the configurations 4, 5, 6 this effect has been experimentally enhanced by at least an order of magnitude. This allows to investigate the effect in more detail and therefore improve the correction of it. In this section an estimate for edge effect will be done. This estimate allows to check, if the bias of the enhancement of the edge effect is corrected in the right direction and in the right order of magnitude. In fig. 3.18 the two neutron beam profiles used during the beam-time 2013 are shown. In blue the normal/wide profile used for the standard measurements (config 1,2,3,7,8), in red the narrow/reduced profile for the enhancement of the effect is drawn (config 4,5,6). Further, the area of the profile, which is projected onto the detector pad 2 (channel 20) is shown as grey area. For details, how these profiles have been measured and the projection is determined, see section 2.2.2. Clearly for both profiles an edge effect is present, with a strong enhancement of the effect for the reduced profile.

The general idea to determine the correction of the edge effect is the following: for each proton energy T_0, the maximal gyration radius r_{max} is determined. This maximal gyration radius determines then the size of area around the edges of the DV from which additional protons are gained/lost. As the gain/loss is proportional to the neutron beam intensity at the place of decay y, it is determined for each y position separately and then added up. By subtraction the gain from outside of the DV from the loss inside of the DV, one

(a)   (b)
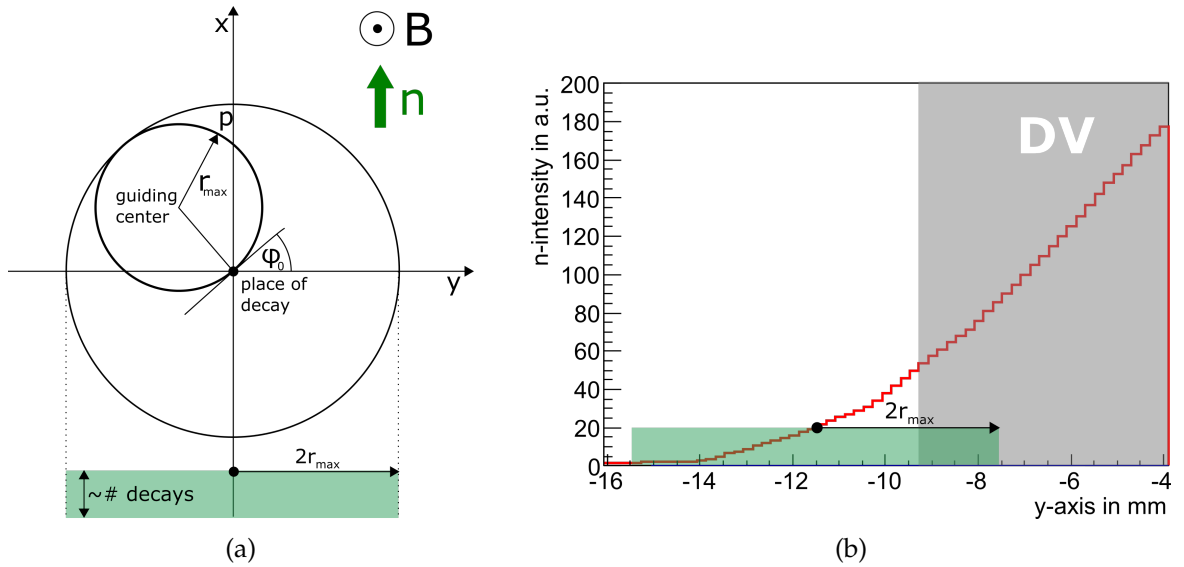
Figure 3.19.: Principle for quantitative determination of the edge effect:
(a) Shown is the gyration of a proton p around its guiding center (inner circle). This proton has been emitted from the place of decay under an azimuthal angle φ_0. The maximal radius r_{max} the proton can have, is realized under a polar angle of $\theta_0 = 90°$. r_{max} depends on the proton energy T_0 (eq. (3.22)). For isotropic distributed emission the probabiltiy of the proton to be detected within the $4r_{max}$ (outer circle) is given by the Point-Spread-Function (PSF). As for aSPECT the divergence of the neutron beam in x-direction is negligible, only the y-direction is of interest, hence the PSF can be reduced to a projection onto the y-axis. This projection is a constant (green rectangle) [DRM+14], which is scaled by the number of neutron decays, or in other words the neutron intensity.
(b) Zoom into the "left" edge y_{left} of the DV for the reduced beam profile. Also shown is the probability of a proton from a decay at $y = -11.5$ mm to be detected within a $2r_{max}$ radius (green rectangle). This proton should not be detected, as it originates from outside the DV. But there is a certain probability for it to be detected, here shown as overlap of the gray DV area and the green probability area. This overlap corresponds to the gain of protons, which can be calculated by summing up all probabilities for $y < y_{left}$ (eq. 3.24). The loss is calculated the same way for $y > y_{left}$ (eq. 3.25). The difference between these two is the net gain/loss for a given T_0. By determining this net gain/loss for all proton energies, a correction for the edge effect is determined, see fig. 3.20. For details, see text.

gets the nett gain/loss at the edges. This is then the nett gain/loss for one given energy only. Performing the whole calculation for all proton energies, one can determine the energy dependent proton gain/loss. This energy dependent gain/loss is then implemented as correction into the differential proton spectrum $\omega_{0C\alpha}$, which is then used to determine a corrected fit function.

The maximal gyration radius r_{max} can be calculated by setting the Lorentz force equal to the centripetal force, resulting in

$$r_{max}(T_0) = \frac{p_p}{eB_{DV}} = \frac{\sqrt{T_0(T_0 + 2m_p)}}{eB_{DV}}. \tag{3.22}$$

Here, p_p is the proton momentum, T_0 the kinetic proton energy, m_p the mass of the proton, B_{DV} the magnetic field in the DV, e the elementary charge. The light velocity is set to $c \equiv 1$. In case of aSPECT the maximal gyration radius for a proton with $T_0 = 751.4\,\text{eV}$ and $\theta_0 = 90\,^\circ$ is $r_{max} \approx 1.8\,\text{mm}$. In fig. 3.19a the top view onto the gyration of a proton in the magnetic field is drawn. The proton is emitted under an azimuth angle φ_0 and a polar angel $\theta_0 = 90\,^\circ$. As one sees, the proton can be detected at a maximal distance of $2r_{max}$ from the place of decay (small circle in fig. 3.19a). Considering many decays with an isotropic emission of protons in φ_0 and θ_0, the area, in which protons can be detected is a circle with an radius of $2r_{max}$ (big circle in fig. 3.19a). The density distribution within this circle is described by the Point-Spread-Function (PSF). For aSPECT the divergence of the neutron beam in x-direction within the DV is very small, so the PSF can be reduced to its projection in y-direction. This projection is uniform in y-direction [DRM$^+$14] and shown in fig. 3.19a as green rectangle. The height of this projection is proportional to the number of decays/protons emitted. In fig. 3.19b a zoom into the "left" edge of the DV is drawn, including the projection of the PSF for protons emitted at $y = -11.5\,\text{mm}$. This position is outside of the actual DV, which is projected onto the detector. Hence, protons from decays at this position should not be detected in the ideal case. Nevertheless, there is a certain probability p_{gain}, that they are detected. This probability corresponds to the overlap of the projection of the PSF (green rectangle) and the DV

$$p_{gain/loss} = (y - y_{left}) \cdot I(y) \qquad \text{with} \quad |y - y_{left}| \le 2r_{max}(T_0), \tag{3.23}$$

with y_{left} the position of the "left" edge of the DV and $I(y)$ the intensity of the neutron beam at the place y. For places $y < y_{left}$ are additional protons gained, for places $y > y_{left}$ protons are lost. This gain/loss is then the sum over all y

$$\Gamma_{gain}(T_0) \quad = \quad \sum_{y=y_{left}-2r_{max}(T_0)}^{y_{left}} (y - y_{left}) \cdot I(y), \tag{3.24}$$

$$\Gamma_{loss}(T_0) \quad = \quad \sum_{y=y_{left}}^{y_{left}+2r_{max}(T_0)} (y - y_{left}) \cdot I(y). \tag{3.25}$$

The net gain/loss $\Gamma_{net}(T_0)$ of protons is then the difference between $\Gamma_{gain}(T_0)$ and $\Gamma_{loss}(T_0)$.

$$\Gamma_{net}^{left}(T_0) = \Gamma_{gain}(T_0) - \Gamma_{loss}(T_0). \tag{3.26}$$
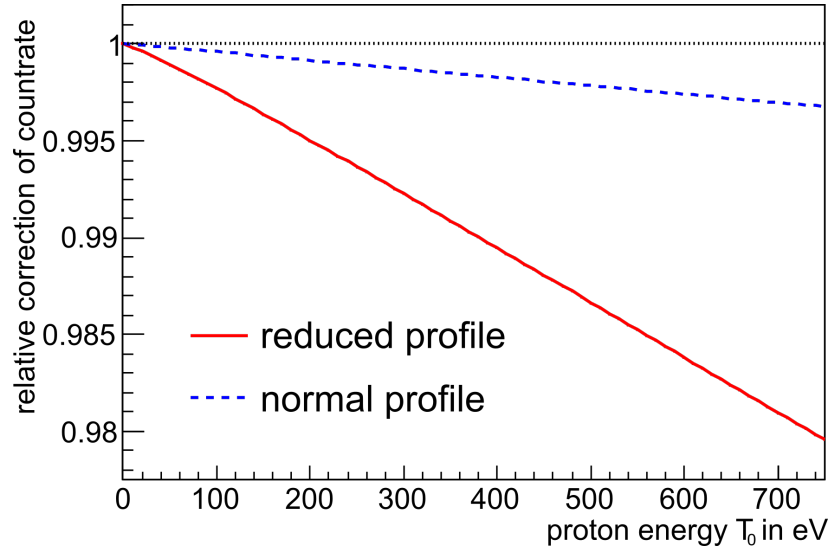
Figure 3.20.: Relative correction $\left\{1 - \Gamma_{net}^{norm}(T_0)\right\}$ (eq. (3.28)), due to the edge effect for the normal (blue, dashed line) and reduced (red, solid line) beam profile. Also drawn is the ideal case of an uniform beam profile, without edge effect, as black dotted line at 1. For measurements with the normal profile the correction is up to $-0.3\,\%$ for the highest proton energies. For the reduced profile, it is up to about $-2\,\%$.

Including these corrections in the fit of *a* shifts the values of *a* by about $10\,\%$ for the configurations with reduced beam profile (config 4,5,6) and about $1\,\%$ for all others, cf. fig. 3.26.

Please be aware, so far just the "left" edge of the DV has been considered. The calculation for the "right" edge is exactly the same, only the protons emitted at $y < y_{right}$ are lost and protons emitted at $y > y_{right}$ are gained. This results in a total gain/loss

$$\Gamma_{net}(T_0) = \Gamma_{net}^{left}(T_0) + \Gamma_{net}^{right}(T_0). \tag{3.27}$$

This total gain/loss is then normalized to the neutron beam intensity inside the DV to achieve a relative gain/loss

$$\Gamma_{net}^{norm}(T_0) = \frac{\Gamma_{net}(T_0)}{\sum_{y_{left}}^{y_{right}} I(y)}. \tag{3.28}$$

This correction is determined for the normal and reduced neutron beam profile. In fig. 3.20 the relative correction $\left\{1 - \Gamma_{net}^{norm}(T_0)\right\}$ is drawn for the normal (blue, dashed line) and reduced (red, solid line) beam profile. The 1 corresponds to an ideal uniform neutron beam profile, which has no edge effect. In case of the normal and reduced beam profiles protons are lost and, as expected, the loss increases with proton energy, due to the bigger r_{max}. This energy dependent correction is almost perfect linear and can be up to about $2\,\%$ in case of the reduced beam profile.

To implement the correction for the edge effect into the fit function f_{fit} (eq. 3.15) the

relative correction $\left\{1 - \Gamma_{net}^{norm}(T_0)\right\}$ is multiplied with the theoretical proton spectrum

$$\omega_{corr\ edge}(T_0) = \omega_{0C\alpha}(T_0) \cdot \left\{1 - \Gamma_{net}^{norm}(T_0)\right\}. \tag{3.29}$$

The corrected proton spectrum $\omega_{corr\ edge}(T_0)$ is then used as input spectrum, instead of $\omega_{0C\alpha}(T_0)$ in eq. 3.15. This has been done for the normal and reduced beam profile separately, leading to two new fit functions. One corrected for the edge effect of the normal and one for the reduced beam profile. Using these corrected fit functions, the different configurations from the beam-time 2013 has been refitted resulting in new *a* values, see fig. 3.26. Please be aware, this ideogram also includes a correction for E- and B-fields in the DV, which effects mostly config 2 MirrOFF, see next section. One can immediately see, that the correction of the edge effect shifts config 4,5, and 6 by about 10 % to more positive *a* values compared to fig. 3.16. Please keep the normalization in mind. The configurations measured with the normal neutron beam profile on the other hand are only shifted by about 1 % to more positive values. Having the correction for the edge effect applied, the fluctuations of *a* values, due to the enhancement of the edge effect, could be reduced significantly. Hence, already this relative simple correction works very well and shows, that the edge effect is understood qualitatively. For a detailed discussion of the effects of the correction, see section 3.3.3. For shortcomings of this method and the idea how to correct the edge effect in the final analysis, see section 3.3.4.

3.3.2.2. Electro-Static Mirror

In the previous section a correction for the edge effect has been determined. In this section a correction for config 2 MirrOff in fig. 3.16 will be investigated and implemented into the fit function. At first glance, one might ask, why there is a difference between the two settings of config 2 with electro-static mirror ON and OFF? By turning off the electro-static mirror, only protons emitted towards the upper hemisphere of *a*SPECT can be detected. Hence, turning off the mirror should decrease the measured countrate by a factor of 2, but not change the shape of the measured proton spectrum. But turning off the electro-static mirror makes the measurement highly sensitive to inhomogeneities of the electric potential Φ_0 and/or the B-field B_{DV} in the DV electrode. Any inhomogeneity of Φ_0 and/or B_{DV} will slightly modify the phase space of the protons leaving the DV. This change in phase space will then cause a slightly different shape of the proton recoil spectrum, hence a different *a* value. Therefore, a difference in the MirrON and MirrOFF measurement is a hint to inhomogeneities inside the DV electrode.

In case of the B-field a gradient inside the DV is applied on purpose, see fig. 3.21. The reason for that is simple: a completely homogeneously flat B-field can experimentally not be achieved, therefore a gradient facing towards the AP (positive z-values) has been applied. This gradient ensures, that protons emitted under a polar angel $90° \leq \theta_0 \leq \theta_{crit}^{DV}$ (flying towards neg. z-values) are reflected, due to the magnetic mirror effect and can be detected. The critical angle θ_{crit}^{DV} depends on the magnetic field strength at the place of the decay B_0 and the maximal field strength the proton experiences B_{max}. So by applying a gradient in the DV protons close to $\theta_0 \approx 90°$ are reflected towards the AP. A gradient in the opposite direction would cause on the other hand a proton trap between the DV and the electro-static mirror, which would change the phase space of the protons leaving the DV and therefore the measured *a* values. To avoid this trap, the gradient facing towards the AP has been applied.

For measurements with the electro-static mirror ON, this B-field gradient has no influence on the measured a value, as all protons emitted towards negative z-values are either reflected at the B-field gradient, or the electro-static mirror. For the measurement without the electro-static mirror (config 2 MirrOFF), the B-field gradient causes a slightly higher countrate, than the expected 50 % compared to measurement with electro-static mirror. To determine this additional countrate, the B-field gradient in the DV region has to be known with high precision, in order to calculate θ_{crit}^{DV}. This B-field gradient was measured with a hall probe and a NMR system in 2013 with high precision [Sch17] and is shown in fig. 3.21. The measured gradient is then used, to calculated the critical angle

$$\theta_{crit}^{DV} = \arcsin \sqrt{\frac{B_0}{B_{max}^{DV}}} \approx 91.5\,^\circ. \tag{3.30}$$

Here, B_0 is the B-field in the middle of the DV ($x = y = z = 0$) and B_{max}^{DV} the local B-field maximum below the DV at $z \approx -0.06$ m. $\theta_0 = 0$ corresponds to protons emitted directly towards the AP, hence protons with $90\,^\circ < \theta_0 \lesssim 91.5\,^\circ$ have a slight initial momentum towards the mirror and are reflected at the B-field gradient. This critical angle θ_{crit}^{DV} causes an additional countrate of resulting in 51 %, relative to the MirrON measurement. But θ_{crit}^{DV} is energy independent, therefore it alone would not change the shape of the proton recoil spectrum. The change of the measured proton spectrum arises from the inverse magnetic mirror effect in the AP. The magnetic field ratio r_B of aSPECT causes only a 80 % conversion of the protons initial perpendicular momentum in the AP. As the endpoint of the proton spectrum is 751.4 eV, this 80 % conversion means protons emitted with $\theta_0 = 90\,^\circ$ can only overcome retardation voltages up to 601 V. For higher voltages, protons emitted close to $90\,^\circ$ can not overcome the AP, no matter what their initial energy T_0 was.

To determine the effect of θ_{crit}^{DV} onto the measured proton spectrum, it is implemented into the Transmission Function. To do so, a short review is given, how the normal Transmission Function of aSPECT is calculated, after that will be explained how θ_{crit}^{DV} is implemented to the Transmission Function. The normal Transmission Function with the electro-static mirror ON is given in eq. (2.6). Here, T_{tr}^{min} denotes the minimal energy required to pass the analysing plane and T_{tr}^{max} the energy a proton will pass the analysing plane independent of its emission angle

$$T_{tr}^{min} \quad = \quad T\left(\theta_0 = 0^\circ\right) = eU_{ret}, \tag{3.31}$$

$$T_{tr}^{max} \quad = \quad T\left(\theta_0 = 90^\circ\right) = \frac{eU_{ret}}{1 - r_B}. \tag{3.32}$$

Protons with $T_{tr}^{min} < T_0 < T_{tr}^{max}$ can only pass the retardation voltage U_{ret}, if their emission angle is below

$$\theta_0 < \theta_{tr}^{AP} = \arcsin \sqrt{\frac{B_0}{B_{ret}} \left(1 - \frac{eU_{ret}}{T_0}\right)}. \tag{3.33}$$

Please be aware of the difference between the two critical angles. θ_{crit}^{DV} is the critical angle between B_0 and the local B-field maximum in the DV, whereas θ_{crit}^{AP} is the critical angle between the B-field minimum B_{ret} in the AP and B_0. The probability of a proton with $T_{tr}^{min} < T_0 < T_{tr}^{max}$ to overcome the retardation voltage is

$$\omega_{tr}(T_0) = \int_0^{\theta_{tr}^{AP}(T_0, U_{ret})} d\theta \sin\theta = 1 - \sqrt{1 - \frac{B_0}{B_{ret}} \left(1 - \frac{eU_{ret}}{T_0}\right)}. \tag{3.34}$$
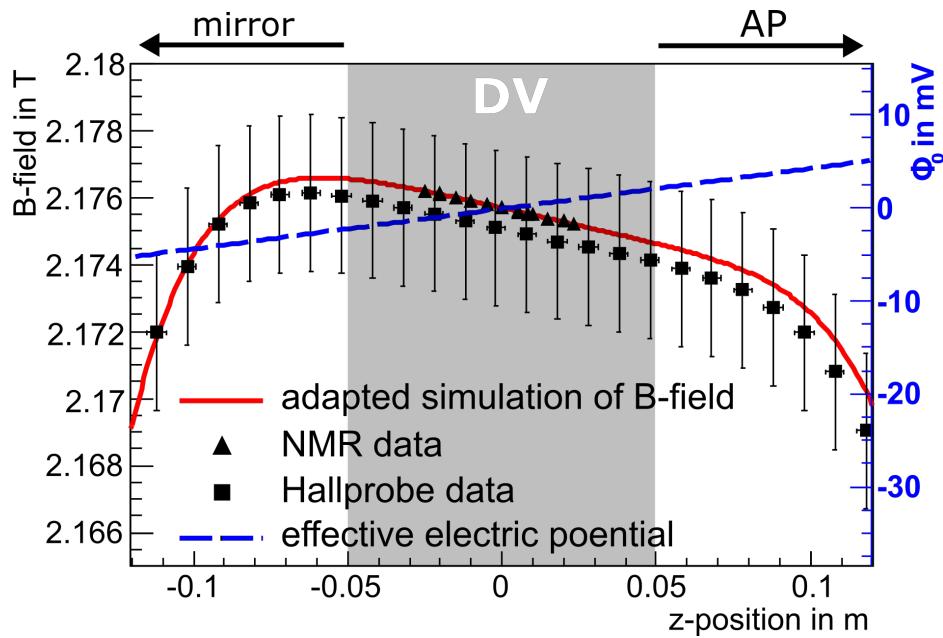
Figure 3.21.: B- and E-field in the DV region. The B-field has been measured with a Hallprobe (rectangles), as well as with a NMR system (triangles). Please be aware, that the error bars of the NMR measurement are smaller than the marker size. To this measurement a B-field simulation has been adapted (red, solid line). The increasing B-field towards negative z-values causes a magnetic mirror effect for protons emitted close to $\theta_0 \approx 90°$, reflecting protons towards the AP. The effect of this magnetic mirror on the countrate ratio mirror off/on is shown in fig. 3.23. This magnetic mirror effect alone can not explain the observed countrate ratio and the shift of the a value of config 2 MirrOFF. From the surface contact potential measurements a difference in the potential of the DV is known, therefore an effective electric potential Φ_0 (blue, dashed line) has been taken into account for this consideration. This increasing potential counteracts to some extend the magnetic mirror. Combining both effects explains the observed countrate ratio and the shift in a of config 2 MirrOFF. For details, see text.

In case the electro-static mirror is switched off all protons emitted with $90° < \theta_0 < \theta_{crit}^{DV}$ are reflected at the local B-field maximum B_{max}^{DV}. To account for this, eq. (3.34) has to be adapted

$$\omega_{tr}^{off}(T_0, \tilde{\theta}_{crit}) = N \cdot \left(\int_0^{\theta_{tr}^{AP}(T_0, U_{ret})} d\theta \sin\theta + \Theta\left(\theta_{tr}^{AP} - \tilde{\theta}_{crit}\right) \cdot \int_{\tilde{\theta}_{crit}}^{\theta_{tr}^{AP}(T_0, U_{ret})} d\theta \sin\theta \right) \quad (3.35)$$

Here, N is a normalisation factor, Θ is the Heaviside function and ensures the 2$^{\text{nd}}$ integral is only considered for $\tilde{\theta}_{crit} \leq \theta_{tr}^{AP}$, with $\tilde{\theta}_{crit} = \pi - \theta_{crit}^{DV}$. The normalisation factor can be derived from $\omega_{tr}^{off}(T_{tr}^{max} = T(90°)) \stackrel{!}{=} 1$ to

$$N = \frac{1}{1 + \cos(\tilde{\theta}_{crit})}. \quad (3.36)$$

Solving eq. (3.35) leads then to a new Transmission Function, including θ_{crit}^{DV}

$$F_{tr}^{off} = \begin{cases} 0 & \text{if } T_0 \leq T_{tr}^{min} \\ \dfrac{1 - \sqrt{1 - \frac{B_0}{B_{ret}}\left(1 - \frac{eU_{ret}}{T_0}\right)}}{1 + \cos(\tilde{\theta}_{crit})} & \text{if } T_{tr}^{min} < T_0 < T_{crit} \\ 1 - \dfrac{2 \cdot \sqrt{1 - \frac{B_0}{B_{ret}}\left(1 - \frac{eU_{ret}}{T_0}\right)}}{1 + \cos(\tilde{\theta}_{crit})} & \text{if } T_{crit} \leq T_0 \leq T_{tr}^{max} \\ 1 & \text{if } T_0 > T_{tr}^{max} \end{cases}, \quad (3.37)$$

with

$$T_{crit} = \frac{eU}{1 - \frac{B_{ret}}{B_0}\sin^2(\tilde{\theta}_{crit})}. \quad (3.38)$$

The critical energy T_{crit} is the energy of protons emitted at θ_{crit}^{DV}, which can still pass the retardation voltage. Hence, in the energy region $T_{crit} \leq T_0 \leq T_{tr}^{max}$ additional protons from the reflection in the local B-field maximum B_{max}^{DV} have to be taken into account. Comparing eq. (2.6) and eq. (3.37) shows, that this is exactly the energy region, where the two Transmission Functions differ from each other, expect for the normalisation factor. In fig. 3.22 the two Transmission Functions for a retardation voltage of 400 V are drawn. One can clearly see the additional countrate from protons with $T_{crit} \leq T_0 \leq T_{tr}^{max}$, due to the B-field gradient in the DV. This reflection then causes a countrate of 51 % for measurements with electro-static mirror off, compared to measurements with mirror on. Using the two Transmission Functions the countrate ratio between MirrOFF and MirrON has been calculated, see fig. 3.23. Here is drawn in black points the measured count rate ratio from config 2, as well as in red (dashed line) the expected countrate ratio from two Transmission Functions. Please be aware, that the 780 V measurements have been subtracted from these measurements, to clear the data points from any background influence. The calculation from the Transmission Functions shows nicely the drop of the countrate ratio for higher retardation voltages caused by the incomplete conversion of the proton momentum. For retardation voltages $U_{ret} \geq 601$ V the difference between the two Transmission function vanishes, as $\theta_{crit}^{DV} > \theta_{crit}^{AP}$, so the protons additionally reflected at θ_{crit}^{DV} can not overcome the the retardation voltage any more. But the calculation also shows a far higher expected count rate ratio of 51 % for lower retardation voltages, than the experimentally observed 50.4 %. This difference in countrate ratios hints to more than just a B-field gradient inside the DV electrode.
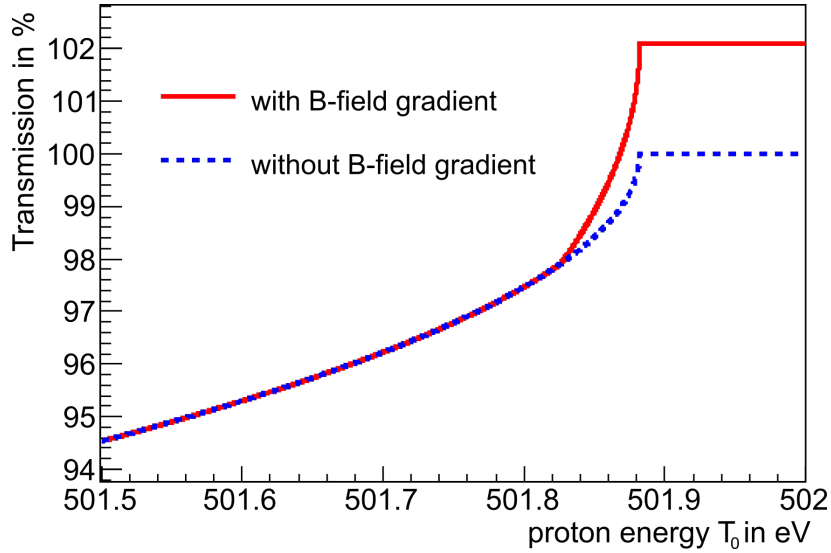
Figure 3.22.: Transmission Function with and without B-field gradient. Shown is a zoom into the standard Transmission Function F_{tr} (eq. (2.6)) for $U_{ret} = 400\,\text{V}$, as well as the adapted Transmission Function F_{tr}^{off} (eq. (3.37)) for the same retardation voltage. Protons emitted with a polar angle $90° \leq \theta_0 \leq \theta_{crit}^{DV}$ (eq. (3.30)) have to counted additionally, due to the magnetic mirror effect in the DV. The adapted Transmission Function F_{tr}^{off} includes these additional protons. Using these two Transmission Functions, the effect of the magnetic mirror effect has been calculated, see fig. 3.23. For details, see text.

As already mentioned, not only the B-field gradient in the DV causes a change of the phase space of the protons leaving the DV, but also inhomogeneities in the electric potential Φ_0 inside the DV will influence the phase space of the protons. This influence can be a slight retardation voltage, or various ExB drifts inside the DV. A slight retardation voltage inside the DV itself would trap a small fraction of the protons with low energy and polar angles close to $\theta_0 \approx 90°$. Hence, these protons would not be detected and therefore a wrong a values be measured. The effect of ExB drifts inside the DV is more complex. Such drifts change the "position" of the DV. The DV is defined as the region of the neutron beam, that is projected onto the detector. This region has been determined with a wire scan for the magnetic projection, see section 2.2.2 and [Vir13]. This magnetic projection changes, if the protons experience an ExB drift, either one applied on purpose in a ExB electrode, or unwanted one, due to inhomogeneities in the electric potential of the DV electrode. Further, ExB drifts are caused by the Lorentz force (eq. (2.1)), which depends on the velocity of the proton and therefore on its energy. So drifts can result in a very irregular shaped DV, which even depends on the energy of the protons. Hence, inhomogeneities in Φ_0 are not only increasing the uncertainty of the Transmission Function, see section 2.2.1, but also cause additional effects, changing the measured a value.

Inhomogeneities of the electric potential originate from fluctuations of the surface contact potential and/or field leakage, see section 2.2.1. These sources, especially the fluctuation of the surface contact potential, cause a complex distribution of the electric potential inside the DV electrode, causing E-fields of different direction and strength. To determine this
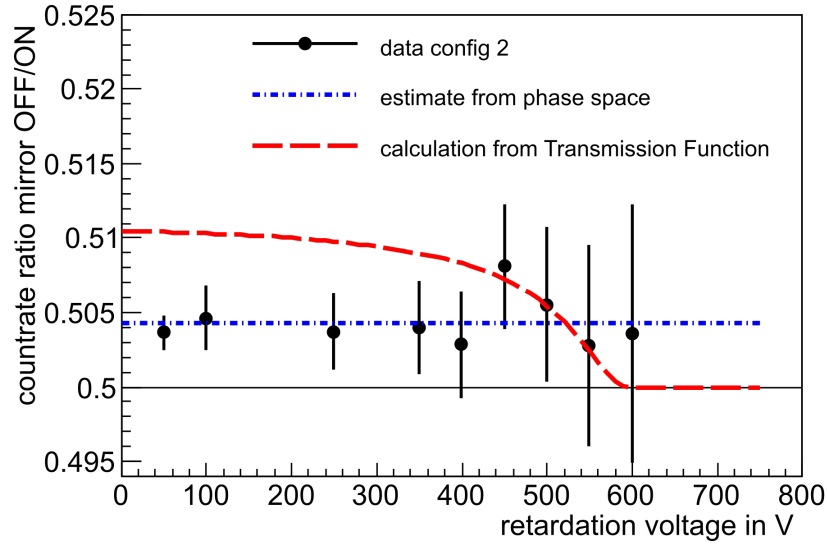
Figure 3.23.: Countrate ratio of measurements with and without electro-static mirror for the different retardation voltages measured. Here, the 780 V measurement has been subtracted from the individual measurements to see the effect of the mirror OFF-ON on the protons only. The ratio measured is in average $\frac{\Gamma_{OFF}}{\Gamma_{ON}} \approx 50.4\%$. Expected is a ratio of about 51%, due to the magnetic mirror effect in the DV. This number has been calculated using the two Transmission Function F_{tr} and F_{tr}^{off} and decreases for higher retardation voltages (red, dashed line), due to the incomplete conversion of proton momentum in the AP. The discrepancy between observed and expected countrate ratio can be explained by an effective electric field inside the DV (cf. fig. 3.21). With this electric field a correction has been found (cf. fig. 3.24), which explains the observed shift in *a* for the config 2 MirrOFF measurement. From this correction also an estimate of the reflected phase space, compared to the total phase space could be gained (eq. (3.46)). This estimate is shown here as blue, dash dotted line and can explain the observed countrate ratios.

distribution, including work function fluctuations and field leakage, is a complex task. This task will be performed by [Sch17] for the final analysis. In this work only an effective electric field in z-direction will be assumed, to explain the reduced countrate ratio (fig. 3.23) and the shift of the *a* value (fig. 3.16) observed for the measurement with electro-static mirror off (config 2 MirrOFF).

A difference of about 100 meV in the surface contact potential between the top and bottom plate of the DV electrode has been measured [Kah15], potentially causing an electric field inside the DV electrode, see fig. 3.21. Such an electric field would counteract the magnetic field gradient and could explain the observed lower countrate ratio, than expected from the magnetic field gradient alone. To determine the exact effect of the electric field, the kinetic energy parallel to the magnetic field has been calculated along the z-direction

$$T_{kin\parallel}^{adiabatic}(z) = T_0 - e\left(\Phi(z) - \Phi_0\right) - \frac{B(z)}{B_0}T_0 \sin^2\theta_0. \tag{3.39}$$

Here T_0 and θ_0 are the initial energy and emission angle of the proton, respectively. Φ_0 and B_0 are the the electric potential and magnetic field at the point of emission, whereas $\Phi(z)$ and $B(z)$ are the electric potential and magnetic field at the place z. Equation (3.39) is used to determine, if a proton originating from the center of the DV ($z = 0$) is either reflected at the electric field, or the magnetic field gradient. To do so, eq. (3.39) has been solved for the each point of the phase space ($0 \leq \theta_0 \leq \pi$, $0 \leq T_0 \leq 751.4$ eV), at each $z \pm 10$ cm around the center of the DV. The actual calculation has been performed using a Mathematica script [Wol15], calculating the kinetic energy $T_{kin\parallel}^{adiabatic}$ for each z in the range from -10 cm to 10 cm in 1 mm steps, for each initial energy T_0 in 1 eV steps and each initial polar angle θ_0 in $0.0216°$ steps. $B_0 = 2.178$ T is known from measurement. For the effective electric field a strength of -0.5 Vm^{-1} has been assumed, as educated guess from the measurements of the surface contact potential and first simulations of the field leakage. This calculation is in a second step check for zero-crossings of $T_{kin\parallel}^{adiabatic}$. A kinetic energy of $T_{kin\parallel}^{adiabatic} = 0$ means the proton has stopped and will be reflected. Depending on the position of the zero-crossing, the direction of the reflection can be determined. Keep in mind, the protons considered here originate from $z = 0$ only, then the direction of the reflection is given by

$$T_{kin\parallel}^{adiabatic}(z < 0) \leq 0 \quad \text{reflection towards AP,} \tag{3.40}$$

$$T_{kin\parallel}^{adiabatic}(z > 0) \leq 0 \quad \text{reflection towards mirror.} \tag{3.41}$$

Protons reflected below the origin (eq. 3.40) are reflected towards the AP and have to be counted additionally. Protons reflected above the origin (eq. 3.41) are reflected towards the mirror and are lost in a mirror off measurement. The result of this comparison is shown in fig. 3.24. Depicted is the region of phase space, influenced by the magnetic field gradient and the effective electric field in the DV. In blue is drawn the phase space reflected towards the mirror (eq. 3.41), in red the one reflected towards the AP (eq. 3.40). As can be seen, only protons emitted with an angle close to 90° are affected, protons with high/low angles (high momentum in z-direction) will simply overcome the gradient/field. For protons with an initial angle between $90° < \theta_0 < 91.2°$ and an energy of 56 eV $\leq T_0 \leq 751$ eV (red area), the dominant effect is the magnetic mirror effect in the DV. In eq. (3.30) the critical angle has been calculated to $\theta_{crit}^{DV} \approx 91.5°$ for a magnetic mirror only. But the magnetic mirror is now influenced by the presence of an electric field, so the critical angle gets lowered, due to the
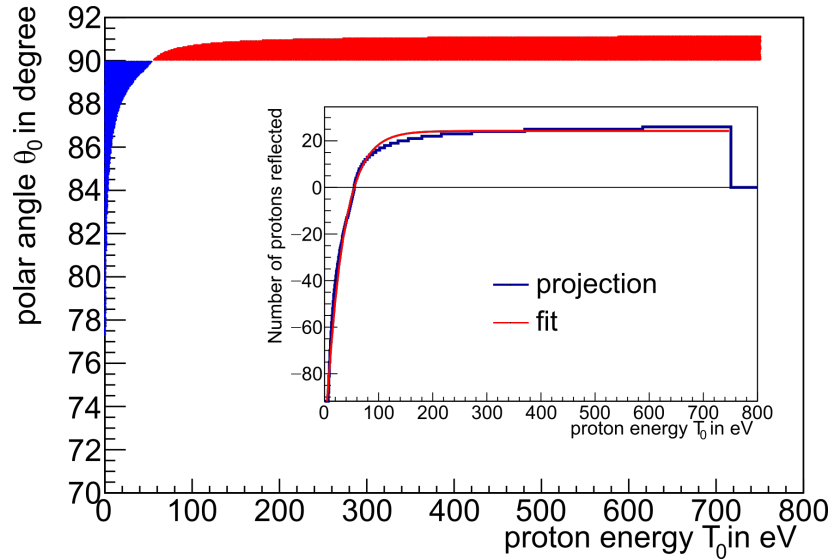
Figure 3.24.: Initial phase space of protons reflected in the DV. Depicted are the initial polar angle θ_0 vs. initial energy T_0 of protons being reflected at the magnetic mirror and/or electric field inside the DV. In blue is drawn the area of initial phase space being reflected towards the electro-static mirror, due to the electric field. In red is shown the area reflected towards the AP, due to the magnetic mirror effect. As inset is drawn the projection of this reflected phase space onto the the energy axis. To this projection an exponential is fitted, which is used to correct the differential proton spectrum. For details of this phase space consideration and the gained correction from it, please see text.

retardation of the electric field to 91.2° for the highest proton energies. For lower energies, the angle gets reduced further, till it vanishes for energies below 56 eV. In the small energy region between 54 eV $< T_0 <$ 56 eV the magnetic mirror effect and the electric field cancel each other, hence no reflection occurs and the protons keep flying in their initial direction. For energies below 54 eV the influence of the electric field is stronger than the magnetic mirror effect. For energies between $0 \leq T_0 \leq 54$ eV and angles between $77.5° \leq \theta_0 < 90°$ (blue area) the protons are reflected, due to the electric field, towards the mirror and can not reach the AP/detector. These protons are therefore lost in a mirror off measurement.

The correction for the reflection of protons due to magnetic mirror effect/electric field inside the DV electrode is done in a similar way, as for the edge effect. First a function $corr^{fields}_{gain/loss}(T_0)$, describing the energy dependent correction is determined. This function is then multiplied with the differential spectrum $\omega_{0C\alpha}$ resulting in an energy weighted correction ω_{fields}. This energy weighted correction is then added to the original spectrum $\omega_{0C\alpha}$ by a relative weight factor w^{fields}, determined by the fraction of the phase space being reflected.

The energy dependent correction is determined by a projection of the reflected phase space onto the energy axis, see inset fig. 3.24. This reduces the T_0, θ_0-dependence of the correction to a pure T_0-dependence, which can be implemented in f_{fit}. Here an exponential

$$corr_{gain/loss}^{fields}(T_0) = c_0 \cdot e^{c_1 \cdot T_0} + c_2 \tag{3.42}$$

is fitted to the projection, see red line in inset. This function is then multiplied with the differential energy spectrum (eq. (1.29))

$$\omega_{fields}(T_0) = \omega_{0C\alpha}(T_0) \cdot corr_{gain/loss}^{fields}(T_0). \tag{3.43}$$

Equation (3.43) is than added as correction with a weight w^{fields} to the original theoretical spectrum

$$\omega_{corr\ fields}(T_0) = \omega_{0C\alpha}(T_0) - w^{fields} \cdot \omega_{fields}(T_0). \tag{3.44}$$

The weight is the fraction of protons being reflected relative to the complete area of phase space

$$w^{fields} = \frac{\sum_{\theta_0} \sum_{T_0} \xi^{reflected}(\theta_0, T_0)}{\sum_{\theta_0} \sum_{T_0} \cos\theta_0 \omega_{0C\alpha}(T_0)}. \tag{3.45}$$

Here, $\sum_{\theta_0} \sum_{T_0} \xi^{reflected}(\theta_0, T_0)$ is the fraction of phase space being reflected, highlighted as blue and red areas in fig. 3.24. $\sum_{\theta_0} \cos\theta_0$ is the sum of the $\cos\theta_0$ distribution and $\sum_{T_0} \omega_{0C\alpha}(T_0)$ is the sum over total spectrum. $\sum_{\theta_0} \sum_{T_0} \cos\theta_0 \omega_{0C\alpha}(T_0)$ therefore the sum over the total phase space. Hence, eq. (3.45) denotes the relative fraction of the phase space being reflected over the total phase space. Sums had to be used, as the calculation of the reflected phase space with the Mathematica script could only be done in discrete steps.

In the same way the countrate ratio in fig. 3.23 has been calculated. To do so, the ideal case is considered without any reflections, due to magnetic mirror and electric field, which would be exactly 0.5 of the total phase space $\sum_{\theta_0} \sum_{T_0} \cos\theta_0 \omega_{0C\alpha}(T_0)$. To this ideal case the additionally reflected fraction of the phase space $\sum_{\theta_0} \sum_{T_0} \xi^{reflected}(\theta_0, T_0)$ is added and then divided by the total phase space, to get a relative number

$$\frac{cps_{MirrOFF}}{cps_{MirrorON}} = \frac{0.5 \cdot \sum_{\theta_0} \sum_{T_0} \cos\theta_0 \omega_{0C\alpha}(T_0) + \sum_{\theta_0} \sum_{T_0} \xi^{reflected}(\theta_0, T_0)}{\sum_{\theta_0} \sum_{T_0} \cos\theta_0 \omega_{0C\alpha}(T_0)} = 50.43\,\%. \tag{3.46}$$

Having determined the corrected differential spectrum $\omega_{corr\ fields}$ for the measurements with electro-static mirror off, it can be used as new input spectrum for the fit function f_{fit}, eq. 3.15. Config 2 MirrOFF shown in fig. 3.16 has been refitted, including the correction for the magnetic mirror effect and the electric field in the DV. The result of the refitting is shown in fig. 3.26. Please keep in mind, these data is also corrected for the edge effect. The implementation of both corrections is explained in section 3.3.3. The correction $\omega_{corr\ fields}$ shifted config 2 MirrOFF towards the mean of all other measurements and coincides with them within their uncertainties. Hence, the previously observed shift of config 2 MirrOFF can be explained by the magnetic mirror effect, combined with an effective electric field, inside the DV.

Why the Effective Electric Field in the DV is Negligible for Mirror On Measurements

The correction $\omega_{corr\ fields}$ can also be calculated for measurement with mirror on. Here, only the reflection, due to the electric field has to be considered, section 3.3.2.2. The effect of this correction of the effective electric field on all measurements with electro-static mirror
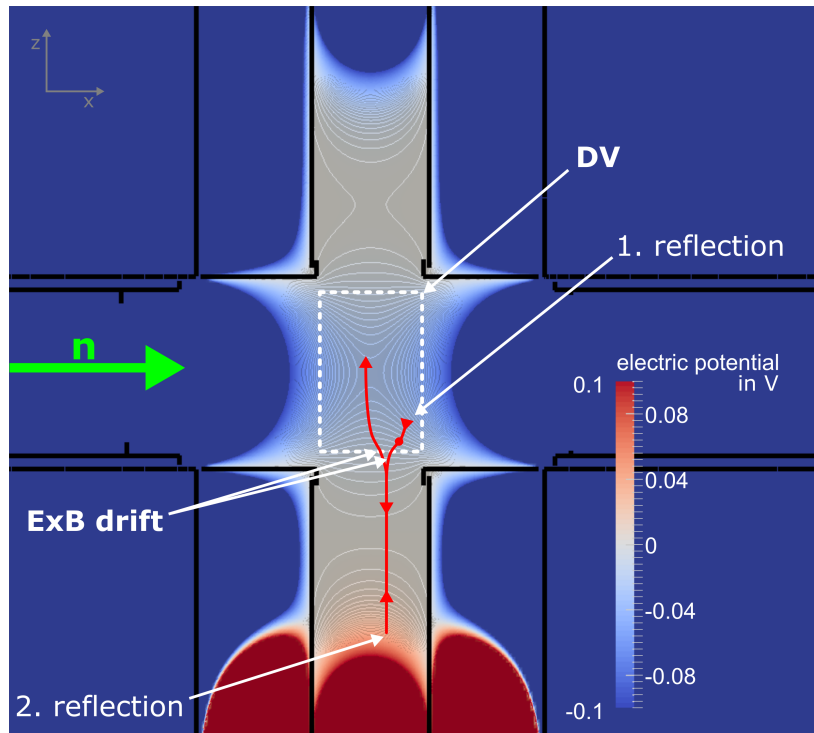
Figure 3.25.: Exemplary track of a proton in the DV. The proton decays in the DV (red dot) and has an initial momentum towards the AP. Due to a local electric field, it gets reflected towards the mirror (1. reflection). For measurements without electro-static mirror, this proton would be lost, for measurements with mirror the proton gets reflected towards the AP (2. reflection). In the ideal case the proton would be trapped between the two points of reflection. But due to local ExB drifts in the DV generated by inhomogeneities of the electric potential the proton can switch the magnetic field line. In this way the proton can pass the DV through a region with lower electric field and be detected. Hence, measurements with electro-static mirror on have a far lower sensitivity to local fields in the DV.

on is in the order of $\Delta a/a = 0.03\,\%$. There are two reasons for this, first the of the electric field effects only very low energetic particles $T_0 \leq 54\,\mathrm{eV}$ and second even more important the field is in reality not homogeneous. This non-homogeneous field causes local ExB drifts in the DV smearing out the magnetic field lines of the protons. In fig. 3.25 is shown an exemplary proton track from a decay in the DV. The proton decays in the DV (red dot) with a momentum towards the AP. Due to a local electric field it gets reflected (1. reflection) towards the mirror electrode. If the electro-static mirror is turned off this proton will be lost. If the mirror is turned on the proton gets reflected a second time (2. reflection) back towards the DV. In the ideal case it would take the same magnetic field line backwards, causing it to be trapped between the points of 1. and 2. reflection. But due to ExB drifts in the DV the proton can switch the magnetic field line. On this new magnetic field line the local electric field in the DV might be lower, so the proton can pass. In this way, protons, which should be trapped between DV and mirror electrode can still pass the local electric field. So turning

on the electro-static mirror reduced significantly the sensitivity to local electric fields inside the DV.

In principle, a proton could already be trapped inside the DV itself between a local electric field and the magnetic field gradient. In this case the proton would travel only a very small distance and therefore a change of the magnetic field line is unlikely. To test this local proton trapping a measurement has been performed, where the electrodes E3 and E6 have been set to 4 V and −4 V, respectively. In this way a strong additional electric field inside the DV is created, see fig. 2.9. This additional field counteracts the assumed electric field from the surface contact potential and is orders of magnitude stronger ($6 \, \mathrm{Vm^{-1}}$) than the assumed one ($-0.5 \, \mathrm{Vm^{-1}}$). If a significant amount of protons would be trapped inside the DV the a value of a measurement with additional field should differ significantly from a measurement without. Config 7 in fig. 3.26 has been measured with an additional electric field. As can be seen even without any correction of systematics config 7 coincides with config 1 within their uncertainties. Therefore, the effect of potentially trapped protons inside the DV is negligible.

3.3.3. Ideogram including First Hand Corrections

In the previous section a first correction for the edge effect $\omega_{corr\ edge}(T_0)$ (eq. (3.29)) and for the magnetic mirror effect/electric field in the DV $\omega_{corr\ fields}(T_0)$ (eq. (3.44)) has been determined. These two corrections are combined, to achieve a common correction

$$\omega_{corr}(T_0) = \omega_{corr\ edge}(T_0) + \omega_{corr\ fields}(T_0). \tag{3.47}$$

This corrected differential spectrum ω_{corr} is convoluted with the Transmission Function, resulting in a new fit function $f_{fit,w/\ corrections}$ including both corrections. Using this new fit function all configurations have been refitted, resulting in new, corrected values of $a_{w/\ corrections}$. Please be aware, the corrections implemented in ω_{corr} are first hand corrections only to check, if the systematics are understood qualitatively. Therefore, they are considered as certain within this theses. For the final analysis, they will be implemented as additional dimension to the fit similar as the background correction, including uncertainties. Hence, the uncertainties given here are not final and can still change. An ideogram of these corrected values $a_{w/\ corrections}$ is shown in fig. 3.26, these values have been normalised to the same value as the uncorrected ones shown in fig. 3.16. Comparing the two ideograms one can immediately see a significant reduction of the fluctuation of a values, due to the correction ω_{corr}. The standard deviation σ of the two ideograms reduces, by a factor of 3.5

$$\sigma_{w/o\ corrections} = 4.9\,\%, \tag{3.48}$$

$$\sigma_{w/\ corrections} = 1.4\,\%. \tag{3.49}$$

So the corrections have significantly reduced the fluctuations of the different configurations, that they coincide within their uncertainties. The correction for the edge effect shifted by about 10 % the configurations with reduced neutron beam profile (config 4, 5, 6) to lower values. All other configurations with normal neutron beam profile, are shifted in the sub-% region. The correction for the magnetic mirror/electric field inside the DV electrode shifts the configuration without electro-static mirror (config 2 MirrOFF) strongest by about 5 % to a higher value. All other values are shifted in the ‰-region, due to the correction of the electric field in the DV.
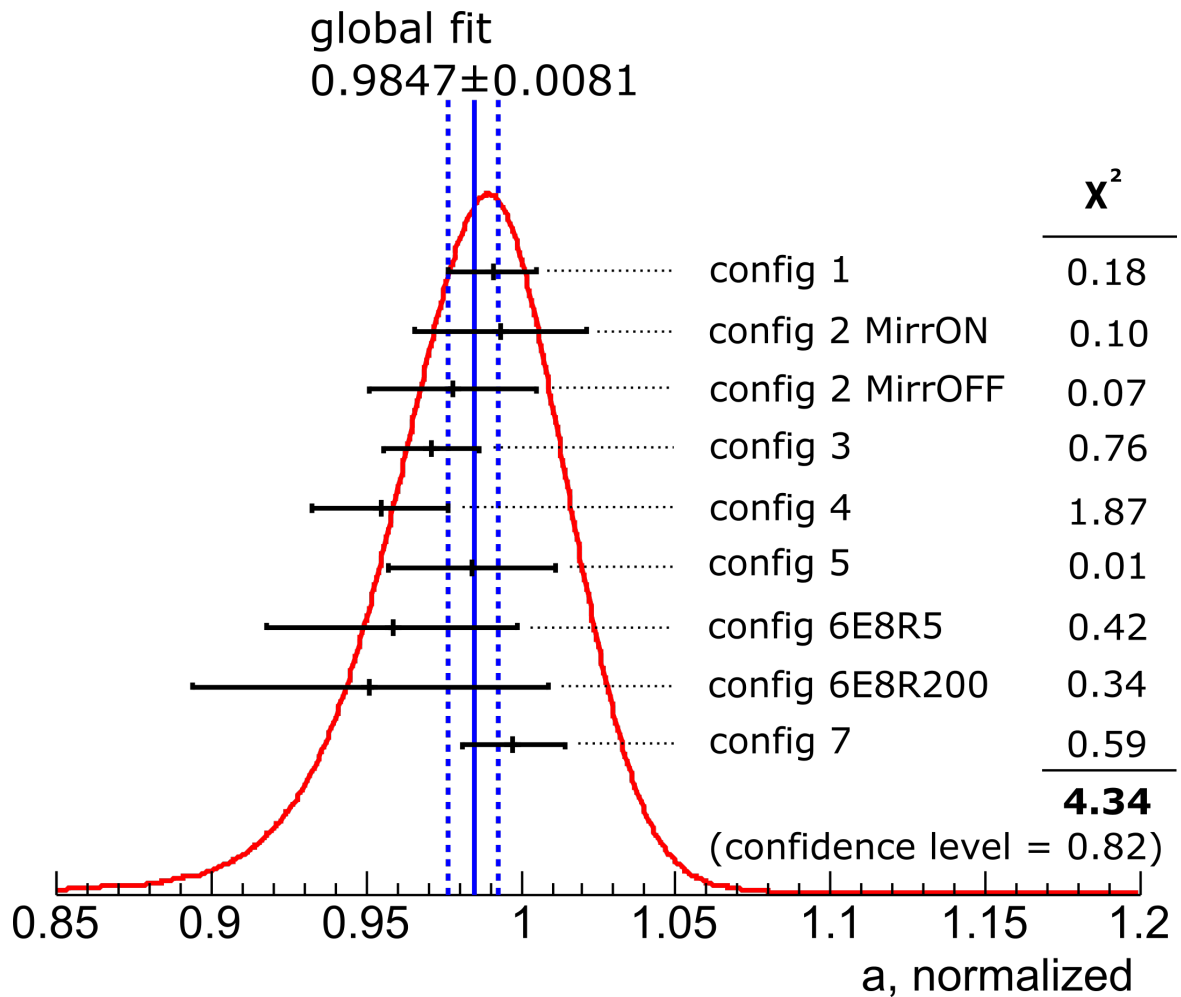
Figure 3.26.: Ideogram of the a values for the different configurations including first hand corrections as given in section 3.3.2. Although these are only first hand corrections, the standard deviation σ of the a values could be reduced significantly from $\sigma_{w/o\ corrections} = 4.9\%$ (cf. fig. 3.16) to $\sigma_{w/\ corrections} = 1.4\%$. The correction of the edge effect mainly shifted the values with the reduced neutron beam profile (config 4,5,6) by about 10 % to lower values. The correction of the inhomogeneities inside the DV electrode on the other hand shifted mainly config 2 MirrOFF by about 5 % to a higher value, so that all values coincide within their uncertainties.

Also shown is the result of a global fit (blue, vertical lines), including all configurations and first hand corrections. The result of this global fit is shifted significantly to a lower a value, as expected from the corrections. The individual values coincide with the global fit, leading to a far improved confidence level of 0.82. Hence, these data agree very well with a Gaussian distribution. The uncertainty of the global fit on the other hand did not decrease in the amount, as expected from the reduction of the standard deviation. This means the uncertainty is limited by missing systematics in the fit function and finally statistics. But the confidence level increased significantly to 0.82 compared to the uncorrected values shown in fig. 3.16. For a detailed discussion of these limitations, see text.

In the same way as for the uncorrected values, a global fit has been performed including all configurations at once with their individual corrections implemented. The result of this global fit is

$$a_{w/\ corrections}^{global} = 0.9847(81). \tag{3.50}$$

It is shown in fig. 3.26 as blue, vertical line with the uncertainty as dashed lines. The corrected value $a_{w/\ corrections}^{global}$ has been shifted significantly to lower values, compared to the one without corrections $a_{w/o\ corrections}^{global}$ (eq. (3.21)). This is expected from the implemented corrections, especially the correction of the edge effects shifts the value of $a_{w/\ corrections}^{global}$. Now the uncertainties of the individual values coincide with the on of the global fit, leading to a significantly better confidence level of 0.82. Hence, these values now agree very well with a Gaussian distribution. But comparing the uncertainties of $a_{w/o\ corrections}^{global}$ and $a_{w/\ corrections}^{global}$ shows only a slight decrease from $\delta_{a_{w/o\ corrections}^{global}} = 0.0083$ to $\delta_{a_{w/\ corrections}^{global}} = 0.0081$. This low reduction of the uncertainty $\delta_{a_{w/\ corrections}^{global}}$ is unexpected. From the classical calculation of uncertainty, a stronger reduction of the uncertainty would be expected. Here, the weighted mean μ_a is calculated as given in eq. (2.18)

$$\mu_a^{w/o\ corrections} = 1.0095(125), \tag{3.51}$$
$$\mu_a^{w/\ corrections} = 0.9813(72). \tag{3.52}$$

The uncertainty of the mean values has been calculated, as given in eq. (2.20). The uncertainty of $\mu_a^{w/o\ corrections}$ has been scaled by $S = 1.92$ to include the observed fluctuation of the uncorrected values, cf. section 2.3.2. This scaling factor S is not needed for the corrected ideogram, so the uncertainty of the mean value with corrections decreases by the factor S. Hence, in this classical calculation the reduction of the standard deviation of the a values corresponds directly to a reduction of the uncertainty of a. The reason, why this reduction is not observed in the global fit, will be investigated in the following paragraphs.

Implementing corrections to the fit function can increase its uncertainty, as the correction itself has an uncertainty. But as the implemented correction ω_{corr} is considered as certain within this thesis, an increase of $\delta_{a_{w/\ corrections}^{global}}$ due to the uncertainty of the correction can be excluded as explanation. This leaves only three possible explanations for the low reduction of $\delta_{a_{w/\ corrections}^{global}}$: First, the global fit with corrections did not converge or is not a valid χ^2 minimisation. Second, the correction ω_{corr} introduced additional correlations between fit parameters. Third, the fit is currently limited by an incomplete description of the measured data and/or statistical noise. In the following these three possibilities will be investigated in more detail, starting with the validity of the global fit.

Validity of the Fit

The first possibility is an invalid fit. According to the fit package the global fit of the corrected a values converged. So from that point of view the fit is valid, the only possibility the fit could be invalid instead of its conversion, would be an invalid χ^2 minimisation, see section 2.3. To check, if a χ^2 minimisation is valid a closer look to the χ^2 surface has been made. For details, how a χ^2 surface is calculated, see section 2.3. If the approach of a χ^2 minimisation is valid, the actual χ^2 surface should not deviate significantly from a perfect
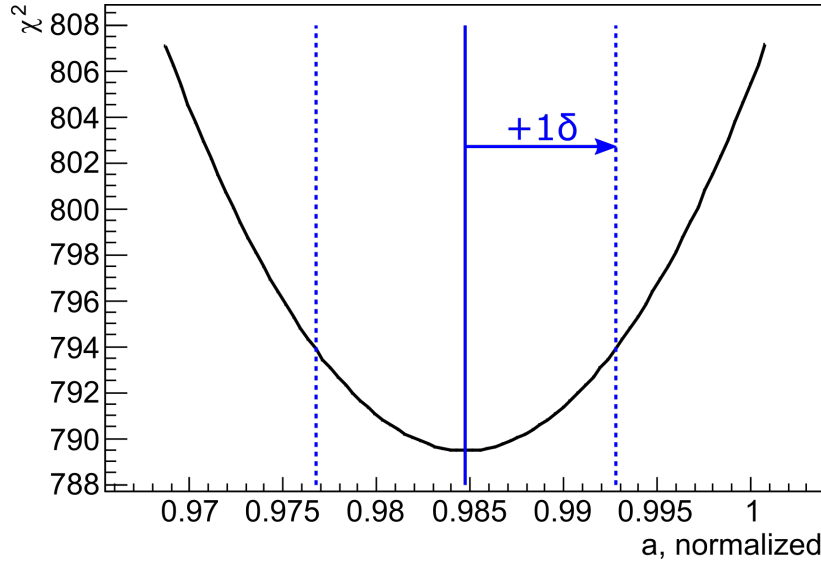
Figure 3.27.: Cut through the χ^2 surface including the corrections given in eq. (3.47). For a valid χ^2 minimisation a parabola is expected for the cut through and a low deviation ϵ (eq. (2.16)) from the ellipsoid. As can be seen from this graph χ^2 follows a parabola and the deviation from the ellipsoid is very low $\epsilon = 3 \times 10^{-10}$. This low deviation shows, that a chi^2 minimisation is valid, therefore the low reduction of the uncertainty of a can not be explained by an invalid fit. For details, how a χ^2 surface is calculated, see section 2.3.

Also shown are the correlated uncertainties in a (blue, dashed lines). These uncertainties are gained from the projection of the ellipsoid onto the a-parameter axis, cf. fig. 2.20.

ellipsoid. As this surface is multi-dimensional it can not be displayed here, therefore a cut through the χ^2 surface for one parameter is shown in fig. 3.27. This χ^2 follows a perfect parabola, which is expected for a valid χ^2 minimisation. In numbers, the actual χ^2 surface deviates only by $\epsilon = 9 \times 10^{-10}$ from a perfect ellipsoid. Hence, as the fit converges and its χ^2 minimisation is valid, the fit result and its uncertainty are can be trusted.

Correlation of fit parameters

The second possibility for such a low reduction of the uncertainty of a are correlations between fit parameters. If a is correlated to other fit parameters or linear combinations of parameters, the fluctuations of these parameters would increase, when the fluctuation of a decreases. Such an increase of correlated parameters would counteract the reduced fluctuation of a and could explain the low reduction of the uncertainty of a. In fig. 3.9 the correlation matrix of a fit to the data of config 1 is shown. The correlation matrix of the global fit shows no different/new correlations to the correlations shown in fig. 3.9, just the number of parameters is increased. Therefore, the correlations can be investigated using the matrix from config 1. Here, a is correlated to the magnetic field ratio r_B with 31 %, to the scaling factor of the spectrum Int with about 14 % and to the constant background cBG with about -32 %. All other parameters are not correlated significantly to a.
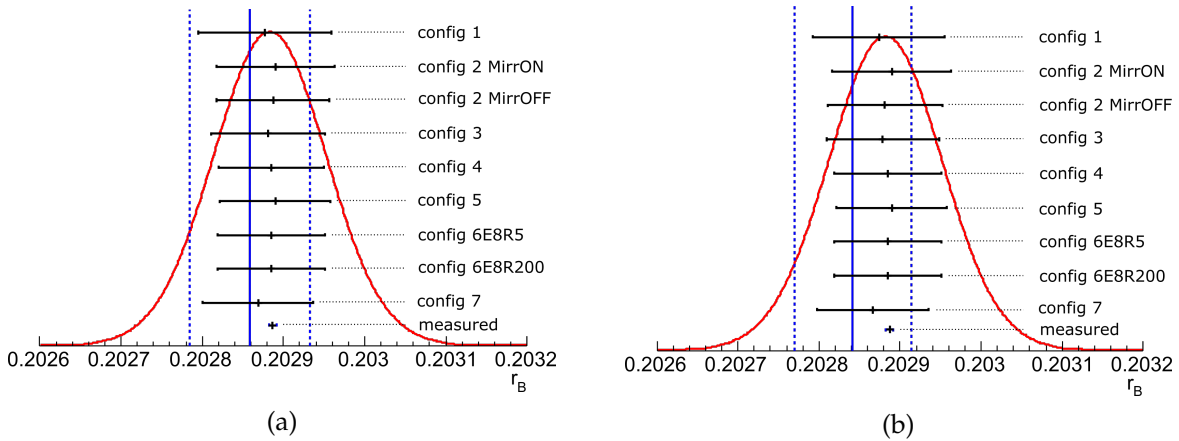
Figure 3.28.: Ideogram of r_B for the fits without corrections (a) and with corrections (b). The r_B values of the fits for the individual configurations fluctuate for both ideograms around the measured value, whereas the ones for the global fits shown as blue vertical lines are shifted in both cases to lower values. This shift hints to systematics not yet included in the fit function, see section 3.3.4, but can not explain the low reduction of the uncertainty in a. Further, thelow correlation between a and r_B did not increase the fluctuation in r_B, see eqs. 3.53 and 3.54. Hence, the this correlation can not be responsible for the low reduction of the uncertainty in a.

The parameters *Int* and *cBG* are local parameters, which means for each channel of each configuration an additional parameter is used, see eq. 3.20. r_B and a on the other hand are global parameters, only one value is fitted to the data, no matter how many channels/configurations are combined. This means for the global fit there are 18 different values for *Int*, which can differ from each other up to a factor of 2 (config 2 MirrON/OFF). It is therefore not suitable to investigate these parameters in an ideogram, due to the large spread of values. For these local parameters the value of the parameter of the individual fit has been compared to the corresponding parameter of the global fit. Any deviation between the two parameters would mean the global fit increased the fluctuation of local parameters to counteract the reduced fluctuation in a. For the correlated parameters *Int* and *cBG* no deviations between the individual and the global fits has been found. Hence, the global fit did not increase the fluctuation of these local parameters, leaving r_B as only possibility of an increased fluctuation. In fig. 3.28 are depicted two ideogram of the r_B values for the uncorrected and corrected fits. Here the fit values of r_B for the individual configurations are drawn, as well as the value measured using a NMR system, see section 2.2.1. The blue, vertical lines correspond to the value of r_B from the global fit. The uncertainty of r_B of the fit is far greater, than the measured one, as the fit takes the uncertainty of the proton spectrum, etc. into account. Nevertheless, the fitted and measured values agree within their uncertainties and the values of the individual fits fluctuate around the measured value. The r_B value of the global fit on the other hand is in both cases shifted to lower values. This hints to a common systematic, not yet included in the fit function. This systematics would be most likely the backscattering of protons at the detector, for details see section 3.3.4. But this shift can not explain the low reduction of the uncertainty, as it is observed for both

global fits. The fluctuations of r_B of the individual configurations did not increase, due to the correction, as can be seen the standard deviation σ of the two ideograms

$$\sigma^{r_B}_{w/o\ corrections} \quad = \quad 3.38 \times 10^{-3}\ \%, \tag{3.53}$$

$$\sigma^{r_B}_{w/\ corrections} \quad = \quad 3.7 \times 10^{-3}\ \%. \tag{3.54}$$

Here, only a slight increase by a factor of 1.1 between the uncorrected and corrected values is observed, whereas the standard deviation for a decreased by a factor of 3.5. Hence, the low reduction of the uncertainty of a in the global fit including the corrections, can not be due to correlations between a and other fit parameters.

Quality of the fit

Having excluded an invalid fit and correlations between fit parameters as cause of the low reduction of the uncertainty in a, the only limit of the uncertainty can be either an incomplete description of the measured spectrum by the fit function or statistical noise. In this paragraph the quality of the fit will be investigated. Therefore, the reduced χ^2_{red} will be compared for the individual configurations, as well as the global fits. This comparison will be done for a different number of systematics implemented, to study the influence of the systematic on the fit quality and the uncertainty of a.

First, fits without any systematic implemented will be considered. For these fits, only the first part of eq. 3.15 has been fitted to the measured spectrum. The fit does not include a retardation voltage dependent background, nor a pile-up correction, or corrections of the edge effect or the fields in the DV, just a constant background cBG has been implemented, to account for the offset in the measured spectrum, due to the electron background. These fits will be called "theoretical spectrum only" to separate them from the fit with systematics implemented. For config 1 and 3 the fits of the theoretical spectrum only result already in a very good fit quality for config 1 $\chi^2_{red,\ theor.\ only} = 1.05$ with an uncertainty of $\delta^{theor.\ only}_{a_1} = 0.0080$. For config 3 the fit quality is worse, but still reasonable: $\chi^2_{red,\ theor.\ only} = 3.22$ with an uncertainty $\delta^{theor.\ only}_{a_3} = 0.0188$. From the statistical point of view, the theoretical spectrum only fit of config 1 is already in perfect agreement with the measured data. From the physics point of view it is not. What the fit does here is, shifting a to a value, so the fit matched the measured data. But the data is influenced by energy dependent systematic effects, see section 2.2, so the resulting a value of a theoretical spectrum only fit to the config 1 data will be precise, but not accurate. Hence, the known systematics have to be included in the fit. The influence of such a systematic effect can be seen in the $\chi^2_{red,\ theor.\ only}$ of config 3. The difference between config 1 and 3 is the E15 dipole electrode (fig. 2.14), which has been used during config 3 as dipole and during config 1 as normal monopole. Already this small change distorts the proton spectrum significantly resulting in a worse $\chi^2_{red,\ theor.\ only}$ for config 3 and a strong shift of a as the fit tries to counteract the sytematic by shifting the value of a, see fig. 3.30.

To correct for these systematic shifts, corrections of the effects are implemented directly into the fit function, as explained in section 2.3 and the data will be fitted as multi-dimensional fit. Implementing the correction of the effect directly into the fit function will therefore influence the quality of the fit, as well as the uncertainty of it. Finally, the quality
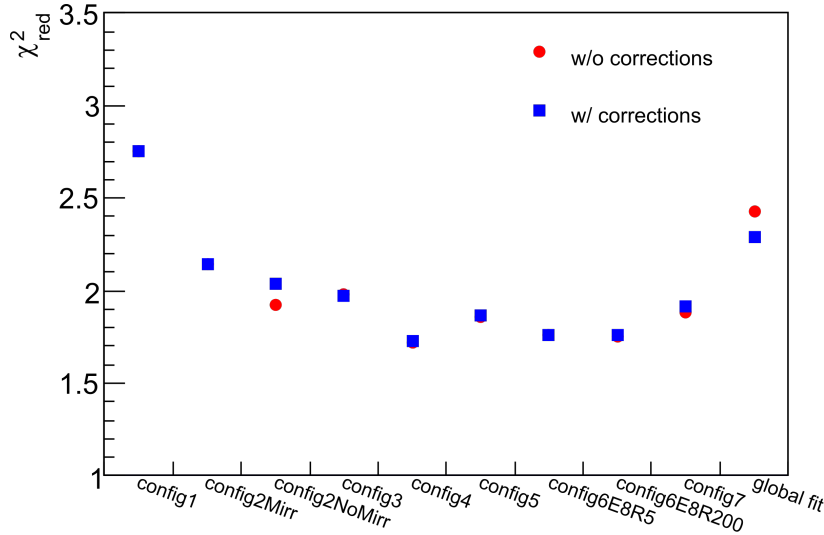
Figure 3.29.: Comparison of the fit quality χ^2_{red} with and without corrections. A $\chi^2_{red} \approx 1$ corresponds to a good agreement between data and fit, $\chi^2_{red} \gg 1$ corresponds to bad description of the data by the fit, see section 2.3.2.
For the individual configurations the implementation of the corrections eq. (3.47) does not influence the quality of the fit. This can be understood, as any systematics can also be compensated by a shift of a, therefore the fit corrects for the missing systematic by shifting a. For the global fit this is not easily possible, as here all configurations are combined. The corrections therefore improve slightly the fit quality, explaining the slight reduction of the uncertainty of a between the two global fits. For the final analysis, with all systematics included, these χ^2_{red} values will improve further, resulting in a more precise and accurate value of a.

of the fit with all systematics implemented, should reach $\chi^2_{red} \approx 1$, meaning, the measured spectrum is described well by the fit function and as all systematics are implemented the result will be precise and accurate. The current quality of the fit is shown in fig. 3.29. Shown are the χ^2_{red} values for the individual configurations, as well as the global fits, with correction for edge effect and fields in the DV (eq. (3.47)) and without. All fits shown here include already include the correction for the retardation voltage dependent background and the pile-up. From fig. 3.29 two things can be seen immediately, first the fit quality with and without corrections for the individual configurations does not differ, only the one for the global fit improves slightly from $\chi^2_{red} = 2.42$ to $\chi^2_{red} = 2.28$. Second the fit quality of config 1 got significantly worse from $\chi^2_{red, \, theor. \, only} = 1.05$ of the theoretical spectrum only to $\chi^2_{red} = 2.75$ with all corrections. On the other hand the fit quality of config 3 improved from $\chi^2_{red, \, theor. \, only} = 3.22$ to $\chi^2_{red} = 1.97$. This means, implementing a correction for the edge effect and fields in the DV shifts the a values of the individual configurations, compare fig. 3.16 to fig. 3.26. But the correction does not improve the quality of the fit to the measured data and therefore also not their uncertainties. For the global fit, the correction improves slightly the χ^2_{red}, as the fluctuations of the individual a got reduces significantly (cf. eq. 3.49). This slight improvement, therefore explains the slight reduction of the uncertainty observed between
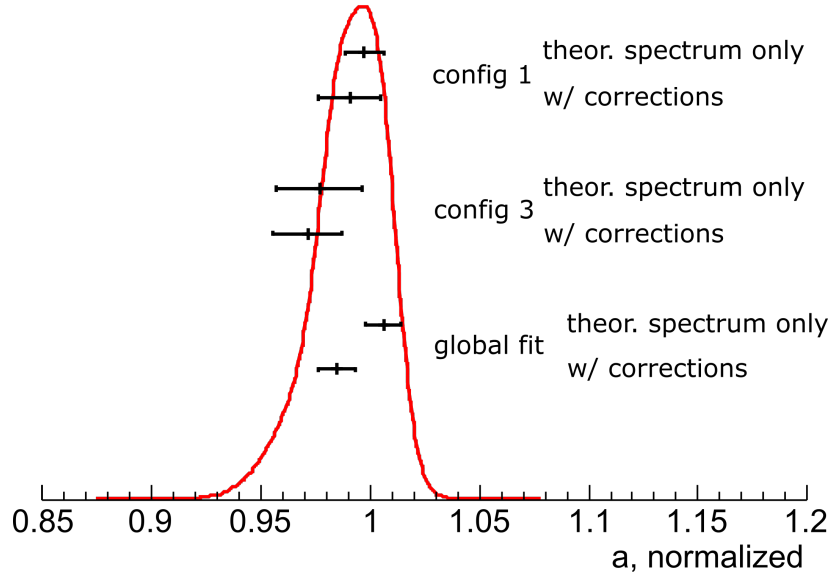
Figure 3.30.: Ideogram to investigate the influence of corrections in the fit and the reachable precision. Shown are the results for a fit without any correction (theor. spectrum only), as well as including all corrections (w/ corrections) for config 1, 3 and the global fit. Implementing the corrections shifts as expected all values, but has different effects on their uncertainties. For config 1 it is increased due to the bad description of the background. This description is better in config 3, see fig. 3.15. Here, the improvement, due to the implementation of the pile-up correction can be seen. For the global fit, the uncertainty does not change significantly, here the uncertainty is limited by the description of the individual fits. Details, see text.

the two global fits with and without corrections of the edge effect and fields in the DV, see fig. 3.16 and fig. 3.26.

Further, the fit quality of the global fit is with χ^2_{red} = 2.28 in the same order as the ones of the individual fits 1.73 $\leq \chi^2_{red} \leq$ 3.22. Therefore can be concluded the global fit is currently limited by the incomplete description of the measured data by the fit function. This is not surprising, as not all systematics are yet included in the fit function, see section 3.3.4. The implementation of all systematics, will reduce the χ^2_{red} of the fit and therefore the uncertainty of a. In this paragraph an investigation how the implementation of systematics influences the uncertainty of a will be performed. In fig. 3.30 an ideogram of the fits results from config 1 and 3, as well as from the global fit is shown. For each fit two values are shown, one for the theoretical spectrum only, the other one with corrections as given in eq. 3.15 including the corrected differential spectrum given in eq. (3.47), labelled "w/ corrections". As already mentioned, the theoretical spectrum only for config 1 describes the measured data very well ($\chi^2_{red,\ theor.\ only}$ = 1.05) and has a low uncertainty of $\delta_{a_1}^{theor.\ only}$ = 0.0080. Implementing the retardation voltage background into the fit worsens this significantly the fit quality of config 1 to $\chi^2_{red,\ bckd}$ = 4.62 and the uncertainty $\delta_{a_1}^{bckd}$ = 0.0180. This is due to the fact, that the retardation voltage dependent backgropund of config 1 does not follow very well a linear,

see fig. 3.15. Therefore, the improvement of implementing a retardation voltage dependent background to the proton spectrum is counteracted by the bad description of the retardation voltage dependent background itself. For config 3 the background is far better described by a linear so the quality of the fit improves from $\chi^2_{red,\ theor.\ only} = 3.22$ to $\chi^2_{red,bckd} = 2.40$, by implementing a background correction. The uncertainty therefore decreases also for config 3 from $\delta_{a_3}^{theor.\ only} = 0.0188$ to $\delta_{a_3}^{bckd} = 0.0168$. A similar effect has the implementation of the pile-up correction fig. 3.7. The pile-up correction is a common correction, influencing all configurations in the same way. Implementing the pile-up correction improves the fit quality significantly, the fit of config 1 improves to $\chi^2_{red,\ bckd,\ pile-up} = 2.75$, the one of config 3 to $\chi^2_{red,\ bckd,\ pile-up} = 1.97$. Their uncertainties improve to $\delta_{a_1}^{bckd,\ pile-up} = 0.0135$ and $\delta_{a_3}^{bckd,\ pile-up} = 0.0152$. These are the uncertainties shown in fig. 3.30. Also shown is the result of the two global fits, fitted with a theoretical spectrum only and with all corrections implemented.

As has been showed, the low reduction of the uncertainty between the global fit without correction of edge effect and fields in the DV, eq. (3.21), compared to the one with correction, eq. (3.50), is due to only a slight reduction of the χ^2_{red} for these fits. The current limit of the uncertainty of a is the incomplete description of the measured data by the fit function, due to missing systematics, not yet implemented (section 3.3.4). Implementing all these systematics into the fit function, will reduce the fit quality further and therefore improve the uncertainty of a. What finally can be expected as lower limit of the uncertainty is estimated in the next paragraph.

Statistical limit

As has been shown in the previous paragraph, the fit of the theoretical spectrum only to the config 1 data has a very good fit quality of $\chi^2_{red,\ theor.\ only} = 1.05$ resulting in a low uncertainty of $\delta_{a_1}^{theor.\ only} = 0.0080$. The $\chi^2_{red,\ theor.\ only} = 1.05$ means the data fluctuate only statistically around the fit function, so this fit is limited mainly by statistics. The statistics of config 1 corresponds to about 1/3 of the complete measurement time, see table 3.2. Therefore, the best what can be reached with the current data will be

$$\delta_{a_{stat}} \approx \frac{\delta_{a_1}^{theor.\ only}}{\sqrt{3}} = 0.0046. \tag{3.55}$$

This is the lower limit for the aSPECT data from 2013. With all systematics included, described in section 3.3.4, an uncertainty between this lower limit and the uncertainty of the global fit without corrections is expected $0.0046 \leq \delta_a \leq 0.0083$.

3.3.4. Systematics to be Included

Within this thesis several systematics, like pile-up (section 3.1.2), background (section 3.2.2), edge effect (section 3.3.2) and fields inside the DV (section 3.3.2) have been investigated. The correction of these systematic effects has been implemented into the fit function (section 3.1.3) of the measured proton spectrum, leading to a first corrected value and uncertainty of a (fig. 3.26). The investigation of the pile-up and the retardation voltage dependent background is final and can be used for the final analysis. The investigation of

the edge effect and the fields inside the DV showed in eq. (3.47) are first estimates only and have to be improved for a final analysis. The needed improvements are described in the next paragraphs, as well as systematics not yet investigated.

ExB drifts smearing out the DV

One of the investigation needed is the exact position of the DV. The DV is defined as the volume of the neutron beam being projected onto the detector. The magnetic projection, without any electric potential, has been measured using an activated copper wire, see section 2.2.2 and [Vir13]. This measurement of the magnetic projection has been used in this work as definition of the DV. But the magnetic projection gets distorted by various ExB drifts. The drift in an ExB electrode is generated by the electric field $\vec{E}$ of the Lorentz force (eq. (2.1)). The stronger the electric field and the longer the protons experience the field, the stronger the drift. Hence, protons with a low velocity in z-direction will experience the ExB drift longer and will therefore be distorted stronger, than protons with high velocity. This means ExB drifts not only shift the position of the DV, but also introduce an energy dependence to it, as low energetic protons and/or protons emitted at a polar angle close to $\theta_0 \approx 90°$ will pass them slower, than high energetic ones. Such ExB drifts can be generated either on purpose to empty traps (e.g. electrodes E8 or E15), or by fluctuations of the surface contact potential of the DV and AP electrodes. In either case the effect is very complicate and can not be handled easily analytically. For the final analysis a particle tracking simulation will determine the influence of the ExB drift electrodes onto the DV. This simulation will also include the measured surface contact potential fluctuations in the DV and AP electrodes and therefore take their ExB drifts into account, as well. With this ExB drifts taken into account the position of the DV and therefore the edge effect can be determined more precisely and will be implemented into the fit function (section 3.1.3) as an additional fit dimension.

Exact determination of U_{ret}

Having determined the position of the DV allows to calculate more precisely the uncertainties δ_{scp} and $\delta_{leakage}$ of the retardation voltage, due to the surface contact potential and field leakage, respectively (cf. eq. (3.14)). So far for the uncertainty δ_{scp} the fluctuations measured with a Kelvin probe have been used. These fluctuations have been measured a few mm above the electrode surfaces, but the protons decay in the central region of the DV electrode. The fluctuation of the electric potential in this region will be far lower, as the fluctuations of the surface contact potential smear out with increasing distance from the surface. A simulation of the electric potential, including the measured surface contact potential allows to calculate this smear out. The same method is applied to the AP electrode, here the flux tube passing through from the DV to the detector is determined. In this flux tube the fluctuation of the electric potential, due to the surface contact potential can be determined as well. Both fluctuations of the potential inside the DV and AP are then combined to an improved δ_{scp}. These simulations of the potentials in the DV and AP could reveal also an offset of the retardation voltage, due to the surface contact potential. Such an offset has to be included to the fit function as well, to achieve the correct value for the retardation voltage. For the uncertainty $\delta_{leakage}$ a similar calculation is performed. The fluctuation, due to field leakage into the DV and AP is determined and combined to a new $\delta_{leakage}$. This field leakage will result in an offset of the retardation voltage, as the field

leakage in the AP depends on the voltage applied to the AP electrode. Hence, this offset of the retardation voltage depends on the retardation voltage and has to be included into the fit function to improve the fit further. How sensitive *a*SPECT is to field leakage can be seen by electric field simulations done by [Kah15]. Here, a retardation voltage of 400 V has been simulated, resulting in an offset in the order of $O(100\,\text{mV})$. This field leakage corresponds to an uncertainty of $\delta a/a \approx 1\,\%$ if not taken into account. For the final analysis, this field leakage will be determined by simulations, resulting in a correction in the order of 1 %.

Backscattering of protons at the detector

In section 3.1.2 it has been described how the pile-up is determined, which is then used as correction to the fit function (cf. eq. 3.15). With the correction of the pile-up all protons being lost due to the upper cut onto the proton region at $11.5\,\text{keV}_{\text{ee}}$ are accounted for. For the lower cut onto the proton region at $5.2\,\text{keV}_{\text{ee}}$ the number of protons lost, due to backscattering and losses in the dead layer of the detector have to be determined. To do so, one has to differentiate between protons, which still reach the active volume of the detector, but depose an energy below $5.2\,\text{keV}_{\text{ee}}$ and protons, never entering the active volume of the detector. The number of protons depositing an energy between $0\,\text{keV}_{\text{ee}}$ to $5.2\,\text{keV}_{\text{ee}}$ can be determined by extrapolating the low energy tail of the proton peak in the pulse-height spectrum, see fig. 3.31. In this pulse-height spectrum the 780 V measurement has been subtracted, to get the pure proton signal. Shown is the low energy tail of this proton region (red area). To this low energy tail an exponential is fitted (red line) and then extrapolated to zero (green line). Integrating over this extrapolation (green are), provides the number of protons being cut off by the lower cut on the proton region. The number of protons never reaching the active volume of the detector can be determined by a SRIM simulation [Zie13]. The SRIM program simulates the scattering processes of the protons in the SDD including the dead layer. Using this simulation the number of protons, which are backscattered and never reach the active volume of the SDD can be determined. Together with the number of protons being cut off by the lower cut, this gives a correction on the measured proton signal, which has to be implemented into the fit function as well.

Scattering of protons at residual gas

In [GBB$^+$05] the effect of elastic and inelastic scattering, as well as charge exchange of protons at residual gas has been calculated. For a critical pressure of $p_c \leq 1 \times 10^{-8}\,\text{mbar}$ the effect of these scatter processes is small enough to achieve an uncertainty of $\delta_a/a = 10^{-4}$. During the beam-time 2013 all pressures have been in the order of $p < 1 \times 10^{-9}\,\text{mbar}$, so at least an order of magnitude lower than the critical pressure. In this calculation of the critical pressure the effect of small angle scatterings have not been taken fully into account. Lets assume a proton with an initial energy T_0 and polar angle θ_0 slightly below the transmission threshold of *a*SPECT. This proton will not overcome the retardation voltage and therefore be trapped between the AP and the electro-static mirror. In the ideal case this proton would be trapped till the retardation voltage is turned off after the DAQ cycle or it is removed by the ExB drift of the E8 electrode. In the real case, this proton can make several small angle scattering processes changing slightly its polar angle θ. These scatter processes can increase the polar angle $\theta > \theta_0$ or decrease it $\theta < \theta_0$. If the angle is increased, the proton will still be trapped between AP and mirror, but if the angle is decreased the proton can overcome the retardation voltage. Hence, the small angle scattering causes a small fraction
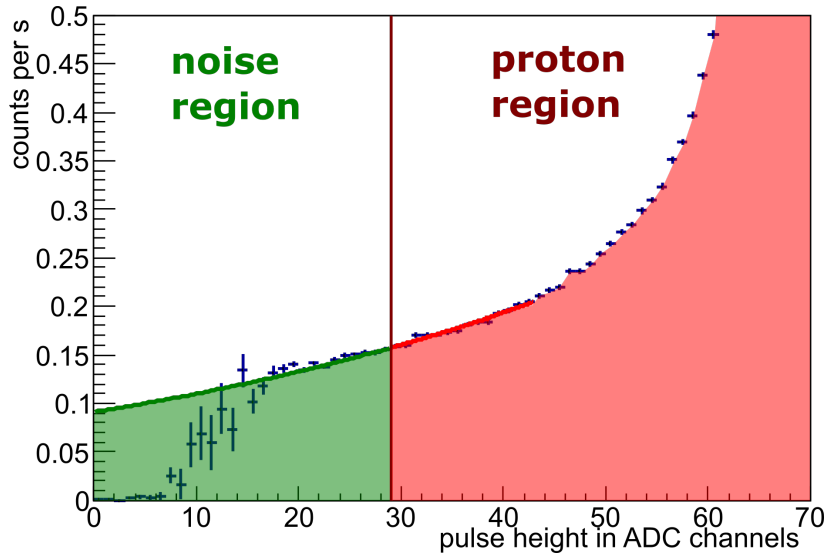
Figure 3.31.: Extrapolation of the low energy tail of the proton peak. In this pulse-height spectrum the 780 V measurement has been subtracted to achieve a background free spectrum. To the low energy tail of the proton peak (read area) an exponential has been fitted (red line) and extrapolated to lower energies/ADC channels (green line). Over this extrapolation is then integrated (green area), which corresponds to the number of protons lost by making a cut at $5.2\,\mathrm{keV_{ee}}$/ADC channel 29. This number of lost protons is then used as correction to the measured proton signal.

of protons slightly below the transmission threshold to overcome this threshold, although they should not. So far this effect has not been quantitatively calculated for *a*SPECT, but with the particle tracking simulation the effect of small angle scattering can easily be determined and implemented into the fit function.

3.4. Possible Improvements for a Future Measurement/Experiment

In the following some suggestions are proposed, how to improve future measurements and/or experiments like *a*SPECT. Some of these suggestions might be hard at the limit of ignoring real world restrictions, but nevertheless should be mentioned. Maybe some day, someone will have a lot of money, time and man power to realise them.

For a new experiment like *a*SPECT, a better magnetic field ratio r_B would be desirable. Better means a lower r_B or in other words a bigger difference between the magnetic field in the AP and DV region. This will increase the energy resolution of the spectrometer and therefore reduce the sensitivity of the Transmission Function to systematics depending on the emission angle of the protons. The influence of fluctuations of the surface contact potential or of the field leakage into the AP and DV electrodes could be decreased, by increasing in physical size of the electrodes. With this simple measure a more homogeneous retardation voltage can be achieved, as the fluctuations/field leakage smear out with distance from the surface/opening. Other useful hardware improvements would be a bigger and thicker detector, as well as a DAQ able to discriminate different pulse shapes of different

particles. Desirable would be a detector big enough in area to cover the whole neutron beam, so no edge effect would be present and more statistics would be gained in the same measurement time. A thicker detector would have the advantage, that the complete electron energy of up to 782 keV could be detected. Measuring also the electron spectrum would allow additional tests of the systematics, independent from the proton spectrum. A DAQ able to discriminate pulse shapes of electrons and protons, possibly even protons and heavier ions, would dramatically increase the understanding of the background. Such a discrimination power would allow to identify the background directly via its pulse shape in an event-by-event analysis and therefore clean the data from background. This will basically erase the background problematic.

As last point of improvements would be more statistics. This includes measuring each retardation voltage for a longer time, as well as measuring more different retardation voltages. Measuring the proton recoil spectrum with more data points/retardation voltages would make the fit more sensitive to the shape of the spectrum. Or in other words distortions of the shape due to systematics could be identified better and therefore corrected more precisely. Each of these data points should be measured at least with the same statistical uncertainty as the current ones of 2.4×10^{-4}. Hence, a future experiment should measure far longer and the different configurations with sufficient statistical sensitivity. For example config 6 shown in fig. 3.26 has been measured with two different settings of the ExB electrode E8. This measurement has been performed over one night, which was far to short (cf. table 3.2) to observe any significant difference between the two settings of the ExB. Therefore, in future such a measurement should either be performed far longer to achieve a statistically significant difference between the two settings, or the measurement time should be used to increase the statistics of the "standard" setting. Furthermore, higher statistics of the individual configurations would also increase the statistics of rare events, like pile-up. In this analysis, only the high statistic runs of config 1, 3 and 7 could be used for the pile-up correction, as all other runs had a too low statistics for a reliable extrapolation to $\Delta t \to 0$. So measuring the individual configurations with more statistics, would also increase the statistics of the pile-up correction and therefore improve it. Finally, a proton recoil spectrum measured with a high number of data points and high statistics, would make it possible to include the start- and end-point of the measured recoil spectrum as fit parameter. Including the start- and end-point as fit parameter would provide the spectrum with an absolute energy scale. Any offset in the retardation voltage could be determined and corrected by the fit itself, improving the accuracy of the retardation voltage measurement.

In conclusion can be said, a future *a*SPECT experiment would benefit most from an improved magnetic field ratio and far more statistics.

Conclusion

The *a*SPECT experiment could overcome the short comings of past beam-times since 2008. The problematic of a saturation of the DAQ system in 2008 was solved using a logarithmic amplification, see section 2.2.4. Using a pulser it has been shown, that no saturation of the DAQ used 2013 is present any more. Additionally, using a ^{133}Ba source the system has been calibrated in terms of energy. The strong background observed in 2011 could be reduced significantly by improving the vacuum using additional vacuum pumps and improved cleaning procedures. Additionally, a new dipole electrode has been installed introducing an ExB field emptying the main Penning-like trap of *a*SPECT, see section 2.2.3. This ExB drift reduces the retardation voltage dependent background down to 0.15 sec−1. Having solved these experimental problems a successful beam-time was performed with *a*SPECT in spring/summer 2013 at the Institut Laue-Langevin (ILL). The goal of this 2013 beam-time is to improve the precision of the $\beta - \bar{\nu}_e$ angular correlation coefficient *a* from currently $\delta a/a \approx 4\,\%$ to about 1 %.

To reach a precision of 1 % the systematic effects of *a*SPECT have to be known on the sub-% level. One of the main systematics of *a*SPECT is the Transmission Function, which is a function of the magnetic field ratio r_B and the retardation voltage U_{ret}, see section 2.2.1. To determine the the uncertainty of the Transmission Function the uncertainty of r_B and U_{ret} had to be determined. A precise measurement of the magnetic field ratio $r_B = 0.202\,887(5)$ using two NMR probes has been performed, corresponding to an uncertainty of $\delta a/a = 0.05\,\%$. Further, an investigation of the surface contact potential of the newly designed DV and AP electrodes (fig. 2.6) has been done. This surface contact potential influences the applied retardation voltage and therefore needs to be known on a level of $O(10\,\text{mV})$. To achieve this knowledge of the surface contact potential, it has been measured at ambient air and under high-vacuum conditions using a Kelvin Probe. For *a*SPECT only the difference of the potential between the DV and the AP electrode is of interest. This difference stays the same in vacuum or ambient air. The same is true for cooling down or freeze out on the electrodes, both electrodes are influenced in the same way, hence the difference stays the same. Using the Kelvin Probe measurements, the mean offset of the retardation voltage and its uncertainty, due to the surface contact potential, has been preliminarily determined to 5(20) mV. Another main systematic of *a*SPECT is the so-called edge effect, see section 2.2.2. To investigate this effect a new manipulator has been installed at *a*SPECT, allowing to measure the neutron beam profile directly inside the DV and therefore improving the knowledge of the neutron beam profile dramatically. Further, this manipulator has been used to determine the exact projection of the DV onto the detector. To do so, a scan with an activated Cu wire has been performed. Additionally the edge effect has been enhanced experimentally by using a second, smaller beam profile, which allows to determine the

effect more precisely.

To handle the billions of events recored during the beam-time one-by-one, a new data structure called Thei*a* has been written within this thesis, cf. section 3.1. Thei*a* combines the data from the DAQ and various spectrometer settings, like voltage on electrodes, pressure, time, etc. in one place. This allows an easy and fast analysis of the data, as well as the identification and quantification of systematic effects. Using Thei*a* the pulse-height of single events has been corrected for noisy events, as well as double peak events using a spline interpolation, see section 3.1.1. The spline interpolation has also been used to determine the pile-up rate and hence the proton rate missed by making an upper cut in the pulse-height spectrum, see section 3.1.2. During the beam-time 2013 several experimental configurations have been investigated, see table 3.1. These individual configurations were measured with enhanced systematic effects allowing to investigate the systematic effects in detail. Any non-statistical fluctuation of the count-rate during one of these configuration, e.g. caused by a fluctuation of the reactor power, could mimic a systematic effect changing *a*. To check for such non-statistical fluctuations, the stability of the count-rate during the individual configurations has been investigated. The measurement time of the individual configurations were in the range of 0.5 days to 3.5 days. During these time periods no non-statistical fluctuation of the count-rate was observed, see section 3.2.1. Knowing the count-rate being stable over one configuration, the systematics of each configuration can be investigated in detail. Having all information of the spectrometer combined at one place in Thei*a* the retardation voltage dependent background has been investigated.

This background was determined using the count rate after the neutron shutter has been closed, cf. fig. 2.15. The count-rate after the neutron shutter has been closed is proportional to the background from ionised residual gas during the measurement, as has been shown in section 3.2.2. The retardation voltage dependent background has been investigated for each configuration individually. This investigation revealed that the background is dominated by the vacuum level in the spectrometer. As this vacuum level improved during the beam-time (fig. 3.13) the retardation voltage dependence of the background got reduced also during the beam-time, resulting in a dependence compatible with zero after the first half of the beam-time. To describe the retardation voltage dependence of the background a linear dependence has been used (eq. 3.17), which is fitted to the after shutter data for each channel and configuration of *a*SPECT separately.

From the pulse-height spectrum of each retardation voltage the integral proton recoil spectrum is extracted, see fig. 3.8. For this measured spectrum a multi-dimensional fit is performed, including the data of both detector channels, see eq. 3.15. This multi-dimensional fit includes further the corrections for the pile-up rate, as well as the retardation voltage dependent background, cf. section 3.1.3. From this fit *a* and its uncertainty is gained, as described in section 2.3. Such multi-dimensional fits have been performed in a first step to the individual configurations without any correction of the experimentally enhanced systematic effects, see fig. 3.16. These values have been normalised to the first one to blind them, as they are still subject to systematic shifts. Additionally to the individual fits a global fit to the configurations 1 to 7 has been performed, resulting in

$$a_{w/o\ corrections}^{global, normalised} = 1.0071(83).$$

This *a* value has already a very good precision of $\delta a/a = 0.82\%$. But the low confidence level of 0.0001 shows, that the observed fluctuation of *a* values, due to the enhanced systematic

effects, is not accounted for correctly. In section 3.3.2 first hand corrections of these enhanced systematics are determined. For the edge effect the probability to detect additional protons, as well as lost protons is determined using the Point-Spread-Function (PSF), see section 3.3.2.1. This allows to calculate the absolute loss of protons and therefore to determine a correction of the edge effect, cf. fig. 3.20. The measurement with electro-static mirror off revealed, that the observed shift in a and the measured count-rate ratio between mirror off and on can not be explained with the implementation of the magnetic field gradient in the DV alone. By assuming an effective electric field of $0.5\,\mathrm{Vm}^{-1}$ inside the DV the observed count-rate ratio and the shift in a could be explained and corrected for, see section 3.3.2.2.

Both corrections, for the edge effect and the field inside the DV, have been implemented into the fit function, cf. section 3.3.3. These corrections reduce significantly the fluctuation of a values from $\sigma_{w/o\ corrections} = 4.9\,\%$ without corrections to $\sigma_{w/\ corrections} = 1.4\,\%$ with corrections, see fig. 3.26. Using the corrected fit function a global, multi-dimensional fit to all configurations has been performed, resulting in an improved a value of

$$a_{w/\ corrections}^{global,normalised} = 0.9847(81).$$

This corrected fit has a far better confidence level of 0.82, due to the significantly reduced fluctuation of a values. Further, the implemented corrections shifted the value significantly to lower values, but did not decrease significantly the uncertainty of the global fit, compared to the one without corrections. It has been shown, that this low reduction of the uncertainty is due to the yet incomplete description of the measured data by the used fit function, see fig. 3.29. The incomplete description of the fit function can be seen in the fit quality of $\chi_{red}^2 = 2.28$ for the global fit. This relatively bad fit quality is not surprising, as there are still systematic effects to be implemented to the fit function, cf. section 3.3.4. With these effects implemented the fit function will describe the measured data correctly, resulting in an accurate value of a and potentially in an even lower uncertainty, cf. section 3.3.3. As lower limit for the uncertainty of the 2013 data has been determined

$$\delta_{a_{stat}^{normalised}} \approx 0.0046.$$

Reaching this limit in a final analysis would be a great success for aSPECT, as with a precision of $\delta a/a \approx 0.5\,\%$ new physics could already be probed.

In conclusion can be said, aSPECT has been be improved significantly to overcome the shortcomings of past beam-times, resulting in a successful beam-time in 2013. The data of the 2013 beam-time has been analysed since then. Many of the systematics, like surface contact potential, magnetic field ratio, detector effects, pile-up, background have been investigated. Further, first corrections for the edge effect and fields inside the DV have been found. Using these correction a multi-dimensional fit of the complete dataset has been performed. The result of this global fit is already very precise and in the sub-% region. By implementing the missing known systematics the result of this fit will also be accurate. Further, implementing the missing systematic effects will potentially pushed down to $0.5\,\%$, a precision where new physics can be probed.

A. Energy Calibration

In section 2.2.4 the principle calibration of the DAQ system has been described. As short reminder, to calibrate the DAQ a ^{133}Ba spectrum source has been used to determine the relation between energy *E* and ADC channel *chADC*. The logarithmic amplification of the shaper[1] has been determined by [Ros15], see eqs. A.1 to A.3. Using a second ^{133}Ba spectrum taken with the DAQ used during the beam-time 2013 [Mai14] the conversation from test DAQ to beam-time DAQ could be performed.

Logarithmic amplification curves of the test DAQ, taken from [Ros15]:

$$chADC_{test}^{19} = \left\{-652.3(9) + 1099.6(3) \cdot \ln\left(\frac{E}{keV}\right)\right\}, \tag{A.1}$$

$$chADC_{test}^{20} = \left\{-708.5(10) + 1108.7(3) \cdot \ln\left(\frac{E}{keV}\right)\right\}, \tag{A.2}$$

$$chADC_{test}^{21} = \left\{-705.9(8) + 1012.9(3) \cdot \ln\left(\frac{E}{keV}\right)\right\}. \tag{A.3}$$

To use this with the DAQ system of the beam-time 2013, the spectrum of ^{133}Ba measured with both systems has been used to calculate a linear conversion. For this linear conversion the following peaks has been used:

$$17.5(38) \text{ keV} \stackrel{\wedge}{=} 139.3(7) \text{ chADC}_{beam-time}^{19} \tag{A.4}$$

$$\stackrel{\wedge}{=} 139.3(7) \text{ chADC}_{beam-time}^{20} \tag{A.5}$$

$$\stackrel{\wedge}{=} 148.7(7) \text{ chADC}_{beam-time}^{21} \tag{A.6}$$

$$^{133}Cs\, K_\alpha:\ 31.50(199) \text{ keV} \stackrel{\wedge}{=} 198.8(1) \text{ chADC}_{beam-time}^{19} \tag{A.7}$$

$$\stackrel{\wedge}{=} 198.8(1) \text{ chADC}_{beam-time}^{20} \tag{A.8}$$

$$\stackrel{\wedge}{=} 213.4(7) \text{ chADC}_{beam-time}^{21} \tag{A.9}$$

$$^{133}Cs\, \gamma_{2,1}/\gamma_{1,0}:\ 80.9(23) \text{ keV} \stackrel{\wedge}{=} 244(3) \text{ chADC}_{beam-time}^{19} \tag{A.10}$$

$$\stackrel{\wedge}{=} 244(3) \text{ chADC}_{beam-time}^{20} \tag{A.11}$$

$$\stackrel{\wedge}{=} 266.6(30) \text{ chADC}_{beam-time}^{21}. \tag{A.12}$$

---

[1] At *a*SPECT the term shaper is used for a spectroscopy amplifier.
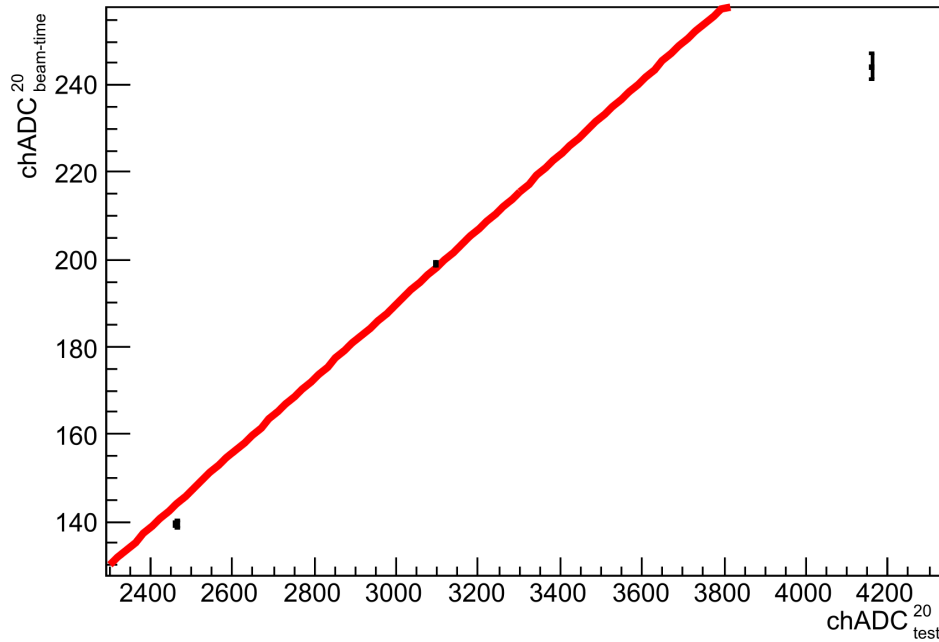
Figure A.1.: Linear conversion between the two ADC system used during the beam-time and the test system. Shown are the three energies for channel 20, as well as a fit through them (red, line). The deviation of the fit from the high energy point is due to its large error bar, compared to the other ones.

For the test system, the $chADC^x_{test}$ have been calculated with the given equations A.1 to A.3, as linear conversion a fit through these points has been used, see fig. A.1. The resulting linears from the fit for all three channels are

$$chADC^{19}_{beam-time} = 8.61(11) \times 10^{-2} \cdot chADC^{19}_{test} - 70.6(34), \quad (A.13)$$

$$chADC^{20}_{beam-time} = 8.54(11) \times 10^{-2} \cdot chADC^{20}_{test} - 66.3(34), \quad (A.14)$$

$$chADC^{21}_{beam-time} = 10.30(12) \times 10^{-2} \cdot chADC^{21}_{test} - 71.3(34). \quad (A.15)$$

With this conversation from $chADC_{beam-time}$ to $chADC_{test}$ the equations A.1 to A.3 can be converted into an energy scale for the DAQ used during the beam-time 2013. This energy conversion is shown in fig. A.2. As can be seen, channel 19 and 20 have the same calibration, whereas channel 21 has a slightly lower energy calibration, due to slight manufacturing differences of the construction components used.
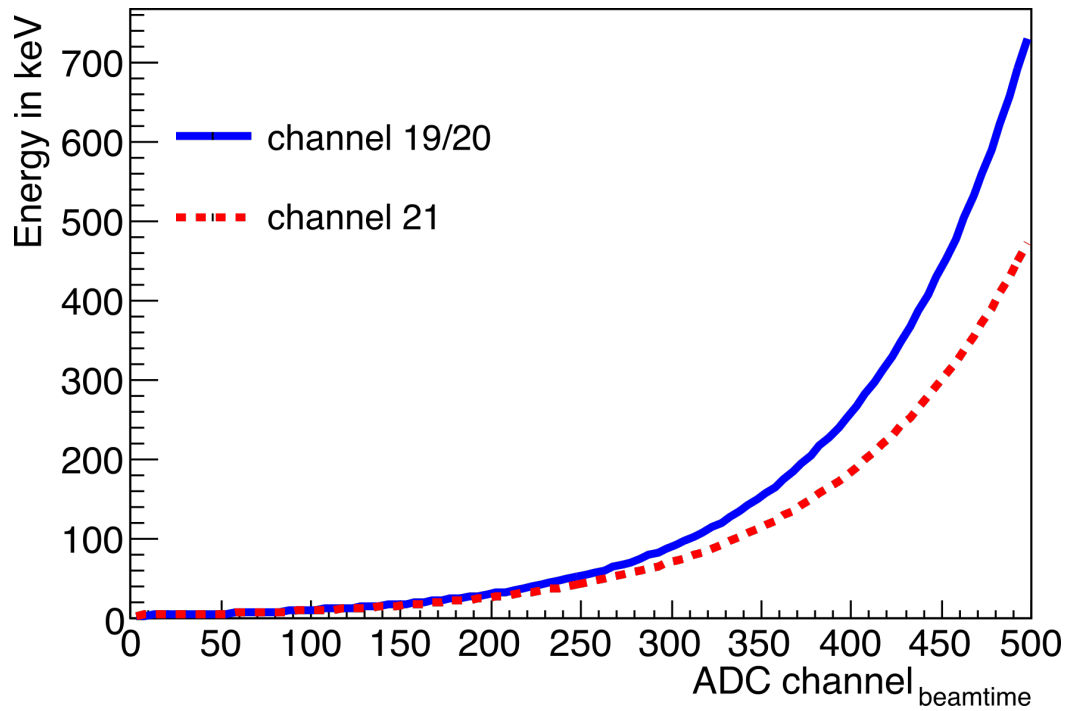
(a)
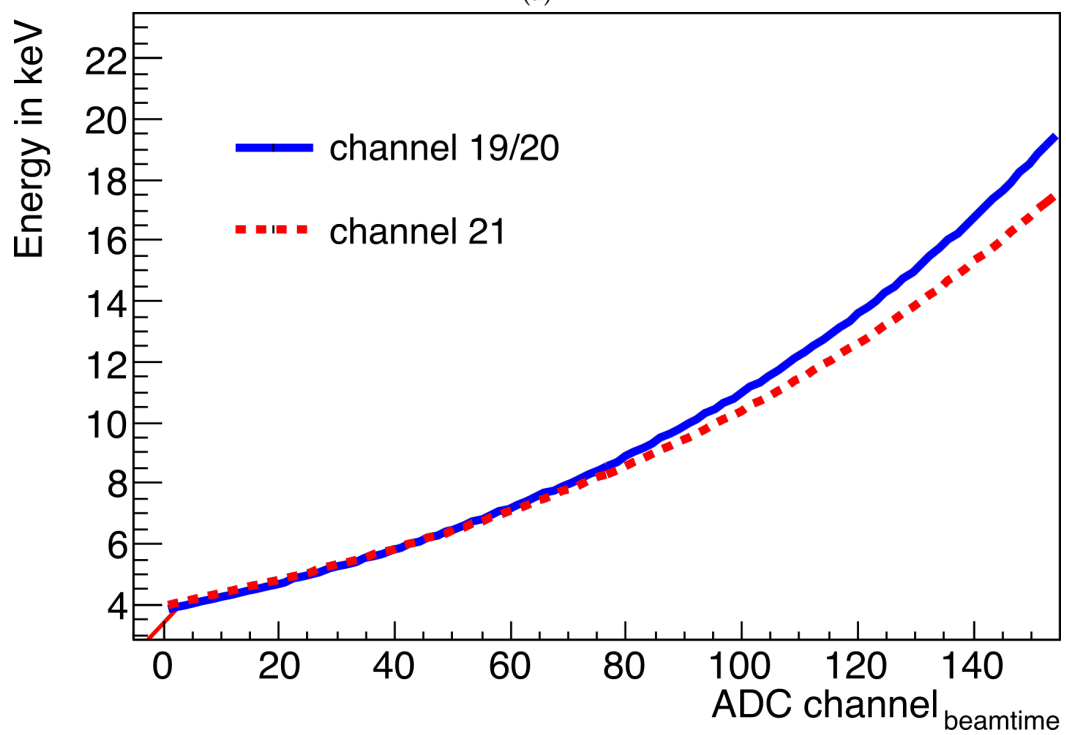
(b)

Figure A.2.: Conversion from ADC channel to energy. Shown are for all three channels the conversion function from $chADC_{beam-time}$ for all three channels. In (a) for the complete energy region and in (b) a zoom onto the proton region.

> "How wonderful that we have met
> with a paradox. Now we have some
> hope of making progress."
>
> *Nils Bohr*

B. Proton Recoil Spectra

In this chapter the proton recoil spectra of the different configurations are given. Included are all corrections applied to the pulse-height spectra, like corrected pulse-height (section 3.1.1) and dead time (eq. (2.11)). Not included are corrections applied in the fit function directly, like retardation voltage dependent background (section 3.2.2), pile-up (section 3.1.2) or edge effect (section 3.3.2).

The integration cuts in the pulse-height spectra were $5.2 \, \text{keV}_{ee}$ to $11.5 \, \text{keV}_{ee}$ for all channels and configurations. This corresponds to 29 ADCchannel to 104 ADCchannel for channel 19 and 20, 28 to 110 for channel 21. Except for config 8 with the uDAQ without a energy calibration. Here, from 50 ADCchannel to 500 ADCchannel has been integrated.

Table B.1.: Proton recoil spectra config 1. Given are the proton count rates of config 1 for each retardation voltage, for details of the settings, see appendix C.

channel 19		channel 20		channel 21	
ret. voltage in V	countrate per s	ret. voltage in V	countrate per s	ret. voltage in V	countrate per s
49.9973(539)	425.877(176)	49.9972(539)	445.648(181)	49.9972(539)	439.818(179)
100.0020(539)	394.905(147)	100.0020(539)	415.337(152)	100.0020(539)	409.391(151)
249.9980(539)	271.534(120)	249.9980(539)	288.304(124)	249.9980(539)	284.499(123)
350.001(54)	180.601(105)	350.001(54)	193.011(108)	350.001(54)	190.013(107)
400.010(54)	137.279(87)	400.010(54)	146.1290(896)	400.010(54)	144.125(89)
450.0050(541)	96.3048(692)	450.0050(541)	102.0490(705)	450.0050(541)	100.7860(701)
500.0100(542)	60.8602(512)	500.0100(542)	63.2163(507)	500.0100(542)	62.5315(504)
550.0050(543)	33.2736(364)	550.0050(543)	32.6968(337)	550.0050(543)	32.3362(337)
600.0090(544)	16.8751(170)	600.0090(544)	14.4626(138)	600.0090(544)	14.4042(139)
780.0120(552)	7.290 88(13500)	780.0120(552)	4.789 29(3350)	780.0120(552)	4.8711(660)

Table B.2.: Proton recoil spectra config 2 MirrorON. Given are the proton count rates of config 2 MirrorON for each retardation voltage, for details of the settings, see appendix C.

channel 19		channel 20		channel 21	
ret. voltage in V	countrate per s	ret. voltage in V	countrate per s	ret. voltage in V	countrate per s
49.9978(539)	425.294(446)	49.9979(539)	445.565(457)	49.9979(539)	440.657(454)
100.0040(539)	395.79(37)	100.0040(539)	414.782(381)	100.0040(539)	410.824(378)
249.9990(539)	271.638(301)	249.9990(539)	288.666(312)	249.9990(539)	284.751(310)
350.001(54)	180.536(263)	350.001(54)	193.405(272)	350.001(54)	190.574(270)
400.011(54)	137.356(221)	400.011(54)	146.645(227)	400.011(54)	144.690(226)
450.0050(541)	96.6553(1750)	450.0050(541)	102.244(179)	450.0050(541)	101.159(178)
500.0110(542)	60.9535(1300)	500.0110(542)	63.6588(1290)	500.0110(542)	62.6679(1280)
550.0060(543)	33.3754(925)	550.0060(543)	32.9175(861)	550.0060(543)	32.6387(866)
600.0100(544)	17.0013(432)	600.0100(544)	14.7381(360)	600.0100(544)	14.8877(363)
780.0130(552)	7.412 69(35800)	780.0130(552)	5.144 29(12800)	780.0130(552)	5.221 18(11000)

Table B.3.: Proton recoil spectra config 2 MirrorOFF. Given are the proton count rates of config 2 MirrorOFF for each retardation voltage, for details of the settings, see appendix C.

channel 19		channel 20		channel 21	
ret. voltage in V	countrate per s	ret. voltage in V	countrate per s	ret. voltage in V	countrate per s
49.9979(539)	218.151(215)	49.9980(539)	226.896(220)	49.9980(539)	224.087(219)
100.0040(539)	202.670(183)	100.0040(539)	211.792(188)	100.0040(539)	208.813(187)
249.9990(539)	140.545(144)	249.9990(539)	147.893(148)	249.9990(539)	146.451(147)
350.001(54)	94.8162(1230)	350.001(54)	99.9591(1260)	350.001(54)	98.5489(1260)
400.011(54)	72.2725(1110)	400.011(54)	76.23344(1140)	400.011(54)	75.4039(1130)
450.0050(541)	51.6831(901)	450.0050(541)	54.4179(912)	450.0050(541)	53.5299(904)
500.0110(542)	33.8815(662)	500.0110(542)	34.6627(646)	500.0110(542)	34.1211(645)
550.0060(543)	20.0339(499)	550.0060(543)	19.0445(456)	550.0060(543)	19.0175(456)
600.0100(544)	11.8676(291)	600.0100(544)	9.912 13(2380)	600.0100(544)	9.9213(242)
780.0130(552)	7.547 45(20300)	780.0130(552)	5.080 88(8760)	780.0130(552)	5.218 03(5520)

Table B.4.: Proton recoil spectra config 3. Given are the proton count rates of config 3 for each retardation voltage, for details of the settings, see appendix C.

| | channel 19 | | channel 20 | | channel 21 |
ret. voltage in V	countrate per s	ret. voltage in V	countrate per s	ret. voltage in V	countrate per s
49.9989(539)	426.908(244)	49.9989(539)	452.332(254)	49.9989(539)	445.868(252)
100.0050(539)	390.424(198)	100.0050(539)	421.888(213)	100.0050(539)	414.825(211)
249.9990(539)	254.376(159)	249.9990(539)	293.269(174)	249.9990(539)	288.695(173)
350.001(54)	163.111(137)	350.001(54)	196.526(152)	350.001(54)	192.779(150)
400.011(54)	121.615(114)	400.011(54)	148.906(127)	400.011(54)	146.035(125)
450.0050(541)	84.3754(903)	450.0050(541)	104.659(100)	450.0050(541)	102.2870(991)
500.0110(542)	52.8257(674)	500.0110(542)	65.0083(724)	500.0110(542)	63.6015(714)
550.0050(543)	29.3752(494)	550.0050(543)	33.9524(490)	550.0050(543)	32.9873(475)
600.0100(544)	15.8104(260)	600.0100(544)	15.5726(210)	600.0100(544)	14.5785(197)
780.0110(552)	8.76095(21100)	780.0110(552)	5.71651(7620)	780.0110(552)	5.02913(4280)

Table B.5.: Proton recoil spectra config 4. Given are the proton count rates of config 4 for each retardation voltage, for details of the settings, see appendix C.

channel 19		channel 20		channel 21	
ret. voltage in V	countrate per s	ret. voltage in V	countrate per s	ret. voltage in V	countrate per s
49.9971(539)	367.818(342)	49.9971(539)	395.816(358)	49.9971(539)	392.779(356)
100.0020(539)	336.461(276)	100.0020(539)	368.729(298)	100.0020(539)	365.080(296)
249.9980(539)	218.691(222)	249.9980(539)	255.866(246)	249.9980(539)	252.188(244)
350.00(54)	138.523(190)	350.00(54)	171.366(214)	350.00(54)	168.655(213)
400.009(54)	102.200(157)	400.009(54)	129.517(178)	400.009(54)	127.690(176)
450.0040(541)	70.5775(1230)	450.0040(541)	90.6019(1400)	450.0040(541)	88.9647(1380)
500.0090(542)	43.1821(914)	500.0090(542)	56.1129(1010)	500.0090(542)	54.9220(998)
550.0040(543)	23.5689(652)	550.0040(543)	28.7261(673)	550.0040(543)	28.0899(659)
600.0080(544)	11.9742(326)	600.0080(544)	12.7763(265)	600.0080(544)	12.2549(251)
780.0100(552)	6.040 82(27600)	780.0100(552)	3.981 45(6600)	780.0100(552)	3.595 31(10700)

Table B.6.: Proton recoil spectra config 5. Given are the proton count rates of config 5 for each retardation voltage, for details of the settings, see appendix C.

channel 19		channel 20		channel 21	
ret. voltage in V	countrate per s	ret. voltage in V	countrate per s	ret. voltage in V	countrate per s
49.9983(539)	368.075(414)	49.9983(539)	393.065(430)	49.9983(539)	389.882(428)
100.0040(539)	340.464(342)	100.0040(539)	365.754(358)	100.0040(539)	362.686(357)
249.9990(539)	232.232(278)	249.9990(539)	253.564(292)	249.9990(539)	252.073(291)
350.001(54)	152.786(230)	350.001(54)	168.656(243)	350.001(54)	167.842(242)
400.011(54)	115.298(202)	400.011(54)	128.631(213)	400.011(54)	127.675(212)
450.0050(541)	80.8155(1600)	450.0050(541)	89.6847(1680)	450.0050(541)	88.9594(1670)
500.0100(542)	50.6577(1120)	500.0100(542)	55.6031(1150)	500.0110(542)	55.0141(1140)
550.0050(543)	27.1967(789)	550.0050(543)	28.6031(770)	550.0050(543)	28.3638(761)
600.0090(544)	13.5751(389)	600.0090(544)	12.9071(324)	600.0090(544)	12.6065(307)
780.0110(552)	6.281 54(33700)	780.0110(552)	4.370 19(10500)	780.0110(552)	3.926 44(17100)

Table B.7.: Proton recoil spectra config 6E8R5. Given are the proton count rates of config 6E8R5 for each retardation voltage, for details of the settings, see appendix C.

channel 19		channel 20		channel 21	
ret. voltage in V	countrate per s	ret. voltage in V	countrate per s	ret. voltage in V	countrate per s
49.9974(539)	364.534(652)	49.9974(539)	389.757(675)	49.9974(539)	386.660(673)
100.0030(539)	338.632(539)	100.0030(539)	362.431(562)	100.0030(539)	360.227(561)
249.9980(539)	230.683(437)	249.9980(539)	251.282(461)	249.9980(539)	250.295(458)
350.00(54)	151.537(380)	350.00(54)	168.706(400)	350.00(54)	166.450(399)
400.009(54)	114.893(318)	400.009(54)	126.937(334)	400.009(54)	126.258(333)
450.0040(541)	80.1488(2520)	450.0040(541)	88.7626(2630)	450.0040(541)	88.1951(2620)
500.0090(542)	50.4663(1830)	500.0090(542)	55.0445(1900)	500.0090(542)	54.6328(1880)
550.0040(543)	26.6858(1290)	550.0040(543)	28.5404(1270)	550.0040(543)	28.162(125)
600.0080(544)	13.1767(619)	600.0080(544)	12.8111(510)	600.0080(544)	12.3185(491)
780.0100(552)	6.082 57(48200)	780.0100(552)	4.140 81(19300)	780.0100(552)	3.836 22(10600)

Table B.8.: Proton recoil spectra config 6E8R200. Given are the proton count rates of config 6E8R200 for each retardation voltage, for details of the settings, see appendix C.

channel 19		channel 20		channel 21	
ret. voltage in V	countrate per s	ret. voltage in V	countrate per s	ret. voltage in V	countrate per s
49.9982(539)	360.788(917)	49.9982(539)	389.840(952)	49.9982(539)	387.382(955)
100.0040(539)	334.088(759)	100.0040(539)	360.432(793)	100.0040(539)	362.685(791)
249.9990(539)	228.818(615)	249.9990(539)	249.96(65)	249.9990(539)	248.983(650)
350.001(54)	150.472(536)	350.001(54)	168.186(566)	350.001(54)	168.114(564)
400.011(54)	114.157(445)	400.011(54)	127.438(472)	400.011(54)	126.620(471)
450.0050(541)	78.7678(3550)	450.0050(541)	88.5517(3740)	450.0050(541)	88.3182(3720)
500.0110(542)	50.0067(2620)	500.0110(542)	55.4425(2700)	500.0110(542)	54.9362(2650)
550.0050(543)	27.3598(1870)	550.0050(543)	28.8798(1800)	550.0050(543)	27.954(178)
600.0100(544)	13.8450(909)	600.0100(544)	12.8494(744)	600.0100(544)	12.5380(698)
780.0110(552)	6.5685(6390)	780.0110(552)	4.393 39(29700)	780.0110(552)	3.870(163)

Table B.9.: Proton recoil spectra config 7. Given are the proton count rates of config 7 for each retardation voltage, for details of the settings, see appendix C.

channel 19		channel 20		channel 21	
ret. voltage in V	countrate per s	ret. voltage in V	countrate per s	ret. voltage in V	countrate per s
49.9969(539)	418.510(263)	49.9969(539)	443.360(273)	49.9969(539)	436.452(271)
100.0020(539)	382.761(212)	100.0020(539)	412.722(227)	100.0020(539)	406.397(225)
249.9980(539)	248.486(168)	249.9980(539)	286.981(184)	249.9980(539)	281.631(183)
350.00(54)	159.443(144)	350.00(54)	191.900(159)	350.00(54)	188.523(158)
400.009(54)	118.589(122)	400.009(54)	145.660(136)	400.009(54)	142.868(134)
450.0030(541)	82.1125(962)	450.0030(541)	102.172(107)	450.0030(541)	100.034(106)
500.0090(542)	51.3500(709)	500.0090(542)	63.4943(767)	500.0090(542)	61.8530(754)
550.0040(543)	28.3287(512)	550.0040(543)	33.1446(512)	550.0040(543)	32.0969(498)
600.0080(544)	15.0244(268)	600.0080(544)	15.0379(217)	600.0080(544)	14.2195(204)
780.0100(552)	8.117 06(21600)	780.0100(552)	5.3007(633)	780.0100(552)	4.703 73(9260)

Table B.10.: Proton recoil spectra config 8. Given are the proton count rates of config 8 for each retardation voltage, for details of the settings, see appendix C.

channel 19		channel 20		channel 21	
ret. voltage in V	countrate per s	ret. voltage in V	countrate per s	ret. voltage in V	countrate per s
50.000(616)	422.669(365)	50.000(616)	442.252(374)	50.000(616)	435.273(371)
100.000(617)	392.391(314)	100.000(617)	412.491(324)	100.000(617)	405.645(321)
250.000(617)	271.394(241)	250.000(617)	288.046(248)	250.000(617)	282.535(246)
350.000(617)	181.765(204)	350.000(617)	193.271(210)	350.000(617)	189.774(208)
400.000(617)	137.907(177)	400.000(617)	147.284(182)	400.000(617)	143.905(180)
450.000(618)	98.5693(1390)	450.000(618)	103.802(141)	450.000(618)	101.548(139)
500.000(618)	63.115(104)	500.000(618)	65.2246(1030)	500.000(618)	63.6944(1010)
550.000(618)	35.7124(762)	550.000(618)	35.1863(721)	550.000(618)	34.2350(708)
600.000(618)	19.336(40)	600.000(618)	17.3068(340)	600.000(618)	16.6514(327)
780.00(62)	10.620(221)	780.00(62)	7.690 24(22600)	780.00(62)	7.101 47(22400)

C. Spectrometer Settings for the Different Runs

In this chapter the settings of *a*SPECT are given for each configuration analysed. Config 1 has been arbitrarily chosen as standard, all changes to this configuration are emphasised in the other configurations.

The magnet system consists of 9 coils, connected in series, named MAIN. This MAIN system generates the magnetic field, as shown in fig. 2.4. Additionally, two pairs of correction coils are installed, one at the DV (C3 and C5) and one at the AP (AHC and HC). In case of the DV the correction coils are used to form the small magnetic field gradient in the DV, cf fig. 3.21. In case of the AP a pair of Helmholtz (HC) and Anti-Helmholtz coils are installed, which can shift the actual magnetic AP a few cm upwards/downwards, respectively. Both correction coils systems do not change the field strength in the DV/AP, just change slightly the local field shape. Hence, the do not change the value of the magnetic field ratio r_B. For details on the magnet system, see [Gua11].

In fig. 2.4 a sketch of the electrode system, generating the electric field in *a*SPECT is shown. Several ExB drift electrodes are installed. The E8 between mirror and AP to empty the proton trap, between these electrodes. The E16 to also accelerate the protons towards the detector and change their projection onto the detector in y-direction. This determines, which part of the neutron beam is projected on the the detector, hence influencing the edge effect. Finally, the E15 installed to introduce an additional ExB drift close to the AP (config 3, 4) to empty the particle trap inside the AP electrode (cf. section 2.2.3). Further, a electric field gradient has been generated in the DV (conf 7) to empty potential proton traps inside the DV (cf. fig. 2.9).

For the neutron beam, two different neutron beam profiles have been used, a wide, normal one (7 cm) and a small, reduced one (3 cm). The reduced neutron beam profile enhances the edge effect dramatically (cf. section 3.3.1), in this way, the effect can be investigated in more detail (config 4, 5, 6). Hence, the correction of it is more precise. Further, as the various ExB drift electrodes change the projection onto the detector enegry-dependent, their influence on the edge effect has been investigated as well (config 6).

Finally, to test the used DAQ system for systematics a different one, without shaper (cf. section 3.1), has been used in one measurement (config 8).

Table C.1.: Config1: Standard configuration of the *a*SPECT spectrometer for the 2013 beam time. For the magnet system, the electrode system and the beam.

magnet system	current set in A
MAIN	70
C3	35
C5	15
AHC	25.5
HC	0

beam profile	width in cm
normal	ca. 7

electrode	voltage set in V
detector	-15 000
E16 side A	-1 750
E16 side B	-2 250
E8 side L	-1
E8 side R	-200
E2 side L	+380
E2 side R	+380
E1	+800
E1b	+860
E15 side L	E15
E3	DV
E6	DV

Table C.2.: Config2: configuration of the *a*SPECT spectrometer for the 2013 beam time for measurements with mirror ON and OFF. Changes to the standard configuration are emphasised.

magnet system	current set in A
MAIN	70
C3	35
C5	15
AHC	25.5
HC	0

beam profile	width in cm
normal	ca. 7

electrode	voltage set in V
detector	-15 000
E16 side A	-1 750
E16 side B	-2 250
E8 side L	-1
E8 side R	-200
E2 side L	+380 **or 0**
E2 side R	+380 **or 0**
E1	+800 **or 0**
E1b	+860 **or 0**
E15 side L	E15
E3	DV
E6	DV

Table C.3.: Config3: configuration of *a*SPECT with asymmetric E15 electrode for background investigations. Changes to the standard configuration are emphasised.

magnet system	current set in A
MAIN	70
C3	35
C5	15
AHC	**40**
HC	0

beam profile	width in cm
normal	ca. 7

electrode	voltage set in V
detector	-15 000
E16 side A	-1 750
E16 side B	-2 250
E8 side L	**-200**
E8 side R	**-5**
E2 side L	+380
E2 side R	+380
E1	+800
E1b	+860
E15 side L	**E11**
E3	DV
E6	DV

Table C.4.: Config4: Configuration of *a*SPECT with asymmetric E15 electrode and reduced beam profile for investigations of the edge effect. Changes to the standard configuration are emphasised.

magnet system	current set in A
MAIN	70
C3	35
C5	15
AHC	**40**
HC	0

beam profile	width in cm
reduced	**ca. 3**

electrode	voltage set in V
detector	-15 000
E16 side A	-1 750
E16 side B	-2 250
E8 side L	**-200**
E8 side R	**-5**
E2 side L	+380
E2 side R	+380
E1	+800
E1b	+860
E15 side L	**E11**
E3	DV
E6	DV

Table C.5.: Config5: standard configuration with reduced beam profile of the *a*SPECT spectrometer to increase the edge effect. Changes to the standard configuration are emphasised.

magnet system	current set in A
MAIN	70
C3	35
C5	15
AHC	25.5
HC	0

beam profile	width in cm
reduced	**ca. 3**

electrode	voltage set in V
detector	-15 000
E16 side A	-1 750
E16 side B	-2 250
E8 side L	**-200**
E8 side R	**-5**
E2 side L	+380
E2 side R	+380
E1	+800
E1b	+860
E15 side L	E15
E3	DV
E6	DV

Table C.6.: Config6: configuration with inverted ExB drift in E8 electrode and reduced beam profile to investigate the edge effect. Changes to the standard configuration are emphasised.

magnet system	current set in A
MAIN	70
C3	35
C5	15
AHC	25.5
HC	0

beam profile	width in cm
reduced	**ca. 3**

electrode	voltage set in V
detector	-15 000
E16 side A	-1 750
E16 side B	-2 250
E8 side L	**-200 or -5**
E8 side R	**-5 or -200**
E2 side L	+380
E2 side R	+380
E1	+800
E1b	+860
E15 side L	E15
E3	DV
E6	DV

Table C.7.: Config7: configuration with electric field gradient in DV to investigate potential proton traps in the DV. Changes to the standard configuration are emphasised.

magnet system	current set in A
MAIN	70
C3	35
C5	15
AHC	**40**
HC	0

beam profile	width in cm
normal	ca. 7

electrode	voltage set in V
detector	-15 000
E16 side A	-1 750
E16 side B	-2 250
E8 side L	**-200**
E8 side R	**-5**
E2 side L	+380
E2 side R	+380
E1	+800
E1b	+860
E15 side L	**E11**
E3	**+4**
E6	**-4**

Table C.8.: Config8: configuration with the DAQ system switched to the uDAQ system, to reveal any severe electronic problems.

magnet system	current set in A
MAIN	70
C3	35
C5	15
AHC	25.5
HC	0

beam profile	width in cm
normal	ca. 7

electrode	voltage set in V
detector	-15 000
E16 side A	-1 750
E16 side B	-2 250
E8 side L	**-200**
E8 side R	**-5**
E2 side L	+380
E2 side R	+380
E1	+800
E1b	+860
E15 side L	E15
E3	DV
E6	DV

D. Accuracy of the Agilent DMM 3458A

In eq. (3.14) in section 3.1.3 the uncertainty of the retardation voltage $\delta_{U_{ret}}$ has been calculated. Part of this uncertainty $\delta_{U_{ret}}$ is the systematic uncertainty δ_{DMM} of the Digital Multimeter (DMM) used during the beam-time 2013. In this chapter will be explained, what contributes to this uncertainty δ_{DMM} and how it is calculated. During the beam-time 2013 an Agilent[1] 3458A DMM. The precision of the Agilent 3458A DMM is limited by several factors:

- general uncertainty of measured value for
  - reading δ_{read}
  - range setting δ_{range}
- uncertainty to absolute value (reference standard) δ_{abs}
- temperature stability δ_T

All uncertainties are given in the data specifications of the Agilent [key]. The general way to calculate the uncertainty δ_{DMM} of the Agilent reading is:

$$\delta_{DMM} = \underbrace{p_{read} \cdot V_{input}}_{\delta_{read}} + \underbrace{p_{range} \cdot V_{range}}_{\delta_{range}} + \underbrace{\left(p_{T,read} \cdot V_{input} + p_{T,range} \cdot V_{range}\right) \cdot \Delta_T}_{\delta_T} + \underbrace{p_{abs} \cdot V_{input}}_{\delta_{abs}} \cdot$$

(D.1)

V_{input} is the voltage applied to the Agilent and V_{range} its range setting. Δ_T is the temperature difference between the reference temperature of the Agilent (23 °C) and the ambient temperature. Without applying an auto-calibration (ACAL) every 24 h this temperature difference may differ by ± 1°C without the need to apply a temperature correction, with auto-calibration every 24 h it can differ up to ± 5 °C. In table D.1 the specifications of the Agilent 3458A are given.

In appendix D.1 some exemplary values for δ_{DMM} are calculated using eq. (D.1) and the specifications given in table D.1 with typical values of V_{input} and Δ_T for aSPECT. For $\delta_{U_{ret}}$ in eq. (3.14) the program generating the integral proton spectrum from the pulse-height

---

[1]Please be aware, meanwhile Agilent has been taken over by Keysight.

Table D.1.: Specifications of Agilent 3458A taken from [key]. Last auto-calibration (ACAL) has to be within the last 24h and the number of integration power line cycles NPLC has to be NPLC $\geq$ 100

Error	value in ppm	comment
p_{read}	2.5	range 1000 V, 24 h measurement
p_{read}	4.5	range 1000 V, 90 days measurement
p_{read}	$12 \cdot \left(\frac{V_{input}/V}{1000}\right)^2$	add. error for inputs $V_{input} > 100\,V$
p_{range}	0.1	range 1000 V
p_{abs}	~ 2	exact value has to be taken from last calibration
$p_{T,read}$	0.15 C^{-1}	with ACAL
$p_{T,range}$	0.01 C^{-1}	with ACAL

spectra for the different retardation voltages calculated for each retardation voltage δ_{DMM} individually, using eq. (D.1). These values for $\delta_{U_{ret}}$ are then used as x-uncertainties for the data point of the integral spectrum.

D.1. Examples

In this section eq. (D.1) will be used to calculated δ_{DMM} using some typical values of V_{input} and Δ_T to get a feeling how big δ_{DMM} is. As typical values for $V_{input} = 50\,V$ and 800 V has been used, which corresponds to the lowest and highest retardation voltage used during the beam-time. As temperature 38 °C has been used, corresponding to a typical value during summer in the neutron guide hall at the ILL. This corresponds to a $\Delta_T = 10$ °C above the reference temperature of the Agilent, taking the additional 5 °C from performing an auto-calibration (ACAL) every 24 h into account. For each set of values the precision within $\Delta t = 24$ h has been calculated, as well as within 90 days, which is more then the complete measurement time.

As can be seen from these examples, δ_{DMM} is currently not the limiting part of $\delta_{U_{ret}}$. The contribution of the fluctuation of the surface contact potential, field leakage and the RF noise are higher. But the uncertainties δ_{DMM} for 800 V are already beyond the originally desired $\delta_{U_{ret}} \leq 10$ mV of *a*SPECT. Therefore, for a future measurement/experiment, with improved surface contact potential, field leakage and RF noise, one will also have to buy a more precise DMM.

$V_{input} = 800\,V$, $\Delta t = 90$ days, $\Delta T = 38$ °C:

$$
\begin{aligned}
\delta_{DMM} = &\left[4.5e^{-6} + 12e^{-6} \cdot \left(\frac{800}{1000}\right)^2\right] \cdot 800\,V &&\}\delta_{read} = 9.744\,mV \\
&+ 0.1e^{-6} \cdot 1000\,V &&\}\delta_{range} = 0.1\,mV \\
&+ \left(0.15e^{-6} \cdot 800\,V + 0.01e^{-6} \cdot 1000\,V\right) C^{-1} \cdot 10\,°C &&\}\delta_T = 1.3\,mV \\
&+ 2e^{-6} \cdot 800\,V &&\}\delta_{abs} = 1.6\,mV \\
&= \underline{12.744\,mV}
\end{aligned}
$$

$V_{input} = 800\,\text{V}, \Delta t = 24\,\text{h}, \Delta T = 38\,^\circ\text{C}$:

$$\delta_{DMM} = \left[2.5e^{-6} + 12e^{-6} \cdot \left(\frac{800}{1000}\right)^2\right] \cdot 800\,\text{V} \qquad\qquad \}\delta_{read} = 8.144\,\text{mV}$$

$$+\, 0.1e^{-6} \cdot 1000\,\text{V} \qquad\qquad\qquad \}\delta_{range} = 0.1\,\text{mV}$$

$$+\, \left(0.15e^{-6} \cdot 800\,\text{V} + 0.01e^{-6} \cdot 1000\,\text{V}\right)\text{C}^{-1} \cdot 10\,^\circ\text{C} \qquad \}\delta_T = 1.3\,\text{mV}$$

$$+\, 2e^{-6} \cdot 800\,\text{V} \qquad\qquad\qquad \}\delta_{abs} = 1.6\,\text{mV}$$

$$=\, \underline{11.144\,\text{mV}}$$

$V_{input} = 50\,\text{V}, \Delta t = 90\,\text{days}, \Delta T = 38\,^\circ\text{C}$:

$$\delta_{DMM} = \left[4.5e^{-6} + 12e^{-6} \cdot \left(\frac{50}{1000}\right)^2\right] \cdot 50\,\text{V} \qquad\qquad \}\delta_{read} = 0.2265\,\text{mV}$$

$$+\, 0.1e^{-6} \cdot 1000\,\text{V} \qquad\qquad\qquad \}\delta_{range} = 0.1\,\text{mV}$$

$$+\, \left(0.15e^{-6} \cdot 50\,\text{V} + 0.01e^{-6} \cdot 1000\,\text{V}\right)\text{C}^{-1} \cdot 10\,^\circ\text{C} \qquad \}\delta_T = 0.175\,\text{mV}$$

$$+\, 2e^{-6} \cdot 50\,\text{V} \qquad\qquad\qquad \}\delta_{abs} = 0.1\,\text{mV}$$

$$=\, \underline{0.6015\,\text{mV}}$$

$V_{input} = 50\,\text{V}, \Delta t = 24\,\text{h}, \Delta T = 38\,^\circ\text{C}$:

$$\delta_{DMM} = \left[2.5e^{-6} + 12e^{-6} \cdot \left(\frac{50}{1000}\right)^2\right] \cdot 50\,\text{V} \qquad\qquad \}\delta_{read} = 0.1265\,\text{mV}$$

$$+\, 0.1e^{-6} \cdot 1000\,\text{V}\} \qquad\qquad\qquad \delta_{range} = 0.1\,\text{mV}$$

$$+\, \left(0.15e^{-6} \cdot 50\,\text{V} + 0.01e^{-6} \cdot 1000\,\text{V}\right)\text{C}^{-1} \cdot 10\,^\circ\text{C} \qquad \}\delta_T = 0.175\,\text{mV}$$

$$+\, 2e^{-6} \cdot 50\,\text{V} \qquad\qquad\qquad \}\delta_{abs} = 0.1\,\text{mV}$$

$$=\, \underline{0.5015\,\text{mV}}$$

Bibliography

[AAB+04]   J. Angrik et al. "KATRIN design report". Technical report, Forschungszentrum Karlsruhe (2004). FZKA Scientific Report 7090.

[AAl+]   R. Alarcon et al. "Funding proposal for the neutron decay spectrometer Nab at SNS". URL `http://nab.phys.virginia.edu/nab_doe_fund_prop.pdf`.

[Abe08]   H. Abele. "The neutron. Its properties and basic interactions". Progress in Particle and Nuclear Physics, volume 60 (2008) (1), 1 – 81. ISSN 0146-6410. URL `http://www.sciencedirect.com/science/article/pii/S0146641007000622`.

[ADF+08]   Altarev, I. et al. "Neutron velocity distribution from a superthermal solid 2H2 ultracold neutron source". Eur. Phys. J. A, volume 37 (2008) (1), 9–14. URL `http://dx.doi.org/10.1140/epja/i2008-10604-8`.

[BAB+12]   J. Beringer et al. "REVIEW OF PARTICLE PHYSICS Particle Data Group". Physical Review D, volume 86 (2012) (1), 010001.

[BBPP14]   S. Baeßler et al. "New precision measurements of free neutron beta decay with cold neutrons". Journal of Physics G: Nuclear and Particle Physics, volume 41 (2014) (11), 114003. URL `http://stacks.iop.org/0954-3899/41/i=11/a=114003`.

[BCK+11]   Beck, M. et al. "First detection and energy measurement of recoil ions following beta decay in a Penning trap with the WITCH experiment". The European Physical Journal A, volume 47 (2011) (3), 45. ISSN 1434-6001. URL `http://dx.doi.org/10.1140/epja/i2011-11045-0`.

[BDvdG+02]   J. Byrne et al. "Determination of the electron-antineutrino angular correlation coefficient a 0 and the parameter $|\lambda| = |\frac{G_A}{G_V}|$ in free neutron β-decay from measurements of the integrated energy spectrum of recoil protons stored in an ion trap". Journal of Physics G: Nuclear and Particle Physics, volume 28 (2002) (6), 1325. URL `http://stacks.iop.org/0954-3899/28/i=6/a=314`.

[BHS05]   G. Bertone, D. Hooper and J. Silk. "Particle dark matter: evidence, candidates and constraints". Physics Reports, volume 405 (2005) (5-6), 279–390. ISSN 0370-1573. URL `http://www.sciencedirect.com/science/article/B6TVP-4DR4K80-1/2/a8e31daa5442663a68a9c31bc0ebfa7c`.

[Bic15]   E. Bickmann. aSPECT experiment measurements with a Kelvin probe. Bachelor thesis, Johannes Gutenberg-Universität Mainz (2015).

[Bor10]   M. Borg. The electron antineutrino angular correlation coefficient a in free neutron decay: Testing the standard model with the aSPECT-spectrometer. Ph.D. thesis, Johannes Gutenberg-Universität Mainz (2010).

[BPT80]   G. Beamson, H. Q. Porter and D. W. Turner. "The collimating and magnifying properties of a superconducting field photoelectron spectrometer". Journal of Physics E: Scientific Instruments, volume 13 (1980) (1), 64. URL `http://stacks.iop.org/0022-3735/13/i=1/a=018`.

[BR97]   R. Brun and F. Rademakers. "ROOT - An object oriented data analysis framework". Nuclear Instruments & Methods in Physics Research Section A-Accelerators Spectrometers Detectors and Associated Equipment, volume 389 (1997) (1-2), 81–86. ISSN 0168-9002. URL `http://root.cern.ch`, 5th International Workshop on Software Engineering, Neural Nets, Genetic Algorithms, Expert Systems, Symbolic Algebra and Automatic Calculations in Physics Research (AIHENP 96), Lausanne, Switzerland, Sep 02-06, 1996.

[Bra99]   S. Brandt. Data Analysis: Statistical and computational methods for scientists and engineers with 273 illustrations, includes CD-Rom, 3rd edition. Ohlin Lectures; 7 (Springer New York, 1999). ISBN 9780387984988.

[BVB+10]   M. Beck et al. "Effect of a sweeping conductive wire on electrons stored in a Penning-like trap between the KATRIN spectrometers". European Physical Journal A, volume 44 (2010) (3), 499–511. ISSN 1434-6001.

[Cab63]   N. Cabibbo. "Unitary Symmetry and Leptonic Decays". Phys. Rev. Lett., volume 10 (1963), 531–533. URL `http://link.aps.org/doi/10.1103/PhysRevLett.10.531`.

[Cha32]   J. Chadwick. "The Existence of a Neutron". Proceedings of the Royal Society of London A: Mathematical, Physical and Engineering Sciences, volume 136 (1932) (830), 692–708. ISSN 0950-1207. URL `http://rspa.royalsocietypublishing.org/content/136/830/692`.

[CRM13]   V. Cirigliano and M. J. Ramsey-Musolf. "Low energy probes of physics beyond the standard model". Progress in Particle and Nuclear Physics, volume 71 (2013), 2–20. ISSN 0146-6410. URL `http://www.sciencedirect.com/science/article/pii/S0146641013000215`, fundamental Symmetries in the Era of the {LHC}.

[DBvdG+00] P. Dawber et al. "Determination of the electron-antineutrino correlation coefficient a in neutron β-decay by measurement of the integrated proton spectrum". Nuclear Instruments and Methods in Physics Research Section A: Accelerators, Spectrometers, Detectors and Associated Equipment, volume 440 (2000) (3), 543–547. ISSN 0168-9002. URL `http://www.sciencedirect.com/science/article/pii/S0168900299010347`.

[DRM+14]   D. Dubbers et al. "The point spread function of electrons in a magnetic field, and the decay of the free neutron". Nuclear Instruments and Methods in Physics Research Section A: Accelerators, Spectrometers, Detectors and Associated Equipment, volume 763 (2014), 112–119. ISSN

0168-9002. URL `http://www.sciencedirect.com/science/article/pii/S0168900214007244`.

[DS11]   D. Dubbers and M. G. Schmidt. "The neutron and its role in cosmology and particle physics". Rev. Mod. Phys., volume 83 (2011), 1111–1171. URL `http://link.aps.org/doi/10.1103/RevModPhys.83.1111`.

[Dub91]   D. Dubbers. "Particle physics with cold neutrons". Prog. Part. Nucl. Phys., volume 26 (1991), 173–252.

[Fer]   E. Fermi. "Versuch einer Theorie der β-Strahlen. I". Zeitschrift für Physik, volume 88 (3), 161–177. ISSN 0044-3328. URL `http://dx.doi.org/10.1007/BF01351864`.

[FGT⁺]   D. Furse et al. "Kassiopeia: A Modern, Extansible C++ Particle Tracking Package". Paper in preparation.

[Fla88]   C. Flammarion. L'atmosphère: météorologie populaire, volume 1 (Hachette (Paris), 1888). URL `http://catalogue.bnf.fr/ark:/12148/cb304399579`.

[GBB⁺05] F. Glück et al. "The neutron decay retardation spectrometer aSPECT: Electromagnetic design and systematic effects". European Physical Journal A, volume 23 (2005) (1), 135–146. ISSN 1434-6001.

[GJL95]   F. Glück, I. Joo and J. Last. "Measurable parameters of neutron decay". Nuclear Physics A, volume 593 (1995) (2), 125 – 150. ISSN 0375-9474. URL `http://www.sciencedirect.com/science/article/pii/0375947495003544`.

[Gla61]   S. L. Glashow. "Partial-symmetries of weak interactions". Nuclear Physics, volume 22 (1961) (4), 579 – 588. ISSN 0029-5582. URL `http://www.sciencedirect.com/science/article/pii/0029558261904692`.

[Glü93]   F. Glück. "Measurable distributions of unpolarized neutron decay". Physical Review D, volume 47 (1993) (7), 2840–2848. ISSN 0556-2821.

[GT36]   G. Gamow and E. Teller. "Selection Rules for the β-Disintegration". Phys. Rev., volume 49 (1936), 895–899. URL `http://link.aps.org/doi/10.1103/PhysRev.49.895`.

[Gua11]   F. A. Guardia. Characterization of electromagnetic fields in the aSPECT spectrometer and reduction of systematic errors. Ph.D. thesis, Johannes Gutenberg-Universität Mainz (2011).

[Hay12]   W. Haynes. CRC Handbook of Chemistry and Physics, 93rd Edition. CRC Handbook of Chemistry and Physics (Taylor & Francis, 2012). ISBN 9781439880494.

[HH76]   T. Hsu and J. L. Hirshfield. "Electrostatic energy analyzer using a nonuniform axial magnetic field". Review of Scientific Instruments, volume 47 (1976) (2), 236–238. URL `http://scitation.aip.org/content/aip/journal/rsi/47/2/10.1063/1.1134594`.

[Hor11]   R. M. Horta. First measurements of the aSPECT spectrometer. Ph.D. thesis, Johannes Gutenberg-Universität Mainz (2011).

[Hor15]   R. Horn. Simulation und Untersuchung der elektrischen Potentiale des *a*SPECT-Experiments. Bachelorarbeit, Johannes Gutenberg-Universität Mainz (2015).

[HSH+01]   C. D. Hoyle et al. "Submillimeter Test of the Gravitational Inverse-Square Law: A Search for "Large" Extra Dimensions". Phys. Rev. Lett., volume 86 (2001), 1418–1421. URL http://link.aps.org/doi/10.1103/PhysRevLett.86.1418.

[HT15]   J. C. Hardy and I. S. Towner. "Superallowed $0^+ \rightarrow 0^+$ nuclear β decays: 2014 critical survey, with precise results for V_{ud} and CKM unitarity". Phys. Rev. C, volume 91 (2015), 025501. URL http://link.aps.org/doi/10.1103/PhysRevC.91.025501.

[ILL]   URL http://www.ill.eu.

[Jac75]   J. Jackson. Classical electrodynamics (Wiley, 1975). ISBN 9780471431329. URL https://books.google.de/books?id=_7rvAAAAMAAJ.

[Jam06]   F. James. Statistical Methods in Experimental Physics (World Scientific Publishing, 2006). ISBN 9789812567956.

[JTW57]   J. D. Jackson, S. B. Treiman and H. W. Wyld. "Possible Tests of Time Reversal Invariance in Beta Decay". Phys. Rev., volume 106 (1957), 517–521. URL http://link.aps.org/doi/10.1103/PhysRev.106.517.

[Kah15]   J. Kahlenberg. Characterisation of the work function distribution of the *a*SPECT experiment's electrodes. Master thesis, Johannes Gutenberg-Universität Mainz (2015).

[key]   URL http://www.keysight.com/.

[KGB+09]   G. Konrad et al. "The Proton Spectrum in Neutron Beta Decay: Latest Results with the aSPECT Spectrometer". NUCLEAR PHYSICS A, volume 827 (2009) (1-4), 529C–531C. ISSN 0375-9474. 18th Particles and Nuclei International Conference (PANIC08), Eilat, ISRAEL, NOV 09-14, 2008.

[KIT]   URL https://www.itep.kit.edu/376.php.

[Kno00]   G. Knoll. Radiation Detection and Measurement (John Wiley & Sons, 2000). ISBN 9780471073383.

[Kom16]   A. Komives. "A Measurement of the Electron-Antineutrino Correlation in Free Neutron Beta Decay". In "PSI2016 conference", (2016).

[Kon11]   G. E. Konrad. Measurement of the proton recoil spectrum in neutron beta decay with the spectrometer aSPECT : study of systematic effects. Ph.D. thesis, Johannes Gutenberg-Universität Mainz (2011).

[KR83]   P. Kruit and F. H. Read. "Magnetic field paralleliser for 2π electron-spectrometer and electron-image magnifier". Journal of Physics E: Scientific Instruments, volume 16 (1983) (4), 313. URL http://stacks.iop.org/0022-3735/16/i=4/a=016.

[KWZ79]   A. Kiejna, K. F. Wojciechowski and J. Zebrowksi. "The temperature dependence of metal work functions". Journal of Physics F: Metal Physics, volume 9 (1979) (7), 1361. URL `http://stacks.iop.org/0305-4608/9/i=7/a=016`.

[lab]   URL `http://www.ni.com/labview/d/`.

[Leo94]   W. Leo. Techniques for Nuclear and Particle Physics Experiments: A How-to Approach (Springer, 1994). ISBN 9780387572802.

[LY56]   T. D. Lee and C. N. Yang. "Question of Parity Conservation in Weak Interactions". Phys. Rev., volume 104 (1956), 254–258. URL `http://link.aps.org/doi/10.1103/PhysRev.104.254`.

[Mag]   URL `https://nationalmaglab.org/about/facts-figures/world-records`.

[Mai14]   R. Maisonobe. Measurement of the angular correlation coefficient a between electron and antineutrino in neutron β-decay with the spectrometer aSPECT. Ph.D. thesis, Universite de Grenoble (2014).

[MGK+06]   A. Mann et al. "A Sampling ADC Data Acquisition System for Positron Emission Tomography". IEEE Transactions on Nuclear Science, volume 53 (2006) (1), 297.

[Mil12]   P. G. Milan. Investigation of particle traps in the aSPECT spectrometer. Internship report, Groupe NPP - Institut Laue-Langevin (2012).

[MMD+13]   D. Mund et al. "Determination of the Weak Axial Vector Coupling lambda = g(A)/g(V) from a Measurement of the beta-Asymmetry Parameter A in Neutron Beta Decay". Physical Review Letters, volume 110 (2013) (17). ISSN 0031-9007.

[MPB+13]   M. P. Mendenhall et al. "Precision measurement of the neutron beta-decay asymmetry". Physical Review C, volume 87 (2013) (3). ISSN 0556-2813.

[Nac68]   O. Nachtmann. "Relativistic Corrections to Recoil Spectrum in Neutron beta-Decay". Zeitschrift für Physik, volume 215 (1968) (5), 505–&.

[NCGA13]   O. Naviliat-Cuncic and M. González-Alonso. "Prospects for precision measurements in nuclear β decay in the LHC era". Annalen der Physik, volume 525 (2013) (8-9), 600–619. ISSN 1521-3889. URL `http://dx.doi.org/10.1002/andp.201300072`.

[Nob65]   "Nobel Lectures, Physics 1922-1941". Elsevier Publishing Company, Amsterdam (1965).

[O+14]   K. Olive et al. "Review of Particle Physics". Chin.Phys., volume C38 (2014), 090001. Particle Data Group.

[OF50]   J. Orear and E. Fermi. Nuclear Physics: A Course Given by Enrico Fermi at the University of Chicago. Midway Reprints (University of Chicago Press, 1950). ISBN 9780226243658. URL `https://books.google.de/books?id=WQtkYCWTcicC`.

[PAA+09]   D. Pocanic et al. "Nab: Measurement principles, apparatus and uncertainties". Nuclear Instruments and Methods in Physics Research Section A: Accelerators, Spectrometers, Detectors and Associated Equipment, volume 611 (2009) (2–3), 211 – 215. ISSN 0168-9002. URL http://www.sciencedirect.com/science/article/pii/S0168900209015289, particle Physics with Slow Neutrons.

[Pau11]   P. Pauly. Characterization of the aSPECT spectrometer. Internship report, Institut polytechnique de Grenoble (2011).

[Pay11]   D. Payne. FUG-Agilent tests. Internship report (2011).

[PBB+92]   A. Picard et al. "A solenoid retarding spectrometer with high resolution and transmission for keV electrons". Nuclear Instruments and Methods in Physics Research Section B: Beam Interactions with Materials and Atoms, volume 63 (1992) (3), 345–358. ISSN 0168-583X. URL http://www.sciencedirect.com/science/article/pii/0168583X9295119C.

[PBH+94]   G. Pausch et al. "Particle identification in a wide dynamic range based on pulse-shape analysis with solid-state detectors". Nuclear Instruments and Methods in Physics Research Section A: Accelerators, Spectrometers, Detectors and Associated Equipment, volume 349 (1994) (1), 281 – 284. ISSN 0168-9002. URL http://www.sciencedirect.com/science/article/pii/0168900294906343.

[Pen77]   F. M. Penning. "The Glow Discharge at Low Pressure Between Coaxial Cylinders in an Axial Magnetic Field". SLAC-TRANS-0175, (1977).

[Pet07]   G. Petzold. Measurement of the electron-antineutrino angular correlation coefficient a in neutron beta decay with the spectrometer aSPECT. Dissertation, Technische Universität München (2007).

[PRSZ06]   B. Povh et al. Teilchen und Kerne: Eine Einführung in die physikalischen Konzepte. Springer-Lehrbuch (Springer, 2006). ISBN 9783540366850. URL https://books.google.de/books?id=yPRSPwAACAAJ.

[pst]   URL http://physics.nist.gov/PhysRefData/Star/Text/PSTAR.html.

[Rob51]   J. M. Robson. "The Radioactive Decay of the Neutron". Phys. Rev., volume 83 (1951), 349–358. URL http://link.aps.org/doi/10.1103/PhysRev.83.349.

[Ros15]   K. U. Ross. Inbetriebnahme und Tests des Protonendetektors bei τSPECT. Bachelorarbeit, Johannes Gutenberg-Universität Mainz (2015).

[SAB+00]   U. Schmidt et al. "Neutron Polarization Induced by Radio Frequency Radiation". Phys. Rev. Lett., volume 84 (2000), 3270–3273. URL http://link.aps.org/doi/10.1103/PhysRevLett.84.3270.

[Sal69]   A. Salam. "Weak and electromagnetic interactions". (1969). Proc. of the 8th Nobel Symposium on 'Elementary particle theory, relativistic groups and analyticity', Stockholm, Sweden, 1968, edited by N. Svartholm, p.367-377.

[SBNC06]   N. Severijns, M. Beck and O. Naviliat-Cuncic. "Tests of the standard electroweak model in nuclear beta decay". Rev. Mod. Phys., volume 78 (2006), 991–1040. URL http://link.aps.org/doi/10.1103/RevModPhys.78.991.

[Sch12]   C. Schmidt. Investigation of the work function fluctuations for the precision experiments *a*SPECT and KATRIN. Diplomarbeit, Johannes Gutenberg-Universität Mainz (2012).

[Sch15]   U. Schmidt. "DatFit". Universität Heidelberg, (2015), private communication.

[Sch17]   C. Schmidt. Determination of the $\beta - \nu$ angular correlation coefficient a and its systematic and statistical errors from the 2013 beamtime of the aSPECT experiment. Ph.d. thesis in preperation, Johannes Gutenberg-Universität Mainz (2017).

[SDW78]   C. Stratowa, R. Dobrozemsky and P. Weinzierl. "Ratio $|\frac{g_A}{g_V}|$ derived from the proton spectrum in free-neutron decay". Phys. Rev. D, volume 18 (1978), 3970–3979. URL `http://link.aps.org/doi/10.1103/PhysRevD.18.3970`.

[SGB$^+$09]   M. Simson et al. "Measuring the proton spectrum in neutron decay-Latest results with aSPECT". Nuclear Instruments & Methods in Physics Research Section A-Accelerators Spectrometers Detectors and Associated Equipment, volume 611 (2009) (2-3), 203–206. ISSN 0168-9002. 5th International Workshop on Particle Physics with Slow Neutrons, Inst Laue Langevin, Grenoble, FRANCE, MAY 29-31, 2008.

[Sim10]   M. Simson. Measurement of the electron antineutrino angular correlation coefficient a with the neutron decay spectrometer aSPECT. Dissertation, Technische Universitaet Muenchen, Muenchen (2010).

[Sti15]   D. Stipp. Datenanalyse bei *a*SPECT mit Schwerpunkt auf Pulshöhenspektren. Bachelorarbeit, Johannes Gutenberg-Universität Mainz (2015).

[TBC$^+$13]   V. Tishchenko et al. "Detailed report of the MuLan measurement of the positive muon lifetime and determination of the Fermi constant". Phys. Rev. D, volume 87 (2013), 052003. URL `http://link.aps.org/doi/10.1103/PhysRevD.87.052003`.

[TFK78]   P. Tyuryukanov, I. Fetisov and G. Khodachenko. "Ignition Conditions of Low-Pressure Discharge in Crossed Axially-Symmetric Uniform Electric and Nonuniform Magnetic-Fields". Zhurnal Tekhnicheskoi Fiziki, volume 48 (1978) (8), 1629–1636. ISSN 0044-4642.

[Val09]   K. Valerius. Spectrometer-related background processes and their suppression in the KATRIN experiment. Dissertation, Universitaet Muenster (2009).

[Vir13]   R. Virot. Characterization of the new Data Acqusition System and the Detector Alignment for the aSPECT experiment. Internship report, Institut polytechnique de Grenoble (2013).

[WAH$^+$57]   C. S. Wu et al. "Experimental Test of Parity Conservation in Beta Decay". Phys. Rev., volume 105 (1957), 1413–1415. URL `http://link.aps.org/doi/10.1103/PhysRev.105.1413`.

[WBC$^+$09]   F. Wietfeldt et al. "aCORN: An experiment to measure the electron–antineutrino correlation in neutron decay". Nuclear Instruments and Methods in Physics Research Section A: Accelerators, Spectrometers, Detectors

and Associated Equipment, volume 611 (2009) (2–3), 207 – 210. ISSN 0168-9002. URL `http://www.sciencedirect.com/science/article/pii/ S0168900209015277`, particle Physics with Slow Neutrons.

[WDB⁺99]   C. Weinheimer et al. "High precision measurement of the tritium β spectrum near its endpoint and upper limit on the neutrino mass". Physics Letters B, volume 460 (1999) (1–2), 219 – 226. ISSN 0370-2693. URL `http://www. sciencedirect.com/science/article/pii/S0370269399007807`.

[Wei67]   S. Weinberg. "A Model of Leptons". Phys. Rev. Lett., volume 19 (1967), 1264– 1266. URL `http://link.aps.org/doi/10.1103/PhysRevLett.19.1264`.

[WFT⁺05]   F. Wietfeldt et al. "A method for an improved measurement of the electron– antineutrino correlation in free neutron beta decay". Nuclear Instruments and Methods in Physics Research Section A: Accelerators, Spectrometers, Detectors and Associated Equipment, volume 545 (2005) (1–2), 181 – 193. ISSN 0168-9002. URL `http://www.sciencedirect.com/science/article/ pii/S0168900205005863`.

[Wol15]   Wolfram Research Inc., Champaign, Illinois. Mathematica, version 10.2 edition (2015).

[ZBvdG⁺00]   O. Zimmer et al. ""aspect" - a new spectrometer for the measurement of the an- gular correlation coefficient a in neutron beta decay". Nuclear Instruments & Methods in Physics Research Section A-Accelerators Spectrometers Detectors and Associated Equipment, volume 440 (2000) (3), 548–556. ISSN 0168-9002. International Workshop on Particle Physics with Slow Neutrons, INST LAUE LANGEVIN, GRENOBLE, FRANCE, OCT 22-24, 1998.

[Zie13]   J. Ziegler. "SRIM - The Stopping and Range of Ions in Matter" (2013). URL `www.srim.org`.

Erklärung

Hiermit versichere ich die vorliegende Arbeit selbstständig verfasst und nur die angegebenen Hilfsmittel verwendet zu haben. Alle, auch sinngemäße, Textstellen und Grafiken anderer Arbeiten wurden an den entsprechenden Stellen, unter Angabe der Quellen, kenntlich gemacht.

Alexander Wunderle

Mainz, den 9.11.2016

Acronyms

ADC Analog-to-Digital-Converter

AP Analysing Plane

CDF Cumulative Distribution Function

CKM Cabibbo-Kobayashi-Maskawa

CMS Center of Mass System

DAQ Data AcQuisition

DMM Digital Multimeter

DV Decay Volume

HV High Vacuum

ILL Institut Laue-Langevin

LabVIEW Laboratory Virtual Instrumentation Engineering Workbench

LHC Large Hadron Collider

MAC-E filter Magnetic Adiabatic Collimation with Electrostatic filter

NMR Nuclear Magnetic Resonance

OFHC Oxygen-free high thermal conductivity

PDG Particle Data Group

PSF Point-Spread-Function

RMS Root-Mean-Square

ROOT Root Object-Oriented Technology

SDD Silicon Drift Detector

SM Standard Model of particle physics

TMP Turbo Molecular Pump

TOF Time Of Flight

UHV Ultra-High Vacuum

Alexander Georg Wunderle

curriculum vitae

Am Gonsenheimer Spieß 47
55122 Mainz
✉ *alexander@wunderle.email*

Vita

Geburtsdatum	24. Juni 1983
Geburtsort	Bad Säckingen
Familienstand	ledig, keine Kinder
Staatsangehörigkeit	deutsch

Abschlüsse

Diplom in Physik

Titel	**Modeling of neutron signatures in Germanium bolometers of the EDELWEISS experiment**
Betreuer	Prof. Dr. Johannes Blümer, Dr. Klaus Eitel
Beschreibung	Detaillierte Nachbildung von Neutronensignaturen zur Untersuchung von koinzidenten Ereignissen im Bolometerarray des EDELWEISS Experiments. Hierbei wurden die Parameter der einzelnen Bolometer und eine detaillierte Beschreibung der Propagation von Ladungsträgern in sub-Kelvin Germanium berücksichtigt. Die aus der Simulation gewonnenen Daten wurden mit experimentellen Daten des EDELWEISS Experiments verglichen, wobei die detaillierte Nachbildung der Signaturen zum ersten Mal auch den Vergleich von Koinzidenzen innerhalb eines Bolometers ermöglichten.

Master of Physics

Titel	**Electronic excitation in model biological systems**
Betreuer	Prof. Dr. Ian Galbraith, Dr. David Townsend

Beschreibung Detaillierte Nachbildung von elektronischen Anregungszuständen von Molekülen in biologischen Systemen, namentlich verschiedene Imidazole. Diese Zustände wurden auf Relaxationsmechanismen untersucht, der Fokus lag hierbei auf den biologisch interessanten nicht-radiativen, zerstörungsfreien Mechanismen. Die gewonnen Daten wurden mit experimentellen Daten verglichen. Weiterhin wurden die Spektren von verschiedenen Purinen und Adenin modelliert und mit experimentellen Daten verglichen bzw. für zukünftige experimentelle Untersuchungen generiert.

Veröffentlichungen

2016 **The *a*SPECT experiment - an overview and latest results**, *Eingeladener Vortrag*, Seminar am Instituut voor Kern- en Stralingsfysica, K.U. Leuven.

2016 **The *a*SPECT experiment - current status of the analysis**, *Poster*, Physics of fundamental Symmetries and Interactions PSI2016.

2016 **The *a*SPECT experiment - an overview and latest results**, *Gruppenbericht*, Verhandlungen DPG 4/2016, HK 26.1.

2016 **The *a*SPECT experiment - an overview and latest results**, *Vortrag*, International Workshop: Probing Fundamental Symmetries and Interactions with UCN.

2016 **The *a*SPECT experiment - an overview and latest results**, *Gruppenbericht*, Verhandlungen DPG 4/2016, HK 26.1.

2015 **The *a*SPECT experiment - an overview and latest results**, *Vortrag*, Status Treffen DFG Schwerpunkt 1491.

2015 **Latest results from *a*SPECT**, *Eingeladener Vortrag*, NPP Seminar, Institute Laue-Langevin.

2014 **Latest results from the *a*SPECT experiment**, *Talk*, PANIC14 preceedings, DOI:10.3204/DESY-PROC-2014-04/72.

2014 **Current status of *a*SPECT**, *Vortrag*, Verhandlungen DPG 2/2014, HK 9.6.

2013 **Investigation of systematic uncertainties of the *a*SPECT experiment**, *Poster*, Physics of fundamental Symmetries and Interactions PSI2013.

2013 **aSPECT, prepared for a new physics run**, *Vortrag*, Verhandlungen DPG 2/2013, HK 78.5.

2012	**Improvements of the *a*SPECT retardation spectrometer**, *Vortrag*, Verhandlungen DPG 3/2012, HK 33.8.
2011	**Measurement with the *a*SPECT experiment**, *Vortrag*, Status Treffen DFG Schwerpunkt 1491.
2011	**Untersuchung der Topologie von Neutronenstößen in Ge-Bolometern zur Suche nach Dunkle Materie**, *Vortrag*, Verhandlungen DPG 2/2011, HK 6.8.

Lehrtätigkeiten

Vorlesungen

| WS 2014/15 | **Übungsleiter**, *Einführung in die Neutronenphysik*, Johannes Gutenberg-Universität Mainz. |

Praktika

WS 2011/12 - WS 2012/13	**Betreuer**, *Fortgeschrittenenpraktikum*, Johannes Gutenberg-Universität Mainz.
WS 2009/10 - WS 2010/11	**Betreuer**, *Praktikum für Nebenfächler*, Karlsruher Institut für Technologie.
SS 2008	**Betreuer**, *Praktikum in Physik für Maschinenbauer*, Karlsruher Institut für Technologie.

Studium

WS 2005/06 - WS2010/11	**Physik**, *Diplom*, Karlsruher Institut für Technologie, Note: 1,9.
WS 2008/09 - SS 2009	**Physik**, *Master of Physics in Optoelectronics and Lasers*, with Honours of the Second Class (Upper Division), Heriot-Watt University (Schottland).
WS 2003/04 - WS 2004/05	**Nanowissenschaften**, *Bachelor (kein Abschluss)*, Universität Basel (Schweiz), Wechsel zu Physik.

Schulausbildung

| 1994 - 2003 | **Scheffel-Gymnasium**, *Abitur*, Bad Säckingen, Note: 1,7. |
| 1990 - 1994 | **Grund- und Hauptschule**, *Wehr-Öflingen*. |

Computerkenntnisse

Linux	**sehr gut**.
LaTeX	**sehr gut**.
C++	**sehr gut**.
ROOT	**sehr gut**.

Geant4	**gut**.
Office Prg	**gut**.
Perl	**Grundkenntnisse**.

▬ Sprachen

Englisch	**sehr gut**, *in Wort und Schrift.*
Latein	**Grundkenntnisse**, *Großes Latinum.*
Altgriechisch	**Grundkenntnisse**, *Græcum.*